Structure–Property Relationships in Framework Materials: Anomalous Mechanics by Design

Ines E. Collings

Balliol College



A thesis submitted for the degree of

Doctor of Philosophy

Department of Chemistry

University of Oxford

Trinity Term 2014

Declaration

This dissertation is the result of my own original work, and where it draws on the work of others, this is acknowledged at the appropriate points in the text. This dissertation has not been submitted in whole or in part for a degree at this or any other institution.

Ines Collings

Structure–Property Relationships in Framework Materials: Anomalous Mechanics by Design

Ines E. Collings, Balliol College, Trinity Term 2014
A thesis submitted for the degree of Doctor of Philosophy to the
division of Mathematics, Physical and Life Sciences at the University of Oxford

Abstract

Framework materials that contain *molecular* bridging ligands between metal nodes—as seen in coordination polymers—not only give rise to enhanced structural diversity, but also to a range of useful and unusual mechanical properties. This thesis demonstrates the general structure–property relationships that are developed for coordination polymers in order to enable prediction and design of their mechanical properties, and hence structural flexibility. Variable-temperature and -pressure diffraction experiments are employed for the determination of their mechanical properties, namely by calculating thermal expansion and compressibility coefficients. The anomalous and varied mechanical responses observed are rationalised by the important structural features, or the so-called mechanical building units (XBUs), of the coordination polymers. The XBUs are considered within the setting of framework topology, geometry, and composition in order to establish general design principles for targeting different degrees of flexibility within coordination polymers. The XBUs are identified first in silver(I) 2-methylimidazolate, Ag(mim), a framework which is comprised of structural motifs of varying strength, namely argentophilic interactions, hinge points and metal–ligand bonding. The anomalous mechanical responses in Ag(mim) are shown to be rationalised entirely by the XBUs present in the structure. The XBU abstraction is then applied to a range of other coordination polymers and shown to correspond directly with the anomalous responses known in these materials. The metal–ligand–metal linker XBU is investigated further in both cadmium imidazolate, $Cd(im)_2$, and zinc cyanide, $Zn(CN)_2$. Here, the linker chemistries are completely different between the two frameworks, but the diamondoid arrangement of the linkers, and thus the topology, is the same. The structural responses of the two frameworks are examined to unravel the extent of topology- and chemistry-driven mechanics. It is found that the topology dominates the atomic displacements of both frameworks, indicating the existence of common soft-mode dynamics which are likely to extend to other coordination polymers with the same topology. The three-dimensional framework-hinging XBUs in zinc isonicotinate, $Zn(ISN)_2$, and indium deuterium terephthalate, $InD(BDC)_2$, are considered next. These frameworks have the same topology but contrasting framework geometries, evident from the differing c/a-lattice parameter ratios. In this case, a geometric formalism is derived which can predict the direction of framework mechanical anisotropy in $Zn(ISN)_2$ and $InD(BDC)_2$ and other uniaxial coordination polymers. Finally, a family of ABX_3-type transition metal(II) formates are investigated, where both the B-site and A-site cations are varied. The chemical modifications give rise to variations in B- or A-site cation sizes, which are found to correlate with the magnitude of mechanical responses. These structure–mechanical property relationships—based upon framework topology, geometry and composition—are presented in separate chapters, and in each case generalised so that they can be applied to a range of coordination polymers. Hence the design principles determined here can provide the materials science community with an intuition on the type and magnitude of responses possible in these materials under different external stimuli.

Publications

I. E. Collings, M. G. Tucker, D. A. Keen, and A. L. Goodwin, Static disorder and local structure in zinc(II) isonicotinate, a quartzlike metal–organic framework, *Z. Kristallogr.*, 2012, **227**, 313–320.

J. M. Ogborn, I. E. Collings, S. A. Moggach, A. L. Thompson, and A. L. Goodwin, Supramolecular mechanics in a metal–organic framework, *Chem. Sci.*, 2012, **3**, 3011–3017.

I. E. Collings, A. B. Cairns, A. L. Thompson, J. E. Parker, C. C. Tan, M. G. Tucker, J. Catafesta, C. Levelut, J. Haines, V. Dmitriev, P. Pattison, and A. L. Goodwin, Homologous critical behaviour in the molecular frameworks $Zn(CN)_2$ and Cd(imidazolate)$_2$, *J. Am. Chem. Soc.*, 2013, **135**, 7610–7620.

I. E. Collings, M. G. Tucker, D. A. Keen, and A. L. Goodwin, Geometric switching of linear to area negative thermal expansion in uniaxial metal–organic frameworks, *CrystEngComm*, 2014, **16**, 3498–3506.

Acknowledgements

Firstly, I am extremely thankful to my supervisor Prof Andrew Goodwin for his enthusiasm, support and guidance throughout this project. From local structure, phonons, paper writing, presentations, mathematical derivations, to the making of a perfect figure, I have learned a lot from Andrew over the course of this DPhil. I couldn't have hoped for a more brilliant and kind supervisor.

I would like to thank colleagues who have helped with all the diffraction data collected for this investigation and for my greater understanding of diffraction. In particular, I am indebted to Dr Amber Thompson and Dr Phil Wiseman for single-crystal and powder diffraction at Oxford, Prof David Keen and Dr Matthew Tucker at ISIS for neutron diffraction, and Dr Stephen Moggach at the University of Edinburgh for the high-pressure single-crystal diffraction. I am thankful to Dr Julia Parker and Dr Chiu Tang (I11, Diamond), and Dr Vladimir Dmitriev (ESRF), Dr Philip Pattison (ESRF) and Dr Julian Haines (University of Montpellier) for the synchrotron powder diffractions they collected on $Cd(im)_2$ and $Zn(CN)_2$.

I am very grateful for the help I have had with regards to the use of different programs, particularly from: Josh M. and Nick for TOPAS; Dr Richard Cooper and Nick for CRYSTALS; Leila, Richard, Matt C. and Andrew for Fortran programming; Callum, Nick and Andrew for RMCPROFILE; and Dave, Matt T. and Nick for GUDRUN. I am thankful for the specific computational codes written by Nick, Matt C., and Andrew, which I have used.

Everyone in the Goodwin group has helped in this investigation, be it through discussions, keeping me up to date with the literature or creating a great work environment. Thanks to Andrew C., Josh H., Joe P., Callum, Matt C., Nick, Jasper, Paul, and Peter. In particular, there are collaborative aspects to this thesis in Chapters 3 and 4 for which I am indebted to Joseph Ogborn and Andrew Cairns, respectively. I have appreciated discussions with Matt C., Josh H., and Andrew C., as well as Josh and Andrew's help with the high-throughput Diamond experiment. I am especially grateful to Nick who has helped with many queries I've had over the years! Thanks for the social secretaries Andrew C. and Karim for organising many events (I did come to a few pub quizzes!), and to all the master students who were part of the group: Joe, Ed, Sarah, Vanessa, Charlotte,

Sarah, Alex, Max, Tim, Chloe, Will, Chris, Elena, Jamie, and the ChemCryst past and present members.

Finally, I am extremely grateful to Andrew, Nick, Paul, and Neil for their comments and suggestions on reading this thesis. I would also like to thank Dr François-Xavier Coudert and Prof Simon Clarke for agreeing to examine this thesis.

On a more personal level, I am thankful to Holly, Carla, Sara, and Sylvain who have encouraged and motivated me during thesis writing, and also provided me with delicious meals and desserts to keep me going. The Balliol MCR at Holywell Manor has been a great environment where I've met many amazing people and friends. In particular I want to thank Carla, Sara, Aoife, Phoebe, Rahul, Seb, Stephen, Martha, Georgina, Indrek, Gabi, Andy, Thea, the Nathans, Alec, Tom, the Adams, and to my chemist friends: Holly (also lunch buddy!), Ed, and Emma for making my time at Oxford so enjoyable! I am also very grateful to my friends Izzie, Louisa and Rachael for their great friendship over the years. Thanks to my family: my loving parents Lydia and Neil, and my amazing siblings Emma and Ernest for their support and their many visits to Oxford, and to my caring grandparents Marie and Simon. Lastly, I would like to thank Sylvain who has supported and encouraged me throughout my DPhil: from listening to all my conference talks, helping me with the cooking for the 'Group Come Dine with me' evenings, to the many fun travelling adventures we have shared.

Contents

List of Figures **xi**

List of Tables **xvi**

1 Introduction **1**

1.1 Dynamical properties of oxides . . . 3

1.1.1 Perovskites . . . 3

1.1.2 Silica . . . 7

1.2 Structures of coordination polymers . . . 9

1.2.1 Metal–cyanide frameworks . . . 11

1.2.2 Metal–organic frameworks (MOFs) . . . 12

1.2.2.1 'Breathing' MOFs . . . 14

1.3 Mechanical properties of framework materials . . . 16

1.3.1 Thermal expansion . . . 18

1.3.2 Compressibility . . . 25

1.3.3 Elastic properties . . . 31

1.4 Structure–property relationships . . . 35

1.5 Thesis structure . . . 36

2 Methods **39**

2.1 Synthesis of coordination polymers . . . 39

2.2 Diffraction techniques . . . 40

2.2.1 Single-crystal X-ray diffraction . . . 41

2.2.2 High-pressure single-crystal X-ray diffraction . . . 43
2.2.3 Powder X-ray diffraction . . . 44
2.2.4 Neutron total scattering . . . 46
2.2.4.1 Data correction . . . 47
2.2.4.2 Reverse Monte Carlo . . . 49
2.3 Thermal expansion and compressibility determination . . . 50

3 Mechanical Building Units 52
3.1 Structure of Ag(mim) . . . 53
3.2 Experimental details of Ag(mim) . . . 54
3.2.1 Synthesis . . . 54
3.2.2 Variable-temperature single-crystal X-ray diffraction . . . 54
3.2.3 Variable-pressure single-crystal X-ray diffraction . . . 55
3.2.4 Single-crystal data solution and refinement . . . 56
3.2.5 Variable-temperature powder X-ray diffraction . . . 56
3.3 Temperature- and pressure-induced mechanics of Ag(mim) . . . 56
3.4 Mechanical building units of Ag(mim) . . . 58
3.5 Discussion: Generality of XBUs . . . 64
3.6 Summary . . . 66

4 Topology 67
4.1 Structures of $Zn(CN)_2$ and $Cd(im)_2$ . . . 68
4.2 Experimental details for $Zn(CN)_2$ and $Cd(im)_2$ . . . 69
4.2.1 Synthesis . . . 69
4.2.2 Variable-temperature single-crystal X-ray diffraction . . . 70
4.2.3 Variable-pressure single-crystal X-ray diffraction . . . 71
4.2.4 Variable-temperature powder X-ray diffraction . . . 71
4.2.5 Variable-pressure powder X-ray diffraction . . . 72
4.3 Background on the NTE mechanism of $Zn(CN)_2$ . . . 74
4.4 Variable-pressure behaviour of $Zn(CN)_2$ . . . 75

4.4.1 Phase transition mechanism . . . 76
4.4.2 Compressibilities . . . 77
4.5 Variable-temperature behaviour of $Cd(im)_2$ . . . 80
4.5.1 Expansivities . . . 81
4.5.2 Critical behaviour . . . 82
4.6 Variable-pressure behaviour of $Cd(im)_2$ . . . 85
4.6.1 Phase transition mechanism . . . 86
4.6.2 Compressibilities . . . 86
4.7 Discussion: Homologous behaviour of $Zn(CN)_2$ and $Cd(im)_2$ . . . 88
4.7.1 Mechanical properties . . . 88
4.7.2 Critical behaviour . . . 90
4.8 Summary . . . 94

5 Geometry **95**

5.1 Structures of $Zn(ISN)_2$ and $InH(BDC)_2$ . . . 96
5.2 Experimental details of $Zn(ISN)_2$ and $InD(BDC)_2$ . . . 97
5.2.1 Synthesis . . . 97
5.2.2 Variable-temperature neutron powder diffraction . . . 98
5.3 Temperature-induced mechanics of $Zn(ISN)_2$ and $InD(BDC)_2$ . . . 100
5.4 Geometric formalism . . . 103
5.5 Discussion: Generality of geometric formalism . . . 106
5.6 Summary . . . 112

6 Composition **113**

6.1 Structures of $[A][M(HCOO)_3]$ . . . 114
6.2 Experimental details of $[A][M(HCOO)_3]$ . . . 117
6.2.1 Synthesis . . . 117
6.2.2 Variable-temperature single-crystal X-ray diffraction . . . 118
6.2.3 Variable-temperature powder X-ray diffraction . . . 119
6.3 Rietveld fits of $[A][M(HCOO)_3]$ . . . 120

6.4 Temperature-induced mechanics of [A][M(HCOO)$_3$] . . . 123
6.4.1 Geometric formalism in uniaxial [A][M(HCOO)$_3$] . . . 132
6.5 Discussion: Composition-dependent mechanics . . . 136
6.6 Summary . . . 138

7 Conclusions **139**

Bibliography **143**

A Supporting information for Chapter 3 **172**
A.1 Principal axes . . . 172
A.2 Empirical equation derivatives for T and p . . . 173
A.3 Energy cost of transverse vibrations . . . 173

B Supporting information for Chapter 4 **174**
B.1 Absorption correction for Cd(im)$_2$ . . . 174
B.2 Empirical equation derivative for p . . . 175
B.3 XBU-driven lattice parameter evolutions for Zn(CN)$_2$-II and Cd(im)$_2$ . . . 175
B.4 Local structure evolutions for Zn(CN)$_2$-II and Cd(im)$_2$ . . . 177
B.5 Polyhedral tilt parameter for Cd(im)$_2$ . . . 178
B.6 Individual order parameters for Cd(im)$_2$ and Zn(CN)$_2$ . . . 179

C Supporting information for Chapter 5 **181**
C.1 IGA measurement of Zn(ISN)$_2$ . . . 181
C.2 Rietveld fits for Zn(ISN)$_2$·guest and InD(BDC)$_2$·guest . . . 182
C.3 Variable-temperature lattice parameter data . . . 183
C.4 Framework angle expansivity derivation . . . 184
C.5 Lattice parameter evolutions for desolvated Zn(ISN)$_2$ and InD(BDC)$_2$ . . . 188

D Supporting information for Chapter 6 **191**
D.1 Rietveld fits for [A][M(HCOO)$_3$] . . . 191
D.1.1 Phase transitions . . . 200

D.2 Lattice parameter evolutions for [A][M(HCOO)$_3$] 201

E Local structure and dynamics in MOFs **206**

E.1 Low-temperature dynamics of Zn(ISN)$_2$ 207

E.1.1 Experimental 207

E.1.1.1 Neutron total scattering measurements 207

E.1.1.2 Total scattering data correction 207

E.1.1.3 Rietveld refinement 208

E.1.1.4 Reverse Monte Carlo refinement 209

E.1.2 Average structure of Zn(ISN)$_2$ 211

E.1.3 Local structure of Zn(ISN)$_2$ 213

E.1.4 Discussion 217

E.1.5 Summary 219

E.2 Ferroelectric ordering in [NH$_4$][Zn(HCOO)$_3$] 220

E.2.1 Experimental 221

E.2.1.1 Synthesis 221

E.2.1.2 Neutron total scattering measurements 222

E.2.1.3 Total scattering data correction 222

E.2.1.4 Rietveld refinement 223

E.2.1.5 Reverse Monte Carlo refinement 224

E.2.2 Temperature-induced mechanics 226

E.2.3 Average structure of [N(H/D)$_4$][Zn(DCOO)$_3$] 227

E.2.4 Local structure of [N(H/D)$_4$][Zn(DCOO)$_3$] 228

E.2.5 Tracking the order–disorder transition with RMC 231

E.2.6 Discussion and future work 233

E.2.7 Summary 234

E.3 Conclusions 235

F CD contents **236**

List of Figures

1.1 Dimensionalities and topologies of frameworks 2

1.2 Ideal perovskite structure 4

1.3 Critical behaviour of $PbTiO_3$ and $SrTiO_3$ 5

1.4 α–β phase transition in quartz and cristobalite 8

1.5 Common ligands used in the synthesis of coordination polymers 9

1.6 The three generations of porous coordination polymers 10

1.7 The Prussian Blue and $Zn(CN)_2$ structures 11

1.8 Structures of $Zn[Au(CN)_2]_2$ and $Ag_3[Co(CN)_6]$ 12

1.9 Structures and SBUs of MOF-5, HKUST-1, and MIL-88B 13

1.10 Binding angles in $Zn(im)_2$ and SiO_2 14

1.11 The six 'breathing' classes 15

1.12 Structures and breathing transitions of MIL-53 and MIL-88B 16

1.13 Anharmonic bonding potential 19

1.14 Transverse and longitudinal vibrations of node–link–node units 20

1.15 Schematic representation of RUMs and their visualisation in β-cristobalite 21

1.16 Schematic representation of a wine-rack hinging mechanism 24

1.17 Structures of MOFs that exhibit hinging mechanisms 24

1.18 Induced uniaxial strain in 2D and 1D frameworks 29

1.19 Elastic modulus *versus* hardness materials property map 32

1.20 Directional Young's moduli for sodalite, ZIF-8, and MIL-53 33

2.1 H-cell setup 40

2.2 Single-crystal and powder diffraction images 42
2.3 Merrill-Bassett diamond anvil cell 43
2.4 I11 diffractometer 46
2.5 GEM diffractometer 48

3.1 Crystal structure of Ag(mim) 53
3.2 Lattice parameter evolutions, expansivities and compressibilities for Ag(mim) . . . 57
3.3 XBUs of Ag(mim) 59
3.4 XBU expansivities and compressibilities of Ag(mim) 60
3.5 NLC–PLC transition in Ag(mim) 61
3.6 Thermal parameters of 2-methylimidazolate 62
3.7 XBU prediction summary 64
3.8 XBUs in MOF-5 and MIL-53 65

4.1 Crystal structures of $Cd(im)_2$, $Zn(CN)_2$, and cristobalite 69
4.2 Rietveld fits for $Cd(im)_2$ at 473 K and 680 K 73
4.3 Pressure-dependent lattice parameters and structural changes for $Zn(CN)_2$ 76
4.4 Rietveld fit for $Zn(CN)_2$-II at 1.85 GPa 77
4.5 Compressibilities of $Zn(CN)_2$ 79
4.6 XBU relationships to lattice parameters in $Zn(CN)_2$-II 80
4.7 Temperature-induced lattice parameter evolutions for $Cd(im)_2$ 81
4.8 Critical behaviour in $Zn(CN)_2$ and $Cd(im)_2$ 82
4.9 Temperature-induced polyhedral tilt evolution in $Cd(im)_2$ 83
4.10 Thermal variation of the aspect ratios in pairwise CdX_4 columns 84
4.11 Pressure-dependent lattice parameter and φ evolutions in $Cd(im)_2$ 86
4.12 High-pressure phase transition in $Cd(im)_2$ 87
4.13 Calculated phonon dispersion curves for $Zn(CN)_2$ 88
4.14 Cu_2O structure and its translational modes 89
4.15 Order parameters for $Cd(im)_2$ and $Zn(CN)_2$ 91
4.16 Correspondence of $Zn(CN)_2$ and $Cd(im)_2$ with brookite 92

4.17 Packing efficiency at high p and low T 93

5.1 Uniaxial compression of honeycomb lattices 96
5.2 Framework structures of $Zn(ISN)_2$ and $InH(BDC)_2$ 97
5.3 Rietveld fits for $Zn(ISN)_2$ and $InD(BDC)_2$ 99
5.4 Relative lattice parameter evolution and expansivities for $Zn(ISN)_2$ and $InD(BDC)_2$ 101
5.5 r and θ evolutions, and framework hinging in $Zn(ISN)_2$ and $InD(BDC)_2$ 102
5.6 Calculated CTEs at different ρ values for $Zn(ISN)_2$ and $InD(BDC)_2$ 105
5.7 Unit cell relation of a single and double net of $InD(BDC)_2$ 107
5.8 The **r** vector in $[NH_4][M(HCOO)_3]$ 109
5.9 Diamondoid frameworks ordered by observed ρ values 111

6.1 Structures of $[C(NH_2)_3][Co(HCOO)_3]$ and $BaTiO_3$ 114
6.2 Ferroelectric phase transition in $[(CH_3)_2NH_2][Mn(HCOO)_3]$ 115
6.3 Molecular structures of the A-site cations 116
6.4 The octahedral tilts in $[A][M(HCOO)_3]$ 122
6.5 Variable-temperature lattice parameter evolutions for $MeNH_3$-Mn 123
6.6 CTEs as a function of metal cation size in $MeNH_3$-M and Gua-M families 125
6.7 Metal cation size dependence of U_{iso} in $MeNH_3$-M and T_c in $[A][M(HCOO)_3]$ . . . 126
6.8 Jahn-Teller distortion in Gua-Cu and XBUs in orthorhombic $[A][M(HCOO)_3]$ . . . 127
6.9 XBU-derived lattice expansivities in $MeNH_3$-M and Gua-M families 128
6.10 Equivalent XBU cells in different $[A][M(HCOO)_3]$ structures 129
6.11 XBU-driven expansivities for $[A][Mn(HCOO)_3]$ with different A-site cations 131
6.12 XBU relationships to lattice parameters in hexagonal $[A][M(HCOO)_3]$ 133
6.13 Types of framework hinging 135
6.14 Correlation between metal cation size and CTE in the Prussian Blue analogues . . 136
6.15 Young's moduli and expansivities for Me_2NH_2-M structures 137

A.1 Binding angle change for a 1% reduction in Zn–im–Zn unit distance 173

B.1 Computed X-ray absorption for $Cd(im)_2$ 174

B.2 XBU relationships to the lattice parameters in $Cd(im)_2$ . . . 175
B.3 XBU-driven lattice parameter evolutions for $Zn(CN)_2$-II and $Cd(im)_2$ . . . 176
B.4 Evolutions of local structure parameters in $Zn(CN)_2$-II and $Cd(im)_2$ . . . 177
B.5 Schematic illustration of φ angle calculation for $Cd(im)_2$ . . . 178
B.6 Evolutions of the four φ angles with temperature in $Cd(im)_2$ . . . 179
B.7 Metal and ligand order parameters for $Zn(CN)_2$ and $Cd(im)_2$ . . . 179
B.8 Metal and ligand order parameters towards brookite for $Zn(CN)_2$ and $Cd(im)_2$ . . 180

C.1 Intelligent gravimetric analysis spectrum of $Zn(ISN)_2$ . . . 181
C.2 Rietveld fits of $Zn(ISN)_2$·guest and $InD(BDC)_2$·guest . . . 182
C.3 The **r** vectors and framework angles in $InD(BDC)_2$ . . . 185
C.4 Relative lattice parameter evolutions of desolvated $Zn(ISN)_2$ and $InD(BDC)_2$ . . . 190

D.1 Rietveld fits for $MeNH_3$-M with M = Mn, Fe, Co . . . 192
D.2 Rietveld fits for $MeNH_3$-M with M = Mg, Zn, Cd . . . 193
D.3 Pawley fits for $MeNH_3$-Cu and Rietveld fits for Aze-Mn . . . 194
D.4 Rietveld fits for $EtNH_3$-Mn and Me_2NH_2-Cu . . . 195
D.5 Rietveld fits for Me_2NH_2-M with M = Mn, Co, Zn . . . 196
D.6 Rietveld fits for Gua-M with M = Mn, Fe, Co . . . 197
D.7 Rietveld fits for Gua-M with M = Ni, Cu, Zn . . . 198
D.8 Rietveld fits for Gua-M with M = Cd, Mg . . . 199
D.9 Rietveld fits for $MeNH_3$-Cd and Me_2NH_2-M with M = Mn, Co, Zn . . . 200
D.10 Temperature-dependent lattice parameters for the $MeNH_3$-M family . . . 202
D.11 Temperature-dependent lattice parameters for the Gua-M family . . . 203
D.12 Temperature-dependent lattice parameters for the Me_2NH_2-M family and Gua-Cd 204
D.13 Temperature-dependent lattice parameters for $EtNH_3$-Mn, Aze-Mn, Me_2NH_2-Cu . 205

E.1 Differential cross-section data for $Zn(ISN)_2$ . . . 208
E.2 Rietveld fits and structures for $Zn(ISN)_2$ and $Zn(ISN)_2$·$4H_2O$ . . . 212
E.3 Average structure of $Zn(ISN)_2$ from Rietveld and RMC . . . 213

E.4 RMC fits of Bragg and $G(r)$ functions for $Zn(ISN)_2$ 215
E.5 $Zn(ISN)_2$ RMC bond angle distributions and polyhedra distortions 216
E.6 Calculated $G(r)$ for ordered and statically disordered models of $Zn(ISN)_2$ 218
E.7 Order–disorder transition in $[NH_4][Zn(HCOO)_3]$ 221
E.8 X-ray diffraction of $[N(H/D)_4][Zn(DCOO)_3]$ after different synthesis steps 222
E.9 Differential cross-section data for $[N(H/D)_4][Zn(DCOO)_3]$ 223
E.10 Crystalline and randomised RMC starting models for $[N(H/D)_4][Zn(DCOO)_3]$ . . . 225
E.11 Temperature-dependent lattice parameters for $[N(H/D)_4][Zn(DCOO)_3]$ 226
E.12 Rietveld fits with different H/D concentrations on the ammonium 227
E.13 GSAS Bragg, RMC Bragg, $D(r)$ and $F(Q)$ fits for $[N(H/D)_4][Zn(DCOO)_3]$ 229
E.14 Collapsed RMC configurations for $[N(H/D)_4][Zn(DCOO)_3]$ 230
E.15 N$\cdots$O partial distribution functions for $[N(H/D)_4][Zn(DCOO)_3]$ 231
E.16 Temperature evolution of σ_{z_N} and P_z values from RMC configurations 232
E.17 N$\cdots$O partial distribution functions for LT and HT models 233

List of Tables

1.1 CTEs of selected 3D frameworks 22

1.2 Compressibilities of selected 3D frameworks 30

1.3 The maximum and minimum Young's moduli of selected 3D frameworks 34

2.1 Neutron coherent and incoherent scattering lengths 47

3.1 Principal-axis expansivities and compressibilities of Ag(mim) 58

3.2 XBU expansivities and compressibilities of Ag(mim) 60

3.3 Expansivities and compressibilities of the Ag−mim−Ag unit 62

4.1 Original and XBU-driven compressibilities for $Zn(CN)_2$-II 78

4.2 Original and XBU-driven expansivities for $Cd(im)_2$ 82

4.3 Original and XBU-driven compressibilities for $Cd(im)_2$ 87

4.4 M and ligand coordinates for $Zn(CN)_2$, $Cd(im)_2$, anticuprite, and brookite 91

5.1 Lattice and XBU expansivities for $Zn(ISN)_2$ and $InD(BDC)_2$ 102

5.2 Lattice parameters and ρ values for $Zn(ISN)_2$ and $InD(BDC)_2$ 104

5.3 Expansivities and ρ values of quartz-like frameworks 106

5.4 Diamondoid frameworks with their observed and critical ρ values 111

6.1 Crystallographic details of $[A][Mn(HCOO)_3]$ 116

6.2 The $[A][Mn(HCOO)_3]$ compounds synthesised for this study 117

6.3 Lattice parameters and their expansivities for $[A][M(HCOO)_3]$ 124

6.4 XBU values and their expansivities for $[A][M(HCOO)_3]$ 130

6.5 Effective lengths of the A-site cation molecular ellipsoids 131

6.6 Original and XBU-driven expansivities for hexagonal [A][$M(HCOO)_3$] 132

C.1 Variable-temperature lattice parameters for $Zn(ISN)_2$ and $Zn(ISN)_2$·guest 183

C.2 Variable-temperature lattice parameters for $InD(BDC)_2$ and $InD(BDC)_2$·guest . . . 184

C.3 Derivations of θ_i in terms of a and r 186

C.4 Calculated and experimental α_θ values for $Zn(ISN)_2$ and $InD(BDC)_2$ 187

C.5 Lattice and XBU expansivities of desolvated $Zn(ISN)_2$ and $InD(BDC)_2$ 188

D.1 Calculated expansivities for orthorhombic and monoclinic Aze-Mn phases 201

E.1 Distance-window parameters applied in $Zn(ISN)_2$ RMC refinements 210

E.2 Crystallographic parameters for $Zn(ISN)_2$ at 10 K 211

E.3 Distance-window parameters applied in [$N(H/D)_4$][$Zn(DCOO)_3$] RMC refinements 224

E.4 Potentials applied in [$N(H/D)_4$][$Zn(DCOO)_3$] RMC refinements 225

Abbreviations

BDC^{2-}	benzene-1,4-dicarboxylate (also referred to as terephthalate)
BTC^{3-}	benzene-1,3,5-tricarboxylate
CCR	closed cycle refrigerator
CIF	crystallographic information file
CTE	coefficient of thermal expansion
dabco	1,4-diazabicyclo[2.2.2]octane
DAC	diamond anvil cell
DFT	density functional theory
DMF	dimethylformamide
DMSO	dimethylsufoxide
fu-L^1	alkoxy functionalised 1,4-benzenedicarboxylate
HKUST	Hong Kong University of science and technology
HP	high pressure
HT	high temperature
IGA	intelligent gravimetric analysis
im^-	imidazolate
ISN^-	isonicotinate
LFSE	ligand field stabilisation energy
lp	large pore
LT	low temperature
M	metal
MIL	Materials Institut Lavoisier
mim^-	2-methylimidazolate

MOF	metal–organic framework
NAC	negative area compressibility
NLC	negative linear compressibility
np	narrow pore
NTE	negative thermal expansion
pba^-	3-(pyridin-4-yl)benzoate
PDF	pair distribution function
PLC	positive linear compressibility
PSD	position sensitive detector
PTE	positive thermal expansion
PXRD	powder X-ray diffraction
RMC	reverse Monte Carlo
RUM	rigid unit mode
SBU	secondary building unit
SCXRD	single-crystal X-ray diffraction
XBU	mechanical building unit
ZIF	zeolitic imidazolate framework

Chapter 1

Introduction

Framework materials are network solids that contain nodal units connected *via* bridging linkers to form an extended lattice. Generally, metal cations or metal clusters are the nodes, and single-atom or molecular ligands provide the linkers. The coordination number and geometry of the node, as well as the binding sites of the linker, provide a way to design the framework dimensionality and connectivity,[1–4] and hence the framework topology [Fig. 1.1]. There are two broad categories of framework materials, namely those containing single-atom linkers as seen in oxides with O^{2-} bridges,[5] and those composed of *molecular* linkers, termed coordination polymers.[6] The choice of ligands that could be used in the synthesis of coordination polymers is essentially limitless; likewise there is a large variety of metal node binding geometries, giving rise to a vast chemical and structural diversity of coordination polymers. Considering framework topologies alone, their diversity reaches over 6620 unique types.[7]

In oxide frameworks there exist certain predictive tools to understand their dynamical and structural properties upon application of external stimuli such as temperature or pressure. Conversely, in the more recently studied coordination polymers, general rules to predict their behaviour are much less well determined; the situation is further complicated by the extensive number of structures known. From system-specific studies of coordination polymers, it is apparent that these materials show anomalous and varied mechanical properties to external stimuli.[8–11] These include negative thermal expansion (NTE, contraction upon heating),[8] negative linear compressibility

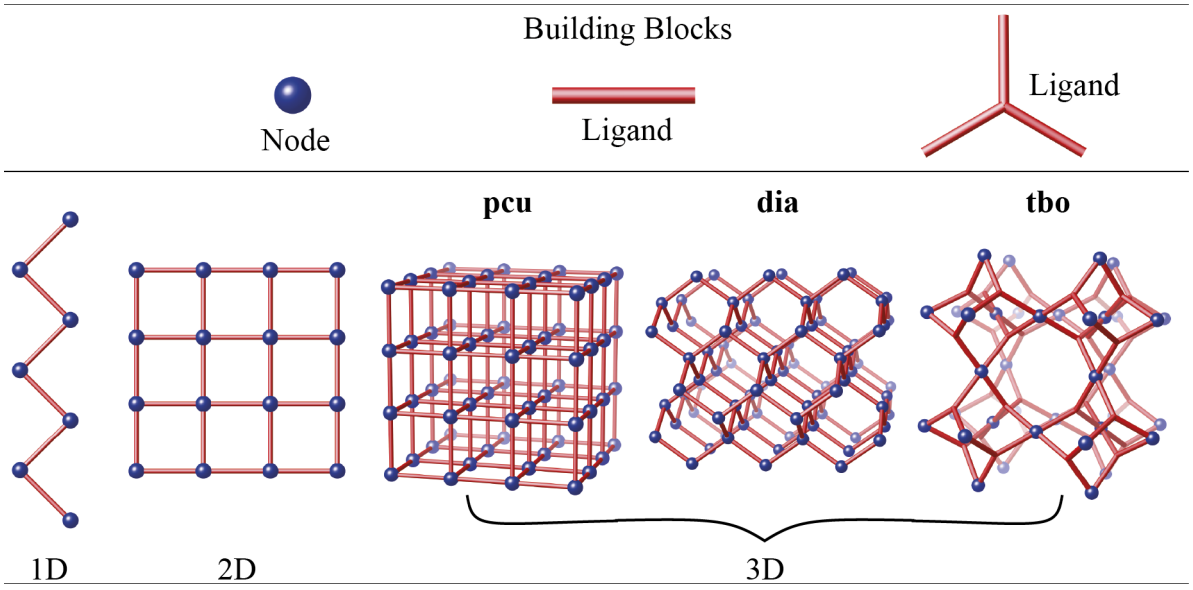

Figure 1.1: Schematic illustration of framework formation from different node coordination environments and binding geometries of the ligands, giving rise to different dimensionalities and topologies. The three-dimensional topologies include the primitive cubic (**pcu**), diamondoid (**dia**), and twisted boracite (**tbo**) nets.

(NLC, uniaxial expansion upon compression),[9] pressure- and temperature-induced amorphisation,[12,13] colossal magnitudes of positive thermal expansion (PTE) or linear compressibility (PLC) and extremely anisotropic thermal and elastic properties.[14] These anomalous mechanics—which can be orders of magnitudes greater than any such behaviour in oxides—indicate that coordination polymers exhibit unprecedented framework flexibility. The structural origin of this flexibility forms part of the main investigation of this thesis.

The structure of this introduction is as follows. The key dynamical properties of well-studied oxide materials are summarised first, and then a brief overview of the different types of coordination polymers of relevance to this thesis is given. The mechanical properties of oxides and coordination polymers are introduced by considering their expansivities, compressibilities and elastic properties, with particular focus on the mechanical behaviour of the latter frameworks. The existing structure–property relationships of coordination polymers are described, but what this thesis aims to show is that more general rules can be derived to quantify and predict framework mechanics in a much broader range of coordination polymers.

1.1 Dynamical properties of oxides

The key structural and dynamical properties are detailed for two important classes of oxides: perovskites and silica polymorphs. These families were chosen because they show important and well-studied dynamical behaviour that bear resemblance to those found in related coordination polymers. Their properties are, in part, elucidated by identifying the low-energy lattice vibrations, known as phonons.[15,16] Phonon energies and their wave-vector dependence can be measured experimentally using inelastic neutron or X-ray scattering, and Brillouin scattering; they can also be investigated computationally *via* molecular dynamics simulations, lattice dynamical and density functional theory (DFT) calculations.[17]

1.1.1 Perovskites

Perovskites have the common chemical formula ABO_3, where the A-site cation occupies the cavity space formed by the framework of corner-sharing BO_6 octahedra. The total charge on the A- and B-site cations must sum to six in order to counter-balance the anionic charge from the three oxide ions. This requirement can be fulfilled with a variety of combinations, such as $BaTiO_3$, $LaAlO_3$, $KMnO_3$, or $MgSiO_3$. The ideal perovskite structure is shown in Figure 1.2, and is referred to as the parent or aristotype perovskite.

The Goldschmidt tolerance factor (t) uses simple geometric rules to predict whether or not it is likely that a given perovskite will adopt the 'ideal' cubic symmetry (and whether the structure is even able to have the perovskite connectivity).[18] For the aristotype phase to form, t must be close to unity when relating the ionic radii of A (r_A), B (r_B), and O (r_O) ions in the following way

$$t = \frac{(r_A + r_O)}{\sqrt{2}(r_B + r_O)}. \tag{1.1}$$

It is relatively uncommon for t values to be close to unity at ambient conditions; examples of aristotype perovskites include $BaZrO_3$ and $SrTiO_3$ which have t values of 1.01 (ionic radii were

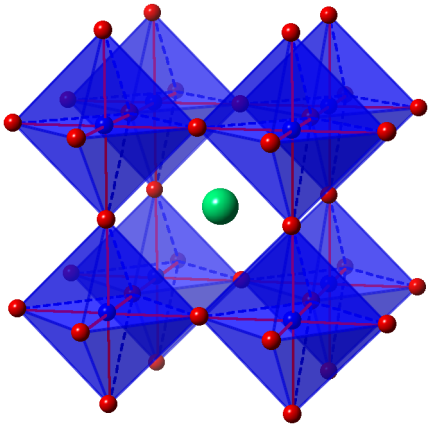

Figure 1.2: Ideal cubic perovskite with $Pm\bar{3}m$ symmetry, with A (green cation) at $\left(\frac{1}{2},\frac{1}{2},\frac{1}{2}\right)$, B (blue cations) at the origin and at the centre of the polyhedra, and O (red anions) at $\left(\frac{1}{2},0,0\right)$.

obtained from Ref. 19 for this calculation). However, the interesting physical properties of perovskites, such as ferroelectricity, ferromagnetism, colossal magnetoresistance, and superconductivity, will usually arise when t is not equal to one. This can be engineered by using contrasting sizes of A- and B-site cations, as well as doping on these sites, consequently leading to distortions in the structure.[20] These distortions are then propagated *via* the tilting of the BO_6 octahedra, or the off-centering of the B- or A-site cations,[21] and are responsible for the rich structural phase transitions of perovskites, essential for their physical properties.[20,22,23]

One of the most technologically important phase transitions within the perovskites is the ferroelectric phase transition, exemplified here in $PbTiO_3$.[24,25] At room temperature, $PbTiO_3$ has tetragonal symmetry with its cations and anions displaced in opposite directions along the c-axis, causing a net polarisation along that direction [Fig. 1.3(a)]. Upon heating, $PbTiO_3$ transforms to the aristotype $Pm\bar{3}m$ cubic perovskite. The overall amplitude of the atomic displacements relative to the high-symmetry coordinates acts as an order parameter, which can be used to quantify the displacive phase transition. This order parameter is equal to zero in the aristotype, and is non-zero in the low-symmetry phase. The transitions are, for the most part, categorised as first- or second-order based upon whether the order parameter exhibits a discontinuous or continuous change, respectively, at the transition temperature (T_c). The term 'critical phenomena' is used to encompass processes occurring in the vicinity of T_c.

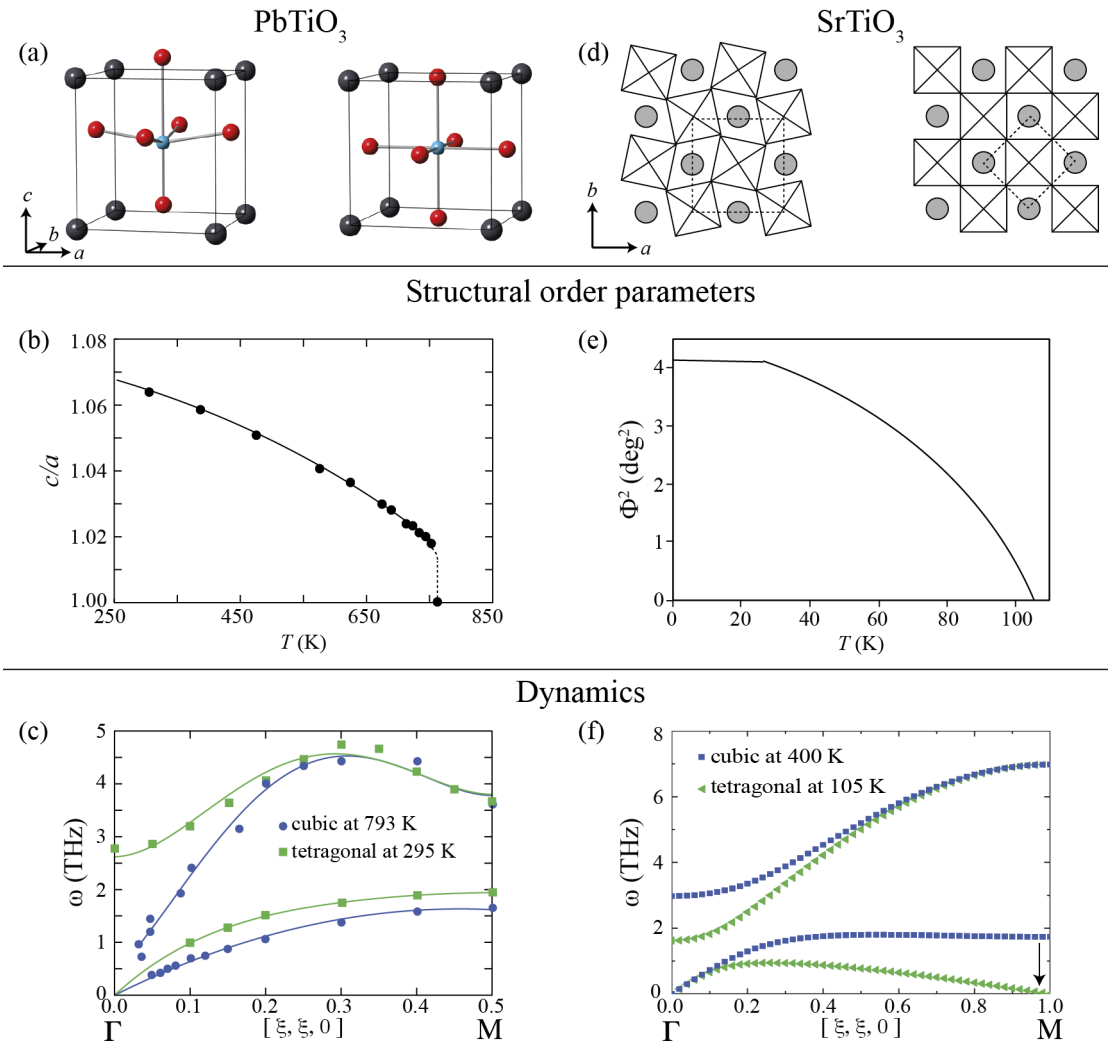

Figure 1.3: (a) First-order phase transition observed in $PbTiO_3$ upon heating to 490°C. In the distorted phase (left), the Ti^{4+} and O^{2-} ions are displaced in opposite directions but regularise in the aristotype phase (right) at 490°C. (b) Order parameter of $PbTiO_3$ using the c/a ratio as function of temperature; figure adapted from Ref. 24. (c) Low-energy phonon dispersion curves for the Γ to M points in reciprocal space for $PbTiO_3$; figure adapted from Ref. 26. (d) Second-order phase transition observed in $SrTiO_3$ at 108 K. The distorted low-temperature phase contains TiO_6 tilts (figure shows an exaggeration of these tilts), which decrease to zero in the aristotype phase; figure adapted from Ref. 27. (e) Order parameter of $SrTiO_3$ using the octahedral tilts as a function of temperature; figure adapted from Ref. 27. (f) Low-energy phonon dispersion curves for the Γ to M points in reciprocal space for $SrTiO_3$. The arrow indicates the phonon softening between the cubic and tetragonal phases; figure adapted with permission from Ref. 28, copyright 2011 by the American Physical Society.

In the case of $PbTiO_3$, the phase transition is first-order as can be seen in the discontinuous change of the c/a ratio as a function of temperature [Fig. 1.3(b)]. Phonon dispersion curves, obtained from inelastic neutron scattering experiments, show that the important mode softening

in $PbTiO_3$ occurs at the Γ point in reciprocal space $(0, 0, 0)$ [Fig. 1.3(c)], corresponding to an in-phase unit cell distortion of the Ti^{4+} and O^{2-} displacements. Conversely, $SrTiO_3$ exhibits a second-order phase transition upon cooling to 108 K, giving rise to the tilting of its TiO_6 octahedra [Fig. 1.3(d)]; the corresponding order parameter shows a continuous change in tilt angle of the octahedra [Fig. 1.3(e)]. The mode softening of the phonons—which are equivalent to those observed in $PbTiO_3$—is now at the M point in reciprocal space $\left(\frac{1}{2}, \frac{1}{2}, 0\right)$ [Fig. 1.3(f)]. This indicates that the phase transition will lead to a doubling of the lattice parameters in the **ab**-plane in order to accommodate the out-of-phase octahedral tilts. These characteristic low-energy phonon dispersion curves are very similar in compositionally varied perovskites—the differences lie in the energy scale and slopes of the phonon curves, which give rise to the variations in mode-softening location in reciprocal space.[16]

The conditions at which the phase transitions are observed in $PbTiO_3$ and $SrTiO_3$, and generally for any other compound, are dependent on their thermodynamic stabilities as formulated by the Gibbs free energy

$$G(T, p) = U + pV - TS, \tag{1.2}$$

where U, p, V, T, and S are the internal energy, pressure, volume, temperature and entropy, respectively. The equilibrium phases observed experimentally are those which have the lowest Gibbs free energy at the given p and T conditions. Phase transitions will arise upon variation of p and/or T in order to modify the packing efficiency. Dense structures will be favoured at high pressures due to the decrease in V, while open structures—such as the aristotype phases—will form at high T in order to accommodate the greater entropy, which is predominantly vibrational motion of atoms. Hence, displacive transitions of aristotype phases are often observed upon decrease in T and increase in p with respect to the aristotype p and T conditions.[29]

The set of general rules, namely the tolerance factor equation,[30] common phonon dispersion curves[16] and octahedral tilting patterns,[30–34] can all be used to understand and predict the structural and dynamical properties of perovskites. These are then crucial for the design of important physical properties in perovskites.

1.1.2 Silica

Silica (SiO_2) exists in a variety of crystalline structures and amorphous phases, such as α-quartz, β-cristobalite, and glass.[35] The majority of these polymorphs have tetrahedral SiO_4 environments in which each oxygen bonds to two neighbouring silicons to form an extended lattice of connected tetrahedra. The important geophysical properties of silica have driven many investigations into their structural and dynamical properties,[36–38] with a particular focus on the α (distorted)–β (high-symmetry) phase transitions in quartz and cristobalite [Fig. 1.4(a,b)].[39]

The important low-energy phonon modes in silica involve those which propagate throughout the crystal lattice while preserving bond lengths and coordination geometries of the SiO_4 or SiO_6 polyhedra.[42] These phonons correspond to rotations and translations of the polyhedra and are named rigid-unit modes (RUMs). As they are low in energy, they are natural candidates for mode-softening associated with displacive phase transitions.[15,42] Indeed, the α–β phase transition in quartz and cristobalite, and other displacive phase transitions in a number of silicates, occurs as a consequence of RUMs.[15,43,44] The α–β phase transitions in quartz and cristobalite are first-order, as can be seen in the discontinuities of the c/a ratio and the fractional unit-cell coordinate order parameters for quartz and cristobalite, respectively [Fig. 1.4(c,e)]. The mode softening of a particular phonon frequency in quartz is shown in Figure 1.4(d), where the frequency is seen to decrease to zero upon reaching T_c.

The RUM model not only gives insight into the displacive transitions in silica, but also can explain properties such as the transition temperature,[45] the role of critical fluctuations in framework structures,[46] and negative thermal expansion (which will be discussed later in Section 1.3.1).[37,47] The program CRUSH can be used to calculate RUMs for silica and many other framework materials,[48] consequently giving insight into structure dynamics[49,50] and displacive phase transition mechanisms.[51] CRUSH utilises a split-atom method where each atom that connects neighbouring polyhedra is split so that individual polyhedra can be treated as separate rigid bodies.[52] The split atoms are linked by fictitious stiff springs of zero equilibrium length, imposing a significant energy penalty should the pair of split atoms move apart.[53] Conversely, there is no energy cost associated with framework movement where none of the split atoms are separated.[53] Using lattice dynamical

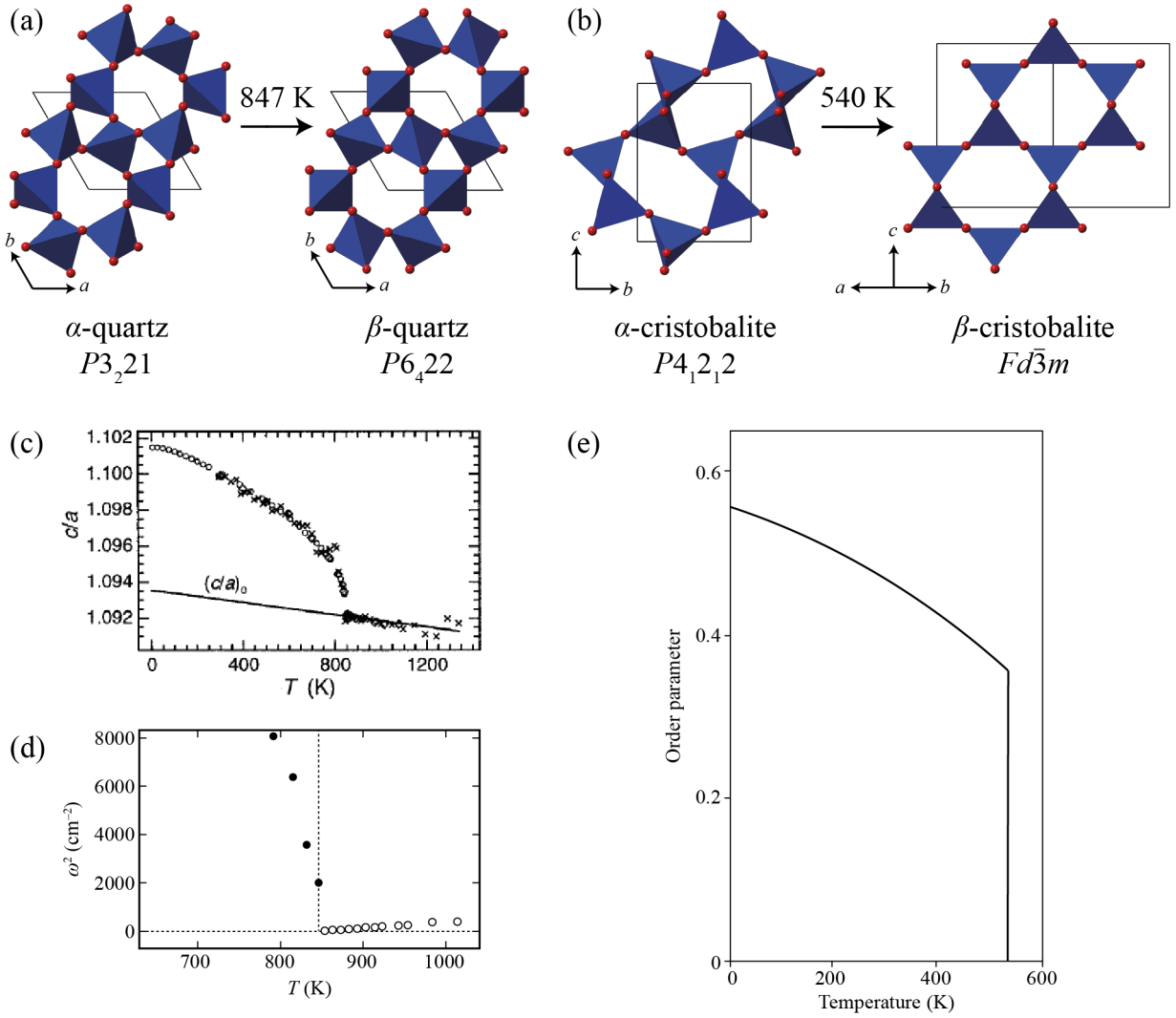

FIGURE 1.4: The α–β phase transition in (a) quartz and (b) cristobalite, where SiO_4 coordination environments are represented as tetrahedra. (c) Order parameter of the c/a evolution as a function of temperature for quartz; figure reproduced from Ref. 40. (d) The squared frequency (ω^2) dependence of a soft mode as a function of temperature, indicating the softening at T_c for quartz; figure adapted from Ref. 40. (e) The order parameter of the α–β cristobalite transition; figure adapted from Ref. 41. The order parameter is calculated using the symmetry-breaking coordinate shifts: $Q_s^2 = \left\{a_t^2\left[(x_{Si}-0.25)^2+(x_O-0.25)^2+(y_O)^2\right]+c_t^2(z_O-0.125)^2\right\}$, where the fractional coordinates x, y, z, and the lattice parameters a_t and c_t refer to the tetragonal α-cristobalite phase.[41]

calculations, the dynamical matrix for the low-energy phonons is determined,[48] and the RUMs are identified as the modes with zero frequency.[53,54]

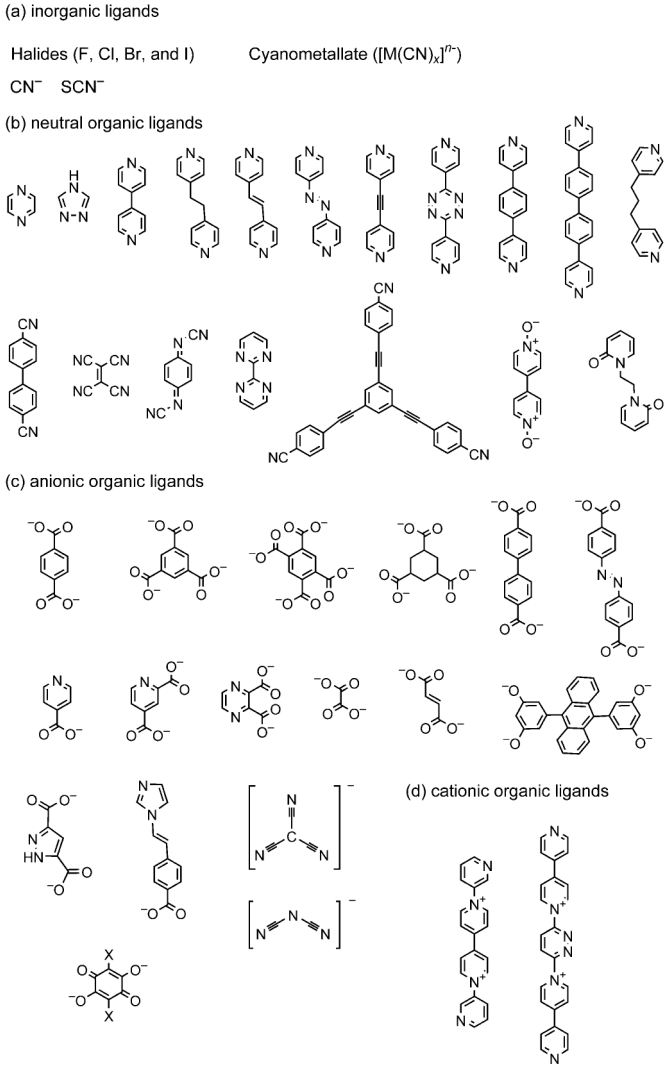

Figure 1.5: Examples of common ligands which are used in the synthesis of coordination polymers; figure reproduced from Ref. 6 with permission from John Wiley & Sons. The halides, and O^{2-} or OH^{-} (not shown) are employed in conjunction with molecular ligands to form a coordination polymer.

1.2 Structures of coordination polymers

There is an immense variety of ligands which can be used in coordination polymer synthesis; a selected few of these are shown in Figure 1.5. As well as the synthesis of metal–[molecular ligand]–metal connectivities, so-called 'hybrid' frameworks exist that contain inorganic connectivities, such as M–O–M, in conjunction with the metal–molecular connectivities.[55,56] This allows porosity to coexist with physical properties usually associated with dense solids, such as magnetism.[55] Other ways to create dense frameworks include interpenetration of the framework nets, or the presence of

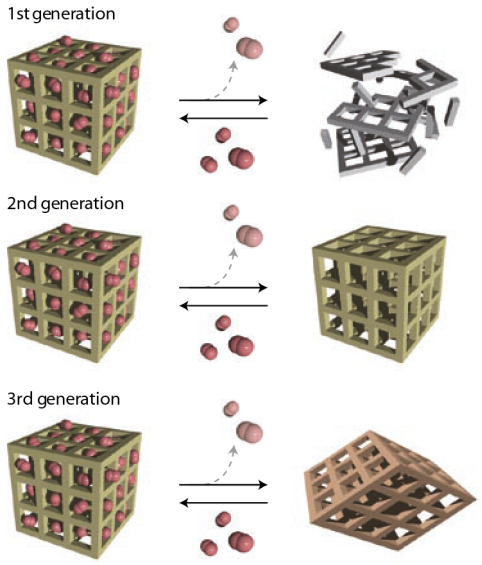

Figure 1.6: The three generations of porous coordination polymers which are identified upon guest removal. This process gives rise to one of the following: framework collapse, unchanged structure, or structural transformation that corresponds to first-, second- and third-generation coordination polymers, respectively. Figure reproduced from Ref. 64 with permission from Macmillan Publishers Ltd: Nature Chemistry, copyright 2009.

counterions within framework cavities. These frameworks can exhibit a range of properties, such as luminescence,[57] ferroelectricity,[58,59] magnetic ordering,[60,61] and non-linear optic behaviour.[62,63]

Porous coordination polymers are usually referred to as metal–organic frameworks (MOFs).[65] The naming terminology for these materials frequently involves the abbreviation of the institute of discovery (*e.g.* MIL for Materials of Institut Lavoisier), or is given as MOF-n where n is a number. For these materials, there exist three types of generation, identified by their corresponding behaviour upon guest removal from the framework pores [Fig. 1.6]. The guest solvent in MOFs acts as a template in synthesis, as known in the synthesis of porous zeolite inorganic solids.[66] Yet crucially the template in MOFs is neutral and does not bind strongly to the host framework, making porous MOFs readily accessible.[55] Porous MOFs have a multitude of different applications such as *in situ* catalysis,[67–69] drug delivery,[70–72] chemical sensing,[73–75] gas storage[76–80] and molecular separation.[81,82] In comparison to porous zeolites, the pore sizes in MOFs can be more than eight times larger.[55] Furthermore, the additional chemical and structural diversity found in MOFs can, for example, give rise to unique adsorption properties due to the coexistence of hydrophilic and hydrophobic regions.[83]

This thesis refers to MOFs interchangeably with coordination polymers, the latter being considered as the general term to encompass all types of extended metal–[molecular ligand] connectivities (regardless of porosity).[65] The structural chemistry of some important classes of coordination polymer of relevance to this thesis is discussed below; their dynamical and mechanical properties are examined in more detail in Section 1.3.

1.2.1 Metal–cyanide frameworks

The cyanide anion (CN^-) is arguably the simplest molecular ligand to be used in coordination chemistry. The first cyanide framework discovered was the synthetic pigment commonly known as Prussian Blue [Fig. 1.7(a)].[84,85] In many of the metal–cyanide frameworks, the cyanide ligand binds in a linear geometry to the metal centres; it is the coordination preference of the metal which dictates the topology observed. In the case of $Zn(CN)_2$, the same diamondoid topology of β-cristobalite is adopted, however, $Zn(CN)_2$ crystallises with two interpenetrated diamondoid nets because of the increased separation between metal nodes [Fig. 1.7(b)].[1]

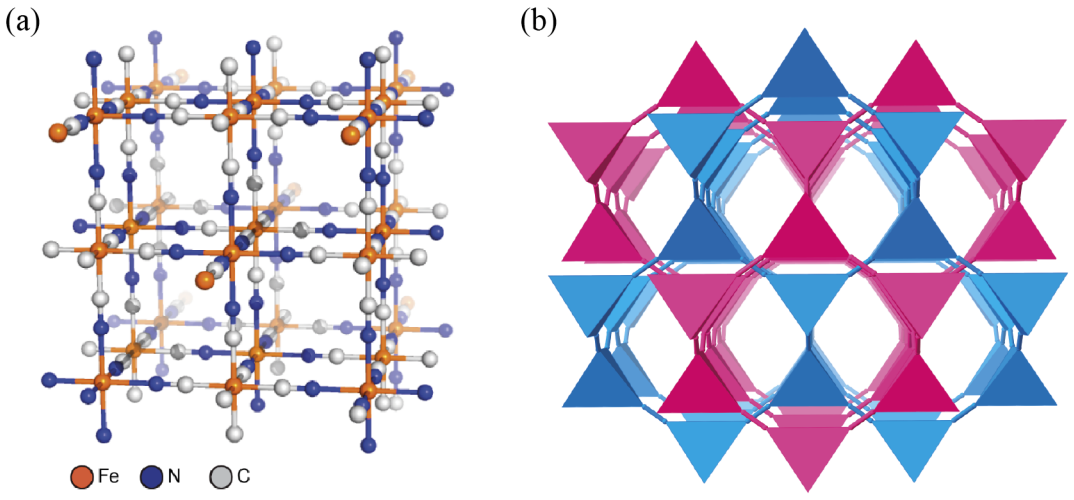

Figure 1.7: (a) Idealised structure of Prussian Blue, composed of octahedral Fe^{II} and Fe^{III} that are bridged by cyanide ligands to generate a cubic 3D array; figure reproduced from Ref. 86 with permission from Chemical Reviews, copyright 2013 American Chemical Society. (b) Two-fold interpenetration in $Zn(CN)_2$ with Zn^{2+} coordination environments shown as tetrahedra. The two nets are highlighted using different colours.

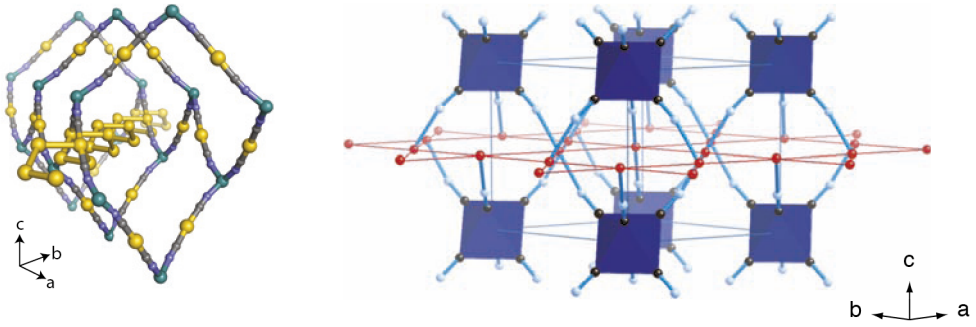

$Zn[Au(CN)_2]_2$ $Ag_3[Co(CN)_6]$

Figure 1.8: (*Left*) A structural representation of $Zn[Au(CN)_2]_2$, where one of the six interpenetrated nets is shown, with highlighted Au...Au interactions when considering all nets; figure reproduced from Ref. 9 with permission from Macmillan Publishers Ltd: Nature Materials, copyright 2013. (*Right*) $Ag_3[Co(CN)_6]$ structure with the Ag...Ag interactions highlighted in red in the **ab**-plane; figure reproduced from Ref. 8 with permission from AAAS.

Longer cyanide linkers can be made by using a two-coordinate metal ion such as Ag^+ or Au^+ to give dicyanoargentate $[Ag(CN)_2]^-$ or dicyanoaurate $[Au(CN)_2]^-$ linkers. These dicyanometallate linkers provide a near-linear binding geometry and double the node spacing to *ca* 10 Å in comparison to the Zn–CN–Zn units. Framework structures composed of these linkers include $Co[Ag(CN)_2]_3$ (preferentially written as $Ag_3[Co(CN)_6]$),[87] $Zn[Au(CN)_2]_2$,[88] and $In[Ag(CN)_2]_3$.[89] The M^{3+} ions in $Co^{III}[Ag(CN)_2]_3$ and $In^{III}[Ag(CN)_2]_3$ show preference for octahedral environments, giving the ReO_3 topology (perovskite topology without the A-site cation in the pore), while $Zn^{II}[Au(CN)_2]_2$ displays a tetrahedral environment around the Zn^{2+}, resulting in a quartz-like topology. These structures are all comprised of interpenetrated networks in order to occupy the void space created by using long linkers. This has the effect of forcing Au^+ or Ag^+ ions into close proximity [Fig. 1.8]—a feature of great importance when considering their mechanical properties (covered in Section 1.3).

1.2.2 Metal–organic frameworks (MOFs)

MOFs are typically synthesised by using a combination of long rigid ligands (usually containing aromatic cores) and secondary building units (SBUs; *i.e.* metal clusters) as nodes, providing a method for obtaining frameworks with large voids. So-called isoreticular MOFs can be readily

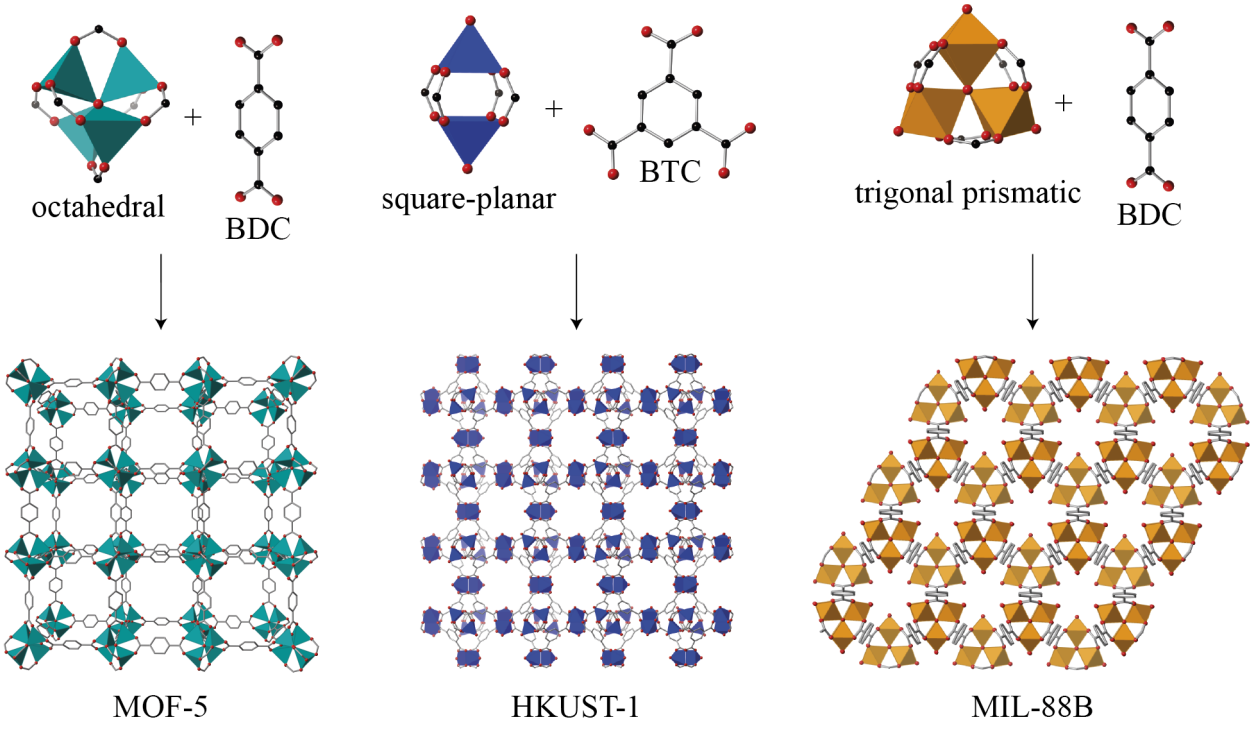

Figure 1.9: MOF structures formed from different binding geometries of SBUs and ligands: MOF-5 ($Zn_4O(BDC)_3$, where BDC = benzene-1,4-dicarboxylate), HKUST-1 ($Cu_3(BTC)_2$, where BTC = benzene-1,3,5-tricarboxylate), and MIL-88B ($Fe_3O(OH)(BDC)_3$).

synthesised where the various MOFs have the same topology, but the organic linker is functionalised or varied in length.[76,90,91] The as-synthesised MOFs will initially contain solvent guest molecules within the framework pores, and it is only by removing this guest that highly porous structures are achieved, with typical porosities greater than 50% of the MOF crystal volume.[92] This corresponds to surface areas which range from 1000 to 10,000 m^2/g, exceeding those of traditional porous materials such as zeolites and carbons.[92] The largest MOF pore aperture reported to date is 98 Å × 85 Å, corresponding to a surface area of 1760 m^2/g, which is sufficient to permit sorption even of vitamin B_{12} and myoglobin.[91] Examples of some well-known SBUs and ligands used in MOF synthesis are shown in Figure 1.9.

Zeolitic imidazolate frameworks (ZIFs) are a subset of MOFs which show topological similarity to zeolites because of similar M–ligand–M binding angles of ∼145° [Fig. 1.10]. They are composed of tetrahedral metal cations, such as Zn^{2+} and Co^{2+}, which coordinate to imidazolate (im) ligands. Functionalisation of imidazolate has led to a large variety of different ZIF structures which have

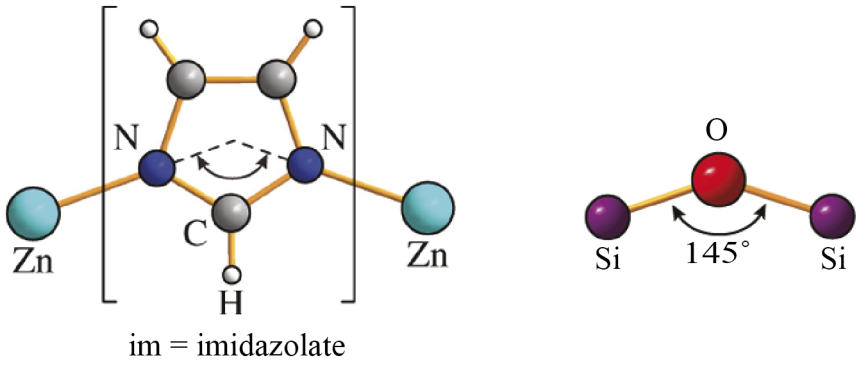

Figure 1.10: The zinc–imidazolate–zinc linkage found in the extended framework of $Zn(im)_2$ compared with the Si–O–Si link found in zeolites; figure reproduced with permission from Ref. 13, copyright 2010 by the American Physical Society.

both known and previously unobserved zeolite topologies.[93–95]

Previous experiments have shown that many ZIFs amorphise—in some cases irreversibly—by heating to 300°C,[13,96] applying modest hydrostatic pressures (∼0.3 GPa),[12] or mechanical grinding in a ball mill.[97] The structures of some of these amorphised phases can be understood in terms of a continuous random network analogous to that of silica glass.[13] The process of amorphisation opens new avenues for trapping toxic guests within the structure through framework porosity collapse,[98,99] as well as functionalisation of ZIF-type glasses,[13] but also highlights that these materials are more mechanically flexible than had been previously thought.

1.2.2.1 'Breathing' MOFs

Before the determination of the mechanical properties in MOFs, the flexibility of certain porous coordination polymers had been studied by quantifying their large structural changes upon solvent guest removal.[100,101] These coordination polymers were termed third-generation frameworks and exhibited reversible atomic displacements which led to unit cell parameters changes of up to several Å while retaining their chemical connectivity [Fig. 1.11].[64] The guest-induced framework transformation shown in Figure 1.11(i-j) is detailed further as it is of particular relevance to this thesis, and is known as the 'breathing' transition.[102]

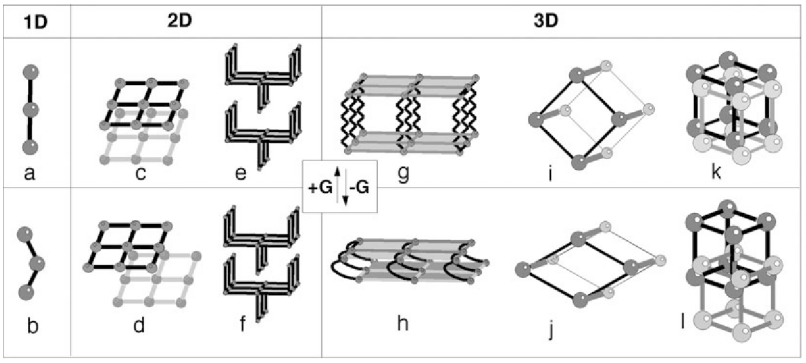

Figure 1.11: The six 'breathing' classes of Ref. 101 induced by guest (G) adsorption and desorption. The structural responses are associated with: 1D chains in a–b, 2D stacked layers in c–d, 2D interdigitated layers in e–f, 3D pillared layers in g–h, 3D expanding and shrinking frameworks in i–j, and 3D interpenetrated frameworks in k–l; figure reproduced from Ref. 102 with permission from the Royal Society of Chemistry.

The MIL-family are well known to show the 'breathing' phenomenon. In particular, the MIL-53 family show water-induced breathing.[103] These materials are metal benzene-1,4-dicarboxylates with the chemical formula [M(OH)(BDC)], where the metal is trivalent Al, Cr, Fe, or Ga. Their structures contain M–BDC–M units that form large 1D rhombic channels, connected in a perpendicular direction by coordination to OH^- [Fig. 1.12]. MIL-53(Cr) shows reversible volumetric changes of up to 40% upon hydration and dehydration cycles.[103] This breathing effect is driven by water–host hydrogen bonding, which causes deformation of the rhombic channels in the framework *via* angle changes between BDC-connected metal centres [Fig. 1.12].

Several factors stabilise the closed form, such as water–host hydrogen bonding, and π–π interactions within the framework.[102] To highlight the balance between these interactions, the isoreticular vanadium analogue (known as MIL-47), [V^{IV}(O)(BDC)], does not show breathing upon water adsorption. This is because it lacks the hydroxide bridges needed for hydrogen bonding to guest water molecules. Likewise [Fe^{III}(OH)(BDC)] has the strongest π-π intra-framework interactions, which stabilise the closed form to such an extent that the framework does not 'breathe' and expand upon dehydration.[104] Chemical variations aside, the topology of the MIL-53 family is crucial for allowing the breathing in the first instance. MIL-68, with the same chemical composition as MIL-53, does not support breathing as it has a more constrained topology. This is purely a

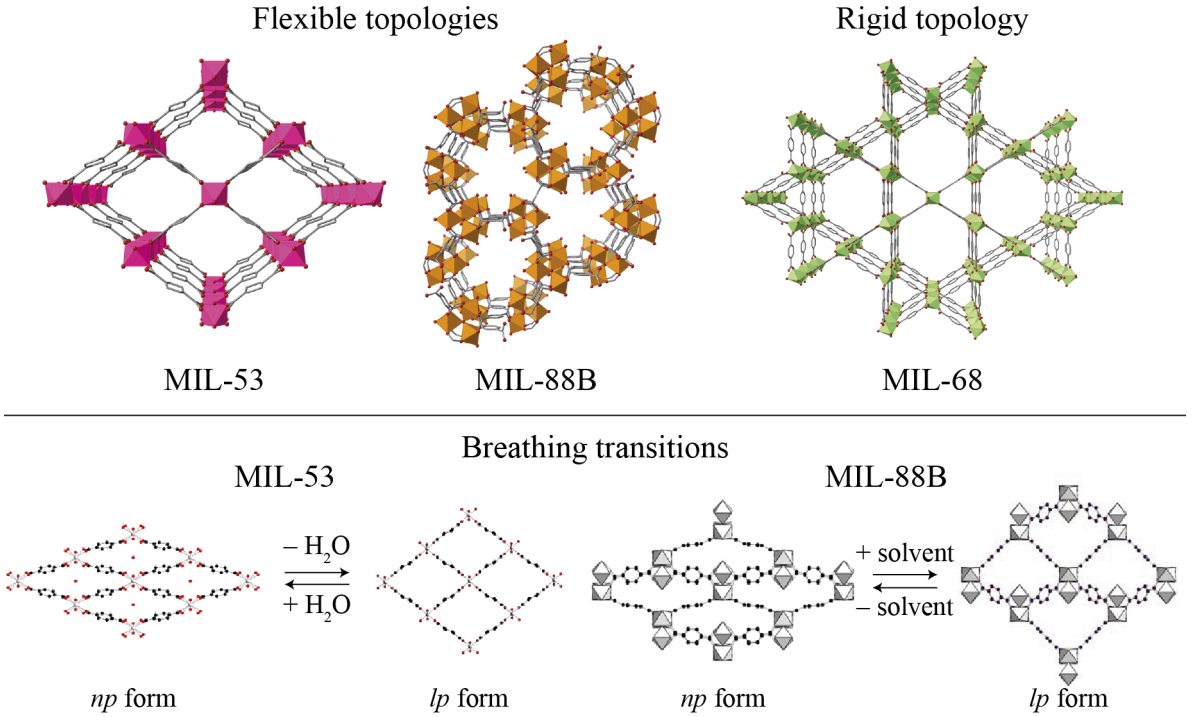

Figure 1.12: MIL frameworks, where MIL-53 and MIL-88B structures show breathing transitions upon guest adsorption, while MIL-68 is rigid to the same external stimuli. The breathing transitions from narrow-pore (*np*) to large-pore (*lp*) forms are illustrated for MIL-53 and MIL-88B upon chemical stimuli; figures reproduced from Ref. 103 with permission from the Journal of the American Chemical Society, copyright 2002 America Chemical Society, and from Ref. 105 with permission from AAAS.

geometric effect: its connectivity inhibits framework flexing as it contains odd cycles in the structure [Fig. 1.12].[102] Finally, the MIL-88 family show one of the largest guest-induced breathing to date, where the volume ratio between the open and closed forms can reach more than 300% [Fig. 1.12].[105]

1.3 Mechanical properties of framework materials

The mechanical properties of a material represent its response to strain created by external conditions. Mechanical properties can be measured on the macroscopic scale—involving measurements of tensile strength, ductility, shear, fatigue and creep responses—and are highly dependent on crystallite grain boundaries and grain sizes.[106] Or, mechanical properties can be investigated on the atomic scale—involving measurements of thermal expansion, compressibility, and elastic

properties—and it is the atomic and crystal symmetry of the structure which influence the mechanical properties. In this thesis, it is the second type of mechanical property that is considered, where the focus lies on characterisation of the intrinsic atomic flexibility within the coordination polymers by determining the coefficients of thermal expansion (CTEs) and compressibility values. In contrast to the framework flexibility quantified using chemical stimuli in Section 1.2.2.1, here the structural flexibility of the host framework is investigated using temperature or pressure stimuli, thus excluding any chemical bias.

Currently, there is relatively little focus in the MOF community on exploiting framework flexibility as a means of enhancing functionality, although this will undoubtedly change with the increasing appreciation of MOF mechanics.[14,64,102,107,108] For example, framework flexibility could be used to amplify sensing capabilities in stress-induced chemical detection mechanisms.[75] Structural flexibility may also be advantageous for the delivery of drug molecules,[71] accommodating new products formed upon *in situ* catalysis, and rigorous recognition of specific guests during molecular sieving using guest-induced fits.[109] The use of a flexible MOF thin-film substrate could induce desirable strains in the material to which it is adhered, creating an order of magnitude increase in sensitivity for piezoelectric sensors.[110] Alternatively, framework rigidity may be equally desirable for the preservation of porosity upon the formation of MOF pellets or monoliths (sample densification), needed for efficient packing to allow greater gas storage capacity.[111,112] MOF thin films on top of solid substrates for applications in *e.g.* sensing and low-κ dielectrics,[113–115] may require particular mechanical properties in order to remain attached to different types of substrate.[116] Therefore, knowledge and understanding of the extent of framework flexibility is crucial for selecting the appropriate coordination polymer for industrial implementation.

In the following sections, some of the key mechanical properties of relevance to this thesis are summarised, namely thermal expansion, compressibility and elastic properties (in particular the Young's modulus).

1.3.1 Thermal expansion

The thermal expansion of a material relates its strain (a second-rank tensor) to temperature (a scalar quantity). In an isotropic material, the coefficient of thermal expansion (α) for its unique a-axis is given by

$$\alpha_a = \frac{1}{a}\frac{\mathrm{d}a}{\mathrm{d}T}. \tag{1.3}$$

The volumetric thermal expansion in these structures is three times the α_a value. For anisotropic materials, the CTEs will have different values for the different crystallographic directions. In structures which contain fixed angles, such as hexagonal, trigonal, and orthorhombic symmetries, the CTEs will be defined along each crystallographic axis, and calculated in the same way as in Eq. (1.3). Monoclinic and triclinic systems, however, are best represented as a 3×3 strain tensor, as in addition to changes in dimension, the angles between axes are subject to thermal variation. The diagonalisation of this tensor matrix then allows the determination of the principal CTEs that are aligned with the so-called principal axes of the structure.

Most materials expand in all directions on heating, thus exhibiting PTE with $\alpha \simeq 0$–$20\,\mathrm{MK}^{-1}$ ($\mathrm{MK}^{-1} = 10^{-6}\ \mathrm{K}^{-1}$),[117] where $20\,\mathrm{MK}^{-1}$ corresponds to a 0.2% increase in dimension per 100 K. This PTE arises due to the anharmonicity of pairwise interactions: successively higher vibrational states correspond to larger interatomic separations [Fig. 1.13].[118] For certain applications in engineering and high-precision optics, it is desirable for materials to exhibit zero thermal expansion. This ensures minimal strain if the material is part of a composite, or simply enables the dimensions and position of the material to remain constant upon temperature fluctuations. In a framework structure, the thermal expansion of the chemical bonds is rarely the only factor which gives rise to the overall thermal expansion of the material. Instead a multitude of phonon modes may be populated and can act to reinforce or counteract the positive bond thermal expansion. Many materials are emerging that exhibit NTE with comparable magnitudes to materials that show regular PTE; *i.e.* up to $-20\,\mathrm{MK}^{-1}$. Interest in NTE materials arises due to the possible realisation of thermal-expansion-adjustable composites for a number of important applications, including diffraction gratings and optical fibres.[118,119]

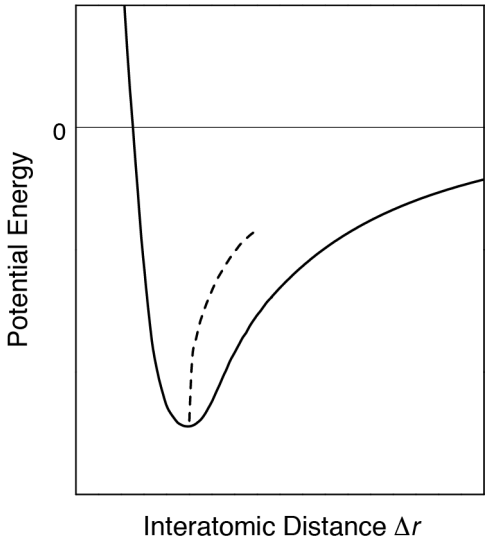

Figure 1.13: Potential energy (solid line) for a typical chemical bond as a function of interatomic distance Δr. The dashed line represents the average interatomic distance; figure reproduced from Ref. 119.

Isotropic expansivities

The relationship between the phonons in a structure and its thermal expansion was established by Grüneisen.[120] The Grüneisen parameter (γ) relates the volumetric thermal expansion of a material (α_V) to its volume (V), specific heat at constant volume (C_V), and volumetric compressibility (K_V):

$$\alpha_V = \frac{\gamma C_V K_V}{V}; \tag{1.4}$$

the link to phonon frequencies ω is *via* the mode Grüneisen parameter

$$\gamma_i = -\frac{V}{\omega_i}\frac{\mathrm{d}\omega_i}{\mathrm{d}V}. \tag{1.5}$$

A weighted sum of all the individual mode Grüneisen parameters gives the average Grüneisen parameter (seen also in Eq. (1.4))

$$\gamma = \frac{\sum c_i \gamma_i}{\sum c_i}, \tag{1.6}$$

where c_i weights the contribution of a mode to the overall specific heat C_V. In general phonon frequencies tend to decrease in magnitude as the volume increases because the increased bond

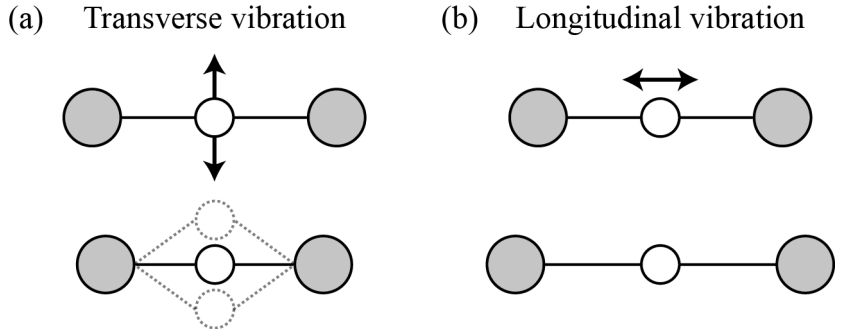

Figure 1.14: Schematic representation of the effect of (a) transverse and (b) longitudinal vibrational modes on the thermal expansion of the node–link–node units.

lengths have weaker interatomic forces. This gives rise to a positive mode Grüneisen parameter.[121] Negative γ_i values are more unusual, as these correspond to situations where phonon frequencies decrease as the volume of the material decreases. The overall sign of the volumetric thermal expansion of a material is a combination from all mode Grüneisen parameters at a given temperature. Therefore, in order to observe volumetric NTE, an overall negative γ value is needed. This requires not only the existence of individual modes with $\gamma_i < 0$, but also that the corresponding c_i are large; thermodynamically, this correlates to small phonon frequencies. Hence, isotropic NTE will be driven by low-energy phonon modes with large negative Grüneisen parameters.

One of the ways to obtain negative Grüneisen parameters is to populate transverse vibrational modes across the node–link–node units in the framework. The transverse vibrations of the linker induce displacements perpendicular to the linear binding geometry, and an overall decrease in the node–node distance follows [Fig. 1.14(a)]. This mechanism contrasts to the normal bond expansion which occurs from longitudinal vibrations of node–link bonds [Fig. 1.14(b)]. If the transverse vibrational modes dominate, then overall NTE will be observed along the node–link–node units. In general, transverse modes are lower in energy than longitudinal modes and are populated more readily at low temperature, which explains why certain materials show small values of NTE at low temperature ($< 50\,\mathrm{K}$) and PTE at higher temperatures.[118,122]

In order to achieve greater magnitudes of NTE over larger temperature ranges, the phonons driving NTE have to be even lower in energy. This can be fulfilled by correlating the transverse vibrational

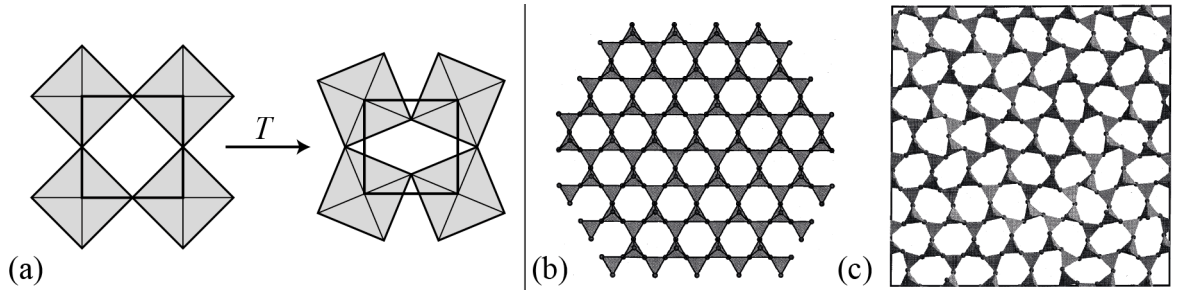

Figure 1.15: (a) Schematic representation of volume reduction in a 2D perovskite induced *via* rotational RUMs. (b) Ideal structure of β-cristobalite, and (c) a molecular dynamics snapshot of a single layer of tetrahedra in β-cristobalite, both viewed down the [111] direction; figure reproduced from Ref. 123 with permission from Springer Science and Business Media.

motions throughout the framework material using RUMs. The definition of the "rigid-unit" may differ from systems to system, but the most common RUM involves rotation of rigid polyhedra, as illustrated for a 2D perovskite in Figure 1.15(a). This permits minimal metal coordination distortion, which can be a high-energy penalty in certain materials. The existence of RUMs will depend on whether the topology is able to support such modes; in general, under-constrained topologies are likely to display RUMs.[52] For example, the modest NTE in β-cristobalite arises from the SiO_4 RUMs, as evident in molecular dynamics simulations [Fig. 1.15(b,c)].[39,123] ZrW_2O_8 has attracted much attention as being an isotropic NTE material over a large temperature range (0.3–1050 K) [Table 1.1].[124] Its mechanism for NTE—elucidated using lattice dynamics and reverse Monte Carlo (RMC) of total neutron scattering data—is also thought to involve RUMs in which corner-linked ZrO_6 octahedra and WO_4 tetrahedra undergo a complex mix of rotation and translation.[47,125,126] Metal coordination polyhedra in many coordination polymers are also thought to exhibit RUMs, thus enhancing transverse vibrational modes, as found in metal–cyanide frameworks,[127–132] MOF-5 and HKUST-1 [Table 1.1].[133–136]

Table 1.1: Linear CTEs in selected 3D framework materials. The unique expansivities are shown for each axis, or for monoclinic cells: ℓ_1, ℓ_2, ℓ_3 indicate the expansivities for the three principal axes. Abbreviations used: HMOF-1 refers to CdI_2(*meso*-tetra-(4-pyridyl)porphine), FMOF-1 refers to Ag(3,5-bis(trifluoromethyl)-1,2,4-triazolate), L = 4-(1*H*-naphtho[2,3-*d*]imidazol-1-yl)benzoate, fu-L^1 = 2,5-bis(2-methoxyethoxy)benzene dicarboxylate, dabco = 1,4-diazabicyclo[2.2.2]octane, pba = 3-(pyridin-4-yl)-benzoate)$_2$. †Indicates expansivities re-calculated using linear fits from the lattice parameters provided in the indicated references; the errors are extracted from the linear fits.

	Compound	T range (K)	axis	α (MK^{-1})	Ref.
Oxides	ZrW_2O_8	2–350	a, b, c	−9.07	137
	Cu_2O	9–240	a, b, c	−2.4	138
	α-quartz†	298–838	a, b	22.0(5)	40
			c	13.7(4)	
	β-quartz†	876–1338	a, b	0.1(3)	40
			c	−1.1(4)	
	α-cristobalite†	292–532	a, b	17.9(4)	41
			c	33.1(6)	
	β-cristobalite†	1200–1977	a, b, c	−1.8(2)	39
	Faujasite-SiO_2	25–573	a, b, c	−4.2	139
	$AlPO_4$-17	18–300	a, b	−15.3	140
			c	−4.52	
Cyanides	$Zn(CN)_2$	25–375	a, b, c	−16.9(2)	128
	$Cd(CN)_2$	150–375	a, b, c	−20.4(4)	128
	$LaCo(CN)_6$	100–420	a, b	−16.58(5)	141
			c	−10.68(7)	
	$Ag_3[Co(CN)_6]$	10–300	a, b	144(9)	142
			c	−126(4)	
	$In[Au(CN)_2]_3$	100–395	a, b	85.0(11)	89
			c	−62.8(6)	
	$Zn[Au(CN)_2]_2$	100–773	a, b	36.91(8)	143
			c	−57.58(8)	
MOFs	MOF-5	4–600	a, b, c	−16	133
	HKUST-1	80–500	a, b, c	−4.1	134
	$[NH_4][Mg(HCOO)_3]$	93–210	a, b	43	144
			c	−30	

Continued on next page

Table 1.1 – continued from previous page

	Compound	T range (K)	axis	α (MK^{-1})	Ref.
MOFs	HMOF-1†	100–380	a	177(7)	145
			b	−21(3)	
			c	2.1(12)	
	FMOF-1	90–295	a, b	230	146
			c	−170	
	$[Zn_2(L)_2(OH)_2]_n$	100–370	a, b	−21	147
			c	127	
	$[Zn_2(\text{fu-L}^1)_2\text{dabco}]_n$	303–463	ℓ_1	−94.3	10
			ℓ_2	373	
			ℓ_3	5.20	
	$[Mn(pba)_2]$	127–673	ℓ_1	2(1)	148
			ℓ_2	224(1)	
			ℓ_3	−107(1)	

Anisotropic expansivities

A structural mechanism that can favour even greater NTE magnitudes is the existence of framework hinging, as illustrated in Figure 1.16. These displacements are only allowed in anisotropic crystal symmetries, and give rise to anisotropic expansivities, where NTE is observed along one crystal dimension and PTE in the other. The energy required for framework hinging will depend on whether it is mediated by translational metal polyhedral RUMs, accommodated by linker deformation, or *via* direct metal coordination angle changes. In both cases, it is usually associated with a low-energy penalty in coordination polymers, giving rise to large magnitudes of change. Framework hinging is observed in many coordination polymers, such as $Ag_3[Co(CN)_6]$,[8] $In[Au(CN)_2]_3$,[89] HMOF-1,[145] FMOF-1,[146] $[Zn_2(\text{fu-L}^1)_2\text{dabco}_2]_n$,[10] $Mn(pba)_2$,[148] and MIL-53,[149] where rhombus-like channels (wine-rack motif) can be seen in the plane or volume which display anisotropic expansivities [Fig. 1.17, Table 1.1]. 'Colossal' thermal expansion—defined as $|\alpha| > 100\,\text{MK}^{-1}$—is observed for those frameworks which have additional weak interactions within the framework

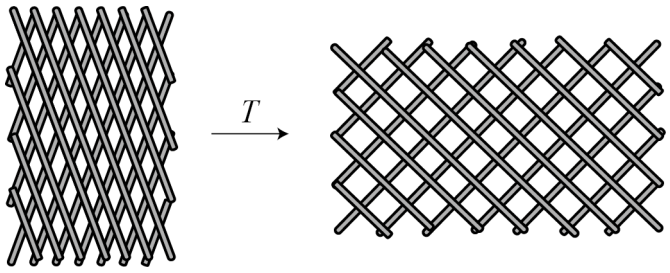

Figure 1.16: Schematic wine-rack, which illustrates the change in angles between the connected nodes as the framework is heated.

wine-rack motif, such as metallophilic, van der Waals, and π–π interactions. The thermal activation of these interactions causes rapid expansion, resulting in an equally drastic contraction (NTE) in the perpendicular direction because of the framework hinging mechanism.[10,142,149]

Table 1.1 shows the expansivities of the frameworks discussed in this section, as well as related structures which have similar mechanisms of structural change to temperature variation. Non-cubic systems exhibit anisotropic thermal expansion along different axes, due to their anisotropic crystal symmetry. Yet there is a marked difference in the anisotropy observed in single-atom frameworks compared to coordination polymers, namely that the anisotropy is much more apparent in the latter. Hence, coordination polymers with non-cubic symmetries and non-constrained topologies seem to have a propensity to support hinging mechanisms. These structural evolutions give rise to the large and anisotropic responses along two or three directions for a 2D or 3D

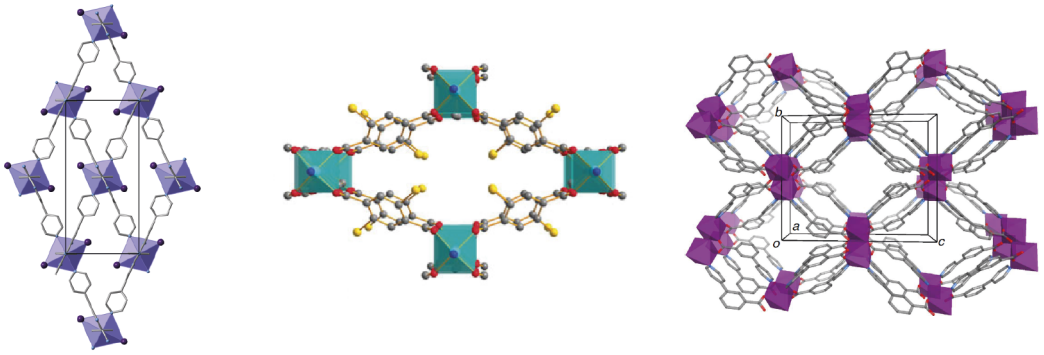

Figure 1.17: MOFs which show anisotropic thermal expansion due to a hinging mechanism (the full chemical formulas of these MOFs are given in Table 1.1); middle figure reproduced from Ref. 10 with permission from John Wiley & Sons and right figure reproduced from Ref. 148 with permission from Macmillan Publishers Ltd: Nature Communications, copyright 2015.

wine-rack motif, respectively, while modest expansions are observed along the direction that is not associated with the framework hinging.

1.3.2 Compressibility

The compressibility of a material relates its strain to a change in uniform (hydrostatic) pressure, and is a second-rank tensor; the same considerations for the strain tensor discussed previously apply here also. For example, the compressibility along the a-axis is calculated as follows

$$K_a = -\frac{1}{a}\frac{\mathrm{d}a}{\mathrm{d}p}. \tag{1.7}$$

In the absence of a structural phase transition, it is a thermodynamic requirement that volume compressibility be positive,[151] although there are certain exceptions found in metamaterials with specifically designed interactions.[152–154] For crystalline materials, the value of K normally lies between 5 TPa^{-1} (stiff material)—*i.e.* a 0.5% reduction in length for every 1 GPa increase in pressure—and 50 TPa^{-1} (soft material), where TPa^{-1} refers to 10^{-12} Pa^{-1}.[155] The bulk modulus (B_0) is the inverse of volumetric compressibility, and therefore is a measure of the material's resistance to uniform compression. B_0 is usually determined by fitting the Birch–Murnaghan or Rose–Vinet equations of state to the pressure-induced volume changes.[156,157]

Isotropic compressibilities

Isotropic structures cannot exhibit negative compressibilities; however, there are still certain anomalous compressibilities that can exist, especially so with the materials that exhibit negative thermal expansivities. For example, pressure-induced softening arises in $\mathrm{Zn(CN)_2}$ up to 1 GPa, which signifies that $\mathrm{Zn(CN)_2}$ becomes more compressible upon increasing pressure.[158] Beyond this pressure, $\mathrm{Zn(CN)_2}$ is observed to undergo a high-pressure phase transition,[159,160] and in this thesis, the relevance of this transition to the behaviour of an isostructural coordination polymer is explored. In fact, many of the isotropic NTE framework materials are likely to exhibit pressure-induced phase transitions due to the existence of low-energy phonons, as seen in

the pressure-induced amorphisations of ZrW_2O_8 at 1.5–3.5 GPa,[161] and MOF-5 at 0.0035 GPa.[162] The importance of obtaining high-pressure phases of NTE materials is because the low-energy phonons responsible for NTE are also likely to be the ones which soften upon compression. The high-pressure phase may then contain the "frozen" phonons, which were crucial for NTE in the ambient phase.[29]

There are special cases where apparent negative volume compressibilities are observed upon compression of porous frameworks such as MOFs and zeolites, yet this phenomenon is not associated with the framework itself, but from the pressure-transmitting medium which is able to enter the framework pores.[163–165] This event does not violate thermodynamics because the total volume, which comprises of the framework and the pressure medium, does decrease with increasing pressure.

Anisotropic compressibilities

While negative volume compressibility is not observed, the anomalous mechanics of negative linear compressibility (NLC; expansion in one direction upon compression) or negative area compressibility (NAC; expansion in two directions upon compression) can be observed in anisotropic materials, so long as the remaining axis or axes displaying positive compressibility are sufficiently large to give an overall positive K_V.[9,166] The increase in both dimension and density along the NLC axis or NAC axes, known as stretch-densification, is an attractive mechanism for the development of sensitive pressure sensors,[110] and artificial muscles.[167,168] In particular, NAC offers two further developments: first, framework pore widening coupled with volume reduction allows, in principle, for volume contraction during solvent uptake. This mechanism could act to compensate for undesirable moisture-induced swelling of concrete- and clay-based engineering materials. Second, as NAC materials increase their surface area under hydrostatic pressure, they could be implemented as substrates to provide order-of-magnitude amplification of piezoelectric response in ferroelectric sensors.[169] Materials that exhibit NLC are often also able to display auxetic behaviour (lateral contraction under axial compression), as occurs in materials with a negative Poisson's ratio,[169,170] and are important in the development of shock-resistant materials.[168]

The same framework hinging that is activated upon heating provides a way to obtain anisotropic mechanics—and thus NLC or NAC responses—as a function of pressure. There is no thermodynamic requirement for framework materials to exhibit the same structural changes upon compression as upon temperature variation, but in practice such a correspondence is frequently observed.[9,171,172] The case where they may be considered as coupled is developed below, based upon the works of Refs. 171,173,174.

In order to relate the anisotropic compressibilities and expansivities using Eq. (1.4), the compressibilities along each axis are expressed in terms of so-called elastic compliances (s_{ij}). These correspond to the strain observed along a direction i due to an applied stress along the direction j, and are covered in more detail in Section 1.3.3. The unique elastic compliances for a uniaxial system (*e.g.* hexagonal or trigonal) are substituted into Eq. (1.4) to obtain

$$\begin{aligned} \alpha_a &= \frac{C_T}{V}[(s_{11}+s_{12})\gamma_a + s_{13}\gamma_c], \\ \alpha_c &= \frac{C_T}{V}(2s_{13}\gamma_a + s_{33}\gamma_c), \end{aligned}$$

where C_T is the isothermal specific heat, and γ_a as well as γ_c are the components of the anisotropic Grüneisen function along the a- and c-axes, respectively.[173] By substituting the compressibility values along the same direction: $K_a = s_{11} + s_{12} + s_{13}$ and $K_c = 2s_{13} + s_{33}$, the equations relating α_a to K_a, and α_c to K_c are

$$\begin{aligned} \alpha_a &= \frac{C_T}{V}\left[K_a\gamma_a + s_{13}(\gamma_c - \gamma_a)\right], \\ \alpha_c &= \frac{C_T}{V}\left[K_c\gamma_c - 2s_{13}(\gamma_c - \gamma_a)\right]. \end{aligned}$$

These relationships highlight that the thermal expansion of an uniaxial material consists of (i) a quasi-isotropic term (*i.e.* $\alpha_a = \frac{C_T}{V}K_a\gamma_a$) and ($ii$) a cross-linking term (*i.e.* $s_{13}(\gamma_c - \gamma_a)$).[173] The individual α values take the quasi-isotropic form only if there is no elastic cross-linking (*i.e.* $s_{13} = 0$), or if the Grüneisen functions are isotropic (*i.e.* $\gamma_a = \gamma_c$). In both cases, the signs of

γ_a and γ_c will dictate whether a direct correspondence between α_a, α_c and K_a, K_c is seen:

$$\begin{aligned} \alpha_a &= \frac{C_T}{V} K_a \gamma_a, \\ \alpha_c &= \frac{C_T}{V} K_c \gamma_c. \end{aligned}$$

The condition $s_{13} = 0$ is most commonly observed in a lattice containing independent chains or layers, yet because of the strong structural anisotropy, it is likely that the γ values will also be very anisotropic, and hence K_a and K_c will not necessarily correlate with α_a and α_c, respectively. If instead the structure gives rise to isotropic Grüneisen parameters, the NTE along one axis will correlate to the same axis exhibiting NLC, as both α_a and α_c will have equivalent contributions from γ_a and γ_c, respectively.[173,174] That isotropic Grüneisen functions should exist in framework materials may be due to the network connectivity, which allows similar and coupled structural changes upon applied stress in different directions [Fig. 1.18]. In β-quartz for example, the ratio $\gamma_a/\gamma_c < 10\%$,[37] while in a layered material such as graphite the ratio $\gamma_a/\gamma_c \simeq -163\%$ with γ_a and γ_c of different sign.[175] The derivation given above can equally be applied to other anisotropic crystal symmetries, as detailed in Ref. 173. In this thesis, many of the framework structures investigated have connectivity as shown in Figure 1.18(a). Consequently, the anisotropic NTE/PTE that arises from the angle variation of the wine-rack motif gives rise to a similar mechanism under pressure—and hence the exhibition of NLC/PLC—with the negative response found along the same axis in both temperature and pressure studies.

The materials $Ag_3[Co(CN)_6]$, $KMn[Ag(CN)_2]_3$ and $Zn[Au(CN)_2]_2$ are examples of coordination polymers which exhibit similar framework hinging mechanisms under compression as upon temperature variation [Table 1.2].[8,9,171,172] As known for the temperature-induced response, the weak argentophilic or aurophilic interactions are key for allowing the large compressibilities observed in these materials. Even though $Ag_3[Co(CN)_6]$ exhibits one of the highest known NLC values, it does so within a limited pressure range (0–0.19 GPa) due to a phase transition.[171] This transition is suppressed in the framework material $KMn[Ag(CN)_2]_3$, which contains the same framework lattice as $Ag_3[Co(CN)_6]$, but with additional K^+ ions within the cavities of the manganese dicyanoargentate framework. It is the presence of the K^+ ions which allows the NLC response to be exhibited

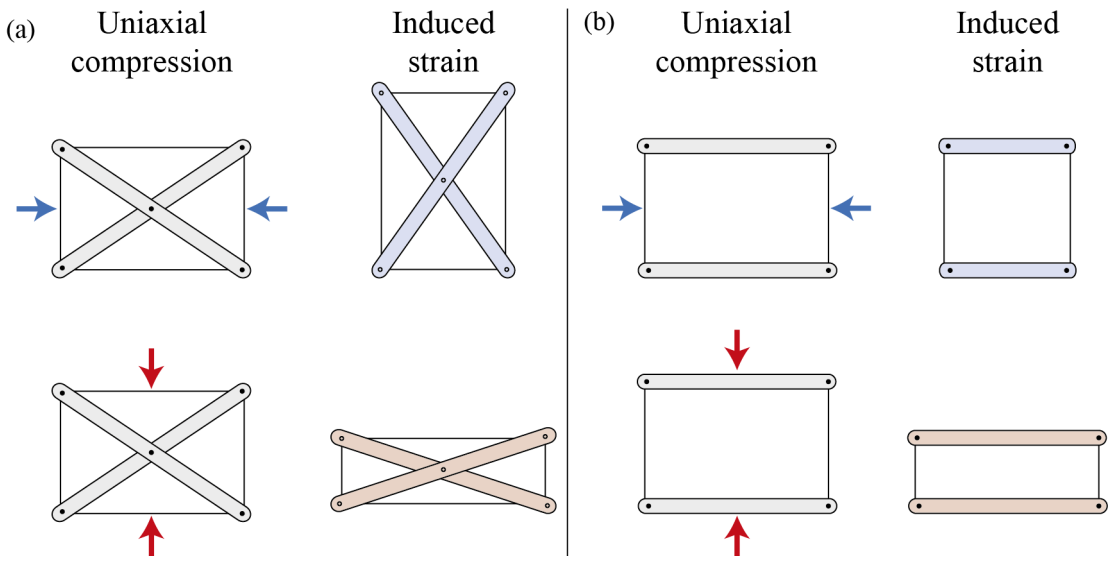

Figure 1.18: Uniaxial compression in different directions for (a) a 2D connected framework, giving rise to coupled strains for the different directions of applied compression, and (b) a 1D layered material which is strongly direction dependent, resulting in strain only along the direction of applied uniaxial compression; figure adapted from Ref. 171.

over a much larger pressure range in this structure.[172] The giant NLC observed in $Zn[Au(CN)_2]_2$ is mediated by the helical arrangement of Au...Au interactions,[9] which are much more compressible than linear Ag...Ag interactions as seen in $Ag_3[Co(CN)_6]$ and $KMn[Ag(CN)_2]_3$. Consequently the large compression along the Au...Au interactions leads to an equally large expansion (*i.e.* NLC) in the perpendicular direction.

Mercury-porosimetry coupled with molecular dynamics simulations were performed on MIL-47 and MIL-53(Cr) and showed that large structural changes occurred in these MOFs upon compression *via* framework hinging [Table 1.2].[176–178] DFT calculations show additionally the extreme anisotropic elastic properties of MOFs capable of breathing, where compressibilities as large as $K_a = -1441\,\mathrm{TPa}^{-1}$, $K_b = -98\,\mathrm{TPa}^{-1}$, and $K_c = 3640\,\mathrm{TPa}^{-1}$ are observed for MIL-53(Ga).[14]

While similar structural changes can occur under variable-temperature and variable-pressure conditions, compression often leads to more substantial structural variations and can even affect chemical bonding, as seen in the cooperative bond rearrangement in ZIF-zni, $Zn(imidazolate)_2$, at 0.5–0.8 GPa.[182] For MIL-47 and MIL-53, a pressure as low as ∼0.3 GPa could induce the *lp*–*np*

Table 1.2: Compressibilities of selected 3D frameworks, where † indicates compressibilities calculated using the data from the reference indicated, using the online program PASCal.[179] Abbreviations used: ZIF-8 = $Zn(mim)_2$ where mim = 2-methylimidazolate, and zni indicates the type of topology observed in $Zn(im)_2$ and $LiB(im)_4$. ⋆For the high-pressure experiment, HKUST-1 was used as-synthesised, and thus contained water within the pores: $Cu_3(BTC)_2(H_2O)_3$.

	Framework Materials	P range (GPa)	axis	K (TPa^{-1})	B_0 (GPa)	Ref.
Oxides	γ-$ZrWO_8$†	0–6.23	a	0.42(9)	580(81)	180
			b	0.47(8)		
			c	0.45(7)		
	$KAlO_4GeO_4$†	0–3.22	ℓ_1	3.1(5)	33(3)	181
			ℓ_2	15.49(18)		
			ℓ_3	2.1(6)		
Coordination Polymers	$Ag_3[Co(CN)_6]$	0–0.19	a	115(8)	6.5(3)	171
			c	−76(9)		
	$Ag_3[Co(CN)_6]$-II	0.19–7.65	ℓ_1	15.2(9)	11.8(7)	171
			ℓ_2	9.6(5)		
			ℓ_3	−5.3(3)		
	$KMn[Ag(CN)_2]_3$	0.2–2.2	a, b	33.2(13)	12.7(11)	172
			c	−12.0(8)		
	$Zn[Au(CN)_2]_2$	0–1.8	a, b	52(6)	16.7(16)	9
			c	−42(5)		
	MIL-47(V)†	0–0.18	a	−410(12)	10(2)	176
			b	500(40)		
			c	17(15)		
	$Zn(im)_2$† (zni)	0–0.54	a, b	29(4)	11.8(9)	182
			c	8(2)		
	$LiB(im)_4$† (zni)	0–1.69	a, b	17(3)	16.3(7)	183
			c	11(3)		
	ZIF-8	0–0.34	a, b, c	69(5)	6.52(35)	12
	HKUST-1⋆	0–1.816	a, b, c	10.5(2)	31.0(7)	184
	$[NH_4][Zn(HCOO)_3]$	0–0.94	a, b	15.8(9)	32.8(16)	185
			c	−1.8(8)		
	$[C(NH_2)_3][Cu(CO_3)_2]$	0–4	a, b	7.7(1)	36.1(3)	186
			c	12.3(1)		

breathing transformation,[176,178] while cooling to 77 K from ambient temperature in MIL-53 does not even fully convert all the *lp* phase to *np*.[149]

Table 1.2 shows the compressibilities and bulk moduli of the framework structures discussed in this section and other related structures. Low values of compressibility (and large values of bulk modulus) indicate framework rigidity, where minimal structural change occurs upon hydrostatic compression. High values of B_0 are usually observed in the densest structures,[187] as seen in the oxides and the dense MOFs [Table 1.2]. The use of tridentate ligands in HKUST-1 does show promise for making particularly rigid structures which maintain porosity upon compression.

1.3.3 Elastic properties

Thermal expansion and compressibility are specific aspects of the more general elastic response of a material. The CTE and compressibility can be calculated directly from the elastic compliances

$$\alpha_i = \frac{C_T}{V} \sum_{j=1}^{6} s_{ij}\gamma_j, \tag{1.8}$$

$$K_i = \sum_{j=1}^{6} s_{ij}. \tag{1.9}$$

The elastic compliance tensor links an induced strain (ϵ) to an applied stress (σ) within the limits of Hooke's law,

$$\epsilon_{ij} = \sum_{kl} s_{ijkl}\sigma_{kl}, \tag{1.10}$$

where i, j, k, l represent the coordinate axes. As both stress and strain are second-rank tensors, the elastic compliance ($\mathbf{S}$) is a fourth-rank tensor. The equation in 1.10 is commonly recast as the inverse of the elastic compliance tensor, corresponding to the elastic constant tensor ($\mathbf{C}$) that relates the value of an applied stress to a given strain value

$$\sigma_{ij} = \sum_{kl} c_{ijkl}\epsilon_{kl}, \tag{1.11}$$

and gives an indication of the stiffness of the structure. The $\mathbf{C}$ and $\mathbf{S}$ tensor representation is usually simplified by using Voigt notation, where the pairs of indices 11, 22, 33, 23, 13, and 12

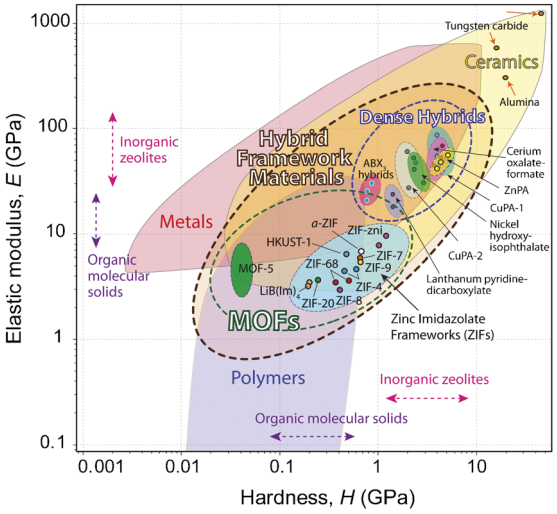

Figure 1.19: Elastic modulus *versus* hardness materials property map encompassing both dense and nanoporous coordination polymers (indicated by hybrid framework materials); figure reproduced from Ref. 107 with permission of the Royal Society of Chemistry.

are replaced by the single indices 1, 2, 3, 4, 5, and 6, respectively.[29,188] Voigt notation was used in Eqs. (1.8) and (1.9), and for the elastic compliances mentioned in Section 1.3.2. The maximum number of independent coefficients for these 4 × 4 matrix tensors is 21 due to the symmetry implicit in the Voigt notation. Further reduction in the number of independent coefficients arises from the crystal symmetry.[188]

The Young's modulus is commonly used to represent the material's stiffness, and is defined as the ratio of the uniaxial stress over the uniaxial strain along the same direction:

$$E = c_{ii} = \frac{\sigma_i}{\epsilon_i}. \tag{1.12}$$

By determining Young's moduli in different directions from the elastic constants, the stiffness of the material can be represented by a 3D surface. Elastic constants can be measured experimentally using ultrasonic measurements,[189] Brillouin scattering,[190] or nanoindentation,[107] however, these techniques all require high-quality single crystals. Elastic constants can also be calculated using computational techniques, such as force-field molecular modelling and DFT *ab initio* quantum mechanical calculations.[14,191–193]

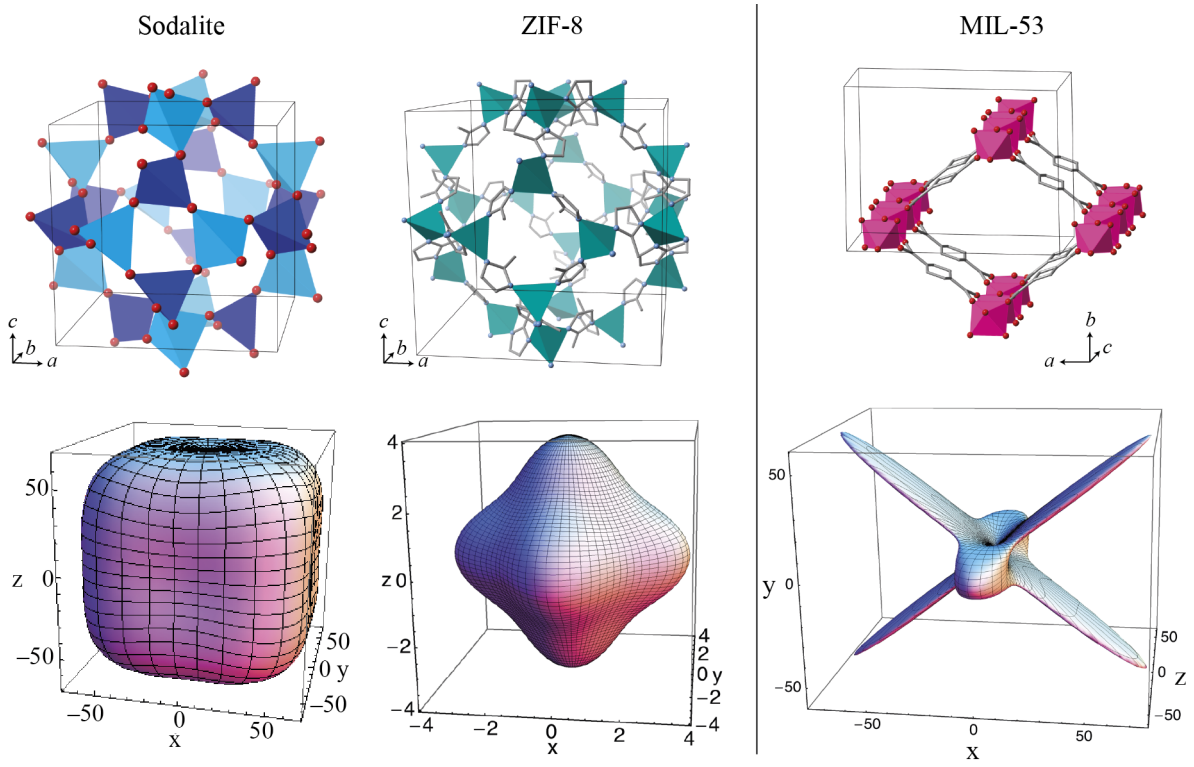

Figure 1.20: Directional Young's moduli for sodalite,† ZIF-8 and MIL-53 represented as 3D surfaces, where the tick marks indicate values in GPa. Lower middle and right figures reproduced with permission from Ref. 14, copyright 2012 by the American Physical Society.

Values of Young's moduli vary considerably for the type of material considered; coordination polymers span many magnitudes of E from those observed in purely organic materials to those seen in ceramic inorganic structures (such as oxides) [Fig. 1.19].[107] In general, the Young's modulus is seen to correlate with framework density and solvent accessible volume, where the denser frameworks with small solvent-accessible volumes have larger Young's moduli, and hence are considered stiff.[194] Additionally, the magnitude of E is observed to be related to the bonding strength in metal imidazolate frameworks,[183] and the ligand field stabilisation energy (LFSE) for dimethylammonium metal formates.[195] The effect of bonding strength and density is shown to have a large influence on the magnitudes of E in the sodalite frameworks chlorosodalite and ZIF-8 [Fig. 1.20, Table 1.3],[192] while their Young's moduli anisotropies remain similar: $E_{\max}/E_{\min} = A_E \simeq 1.4$.

Significant anisotropy in the Young's moduli can be observed when different bonding interactions of

†Calculation of the Young's modulus surface of sodalite was performed by Matthew Ryder, from the Engineering Department, Oxford using the data from Ref. 189.

Table 1.3: The maximum and minimum values of the Young's moduli of selected 3D framework materials. The Young's modulus anisotropy is also shown: $A_E = E_{\max}/E_{\min}$. Chemical compositions of the zeolites include, chlorosodalite: $Na_4Al_3Si_3O_{12}Cl$, natrolite: $Na_2(Al_2Si_3O_{10})\cdot H_2O$, and MFI silicalite: $[(C_3H_7)_4NF]_4[Si_{96}O_{196}]$. Chemical compositions of the MOFs include: MIL-122(In) which refers to $In_2(OH)_2$(NTC) where NTC = 1,4,5,8-naphthalenetetracarboxylate, and MIL-140A represents ZrO(BDC).

Compound	Crystal System	density $g\,cm^{-3}$	$E_{\min}$ (GPa)	$E_{\max}$ (GPa)	A_E	Ref.
Chlorosodalite	cubic	2.31	65.0	89.7	1.4	192, 189
Natrolite	orthorhombic	2.24	57.2	110.8	1.9	192, 190
MFI silicalite	orthorhombic	2.05	52.2	79.2	1.5	192, 196
α-cristobalite	tetragonal	2.3	41.8	70.1	1.7	192, 197
MOF-5	cubic	0.60	9.5	19.7	2.1	14, 198
ZIF-8	cubic	0.95	2.7	3.9	1.4	192
$Zn(im)_2$ (zni)	tetragonal	1.56	8	9	1.1	183, 194
$LiB(im)_4$ (zni)	tetragonal	1.31	2.7	3.3	1.2	183
MIL-122(In)	monoclinic	2.55	42.3	160.4	3.8	193, 199
MIL-140A	monoclinic	1.67	2.5	80.1	31.8	193, 200
MIL-53(Al)	orthorhombic	1.02	0.90	94.7	105	14, 103
MIL-47	orthorhombic	1.00	0.90	96.6	108	14, 201

varying energies are present within the structure.[14,107] For instance, remarkable elastic anisotropy is observed in the MIL frameworks by virtue of the contrast between strong bonding along M–O inorganic chains and M–BDC–M links on the one hand, and weak π-π interactions between the organic ligands on the other hand [Fig. 1.20].[14] From Table 1.3, it can be seen that the low-density MILs have large A_E values, while the denser MIL-122(In) exhibits much lower Young's modulus anisotropy; its framework topology is also constrained by the presence of four-coordinate ligands.

1.4 Structure–property relationships

Isotropic mechanics

The thermal expansion in isotropic frameworks is dependent on the relative abundance of longitudinal bond vibration and that of transverse vibrational modes and RUMs. An equal balance of both PTE and NTE mechanisms envisages zero thermal expansion materials as seen in $[N(CH_3)_4]CuZn(CN)_4$,[202] and $Fe[Co(CN)_6]$.[203] The magnitudes of NTE have been shown to increase by (*i*) increasing the linker length in the isoreticular MOF-5 family,[204] or (*ii*) using larger metal cations in Prussian Blue analogues and in $LnCo(CN)_6$.[132,141,205] Framework density is observed to have greatest impact on the bulk and Young's moduli, which tend to be highest for the denser frameworks.[187,194] Thus the dense structures are associated with small compressibilities and limited framework flexibility.

Anisotropic mechanics

Anisotropic framework deformation is commonly observed in coordination polymers, be it through guest adsorption, heating, or compression, and is often mediated by coupled framework hinging mechanisms. Temperature- and pressure-induced framework hinging mechanisms are observed in $Ag_3[Co(CN)_6]$, $KMn[Ag(CN)_2]_3$ and $Zn[Au(CN)_2]_2$;[8,9,171,172] likewise guest- and temperature-induced framework 'breathing' are present in MIL-53,[103,149] $Ni^{II}_2Ni^{III}(\mu_3\text{-OH})(dcbp)_3$ where dcbp = 2,6-di-*p*-carboxylate phenyl-4,4′-bipyridine,[11] and FMOF-1.[146] The weak interactions in these frameworks are important for amplifying structural changes during the 'breathing' guest-induced transformations of MIL-53,[102] the temperature-induced hinging of dicyanometallate coordination polymers,[89,142] or of the functionalised $[Zn_2(\text{fu-L}^1)_2\text{dabco}]_n$.[10] The guest size, shape and H-bonding interactions with the host framework are able to tune the magnitude of the host-framework mechanics, as seen in $[Zn_2(L)_2(OH)_2]_n$,[147] $Ni^{II}_2Ni^{III}(\mu_3\text{-OH})(dcbp)_3$,[11] and $Mn(pba)_2$.[148]

1.5 Thesis structure

Although there now exist a number of studies which quantify the mechanical properties of certain coordination polymers, the sheer number of coordination polymers means that all-encompassing general rules that allow prediction of their framework mechanics are urgently needed. Indeed, very recently a computational approach on the quantification of framework flexibility in MOFs provides a valuable insight into this area.[206] In this work, MOFs were modelled as rigid units of metal SBUs and ligands, which were connected together *via* hinges. This mechanical model allowed the framework flexing in MOFs to be identified, and showed that there were very few rigid MOFs.

In this thesis, and the various publications to which it has contributed, a similar approach is developed. In particular, the frameworks are deconstructed into their fundamental mechanical building units. Whereas Ref. 206 categorises MOFs into rigid, semi-flexible and flexible, here the magnitude of flexibility is considered on a continuous scale, and is quantified by consideration of the framework chemistry. To enable general predicting rules, the topology and geometry of the coordination polymer are investigated. Both these properties, while they may arise from different chemical compositions, do not directly rely on particular chemical functionalities. Hence, design strategies based upon topology and geometry will be applicable to many families of coordination polymer, irrespective of the particular chemistry.

The great majority of the work detailed in this thesis relies on the determination of crystal structures. The methods used for sample preparation and the types of diffraction experiments employed are given in Chapter 2, along with the corresponding crystallographic theory and refinement methods.

The four result chapters are arranged in terms of the different structure–property relationships that quantify framework flexibility in coordination polymers. Chapter 3 details how the different structural motifs in silver(I) 2-methylimidazolate (Ag(mim)) affect its mechanical properties—namely, the argentophilic interactions, hinge points and coordination bonds. The mechanics of Ag(mim) and other coordination polymers are recast in terms of their structural motifs in order

to understand and predict their framework responses and anomalous mechanics upon external stimuli.

The effect of varying the linker chemistry within two topologically identical frameworks is then examined in Chapter 4, using the particular compounds zinc cyanide and cadmium imidazolate. The key consideration in this chapter is that the diamondoid connectivity is the same for both frameworks, so the interplay between topology- and chemistry-driven mechanical properties is explored.

In Chapter 5, the consequence of varying framework geometry on the anisotropy of CTEs is investigated with reference to the quartz-like frameworks zinc isonicotinate and indium deuterium terephthalate. These MOFs were chosen because they have the same network topology but contrasting framework angles. The anisotropic CTEs in these quartz-like frameworks can be accounted for by a new geometric formalism developed here. This geometric rule is shown to predict CTE or compressibility anisotropy direction in a range of coordination polymers which are capable of exhibiting framework hinging upon external stimuli.

Chapter 6 details the outcome of modifying the chemical composition on the thermal expansion behaviour observed within 19 different ABX_3-type metal(II) formates. The B-site metal cations are varied across the series Mg, Mn, Fe, Co, Ni, Cu, Zn, and Cd, allowing the correlation between the metal cation size and the framework flexibility. The A-site cations are also varied across the series methylammonium, ethylammonium, dimethylammonium, azetidinium, and guanidinium. The shape and size of the A-site cations are shown to correlate with the observed CTEs by affecting the framework hinging mechanism.

Finally, Chapter 7 concludes the general structure–property relationships this work has provided for anticipating and understanding the mechanical properties of coordination polymers.

While the main work of this thesis is comprised of the structure–property rules determined for the mechanical properties of coordination polymers, the dynamical properties and local structure of two coordination polymers were also investigated. This additional work is summarised in Appendix E, and is treated separately so that the main flow of the thesis is maintained. Neutron

total scattering and reverse Monte Carlo techniques were used to characterise the local dynamics in zinc isonicotinate, and the ferroelectric order–disorder transition in ammonium zinc formate.

Chapter 2

Methods

This chapter discusses the experimental and computational techniques that were used in this thesis. The synthesis methods will be detailed, along with the variable-temperature and -pressure X-ray diffraction measurements used for single-crystal and powder samples of coordination polymers. In addition to X-ray scattering techniques, neutron total scattering experiments were performed on deuterated coordination polymers. Computational techniques include using programs such as CRYSTALS for solving single-crystal data, and TOPAS or GSAS for Rietveld refinement of powder diffraction data. The GUDRUN program was used to correct total scattering data, which was then used as input data to the RMCPROFILE program. Simple Fortran codes were written to (*i*) analyse the supercell configurations generated by RMCPROFILE, and (*ii*) calculate bonding distances and framework angles from crystallographic information files (CIFs) for the numerous variable-temperature data sets obtained from this study.

Within this thesis, the specific experimental details are provided within the experimental section of each chapter.

2.1 Synthesis of coordination polymers

All chemicals which were used in the synthesis of coordination polymers were purchased from commercial suppliers (Sigma-Aldrich, Alfa Aesar, Qmx) and used without further purification. In

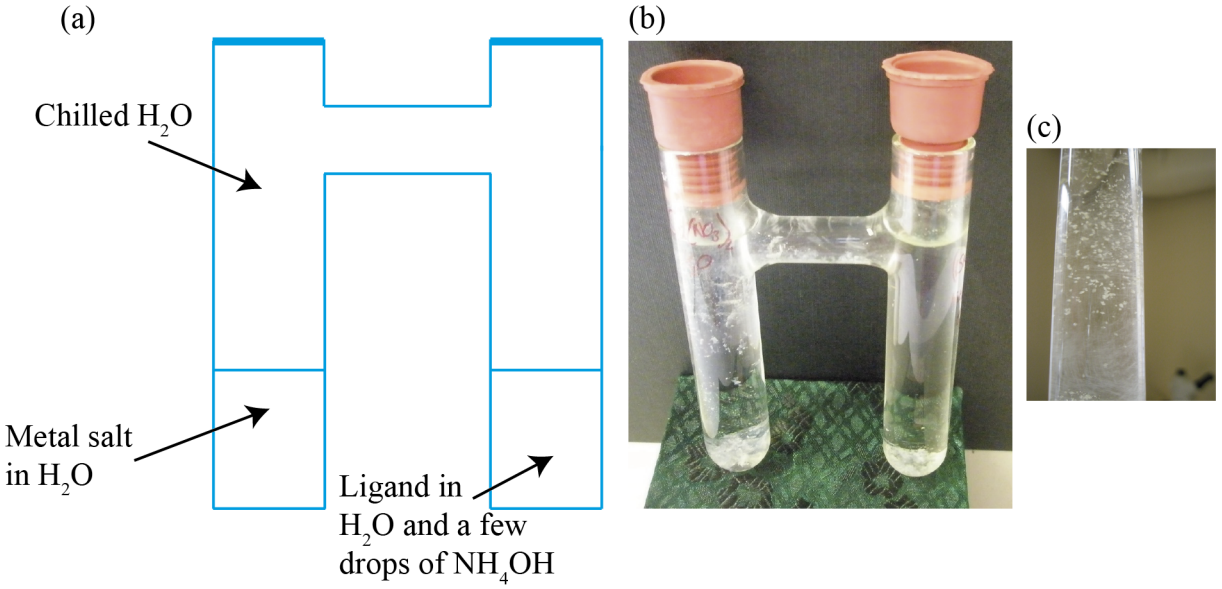

Figure 2.1: (a) Schematic drawing of an H-cell setup; (b) H-cell; (c) single-crystal growth in one side of the tube.

general, the synthesis of coordination polymers was achieved by mixing solutions of stoichiometric quantities of metal salt and ligand, with the addition of base in cases where the ligand required deprotonation. Single-crystal growth methods included slow evaporation and slow diffusion *via* layering of solutions in *e.g.* H-cells [Fig. 2.1]. For an H-cell setup, the metal salt and ligand solutions were separated by placing each solution in either tubes of the H-cell. The H-cell was then filled to allow the slow diffusion of the reactants. Polycrystalline samples were prepared by mixing directly the metal salt and ligand solutions to obtain a precipitate. Hydrothermal synthesis was used in the cases where precipitation did not occur at ambient conditions.

2.2 Diffraction techniques

Diffraction is the scattering of radiation, and for its application to atomic structure determination, the radiation wavelength needs to be comparable to typical interatomic distances. This corresponds to the use of radiation sources as found in the X-ray spectrum, electron beams, or neutron beams. A beam of radiation can either maintain its original wavelength—and hence

energy—or alter its wavelength upon scattering. The former process is known as coherent or elastic scattering, and is the scattering process needed for crystal structure determination, and thus diffraction. Incoherent or Compton scattering corresponds to the situation where the scattered radiation has increased its wavelength upon scattering.

Diffraction patterns arise from the constructive interference of the scattered radiation as defined by Bragg's law

$$2d \sin \theta = \lambda, \tag{2.1}$$

where d signifies the distance between two identical lattice planes (or hkl planes in Miller index notation). The angle of the incident radiation with wavelength λ is given by θ. The diffraction pattern represents the transformation of the atomic structure into reciprocal space, and the three-dimensional distribution of atoms can only be resolved after the diffraction pattern is transformed back into direct space. This is more straightforward from single-crystal diffraction which contains three-dimensional information of the scattered radiation, while in powder diffraction, this information is collapsed onto one dimension [Fig. 2.2]. However, powder diffraction does offer certain advantages over single-crystal diffraction. For instance, (*i*) the powder sample preparation is usually much simpler than single-crystal growth, (*ii*) the powder diffraction patterns are fast and straightforward to obtain, and moreover, (*iii*) the diffraction patterns allow the identification of different phases. It is also usually the case that more accurate lattice parameter determinations are made from powder diffraction profile fitting. For the variable-temperature diffraction experiments performed in this investigation, powder diffraction is ideal for the extraction of lattice parameter evolutions on known phases of coordination polymers. These experiments enable a large number of variable-temperature diffraction data to be collected on many different coordination polymers.

2.2.1 Single-crystal X-ray diffraction

The diffraction pattern of a single crystal is described by the structure factor[209]

$$F(hkl) = \sum_{j=1}^{N} f_j \exp[2\pi \mathrm{i}(hx_j + ky_j + lz_j)], \tag{2.2}$$

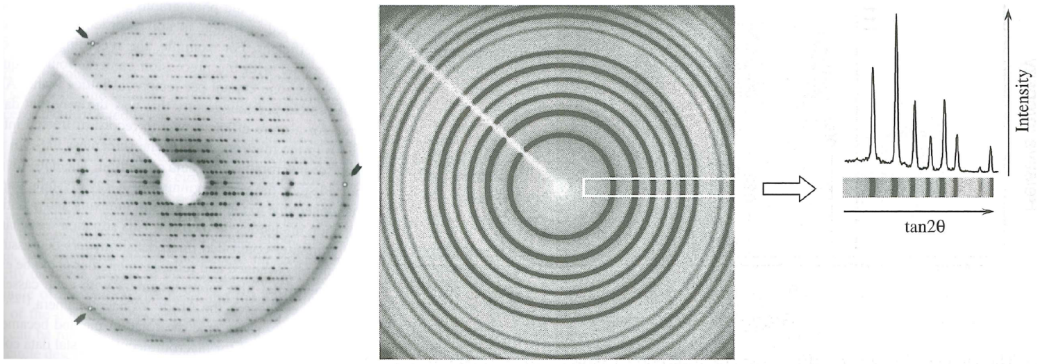

Figure 2.2: Diffraction images from a single-crystal and a powder sample; figures reproduced from Ref. 207 with permission from Oxford University Press and Ref. 208 with permission from Springer Science and Business Media.

where the h, k, l represent the Miller plane indices, corresponding to different orientations of planes in the unit cell. The position of the atom j, out of N atoms, is given by the fractional coordinates x_j, y_j, z_j with the scattering factor f_j. The scattering factor is dependent on the atomic number of atom j and also the Bragg angle. Atoms with large atomic numbers equate to greater scattering power, but the atomic scattering for all atom types decreases with increasing Bragg angle. From the structure factor, the electron density, and hence atomic positions, can be calculated:

$$\rho(x, y, z) = \frac{1}{V} \sum_{hkl} F(hkl) \exp[-2\pi \mathrm{i}(hx_j + ky_j + lz_j)], \tag{2.3}$$

where V is the volume of the unit cell. In a diffraction experiment, however, it is the intensities which are measured, and these are related to the structure factor by

$$I(hkl) \propto |F(hkl)|^2. \tag{2.4}$$

Thus the phases of $F(hkl)$ are not measurable quantities, but are required for $\rho(x, y, z)$ calculations. This is known as the phase problem. One of the ways employed to overcome this is direct methods. This process uses the observed structure factor amplitudes and their relationships to the intensities and indices of reflections to derive the phase angles.[208]

In this thesis, variable-temperature single-crystal X-ray diffraction experiments were carried out in-house on the Agilent technologies SuperNova (graphite-monochromated Mo Kα radiation $\lambda =$

0.71073 Å), and on the Nonius Kappa-CCD diffractometers (graphite-monochromated Mo Kα radiation $\lambda = 0.71073$ Å). Due to the changes in temperature, the single crystal had to be mounted on a glass fibre using either nail polish (up to 300 K) or araldite (up to 500 K) to prevent crystal re-orientation during collection. The presence of metal cations (with high scattering power) in the coordination polymers allowed the structure solution to be readily determined using direct methods as implemented in CRYSTALS.[210]

2.2.2 High-pressure single-crystal X-ray diffraction

High-pressure experiments suffer from the decrease in accessible reciprocal space volume due to the high-pressure cell. This is in part overcome by using particular collection strategies, or by studying high-symmetry structures. The modified Merrill-Bassett diamond anvil cell (DAC) that was used for the study of the pressure-induced response of Ag(mim) and $Cd(im)_2$ is shown in Figure 2.3.[211] Within the high-pressure cell, the single crystal is placed in a hydrostatic medium, alongside small ruby crystals. The former ensures hydrostatic conditions are maintained, and the latter allows the pressure to be measured *via* ruby fluorescence.[212]

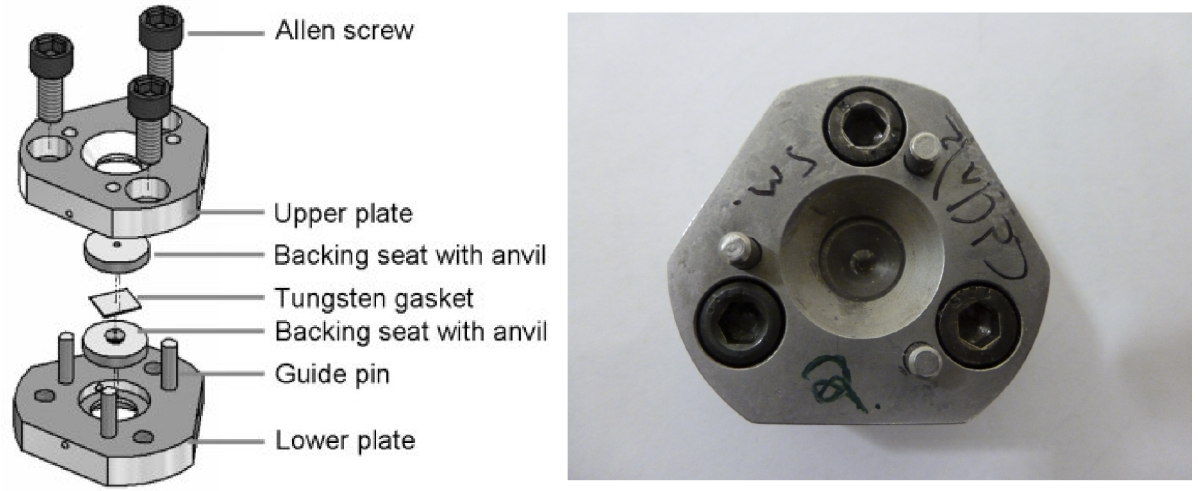

Figure 2.3: Merrill-Bassett diamond anvil cell used for high-pressure *in situ* single-crystal diffraction; left figure was reproduced from Ref. 211, with permission from the International Union of Crystallography.

High-pressure single-crystal diffraction experiments were conducted at Edinburgh University in collaboration with Dr Stephen Moggach, using a Bruker SMART APEXII diffractometer (graphite-monochromated Mo Kα radiation $\lambda = 0.71073\,\text{Å}$).

2.2.3 Powder X-ray diffraction

The three key features of a crystalline powder diffraction are given by the positions, intensities and shapes of the Bragg peaks, and are defined by the crystal structure, the powder sample microstructure and the instrumental parameters. The unit cell parameters determine the position of the peaks, while the atomic parameters (coordinates and thermal parameters) give the intensities. The powder sample microstructure can give rise to preferred orientation of the crystallites, which affects peak intensities, while its grain size, strain, and stress will influence peak shapes.[208]

The process of indexing a powder diffraction pattern involves identifying peak positions and determining a corresponding unit cell metric and crystal symmetry that describe these positions and reflection conditions. The proposed unit cell symmetry can then be verified by performing a Pawley refinement.[213] This refinement uses the unit cell description to identify the location of peaks, while the intensities of the peaks are fitted as least-squares variables. It is only by performing a Rietveld refinement that intensity fitting is performed using a structural model.

The Rietveld method involves refinement of structural and instrumental parameters by fitting a calculated diffraction pattern to the experimentally observed diffraction data.[214,215] The minimised function (Φ) is obtained by a nonlinear least-squares procedure given by

$$\Phi = \sum_{i=1}^{n} w_i \left(Y_i^{\text{obs}} - Y_i^{\text{calc}}\right)^2, \tag{2.5}$$

where Y_i^{obs} and Y_i^{calc} are, respectively, the observed and calculated intensities of a point i out of n total points in the powder diffraction pattern. Each point i is weighted by w_i. To allow sensible atomic configurations during Rietveld refinement, restraints, constraints and rigid bodies may be employed. Restraints are approximate limitations or relationships between parameters, and therefore are sometimes called *soft restraints*. In contrast, constraints impose strict limitations

or exact relationships between specific parameters. The former effectively increase the number of observations, while the latter reduce the number of free variables, both resulting in greater stability of the nonlinear least-squares refinement.[208] Rigid bodies are molecules or groups of atoms that are treated as a single unit; their location and orientation are defined by three positional and three orientational variables.

TOPAS academic version 4.1[216] was used as the main Rietveld refinement program.[§] The main information extracted from the Rietveld refinements in this investigation was the lattice parameters and metal cation positions, which were both reliably defined by the powder diffraction pattern. Bonding restraints and rigid bodies were applied to the metal–ligand bonds and to the organic molecular units, respectively. While the location of the rigid bodies could be easily derived from a published structural model, the orientations were obtained by simulated annealing as implemented in TOPAS. This process involved fixing all parameters, apart from the rigid body orientation angles, which were then randomly varied until a best fit was obtained. The bond lengths and internal angles defining the rigid bodies were refined for the first temperature point, and then kept fixed for the variable-temperature range studied.

For the analysis of related data sets, such as successive diffraction patterns in a variable-temperature study, sequential refinements were undertaken. This strategy involved using a refined model from one diffraction pattern as a starting model for the subsequent data set. In this way, structure refinements for successive temperature points exploited the structural similarity for data sets separated by small temperature changes. For the first refined diffraction pattern, initial parameters such as instrumental zero offset and rigid body internal parameters were refined, but then for the subsequent diffraction patterns these parameters were kept fixed. The relevant bonding distances and framework angles for compounds in Chapter 6 were calculated within TOPAS as part of the refinement. For Chapter 4, Fortran codes were used to extract the appropriate parameters from the CIFs.

Many of the variable-temperature diffraction patterns used in this thesis were measured at the high-resolution powder diffraction beamline I11 at the Diamond Light Source [Fig. 2.4].[217] Due to

[§]Example input files for Pawley and Rietveld refinements were provided by Josh Makepeace.

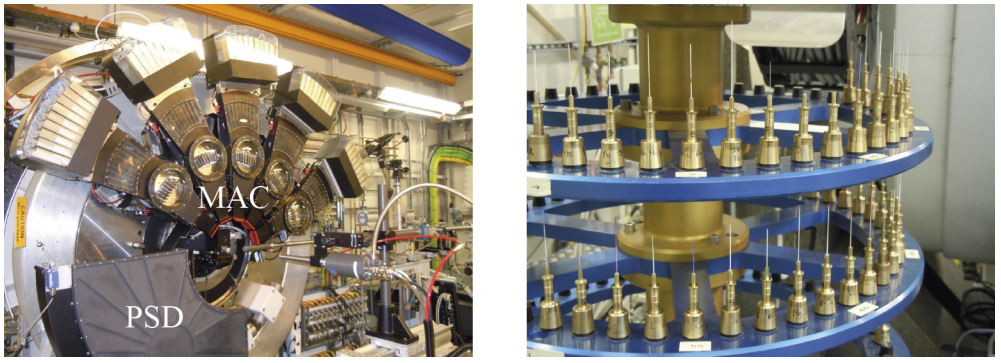

Figure 2.4: (*Left*) I11 diffractometer with the two types detectors indicated, (*right*) powder samples within capillaries and sample holders placed on the carousel *prior* to mounting.

problems with radiation damage, data collections with 5 s exposure times were obtained using the wide-angle position sensitive detector (PSD),[218] allowing a wide range of diffraction temperatures to be measured on the same sample.

2.2.4 Neutron total scattering

Total scattering data measure not only Bragg peaks, but also any diffuse background which may arise from local fluctuations away from the average structure. For these measurements, it is essential to obtain background measurements of the sample environment as this is subtracted from the measured data to provide the sample-dependent background. There are several advantages of using neutron scattering instead of the equivalent X-ray technique. Firstly, the coherent scattering by nuclei is independent of the Bragg angle, so there is no decrease in scattering power with increasing Bragg angle as seen with X-rays. Thus high Q-ranges can be obtained, where Q is proportional to θ by

$$Q = \frac{4\pi}{\lambda} \sin\theta. \tag{2.6}$$

Data that are collected to high Q are essential for the resolution of the pair distribution function which is derived from the data:[219]

$$\Delta r = 3.791/Q_{\max}. \tag{2.7}$$

Secondly, there is no radiation damage to the samples, as neutrons interact weakly with matter. The greatest difference between neutron and X-ray scattering lies in the scattering powers of

Table 2.1: Neutron coherent and incoherent scattering lengths (b_c and b_i, respectively) and absorption cross section (σ_a) for the main isotopes of the atoms within the coordination polymers studied. Values obtained from Ref. 220.

Atom	b_c (fm)	b_i (fm)	σ_a (barn)
H	− 3.7406(11)	25.274(9)	0.3326(7)
D	6.671(4)	4.04(3)	0.000519(7)
C	6.6511(16)	0	0.00353(7)
N	9.37(2)	2.0(2)	1.91(3)
O	5.803(4)	0	0.00010(2)
Zn	5.22(4)	0	0.93(9)
In	4.01(2)	−2.1(2)	202(2)

the atoms in the two techniques. Neutron scattering lengths of the organic C, N, O, D atoms, present in most organic ligands, are equivalent in size to metal scattering lengths [Table 2.1]. This contrasts with X-ray scattering which depends on electron count. Therefore neutron scattering of coordination polymers allows the metal as well as the organic ligands to be equally well defined by the data. Neutron scattering is not a routine measurement because of the long collection times ($\sim$ 6 h) and the large quantities of sample needed (several grams). In addition, because the incoherent scattering of H is very large [Table 2.1], the coordination polymers need to be deuterated, which can be costly.

The neutron time-of-flight general materials (GEM) diffractometer at the ISIS pulsed spallation source was used to collect the total scattering data presented in this thesis [Fig. 2.5].[219,221,222]

2.2.4.1 Data correction

The measured total scattering data—also known as the differential cross-section $\left(\frac{d\sigma}{d\Omega}\right)$—were placed on an absolute scale using GUDRUN,[224] which corrects for beam attenuation, multiple scattering, and background and normalises the data against the scattering measured for a vanadium rod. The formalisms for the relevant functions derived from this data are now introduced; Ref. 225 provides a comprehensive review on the different total scattering formalisms.

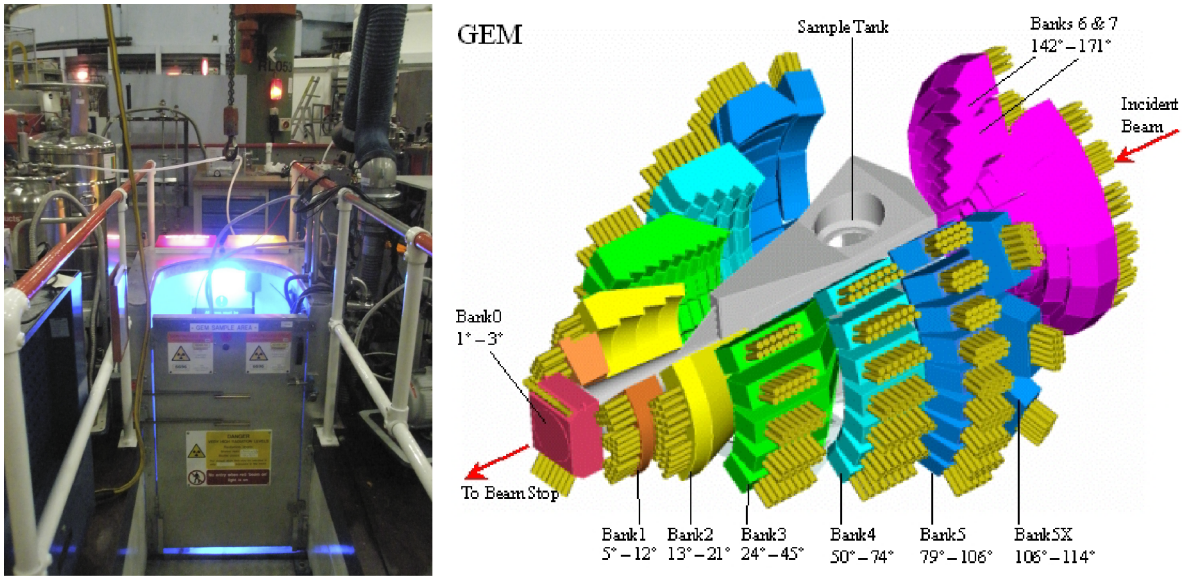

Figure 2.5: GEM diffractometer and the arrangement of the different detector banks; right figure was reproduced from Ref. 223.

The total-scattering intensity is defined by

$$\frac{1}{N}\frac{\mathrm{d}\sigma}{\mathrm{d}\Omega} = F(Q) + \sum_{j=1}^{n} c_j \bar{b}_j^2, \tag{2.8}$$

where $4\pi \sum_j c_j \bar{b}_j^2$ is the total scattering cross-section of the material and the summation is over the n atom types.[226] The $\bar{b}_j$ term is comprised of the average of the scattering lengths of element j over its different isotopes. N and c_j represent the number of atoms in the material and the proportion of atom type j, respectively. The total scattering structure factor, $F(Q)$, is related to the total radial distribution function, $G(r)$, by the Fourier transforms

$$F(Q) = \rho_0 \int_0^{\infty} 4\pi r^2 G(r) \frac{\sin Qr}{Qr} \mathrm{d}r, \tag{2.9}$$

$$G(r) = \frac{1}{(2\pi)^3 \rho_0} \int_0^{\infty} 4\pi Q^2 F(Q) \frac{\sin Qr}{Qr} \mathrm{d}Q, \tag{2.10}$$

where the average atom number density $\rho_0 = N/V$ (in atoms Å^{-3}). $G(r)$ is defined by the partial radial distribution functions $g_{ij}(r)$:

$$G(r) = \sum_{i,j=1}^{n} c_i c_j \bar{b}_i \bar{b}_j [g_{ij}(r) - 1], \tag{2.11}$$

where

$$g_{ij}(r) = \frac{n_{ij}(r)}{4\pi r^2 \mathrm{d}r \rho_j}. \tag{2.12}$$

The term $n_{ij}(r)$ defines the number of pairs of atoms of type i and j separated by distance r and by $r + \mathrm{d}r$. Alternative representations to $G(r)$ include the differential correlation function, $D(r)$, defined as

$$D(r) = 4\pi r \rho_0 G(r). \tag{2.13}$$

The $G(r)$ and $D(r)$ functions are known as the pair distribution functions (PDFs), and both represent a histogram of distances between atoms within the structure. PDFs are visually intuitive: the r distance at which the peak is found and its peak area correspond to the distance between two atoms, and the frequency of that particular distance, respectively. The low-r regions therefore indicate the immediate coordination environments of the atoms in the structure. The $D(r)$ function accentuates high-r variation by scaling with r.

As can be seen from the above equations, correct normalisation of the total scattering data relies on an accurate sample composition, which defines the total scattering cross-section $\left(4\pi \sum_j c_j \bar{b}_j^2\right)$ and the number density of the material (ρ_0).

2.2.4.2 Reverse Monte Carlo

The reverse Monte Carlo (RMC) refinement method[227] and its implementation in the program RMCPROFILE[226] have been particularly successfully for analysing total scattering data of disordered crystalline structures.[228] The basic refinement objective in RMCPROFILE is to produce atomic configurations that account simultaneously for real-space (*e.g.* $G(r)$, $D(r)$), reciprocal-space (*e.g.* $F(Q)$), and Bragg profile ($I(t)$) functions. This is achieved by accepting or rejecting random atomic moves in a large supercell, subject to the metropolis Monte Carlo algorithm, where in this case the Monte Carlo energy function is determined by the quality of the fits to the data. The fit quality is evaluated by calculating a χ^2 for each data set. For example, the χ^2 for the $G(r)$ function is as follows

$$\chi^2_{G(r)} = \sum_j \left[G_{\mathrm{calc}}(r_j) - G_{\mathrm{exp}}(r_j)\right]^2 / \sigma^2_{G(r)}, \tag{2.14}$$

where σ parameters represent standard errors on individual data points j.[226] All atomic moves that decrease the value of χ^2 are automatically accepted, and those that increase χ^2 are accepted within a certain probability that follows a normal distribution with the width σ.[227] This ensures that the configuration does not become trapped in local minima. The RMC method can additionally incorporate restraints, where any calculated quantity f^{calc} in the atomic configuration—such as bond lengths and bonding angles—are compared to the required value f^{req}.[226] The restraints are implemented using

$$\chi_f^2 = \sum_k w_k \left[f_k^{\text{calc}} - f_k^{\text{req}} \right]^2, \tag{2.15}$$

where k are the different restraints applied, and w_k is the weighting factor.

By simultaneously fitting both real-space $G(r)$ and reciprocal-space $F(Q)$ and $I(t)$ functions, the atomic configurations obtained will show local structure which remains consistent with the long-range periodic order reflected in the Bragg intensities. RMC refinements of crystalline materials in which reciprocal-space data are not used have a tendency to become unphysically disordered.[228] Analysis of the RMC atomic configurations can then give insight into local distortions that cannot be obtained using traditional Rietveld analysis. Fortran programming was used to calculate and extract information from these large configurations, which contain several thousands atoms.

2.3 Thermal expansion and compressibility determination

The CTEs or compressibilities for the orthogonal and hexagonal structures presented in this thesis were usually determined using linear fits to the lattice parameters as a function of temperature or pressure, respectively. The errors are then obtained from these fits, and reflect how well the fits represent the individual data points. In most cases, there is usually enough scatter in the lattice parameters to allow sensible errors to be obtained; the errors from the lattice parameters themselves are very small. In the case of $Zn(ISN)_2$ and $InD(BDC)_2$, additional empirical equations were used to fit the lattice parameters in order to capture the nonlinearity at the low-temperature lattice parameter evolutions.

For the monoclinic structures, the lattice parameter evolutions, as well as that of the β angles were provided as input to the web-based principal axis strain calculator, known as PASCal.[179] This program diagonalises the strain matrix, and allows the expansivities of the principal axes to be determined. PASCal was also used for the calculation of the bulk modulus, B_0 and its pressure derivative B'. The calculation is performed by fitting a Birch-Murnaghan equation of state to the variation in volume as a function of pressure. For a limited number of data points the second-order Birch-Murnaghan fit is used to calculate B_0:

$$p(V) = \frac{3B_0}{2}\left[\left(\frac{V_0}{V}\right)^{\frac{7}{3}} - \left(\frac{V_0}{V}\right)^{\frac{5}{3}}\right], \tag{2.16}$$

where V_0 is the zero-pressure unit-cell volume. With many pressure points, a third-order Birch-Murnaghan fit can be performed

$$p(V) = \frac{3B_0}{2}\left[\left(\frac{V_0}{V}\right)^{\frac{7}{3}} - \left(\frac{V_0}{V}\right)^{\frac{5}{3}}\right]\left\{1 + \frac{3}{4}(B_0' - 4)\left[\left(\frac{V_0}{V}\right)^{\frac{2}{3}} - 1\right]\right\}, \tag{2.17}$$

allowing the extraction of B_0 and B'.

Chapter 3

Mechanical Building Units

As highlighted in the introduction, coordination polymers show large and varied magnitudes of mechanical response. This first results chapter investigates the mechanical properties of silver(I) 2-methylimidazolate, Ag(mim), with the aim of establishing general predictive mechanical property rules. Ag(mim) was chosen in particular because it contains different structural building units with varying degrees of strength, such as weak argentophilic interactions, framework wine-rack motif, and coordination bonds. Additionally, the bulk mechanical response of Ag(mim) can be readily linked to the evolutions of the important structural features as these lie directly along each crystallographic axis. The mechanical properties of Ag(mim) were determined using a combination of variable-temperature and -pressure diffraction experiments, allowing the extraction of CTEs and compressibility values. The temperature- and pressure-induced mechanical responses are found to be related, and can both be explained by the structural features in Ag(mim). These features are abstracted into mechanical building units (XBUs), which can be used to interpret known mechanical properties in other coordination polymers, as well as to predict the type and magnitude of mechanical response in these materials. The results of this chapter are found in the publication: J. M. Ogborn, I. E. Collings, S. A. Moggach, A. L. Thompson, and A. L. Goodwin, *Chem. Sci.*, 2012, **3**, 3011–3017.

The experimental work and analysis in this chapter was carried out in collaboration with Joseph Ogborn, a Part II (MChem) student in the group at the time.

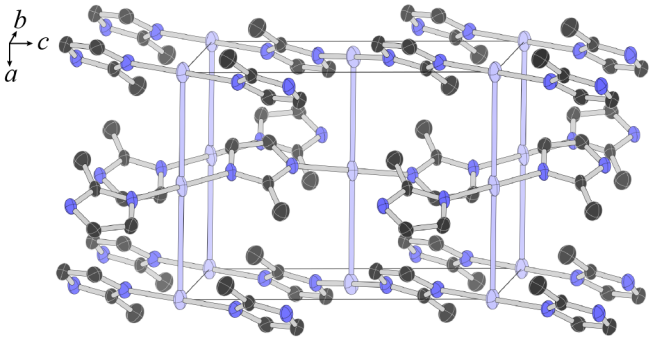

Figure 3.1: Representation of the crystal structure of Ag(mim): Ag atoms in light purple, C atoms in black and N atoms in blue; H atoms are omitted for clarity. Argentophilic interactions are represented as purple cylinders and thermal ellipsoids are given at the 50% probability level.

3.1 Structure of Ag(mim)

Ag(mim) is a one-dimensional coordination polymer, composed of Ag(I) centres which are connected in one direction *via* exo-bidentate 2-methylimidazolate ligands, and in a perpendicular direction by possible ligand-unsupported argentophilic (Ag...Ag) interactions [Fig. 3.1].[229] These interactions are defined as weak attractive forces which would result in Ag^+–Ag^+ distances that are closer than their sum of van der Waals radii (< 3.44 Å),[230–232] and are used to increase framework dimensionality in coordination polymers.[233,234] It is thought that the attractive forces are due to favourable d^{10}–d^{10} interactions, induced by the mixing of 6s, 6p and 5d orbitals brought about by relativistic effects in the case of Au...Au interactions.[235–237]

Ag(mim) has been investigated previously because of its rich host–guest properties,[238] solvent-induced supramolecular isomerism,[229] and due to its effective antimicrobial activities.[239] In addition, often silver-containing coordination polymers give rise to luminescence,[234] which is relevant for sensing capabilities.[240] The framework topology of Ag(mim) is that of the cadmium sulfate (**cds**) net and the crystal symmetry is monoclinic (space group $P2_1/n$, $\beta = 92.454(3)°$), with the lattice parameters $a = 7.8946(6)$ Å, $b = 5.9692(4)$ Å, and $c = 10.8812(10)$ Å.

3.2 Experimental details of Ag(mim)

Joseph Ogborn carried out all the experimental work on Ag(mim); the variable-temperature single-crystal X-ray diffraction was carried out with assistance from Dr Amber Thompson at the University of Oxford, likewise the high-pressure experiments were performed in collaboration with Dr Stephen Moggach from Edinburgh University.

3.2.1 Synthesis

Single crystals of Ag(mim) were prepared *via* slow diffusion of aqueous or methanolic solutions (*ca* 0.2 M) of silver(I) nitrate (Aldrich, 99%) and 2-methylimidazole (Aldrich, 99%). Deprotonation of the organic ligand was achieved by addition of a small quantity of triethylamine (Aldrich, 99%). The single crystal used for variable-temperature measurements was also used in the pressure experiments for $p < 0.3$ GPa. However, the crystal morphology was such that the crystal slipped easily within the gasket during pressurisation, so a second crystal of comparable quality was used for higher pressure measurements. Polycrystalline samples of Ag(mim) were prepared by addition of stoichiometric amounts of aqueous solutions of silver(I) nitrate and 2-methylimidazole, with triethylamine added as a deprotonating agent. The resulting precipitate was washed (H_2O), dried under vacuum and finely ground.

3.2.2 Variable-temperature single-crystal X-ray diffraction

Variable-temperature single-crystal X-ray diffraction experiments were carried out on a Nonius KappaCCD diffractometer (graphite-monochromated Mo Kα radiation $\lambda = 0.71073$ Å) with an Oxford CryoSystems CryoStream 600 open flow cooling device.[241] Data for unit cell determinations were collected on a single crystal on cooling from 300 K to 100 K with a 20° ω-scan recorded every 10 K (cooling rate 300 K h^{-1}). Extended data collections were recorded at 300 K and at 50 K intervals to 100 K. 20° ω-scans were also collected every 20 K on warming at a rate of 120 K h^{-1} to confirm reversibility.

3.2.3 Variable-pressure single-crystal X-ray diffraction

High-pressure single-crystal X-ray diffraction (HP-SCXRD) data were collected using a Bruker SMART APEXII diffractometer (graphite-monochromated Mo Kα radiation $\lambda = 0.71073\,\text{Å}$). An initial sphere of single-crystal diffraction data was collected on a crystal of Ag(mim) at ambient temperature and pressure in order to provide data for comparison with the high-pressure studies. These data were integrated using the program SAINT,[242] while the absorption correction was carried out using the program SADABS.[243] The structure was solved with SHELXS-86[244] and refined in CRYSTALS using full matrix least-squares against $|F|^2$ using all data.[210] The final conventional R-factor was 3.79% for 1340 reflections.

High-pressure experiments were carried out with a modified Merrill-Bassett DAC equipped with 600 μm culet diamonds and a tungsten gasket.[211] The sample and a chip of ruby were loaded into the DAC with a 4:1 mixture of methanol and ethanol used as a hydrostatic pressure-transmitting medium. The ruby fluorescence method was used to determine the cell pressure, and this was measured before and after each data collection.[212] The average of both pressure points were taken with its corresponding standard deviation and used in the analysis.

HP-SCXRD data were collected using ω-scans in eight different settings of 2θ and ϕ angles with a frame and step size of 40 s and 0.3°, respectively (as described in Ref. 245). The data were integrated using the program SAINT,[242] using dynamic masks to avoid integration of regions of the detector shaded by the body of the pressure cell. Absorption corrections for the DAC and sample were carried out with the programs SHADE[246] and SADABS,[243] respectively. Data were collected from 0.3 GPa up to a final pressure of 6.4 GPa. On increasing pressure further the gasket cracked, prohibiting data collection at pressures above 6.4 GPa. Pressure equilibration times varied from data set to data set, and this accounts for the variation in uncertainties in pressure values observed in Figure 3.2.

3.2.4 Single-crystal data solution and refinement

The structure solution for Ag(mim) obtained from the initial ambient data collection was used as a starting point for structure refinements against the low-temperature and high-pressure data within CRYSTALS.[210] In each case, refinement was against $|F|^2$ using all available reflections. The low completeness inherent to high-pressure diffraction experiments meant that additional restraints were included during refinement: namely, all 1,2 and 1,3 distances within the 2-methylimidazolate ligand were restrained to the values observed in the ambient-pressure structure. Ag–N distances, N–Ag–N angles and ligand torsion angles were refined freely. Whereas H atoms attached to C atoms were placed geometrically for the high-pressure data, for the low-temperature data H atom positions were refined with a riding model.[247] Anisotropic thermal parameters were refined for the variable-temperature data, while isotropic displacement parameters and thermal-similarity restraints (C and N atoms) were used for the variable-pressure refinements.

3.2.5 Variable-temperature powder X-ray diffraction

Powder X-ray diffraction (PXRD) data were collected using a Siemens D5000 X-ray diffractometer (Cu Kα and Kβ radiation $\lambda = 1.540598$ Å and $\lambda = 1.544426$ Å) fitted with an Oxford CryoSystems PheniX closed cycle refrigeration unit. The sample was cooled under vacuum to 20 K and data in the 2θ range of 10–60° were collected every 10 K from 20–150 K warming at a rate of 120 K h^{-1}. The cell parameters were determined at each temperature using the Rietveld method as implemented in GSAS[248] and the EXPGUI[249] interface.

3.3 Temperature- and pressure-induced mechanics of Ag(mim)

The temperature-induced response of Ag(mim) was determined using variable-temperature powder (20–150 K) and single-crystal (100–300 K) X-ray diffraction; its pressure-induced response was determined using variable-pressure single-crystal X-ray diffraction measurements (0–6.4 GPa).[211] The measured temperature- and pressure-dependent variations in lattice parameters are shown in Figure 3.2(a,b). As Ag(mim) has monoclinic symmetry, its unit cell parameters need not coincide

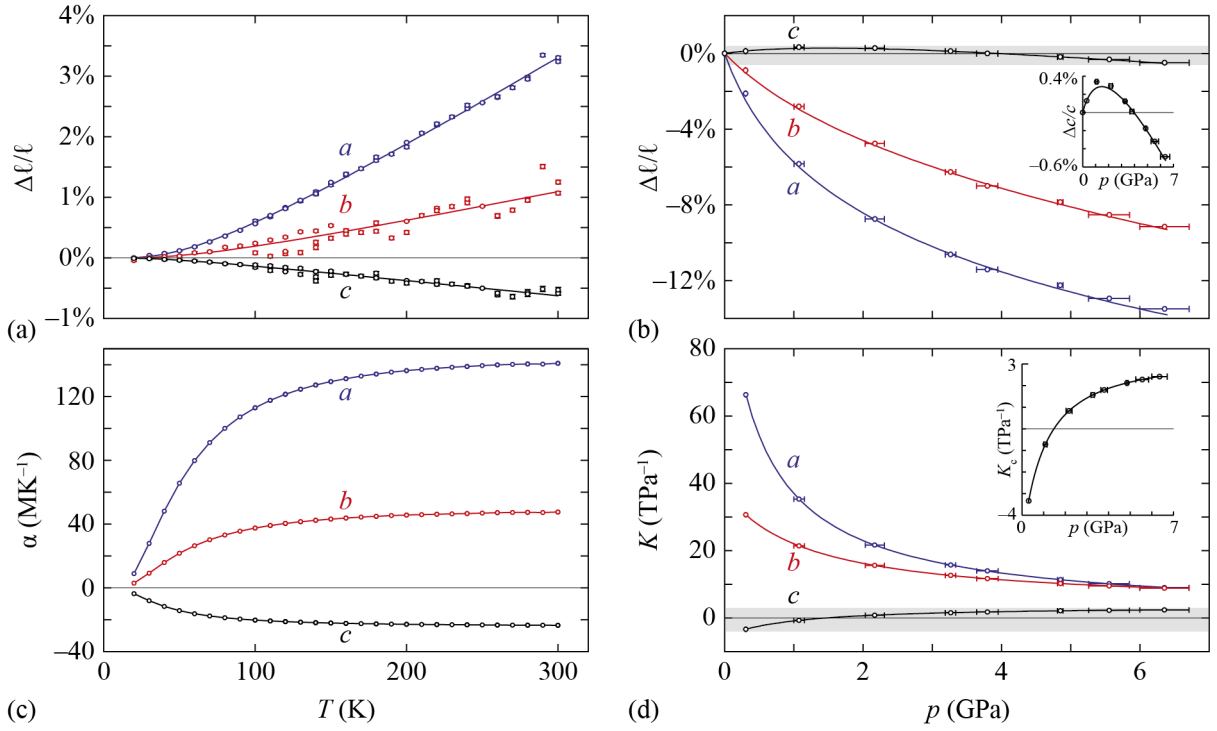

Figure 3.2: Experimental lattice parameter variation observed under changes in (a) temperature (with heating and cooling), and (b) pressure. The corresponding (c) expansivities and (d) compressibilities are determined using empirical fits to the unit cell data. The inset plots in (b) and (d) show the crossover from negative to positive linear compressibility response in Ag(mim) at *ca* 2 GPa; the relevant regions of the main plots are shaded.

with the principal axes. However, the monoclinic β angle in Ag(mim) is close to 90° and largely invariant, therefore the monoclinic unit cell follows closely the behaviour of the corresponding principal axes [Section A.1]. Due to the nonlinearity in the lattice parameter evolutions with temperature or pressure, the following empirical equations were used to fit the lattice parameter (ℓ) evolutions

$$\ell(T) = \ell_0 + \kappa T \left(\frac{T}{T + T_c} \right)^{\lambda}, \tag{3.1}$$

$$\ell(p) = \ell_0 + \eta (p - p_c)^{\nu}. \tag{3.2}$$

The corresponding expansivities and compressibilities were obtained from these empirical fits (Section A.2) and are given in Figure 3.2(c,d); the average expansivity and compressibility values determined from linear fits to the same data are listed in Table 3.1.

Table 3.1: Linear principal-axis expansivities (20–300 K) and compressibilities (0–1 GPa and, marked by an asterisk, 0–6.4 GPa) for Ag(mim), calculated using PASCal.[179]

Prinicipal axis, i	Direction	α_i (MK^{-1})	K_i (TPa^{-1})	K_i^* (TPa^{-1})
$\mathbf{x}_1$	$\sim$ **a**	+130(2)	+55(4)	+21(3)
$\mathbf{x}_2$	**b**	+44(3)	+25.8(10)	+14.2(11)
$\mathbf{x}_3$	$\sim$ **c**	−24.5(8)	−4.32(10)	+0.2(3)

Three especially anomalous properties of Ag(mim) are immediately apparent by inspection of Figure 3.2(c,d) and Table 3.1. First, the material exhibits NTE along its *c*-axis ($\alpha_c = -24.5(8)\,MK^{-1}$), and moreover, the compressibility is also negative in this direction up to 1.5 GPa; at pressures above 1.5 GPa, the structure exhibits PLC instead. A similar effect was reported for the zeolitic framework ZIF-8, which was shown to switch between NLC and PLC behaviour at ∼0.2 GPa (Ref. 164). However, in that study the phenomenon was associated with incorporation of pressure-transmitting fluid within the framework pore structure. Ag(mim) has no accessible pore volume, so the effect observed is an intrinsic compressibility of the material structure itself. And third, while typical in their sign, the magnitudes of expansivity and compressibility observed along **a** are so unusually large as to be comparable to the colossal mechanical responses observed in $Ag_3[Co(CN)_6]$.[8,171]

3.4 Mechanical building units of Ag(mim)

Just as the consideration of molecular building units—supramolecular components with pre-defined coordination geometries—provides a useful predictor of material structure,[250] here the mechanics of Ag(mim) are rationalised by using mechanical building units (XBUs). The XBUs are supramolecular interactions and topological motifs that, when identified within a coordination polymer, might help prediction of its mechanical behaviour.

The mechanical behaviour of Ag(mim) can be deconvoluted in terms of three fundamental XBU motifs [Fig. 3.3]. First, parallel to the **a** crystal axis there are the shortest Ag…Ag interactions

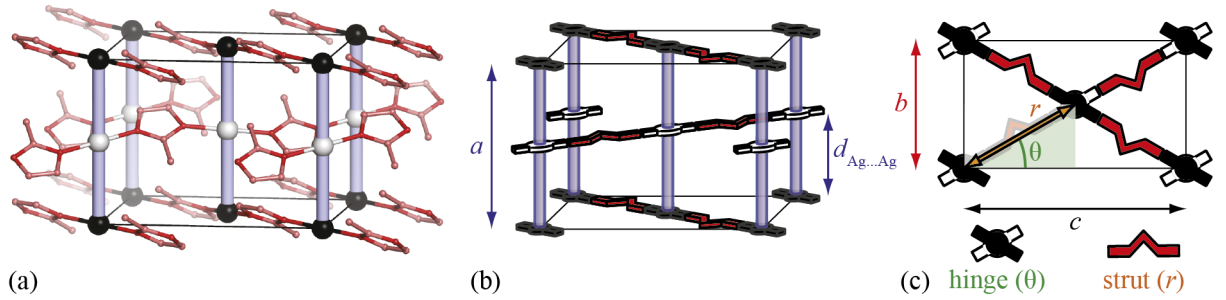

FIGURE 3.3: (a) Representation of the crystal structure of Ag(mim): Ag ions shown as black and white spheres and 2-methylimidazolate anions in red. Argentophilic interactions are shown as purple cylinders. (b, c) Abstract representations of the same structure with atoms replaced by XBUs: argentophilic interactions, hinges and struts. The relationship between the XBU parameters $d_{\mathrm{Ag...Ag}}, r, \theta$ and the unit cell dimensions a, b, c is indicated.

found in the structure. These 1D stacks of Ag^+ ions additionally function as the spindles for the supramolecular hinges (the second XBU), allowing flexing of the covalent –(Ag–mim)$_n$– chains relative to one another in the **bc**-plane. Finally, the bridging 2-methylimidazolate anions are molecular "struts" that connect adjacent hinges, also found within the **bc** plane. Assigning the parameters $d_{\mathrm{Ag...Ag}}$, θ and r to, respectively, the argentophilic Ag. . .Ag distance, the "hinge angle" and the Ag–mim–Ag unit distance [Fig. 3.3(b,c)], the relationships which directly link the XBUs to the lattice parameters are obtained:

$$d_{\mathrm{Ag...Ag}} = a/2, \tag{3.3}$$

$$\theta = \tan^{-1}(b/c), \tag{3.4}$$

$$r = \frac{1}{2}\sqrt{b^2 + c^2}. \tag{3.5}$$

The mechanical properties of Ag(mim) can now be recast in terms of the behaviour of these three XBU motifs. Figure 3.4 shows the XBU expansivities and compressibilities derived from the empirical fits; corresponding linear expansivities and compressibilities are listed in Table 3.2.

The temperature- and pressure-dependent evolutions of the XBUs are now used to comprehend the mechanics of Ag(mim). While the $d_{\mathrm{Ag...Ag}}$ XBU solely influences the a-axis (Eq. (3.3)), both the θ and r XBUs determine the behaviour of the b- and c-axes (Eqs. (3.4) and (3.5)). Thus, by deconvoluting the effects of θ and r, the mechanics of the b- and c-axes can be rationalised.

Table 3.2: Value of XBUs at ambient conditions and their linear expansivities (20–300 K) and compressibilities (0–1 GPa and, marked by an asterisk, 0–6.4 GPa) for Ag(mim), calculated using linear fits to the data. Corresponding enthalpic costs $\Delta H_{1\%}$ associated with 1% linear strains, estimated from published force constant data,[13,251–253] are given in the final column.

XBU	XBU value	α (MK^{-1})	K (TPa^{-1})	K^* (TPa^{-1})	$\Delta H_{1\%}$ ($J\,mol^{-1}$)
Ag...Ag	3.95 Å	+127(2)	+53(5)	+20(3)	40
θ	28.8°	+56.7(19)	+24.3(11)	+11.5(11)	100
r	6.21 Å	−7.5(12)	+3.543(5)	+3.91(7)	270

Figure 3.4(a) shows that the θ value increases with increasing temperature. This has the effect of increasing the b-axis and decreasing the c-axis through the framework hinging mechanism, while the decrease in r with increasing temperature gives rise to a decrease in both the b- and c-axes. Thus variations in θ and r have competing and additive effects: on the one hand the large PTE along **b** induced by framework hinging is marginally dampened by the small NTE along the r struts, and on the other hand, the NTE along **c** is enhanced by the NTE along r. By considering the pressure-dependent XBU evolutions, however, there is a much finer balance between the effects of θ and r on the lattice compressibilities [Fig. 3.4(b)]. This is because the compressibility along r is now positive, thus the responses generated from framework angle decrease, namely the PLC along **b** and the NLC along **c** are enhanced and dampened, respectively. In this case, the NLC along **c** is diminished to such an extent that for pressures above 1.5 GPa, regular PLC is observed

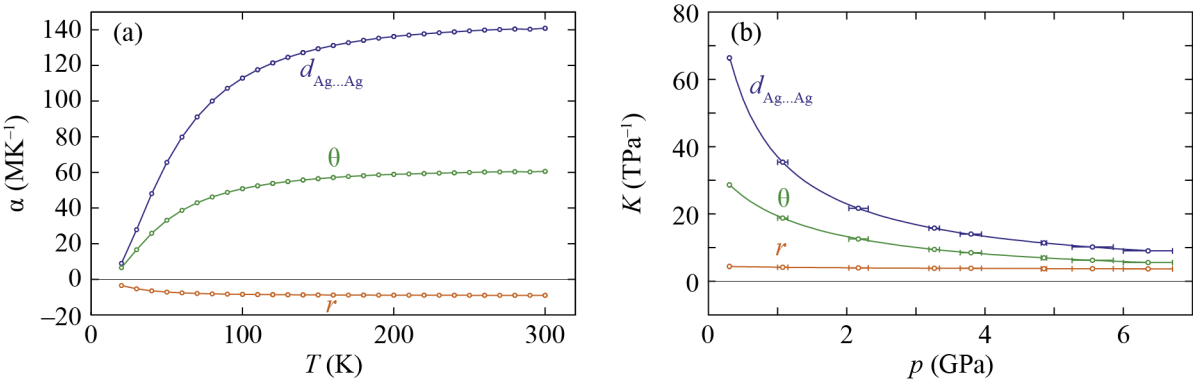

Figure 3.4: (a) Expansivities and (b) compressibilities of the XBUs calculated from empirical fits, which describe the mechanical responses of argentophilic interactions (Ag...Ag), lattice hinging (θ) and framework "struts" (r).

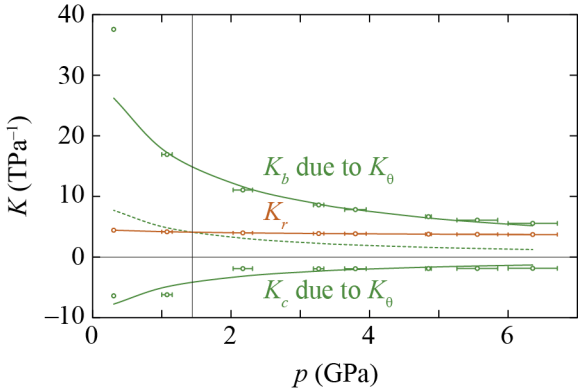

Figure 3.5: Calculated compressibilities obtained *via* empirical fits to the *b*- and *c*-axes using the variation in lattice θ only (due to K_θ). The compressibility along r is shown, along with the negative of the K_c due to K_θ (dotted line). The intersection between these is represented by the black vertical line and indicates the pressure at which the NLC–PLC transition is observed.

instead. This rationalisation is confirmed by calculating the compressibilities of the *b*- and *c*-axes using only the changes in lattice angles while keeping r constant using the following relations

$$b = 2r\sin\theta, \tag{3.6}$$

$$c = 2r\cos\theta, \tag{3.7}$$

$$\begin{aligned} K_b \text{ due to } K_\theta &= -\frac{1}{b}\left(\frac{\partial b}{\partial p}\right)_r = -\frac{2r}{b}\cos\theta\frac{\partial\theta}{\partial p} \\ &= \frac{c}{b}\theta K_\theta, \end{aligned} \tag{3.8}$$

$$\begin{aligned} K_c \text{ due to } K_\theta &= -\frac{1}{c}\left(\frac{\partial c}{\partial p}\right)_r = \frac{2r}{c}\sin\theta\frac{\partial\theta}{\partial p} \\ &= -\frac{b}{c}\theta K_\theta. \end{aligned} \tag{3.9}$$

The compressibilities for 'K_b due to K_θ' and 'K_c due to K_θ' are shown in Figure 3.5. It can be seen that K_c due to framework hinging remains negative throughout the pressure range studied. In practice, it is only at low pressures that the framework hinging effect dominates (note the rapid stiffening of K_θ in Figure 3.4(b)), while at higher pressures, K_r has greater influence over K_c, and hence there is a transition from NLC to PLC behaviour [Fig. 3.5].

This suggests that strong NLC behaviour associated with framework hinging will be most likely wherever network hinges are as flexible as possible (*i.e.* large K_θ) but are connected *via* strong and inflexible struts (*i.e.* small K_r). In addition, linear metal–ligand–metal binding geometries may

Table 3.3: CTEs and compressibilities of the unique Ag−mim−Ag binding angle, Ag−mim and Ag–Ag (linked *via* mim) distances extracted from single-crystal data and analysed as a function of temperature (100–300 K) and pressure (0–6.4 GPa). The 2-methylimidazolate centroid is represented by X, and the CTEs and compressibilities were calculated using linear fits to the data. The large error in the Ag–X–Ag angle is due to the 100 K data point; the expansivity calculated in the 150–300 K range gives $-6.7(7)\,\mathrm{MK}^{-1}$.

units	Ag–X–Ag angle	Ag_1–X	Ag_2–X	Ag_{ave}–X	Ag_1–Ag_2
MK^{-1}	0(4)	−14(2)	−2(2)	−8(2)	−8.4(4)
TPa^{-1}	5.8(5)	2.30(14)	0.6(3)	1.44(10)	3.89(8)

be more efficient at minimising K_r, as it is less likely that the metal–ligand binding angle varies. In Ag(mim), the Ag–mim–Ag binding angle is at 158°, and varies as a function of temperature and pressure, influencing the mechanics of r [Table 3.3]. It is interesting to note that while NTE arising from transverse vibrational modes is usually observed in frameworks containing linear metal–ligand–metal binding geometries,[128,133] here the bent Ag–mim–Ag binding is also capable of supporting these modes [Fig. 3.6].

The strength of the interactions within the XBUs can be estimated by calculating enthalpic costs associated with their deformations. First considering the Ag...Ag XBU, the Au...Au force constant of $0.147\,\mathrm{mdyn\,Å}^{-1}$ for an internuclear separation of *ca* 3.0 Å was used from Ref. 252, as force-constant data for ligand-unsupported argentophilic systems are surprisingly

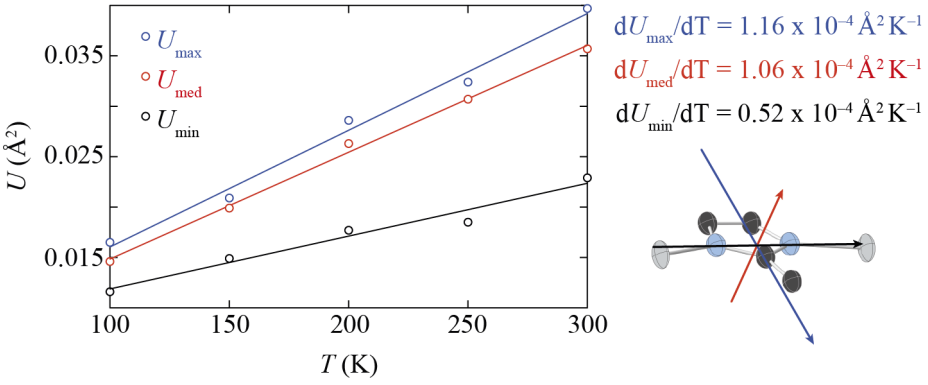

Figure 3.6: Principal components of the diagonalised anisotropic thermal parameters of 2-methylimidazolate as a function of temperature. The corresponding gradients and thermal parameter directions with respect to the ligand centroid are shown on the right of the graph. The largest thermal parameters are associated with directions perpendicular to the Ag−mim−Ag bonding axis, indicative of transverse vibrations.

rare. For ligand-supported argentophilic interactions, the ratio of Ag...Ag:Au...Au force constants is 0.203:0.449,[251] which suggests a ligand-unsupported argentophilic force constant of $0.066\,\mathrm{mdyn\,\AA^{-1}}$. Taking a typical Ag...Ag separation of 3.2 Å, then a 1% strain corresponds to an energy change of

$$\Delta E = k(r \times 1.01)^2 N_A = 41\,\mathrm{J\,mol^{-1}}, \tag{3.10}$$

where the force constant is k, the distance is r and N_A represents Avogadro's number.

In order to estimate framework flexing energies, the dispersive-uncorrected DFT results of Calleja *et al.* for $Ag_3[Co(CN)_6]$ were used.[253] In that study, the energy of $Ag_3[Co(CN)_6]$ was calculated for an array of lattice parameter values, with the lattice-flexing distortion tracing out a low-energy "valley" in phase space. A quadratic fit to the energy within this valley according to the expression

$$E(a) = E_0 + \alpha(a - a_0)^2 \tag{3.11}$$

gives parameters $E_0 = 247\,\mathrm{meV}$, $\alpha = 185\,\mathrm{meV\,\AA^{-2}}$ and $a_0 = 7.58\,\text{Å}$. Consequently, a 1% linear strain in the lattice parameter corresponds to an energy change of

$$\Delta E = E_0 + \alpha(a_0 \times 1.01)^2 - E_0 = 103\,\mathrm{J\,mol^{-1}}. \tag{3.12}$$

Finally, the molecular potentials used in a RMC study of ZIF-4 (composition $Zn(im)_2$) were used to estimate the energy cost of a 1% strain in the Ag–mim–Ag linkage through transverse displacements.[13] The basic form of the angular potential is

$$E = \frac{1}{2}K\left(\cos\theta - \cos\theta_0\right)^2, \tag{3.13}$$

with Zn–N–C angle force constant estimated at $K = 20\,\mathrm{eV}$ and ground-state Zn–N–C angle $\theta_0 = 120°$. Straightforward trigonometry gives a reduction in θ by 0.78° following a 1% reduction in the Zn···Zn separation by transverse displacement of the imidazolate anion [Fig. A.1]. The corresponding energy penalty (noting that two Zn–N–C angles are affected) is

$$\Delta E = \frac{1}{2}K\left(\cos(\theta_0 - 0.78) - \cos\theta_0\right)^2 \times 2 = 270\,\mathrm{J\,mol^{-1}}. \tag{3.14}$$

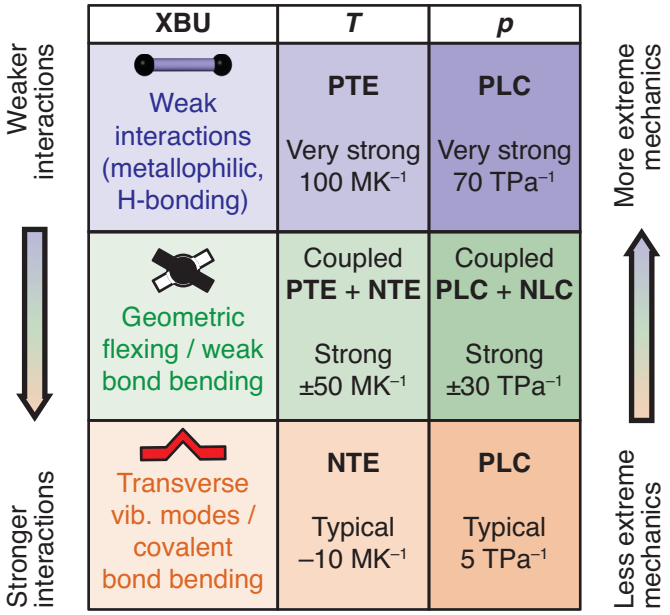

Figure 3.7: Tabular summary of the mechanical properties of different classes of supramolecular motifs in framework materials.

These calculated ΔE values provide estimates to the corresponding energy penalties for the XBU distortions in Ag(mim), and are shown in Table 3.2; what emerges is a clear distinction in magnitude of mechanical response that scales inversely with strength of interaction. So, as intuition would demand, the strongest interactions are most weakly affected by temperature or pressure.

3.5 Discussion: Generality of XBUs

Using XBUs to predict framework mechanics not only identifies the type of response, but also its magnitude [Fig. 3.7]. While the mechanical properties of a single framework are determined for Ag(mim), the fundamental trends observed here can be applied across many other coordination polymers of different underlying chemistry. For example, all three of the cubic frameworks MOF-5, $Zn(CN)_2$ and HKUST-1 can be thought of as an array of connected "strut" XBUs [Fig. 3.8(a)]; consequently, one anticipates the three materials to exhibit qualitatively-similar moderate NTE and PLC effects, as indeed they do.[128,133,134,184] Likewise the framework structures of $Ag_3[Co(CN)_6]$, MIL-53 and $[Zn_2(fu\text{-}L^1)_2dabco]_n$ can be represented by a connected network of hinges coupled *via* very soft interactions (Ag...Ag, weak π–π and Van der Waals interactions,

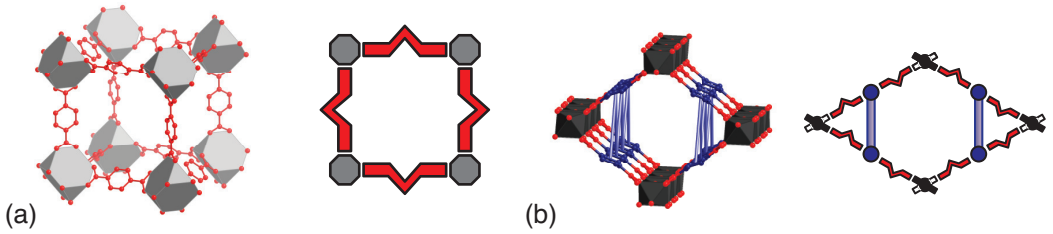

Figure 3.8: Schematic representations of XBUs in 2D MOF analogues. (a) MOF-5, like $Zn(CN)_2$ and HKUST-1 (not shown), consists of a connected array of linker XBUs; (b) MIL-53, like $Ag_3[Co(CN)_6]$, $[Zn_2(fu\text{-}L^1)_2dabco]_n$ (also not shown), can be thought of as an array of connected hinge XBUs with very soft additional interactions. Frameworks of the first type would be expected to show weak NTE and PLC effects; whereas frameworks of the second type should exhibit very strong anisotropic NTE/PTE and NLC/PLC behaviour.

respectively) [Fig. 3.8(b)].[8,10,254] For these materials the qualitative rules depicted in Figure 3.7 now predict very strong anisotropic NTE/PTE and NLC/PLC effects, as is observed experimentally.[8,10,149,171,177,255]

The temperature- and pressure-induced responses are related due to the isotropic Grüneisen parameters framework materials are prone to display.[171] As seen in Ag(mim), the 2D framework hinging is observed upon variation of temperature and pressure, giving rise to PTE/NTE and PLC/NLC responses, respectively. However, the correspondence between the negative mechanics upon temperature and pressure changes is reduced for higher pressures. This is due to the low framework angle variation at high pressure, possibly due to steric effects, while temperature changes do not appear to constrain the hinging mechanism. Hence, NTE–PTE transitions are not likely to be observed, while NLC–PLC transitions are anticipated for coordination polymers which have a fine balance between framework hinging and bond compression mechanisms, as is observed at pressures above 1.5 GPa for Ag(mim).

Within a given structure type, the choice of XBUs will allow fine-tuning of the magnitude of mechanical response: examples would include replacement of argentophilic for stronger aurophilic or weaker cuprophilic interactions, substitution of π-active for π-inactive ligands (*e.g.* phenyl *vs* cyclohexyl substituents), or interconversion of hydrogen- and halogen-bonding motifs. While it is generally the case that increasing the strength of supramolecular interactions translates to stiffer mechanics, there will likely be interesting anomalies, such as the drastic reduction of O–H force

constants in "strong" O–H. . .O hydrogen bonds as their potential surface switches from bimodal to unimodal.[256] As must be the case for any qualitative property-predicting tool, the XBU approach is a simplification that overlooks many system-specific details. Nonetheless the ability to predict mechanical behaviour in framework materials—even in general terms—starts to enable framework mechanics to be combined intelligently with chemical and/or electronic functionality.

3.6 Summary

Consideration of a framework structure in terms of its mechanical building units can be used as a predictive tool for framework flexibility and response under external stimuli such as temperature or pressure. In particular, the expansivities and compressibilities of the framework Ag(mim)—with varied structural features—was shown to be fully understood by considering its XBUs. Many of the mechanical behaviour in other coordination polymers can be rationalised using the XBU abstraction detailed here. The generality of this approach is clearly a powerful way of evaluating the mechanics of these materials by simple inspection of their crystal structures.

Chapter 4

Topology

The XBUs identified in Chapter 3 allow one to predict readily mechanical response along the direction or plane in which the XBUs are positioned. The metal–linker–metal framework connectivities will dictate the type of XBUs that can be found, and also their position within the structure relative to the cell axes. Thus, for both these reasons, framework topology might be expected to have a profound effect on the mechanical properties. In this chapter, two diamondoid coordination polymers are investigated: zinc cyanide, $Zn(CN)_2$, and cadmium imidazolate, $Cd(im)_2$. These frameworks were chosen because they have similar arrangements of strut XBUs, while the chemistry of the strut is very different between the two frameworks. In this way, the effect of changing the chemistry of the strut XBU is investigated directly, and compared to the topology-driven mechanics in both structures. $Zn(CN)_2$ is known to exhibit large isotropic NTE, and in order to obtain greater understanding into its NTE mechanism, the pressure-induced response is investigated. Both variable-temperature and -pressure diffraction experiments were carried out for $Cd(im)_2$, and the structural evolutions of $Cd(im)_2$ upon heating are compared to those observed in $Zn(CN)_2$ as a function of pressure. The results of this chapter are found in the publication: I. E. Collings, A. B. Cairns, A. L. Thompson, J. E. Parker, C. C. Tan, M. G. Tucker, J. Catafesta, C. Levelut, J. Haines, V. Dmitriev, P. Pattison, and A. L. Goodwin, *J. Am. Chem. Soc.*, 2013, **135**, 7610–7620.

All the experimental work on $Zn(CN)_2$ in this chapter was performed by Andrew Cairns, another DPhil student in the group. The discussion regarding the relationship between the critical responses of $Zn(CN)_2$ and $Cd(im)_2$ was developed collaboratively.

4.1 Structures of $Zn(CN)_2$ and $Cd(im)_2$

Both $Zn(CN)_2$ and $Cd(im)_2$ framework structures are composed of tetrahedral metal cations (Zn^{2+} or Cd^{2+}) connected *via* molecular anions (CN^- or im^-) to form two-fold interpenetrated diamondoid nets [Fig. 4.1]. In the case of $Zn(CN)_2$, the framework adopts the anticuprite topology[§] with linear Zn–CN–Zn binding geometries, crystallising in the $Pn\bar{3}m$ space group ($a = 5.8917$ Å).[1,257] This is the highest symmetry known for two-fold interpenetrated diamondoid nets, hence this phase will be referred to as the aristotype. The consideration of only one $Zn(CN)_2$ net gives topological equivalence to β-cristobalite. With $Pn\bar{3}m$ cell symmetry, the cyanide orientations are disordered throughout the structure such that the C and N atoms cannot be distinguished. This has been verified independently by neutron scattering,[258] spectroscopic measurements,[259] and solid-state NMR.[260] $Zn(CN)_2$ has been studied extensively due to its large isotropic NTE,[127,128,258,260] and the mechanism of NTE will be discussed further in Section 4.3.

$Cd(im)_2$ contains bent Cd–im–Cd linkages at an angle of ∼156°, and crystallises in the *Pbca* space group with lattice parameters $a = 14.6045(5)$ Å, $b = 10.7385(3)$ Å, and $c = 9.9229(4)$ Å.[93,261] The single net of $Cd(im)_2$ resembles the distortion seen in α-cristobalite (*cf.* Si–O–Si angles at 146°). $Cd(im)_2$ is of interest due to its structural similarity to cristobalite, especially so as it is one of the few diamondoid ZIFs to form.[262] This may be due to the large Cd^{2+} cation used which allows two-fold interpenetration of the diamondoid nets, thus stabilising the structure. The use of smaller metal cations, such as Zn^{2+}, gives rise to a single net because of the shorter Zn–Zn separations.[262] The greater porosity associated with a single net is perhaps one of the reasons why diamondoid $Zn(im)_2$ has not yet been observed experimentally. The diamondoid $Cd(im)_2$

[§]Referred to as anticuprite because the O^{2-} ligands in cuprite act as the tetrahedral nodes, while the Cu^+ cations adopt the linker positions.

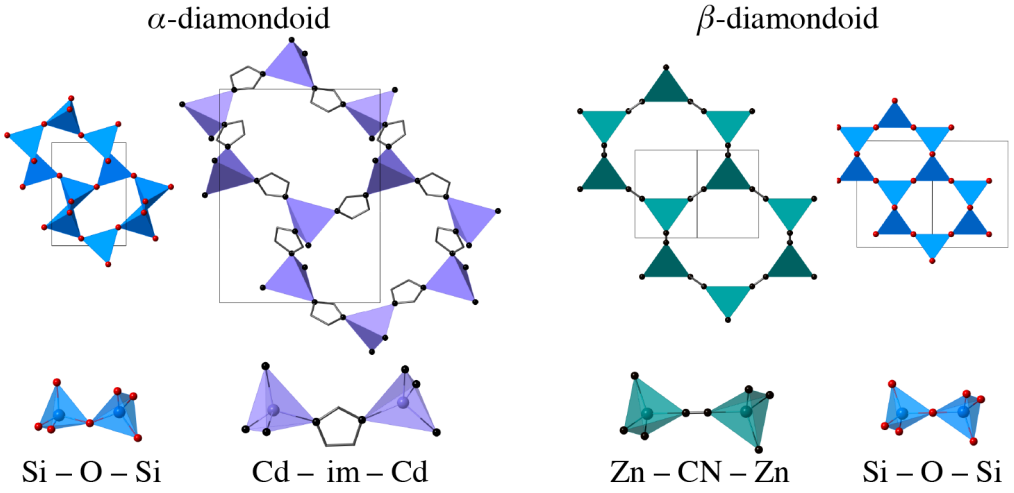

Figure 4.1: Crystal structures and coordination environments of frameworks with distorted low-symmetry (α) and high-symmetry (β) diamondoid networks: (left–right) α-cristobalite, $Cd(im)_2$, $Zn(CN)_2$ and β-cristobalite. All structures are shown at the same scale. Only one of the two networks is shown for both coordination polymers in order to accentuate the diamondoid connectivity.

has been investigated for photoluminescence properties,[263] and functionalised porous cadmium imidazolates (of different topologies) have been studied for gas storage.[264]

4.2 Experimental details for $Zn(CN)_2$ and $Cd(im)_2$

Variable-temperature single-crystal and powder X-ray diffraction, as well as variable-pressure single-crystal X-ray diffraction were carried out for $Cd(im)_2$. Variable-pressure powder X-ray diffraction was performed on $Zn(CN)_2$.

4.2.1 Synthesis

The polycrystalline $Zn(CN)_2$ sample was purchased from Sigma-Aldrich (99%) and used as received.

Single crystals of $Cd(im)_2$ were prepared *via* slow diffusions of metal salt and ligand aqueous solutions using a H-cell setup. Cadmium(II) nitrate tetrahydrate (0.206 g, 0.668 mmol; Sigma-Aldrich, 99%) and imidazole (0.0909 g, 1.336 mmol; Sigma-Aldrich, 99%) were each dissolved

separately in 5 ml of water. Deprotonation of imidazole was achieved by addition of a small quantity of ammonium hydroxide (0.0385 g, 2.487 mmol; Sigma-Aldrich, 99%). The two solutions were each placed in separate tubes of the H-cell, and cold water (∼15 ml) was layered on top until the H-cell was full. Crystals suitable for single-crystal X-ray diffraction experiments were obtained within 14 days. Polycrystalline samples of $Cd(im)_2$ were obtained by direct precipitation from stoichiometric mixtures (1:2 mol ratio) of aqueous solutions of cadmium(II) nitrate tetrahydrate and imidazole, with a small quantity of ammonium hydroxide acting as deprotonating agent. The resulting precipitate was washed (H_2O), dried under vacuum and finely ground.

4.2.2 Variable-temperature single-crystal X-ray diffraction

Variable-temperature single-crystal X-ray diffraction experiments were carried out on an Agilent technologies SuperNova diffractometer (graphite-monochromated Mo Kα radiation, λ = 0.71073 Å) fitted with an Oxford Cryosystems Cryostream 600 open flow cooling device.[241] A single crystal of $Cd(im)_2$ (0.10 × 0.17 × 0.18 mm) was mounted on a glass fibre using araldite. Diffraction data were collected first on cooling from 500 to 100 K, and then on heating from 110 to 310 K in 20 K intervals. For all data collections a single collection strategy was applied: namely, scanning through a full ω circle and collecting to a resolution of 0.77 Å. These measurements were carried out with assistance from Dr Amber Thompson.

Data indexing, reduction and absorption corrections were performed using CrysAlisPRO.[265] Structure solution was carried out with SIR92,[266] using the data collected at 100 K. Hydrogen atoms were added geometrically and regularised using standard restraints. Structure refinement against $|F^2|$ was carried out using CRYSTALS.[210] Anisotropic thermal parameters were refined for all non-H atoms. This refined model was then used as a starting point for refinement against the 110 K data set. In this way, structure refinements for successive temperature points made use of the final model from the previous data set as a starting point.[§] All refinements were carried out in an identical manner to that of the 100 K data set.

[§]Dr Richard Cooper assisted in making a script within CRYSTALS to allow automated successive refinements.

4.2.3 Variable-pressure single-crystal X-ray diffraction

High-pressure single-crystal diffraction was carried out at the Department of Chemistry, University of Edinburgh by Dr Stephen Moggach. A modified Merrill-Bassett DAC equipped with 600 μm culet diamonds and a tungsten gasket was used.[211] The $Cd(im)_2$ single crystal and a chip of ruby were loaded into the DAC with a 4:1 mixture of methanol and ethanol used as a hydrostatic pressure-transmitting medium. The ruby fluorescence method was used to determine the cell pressure, and this was measured before each data collection.[212] HP-SCXRD were measured at pressures of 0.3 GPa, 0.85 GPa and 2.1 GPa. Subsequent higher pressures were not collected as the crystal had started to move half-way through the 2.1 GPa data collection.

High-pressure diffraction data were collected using a Bruker SMART APEXII diffractometer (graphite-monochromated Mo Kα radiation $\lambda = 0.71073$ Å). First, a sphere of single-crystal diffraction data was collected on the crystal at ambient temperature and pressure in order to provide data for comparison with the high-pressure studies. High pressure diffraction data were collected up to a resolution of 0.8 Å, with a data completeness of 68% for the 0.3 and 0.85 GPa pressure points, and 40% for the 2.1 GPa data collection.

The data were integrated using SAINT,[242] utilising dynamic masks to avoid integration of regions of the detector shaded by the body of the pressure cell. Absorption corrections for the DAC and sample were carried out with the programs SHADE[246] and SADABS,[243] respectively. The structure was solved with SHELXS-86[244] and refined in CRYSTALS using full matrix least-squares against $|F|^2$ using all data.[210] The 1,2 and 1,3 thermal similarity and vibrational restraints were applied to the imidazolates, while hydrogen atoms were added geometrically and regularised using standard restraints.

4.2.4 Variable-temperature powder X-ray diffraction

Synchrotron powder diffraction data were collected on the I11 beamline at the Diamond Light Source ($\lambda = 0.8261$ Å) with Dr Julia Parker and Dr Chiu Tang. The sample was loaded in a 0.5 mm diameter borosilicate capillary and mounted in a horizontal spinner. The sample temperature was

controlled using a cyberstar hot air blower placed underneath the capillary; an initial data set was collected at a temperature of 200 °C and the temperature was then ramped at a rate of 10 °C/min. The diffraction data were measured using the Mythen2 PSD (5 s exposures at two angular orientations offset by 0.25°),[218] resulting in a separation of approximately 3 °C between successive data sets.

The Rietveld refinement of $Cd(im)_2$ data was performed in TOPAS academic version 4.1.[216] The refinements employed rigid body constraints for the imidazolate anions (hydrogens were excluded from the refinement), and a soft Cd–N bond restraint (2.2 Å) to prevent unphysical imidazolate reorientations (X-rays being relatively insensitive to imidazolate orientations differing by 360°/5 by virtue of the weak C/N contrast). A single isotropic thermal parameter was refined for the imidazolate atoms, and a separate thermal parameter was allowed to refine for the cadmium ion. The peak shapes were modelled using the Pseudo-Voigt function, with further anisotropic peak broadening terms to capture the asymmetric profiles. Corrections for capillary wobble and absorption were refined for the initial temperature dataset [Fig. B.1], and then both these parameters were kept fixed for all other temperatures. The variable-temperature data were refined sequentially, where the model from the previous temperature refinement was used as a starting model for the subsequent temperature refinement. During these sequential refinements, the parameters that were refined included: background terms, lattice parameters, a scale factor, isotropic thermal parameters, imidazolate translation and rotation, cadmium coordinates, and peak shapes. Representative Rietveld fits for the first and last temperature points are shown in Figure 4.2.

4.2.5 Variable-pressure powder X-ray diffraction

Synchrotron high-pressure powder diffraction data were collected for $Zn(CN)_2$ at the ESRF using the Swiss-Norwegian beamline BM01A ($\lambda = 0.7092$ Å) with Dr Philip Pattison and Dr Vladimir Dmitriev. All measurements were carried out at room temperature. The sample was loaded into a ETHZ standard DAC, with a mixture of methanol/ethanol (4:1) as pressure-transmitting fluid and a ruby chip for pressure calibration. The distance and the detector parameters were calibrated using a LaB_6 reference powder sample; calibration and subsequent integration were

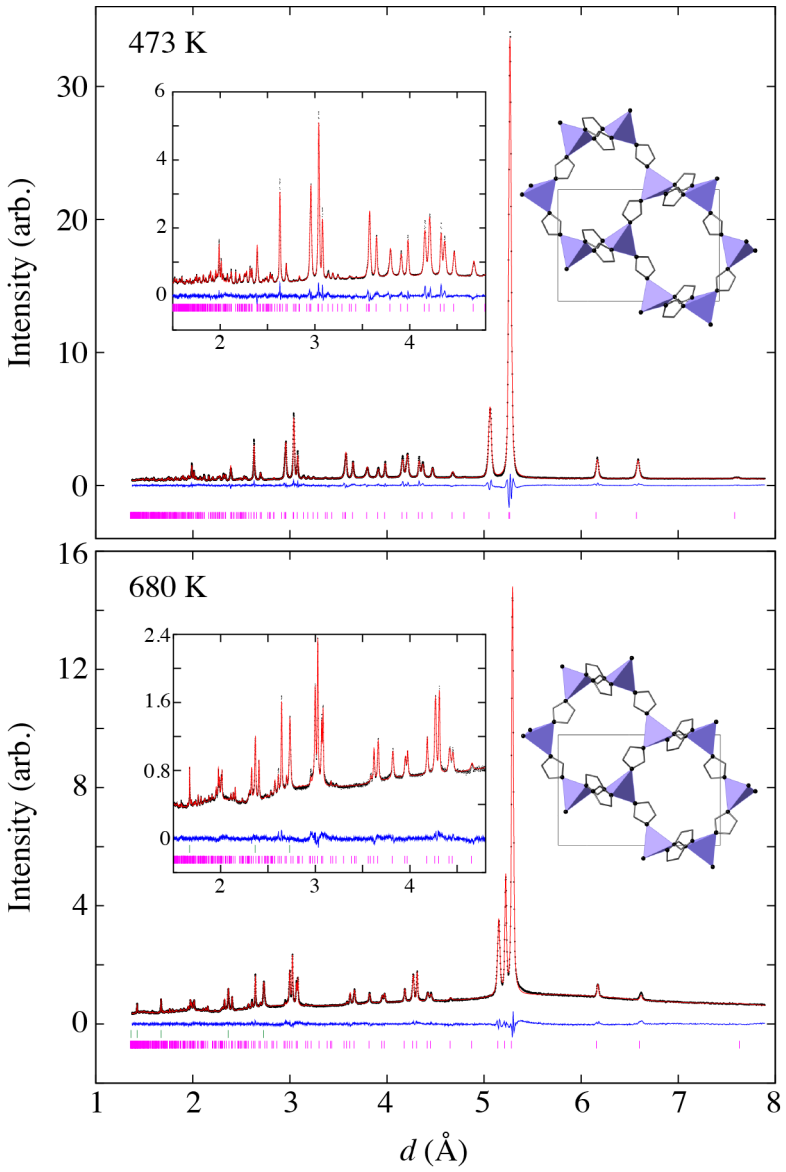

Figure 4.2: Rietveld fit of $Cd(im)_2$ to powder data at 473 K and 680 K. Experimental data are given as black points, the fitted profile as a solid red line, and the difference (data−fit) as a blue line. The additional peaks at 680 K refer to the presence of CdO (green *hkl* tick marks).

performed using FIT2D.[267,268] PXRD measurements were collected up to a pressure of 12.2 GPa. Subsequent higher pressures were not measured as the 4:1 methanol/ethanol mixture exhibits its glass transition at 10.5 GPa,[269] and thus pressures above this transition may not be completely hydrostatic.

Rietveld analysis was carried out by Andrew Cairns using GSAS as implemented within the EXPGUI user interface.[249,270] For each pressure point, the background, scale factor, lattice parameters and

atomic positions were refined, with a C–N and Zn–(C/N) bond distance restraint used for pressures above 1.52 GPa to ensure sensible bond distances. Significant background subtraction and peak broadening terms were required at the highest pressure points.

4.3 Background on the NTE mechanism of $Zn(CN)_2$

On heating $Zn(CN)_2$, its cubic lattice parameter a (and hence volume V) decreases monotonically at a rate $\alpha_V = -50.7(6)\,MK^{-1}$ over the temperature range 25–375 K.[128,258] This isotropic NTE is among the most extreme known;[128,131] consequently, there have been many studies on $Zn(CN)_2$ in order to elucidate its NTE mechanism. From these investigations, it is thought that correlated rotations of rigid $Zn(C/N)_4$ tetrahedra (RUMs) allow transverse displacements of the cyanide linkages away from the Zn$\cdots$Zn axes, resulting in a reduction of the Zn$\cdots$Zn separation and thus overall bulk NTE is observed.[127,128] The local transverse vibrational modes were observed using X-ray and neutron PDF experiments,[127,260] while the identification of RUMs was achieved using the program CRUSH.[128] The energy dependence of the softest phonon modes from calculated phonon dispersion curves agree with the experimental theory that transverse vibrational modes of the cyanide are important contributors to NTE.[271–273]

While no thermally-induced structural transition is observed in $Zn(CN)_2$ in the 25–775 K temperature range,[128] the ambient phase is only stable under hydrostatic pressures up to 1 GPa using a methanol/ethanol/water as the pressure-transmitting medium,[274] or up to 1.6 GPa using a methanol/ethanol mixture.[275] The compression behaviour of $Zn(CN)_2$ up to 1 GPa is also unusual: in particular, its bulk modulus $B = -V(\mathrm{d}p/\mathrm{d}V)$ decreases with increasing pressure, indicating that it becomes mechanically softer on compression.[158] Moreover its coefficient of thermal expansion becomes increasingly negative at higher pressures.[158] These observations suggest that the phonon modes responsible for NTE in $Zn(CN)_2$ are also those that soften most quickly on compression, and therefore the high-pressure phase may provide insight into the mechanism for NTE in the ambient phase.[180,276–278]

4.4 Variable-pressure behaviour of $Zn(CN)_2$

In preparation for the $Zn(CN)_2$ high-pressure diffraction experiment, there was evidence suggesting that $Zn(CN)_2$ in fact reacted with the water in the methanol/ethanol/water transmitting medium, a finding that was confirmed by a parallel study on the effect of the pressure-transmitting media on the polymorphism of $Zn(CN)_2$ under pressure.[160] Consequently, for this work a methanol/ethanol mixture was used as the pressure-transmitting medium.

The variation of the unit cell parameters in $Zn(CN)_2$ as a function of pressure is shown in Figure 4.3(a). The ambient phase, termed $Zn(CN)_2$-I, persisted up to 1.52 GPa, at which point coexistence with a lower symmetry high-pressure phase, named $Zn(CN)_2$-II, occurred. The abrupt volume change between the two phases suggests that the transition is first order in nature. At pressures above 1.85 GPa, the $Zn(CN)_2$-I phase had completely transformed to $Zn(CN)_2$-II. The high-pressure diffraction pattern of $Zn(CN)_2$-II was indexed to an orthorhombic cell related to the cubic phase by the transformation

$$\begin{bmatrix} \mathbf{a} \\ \mathbf{b} \\ \mathbf{c} \end{bmatrix}_{\text{ortho}} = \begin{bmatrix} 2 & 0 & 0 \\ 0 & 1 & 1 \\ 0 & -1 & 1 \end{bmatrix} \begin{bmatrix} \mathbf{a} \\ \mathbf{b} \\ \mathbf{c} \end{bmatrix}_{\text{cubic}}, \tag{4.1}$$

as illustrated within Figure 4.3(a).

The observed reflection conditions were consistent with the orthorhombic space group *Pbca*, which coincidentally is the same space group observed for $Cd(im)_2$. Thus the metal and imidazolate centroid positions in $Cd(im)_2$ were used as a starting point to refine the $Zn(CN)_2$-II structure. Rietveld refinements were performed on all the synchrotron X-ray data collected at pressures $1.52 < p < 12.2$ GPa using the *Pbca* model [Fig. 4.4]. The lattice parameters at 1.85 GPa are $a = 12.3212(18)$ Å, $b = 7.6438(9)$ Å, and $c = 7.4947(10)$ Å. For the data collected at the critical transition pressure $p_c = 1.52$ GPa itself, the refined unit cell parameters for both phases show a volume collapse of *ca* 5%: $V(Pn\bar{3}m)/Z = 193.52(2)$ Å^3 and $V(Pbca)/Z = 183.0(3)$ Å^3, providing the necessary $p\Delta V$ contribution to free energy as the driving force responsible for the transition.

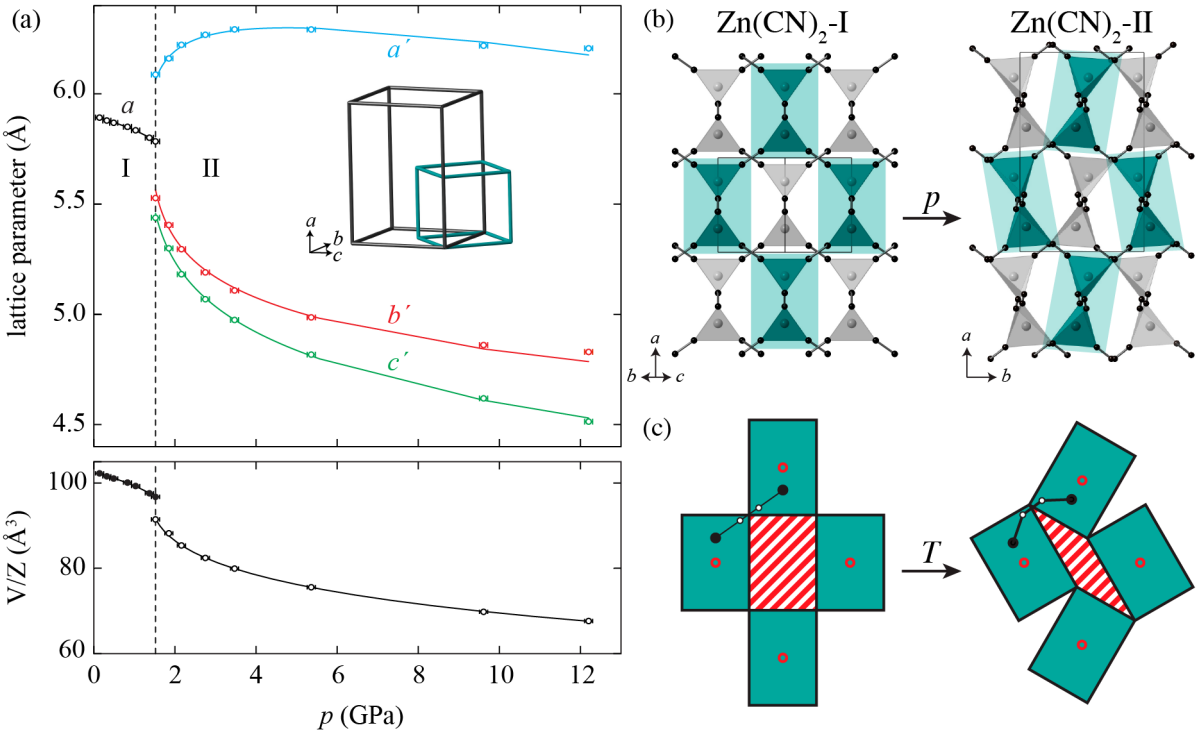

FIGURE 4.3: (a) Evolution of the cubic (low-pressure) and pseudocubic (high-pressure) lattice parameters in $Zn(CN)_2$. The lines show fits to data using a third-order Birch–Murnaghan equation of state in the case of $Zn(CN)_2$-I, and the empirical expressions shown in Eqs. (4.2) and (4.3) in the case of $Zn(CN)_2$-II. The pseudocubic lattice parameters of the high-pressure phase are related to the orthorhombic lattice parameters by $a' = a/2$, $b' = b/\sqrt{2}$ and $c' = c/\sqrt{2}$. The inset figure illustrates the orthorhombic cell in black and the cubic cell in green. (b) The structural changes associated with the phase transition between $Zn(CN)_2$-I and $Zn(CN)_2$-II; one of the nets in the structure has been highlighted to emphasise the rotations of pairwise $Zn(C/N)_4$ tetrahedra about the $\langle 110 \rangle$ directions of the $Pn\bar{3}m$ cell. (c) Schematic representation of pairwise $Zn(C/N)_4$ tetrahedra translations and rotations, important in driving large NTE in the $Zn(CN)_2$-I phase. Figure reproduced with permission from Andrew Cairns.

4.4.1 Phase transition mechanism

The primary distortion associated with the I/II phase transition involves concerted rotations of columns of pairwise $Zn(C/N)_4$ tetrahedra about axes parallel to the cubic $\langle 110 \rangle$ directions, as illustrated in Figure 4.3(b). The axis of rotation does not pass through the centres of individual tetrahedra, but rather through the midpoints of connected pairs of tetrahedra, such that the Zn centres are translated in a direction perpendicular to the rotation axis. This implies that the key NTE modes of $Zn(CN)_2$-I involve translations of $Zn(C/N)_4$ tetrahedra in addition to the rotational modes already identified elsewhere.[128,271] This NTE mechanism is fully consistent with

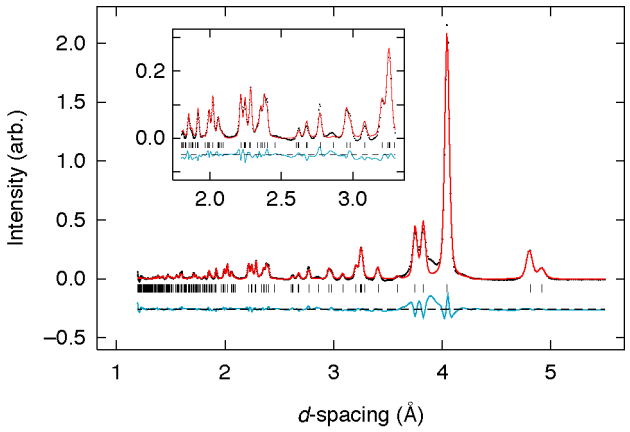

Figure 4.4: Representative Rietveld fit to synchrotron X-ray powder data collected at 1.85 GPa. Experimental data are given as points, the fitted profile as a solid red line, and the difference (data−fit) as a blue line, displaced downwards vertically by 0.2 units. Figure reproduced with permission from Andrew Cairns.

DFT and neutron spectroscopy results that implicate the transverse acoustic modes in driving NTE.[130,271,273] This displacement pattern is crucial—it is capable of accommodating even greater transverse CN^- vibrations that drive the large NTE [Fig. 4.3(c)].

4.4.2 Compressibilities

Considering first the ambient phase, a third-order Birch–Murnaghan equation-of-state fit to the data gives a zero-pressure bulk modulus B_0 and its pressure derivative B' of 37(2) GPa and −8.6(13), respectively, calculated using PASCal.[179] These values are in good agreement with a previous high-pressure study of $Zn(CN)_2$ from Ref. 158 (namely, $B_0 = 34.2(2)$ GPa and $B' = -6.0(7)$). Usually upon increasing pressure, materials will become harder to compress, *i.e.* $B' > 0$, however $Zn(CN)_2$-I exhibits a rare property where it softens under pressure, characterised by its $B' < 0$. Although negative B' are known in other systems such as $Zn[Au(CN)_2]_2$ and the mineral malayaite, for which $B' = -1.7(11)$ and $-3(5)$ respectively,[9,179,279] the B' value of $Zn(CN)_2$ is the most negative value known to date. The linear compressibility of $Zn(CN)_2$-I along its cubic a-axis is $K_a = 14.1(11)\ \mathrm{TPa}^{-1}$.

Table 4.1: Linear compressibilities for $Zn(CN)_2$-II at different pressure ranges, calculated using linear fits to data for the original lattice parameters evolutions, as well as those calculated either by considering only framework angle variation (K due to K_θ), or by using only $Zn\cdots Zn$ bond length changes (K due to K_r).

axis	K (TPa^{-1})					
	1.85–3.47 GPa			5.36–12.2 GPa		
	original	K due to K_θ	K due to K_r	original	K due to K_θ	K due to K_r
a	−12(3)	−24(5)	12(2)	2.1(5)	−0.19(13)	2.3(4)
b	33(5)	22(6)	11(4)	4.8(9)	6.6(5)	−1.8(5)
c	38(6)	24(5)	13(4)	9.6(3)	2.7169(2)	6.9(3)

In the high-pressure phase, empirical fits were used to fit the lattice parameter evolution in order to capture the nonlinearity using equations of the form

$$\ell(p) = \ell_0 + \eta(p - p_c)^\nu, \tag{4.2}$$

for lattice parameters b and c, and of the form

$$\ell(p) = \ell_0 + \eta(p - p_c)^\nu + \beta p, \tag{4.3}$$

for the a lattice parameter, where ℓ_0, η, ν and β are variables, and p_c refers to the critical pressure of 1.52 GPa. The incorporation of an additional linear term in pressure (βp) allows fitting of the NLC–PLC transition observed at ∼5 GPa. The compressibilities obtained from the derivatives of these empirical fits (Eqs. (A.2) and (B.1)), as well as those determined from the Birch–Murnaghan equation-of-state fit to the ambient phase are shown in Figure 4.5. The compressibilities indicate that the structure stiffens rapidly over the 1.52–4 GPa pressure range, and that over the same pressure range, $Zn(CN)_2$-II exhibits large NLC along the a-axis. This negative response then reverts to regular PLC at pressures above 5 GPa. This is reminiscent of the NLC–PLC transition observed in Ag(mim). Linear fits to sections of the pressure range for the lattice parameter evolutions of $Zn(CN)_2$-II are shown in Table 4.1.

The XBUs present in $Zn(CN)_2$-II were used in order to rationalise its compressibility behaviour. These comprise of the two unique cyanide-connected $Zn\cdots Zn$ distances, referred to as r, and the

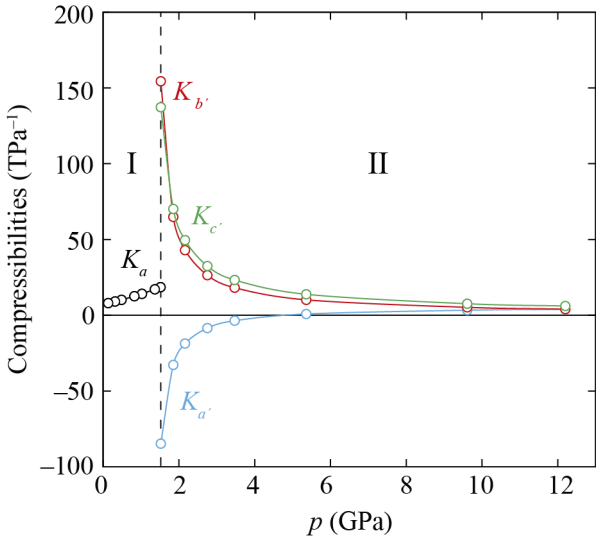

Figure 4.5: Compressibilities of $Zn(CN)_2$-I (K_a), and for $Zn(CN)_2$-II ($K_{a'}, K_{b'}, K_{c'}$). The vertical dotted line indicates the phase transition pressure of 1.52 GPa. Figure reproduced with permission from Andrew Cairns.

framework angles between cyanide-connected Zn$\cdots$Zn$\cdots$Zn (of which there are six unique angles). The XBU relationships to the lattice parameters are shown in Figure 4.6, and indicate that the pressure-induced *b*- and *c*-axis evolutions are affected by the variation in r distances as well as the angle which relates them. For the *a*-axis, the two r distances and the corresponding angle connecting them makes up the edge l, and both the variation in l lengths with its corresponding angle impact on the changes in the *a*-axis.

Using the relationships shown Figure 4.6(c), not only is it possible to calculate the known pressure-induced lattice parameters from the variations in the values of r and θ, but also the deconvoluted lattice compressibilities [Fig. B.3]. These are categorised into the compressibilities which arise from the relevant framework angle changes, implying $K_r = 0$ and referred to as 'K due to K_θ', and those arising from r distance variations, implying $K_\theta = 0$, referred to as 'K due to K_r'. These pressure-induced lattice parameter evolutions are calculated by either maintaining r at its initial value at ambient pressure, as a function of pressure, or by using the ambient pressure θ angles throughout the pressure range. The linear compressibilities associated with these calculated lattice evolutions are given in Table 4.1. The different K values highlight that framework angle changes are responsible for the NLC observed and for the large magnitudes of compressibility in the low pressure regime (1.52–4 GPa). While at higher pressures, framework angle variations are reduced

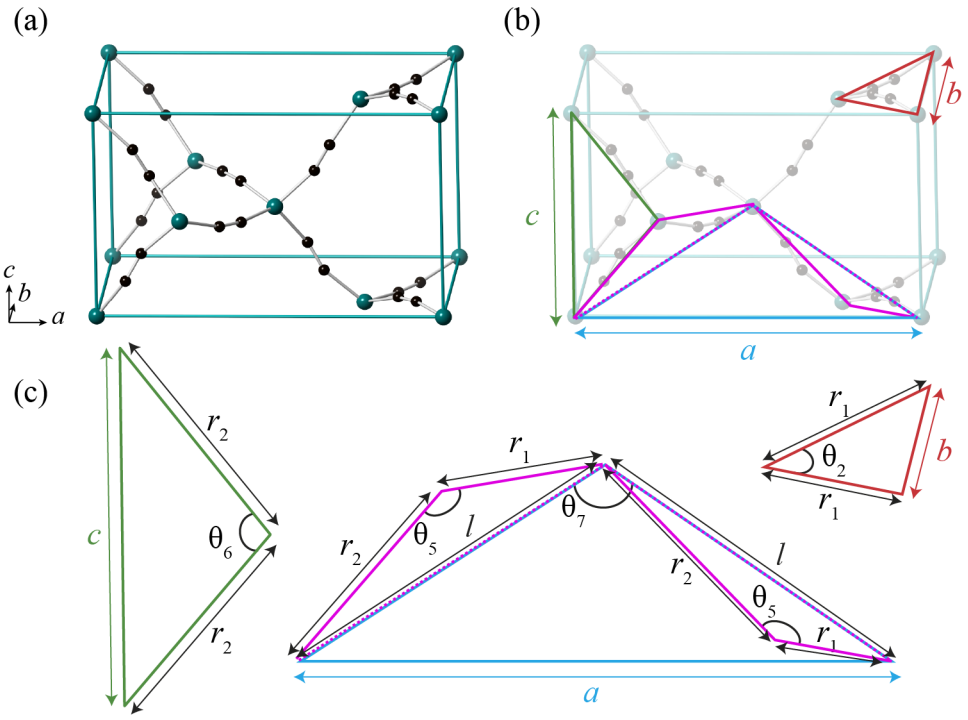

Figure 4.6: (a) Extended structure of a single net of $Zn(CN)_2$ with its unit cell translated so that Zn cation sit at its corners. (b) The same extended structure of $Zn(CN)_2$ with the $Zn\cdots Zn$ (r) distances and framework angles (θ) XBUs and their relation to the lattice parameters. (c) The trigonometric relations of the XBUs and lattice parameters from those seen in (b). The evolutions of the different XBUs with pressure are shown in Figure B.4.

considerably, instead bond compression along r distances becomes dominant, thus giving rise to the NLC–PLC transition, and the lower magnitudes of compressibility.

4.5 Variable-temperature behaviour of $Cd(im)_2$

Despite the different chemistries of the imidazolate and cyanide ions, the structure of $Cd(im)_2$ is isostructural to the $Zn(CN)_2$-II phase. The structural relationship is straightforward: Cd centres replace Zn, and imidazolate anions occupy the CN^- sites in the same *Pbca* space group. Just as $Zn(CN)_2$-II is a distorted variant of the parent $Zn(CN)_2$-I phase, so too might the ambient phase of $Cd(im)_2$ be considered a distorted variant of a hypothetical $Pn\bar{3}m$ parent. Variable-temperature diffraction experiments were performed for $Cd(im)_2$ in order to investigate a possible increase in symmetry upon heating.

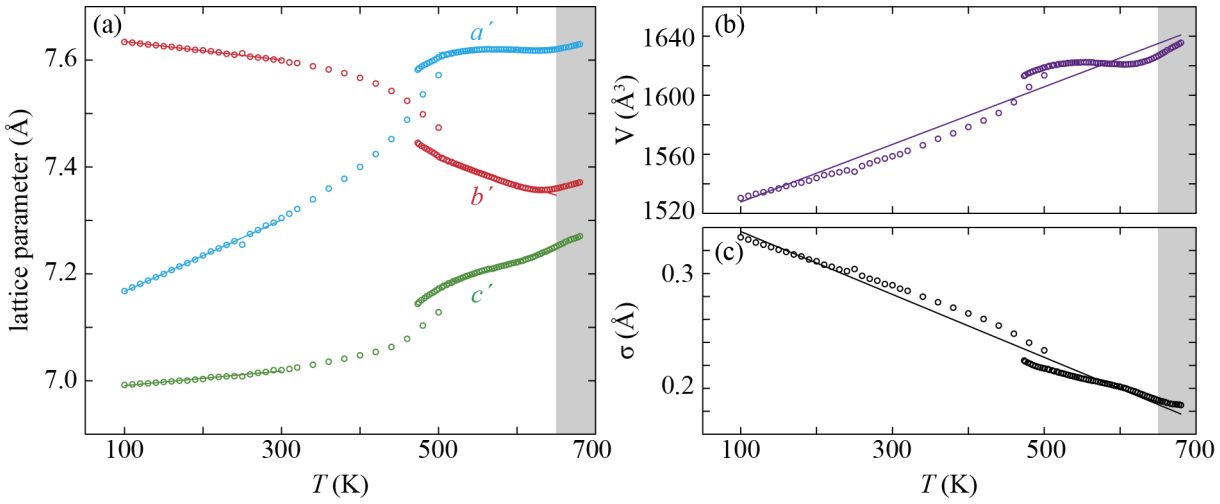

Figure 4.7: (a) Temperature-dependent pseudocubic lattice parameters for $Cd(im)_2$ as determined from single-crystal (100–500 K) and powder (473–680 K) X-ray diffraction measurements with linear fits indicated at two different temperature regimes. (b) The corresponding variation in unit cell volume, and (c) the standard deviation of the pseudocubic lattice parameters: $\sigma(a', b', c')$ as a function of temperature.

Using a combination of variable-temperature single-crystal (100–500 K) and powder X-ray diffraction (473–680 K), the structural and lattice parameter variations were obtained for $Cd(im)_2$. The pseudocubic lattice parameter variations, where $a' = a/2$, $b' = b/\sqrt{2}$ and $c' = c/\sqrt{2}$, are shown in Figure 4.7. Throughout the temperature range 100–680 K there is no phase transition; although for temperatures above *ca* 600 K the sample decomposes into a range of products including CdO. The grey shading for temperatures above 650 K in Figure 4.7 indicates reduced confidence in the lattice parameters, where decomposition of $Cd(im)_2$ is above 3%. The slight discontinuities near 500 K reflect the different experimental conditions between single-crystal and powder diffraction measurements.

4.5.1 Expansivities

The variations in the lattice parameters with temperature show two main features. First, the CTEs are anomalous both in sign ($\alpha_b < 0$) and in magnitude ($|\alpha|$ values often greater than $50\,MK^{-1}$). Second, the expansivities are highly nonlinear and anisotropic [Table 4.2]. To gain insight into this behaviour, the XBU-driven lattice expansivities were calculated in the same way as described for $Zn(CN)_2$-II, allowing the effect of framework angle and r variation to be deconvoluted from

Table 4.2: Linear expansivities for $Cd(im)_2$ determined over two temperature ranges using linear fits to the original lattice parameter evolutions, and to the evolutions calculated due to α_θ, or α_r.

axis	α (MK^{-1})					
	100–300 K			500–650 K		
	original	α due to α_θ	α due to α_r	original	α due to α_θ	α due to α_r
a	92.6(16)	79.2(13)	13.4(3)	6.5(11)	14.4(13)	−7.9(8)
b	−22.5(5)	−41.7(8)	19.2(4)	−59.6(19)	−114.6(15)	55.0(18)
c	19.5(7)	11.7(5)	7.8(3)	65.6(9)	137.4(16)	−72(2)

the bulk expansivities [Table 4.2]. From these different expansivities, it is clear that framework angle changes dominate the observed lattice parameter evolution of $Cd(im)_2$ and are responsible for the negative response observed along the b-axis. The origin of the nonlinearity in the lattice parameter evolutions is discussed later on.

4.5.2 Critical behaviour

The absence of an experimentally observed phase transition in $Cd(im)_2$ upon heating means that only a hypothetical aristotype phase can be considered; this would correspond to a phase isostructural to $Zn(CN)_2$-I. Figure 4.8 shows the likely *Pbca*–$Pn\bar{3}m$ structural change for $Cd(im)_2$, related to that seen in the $Zn(CN)_2$-I/$Zn(CN)_2$-II high-pressure transformation.

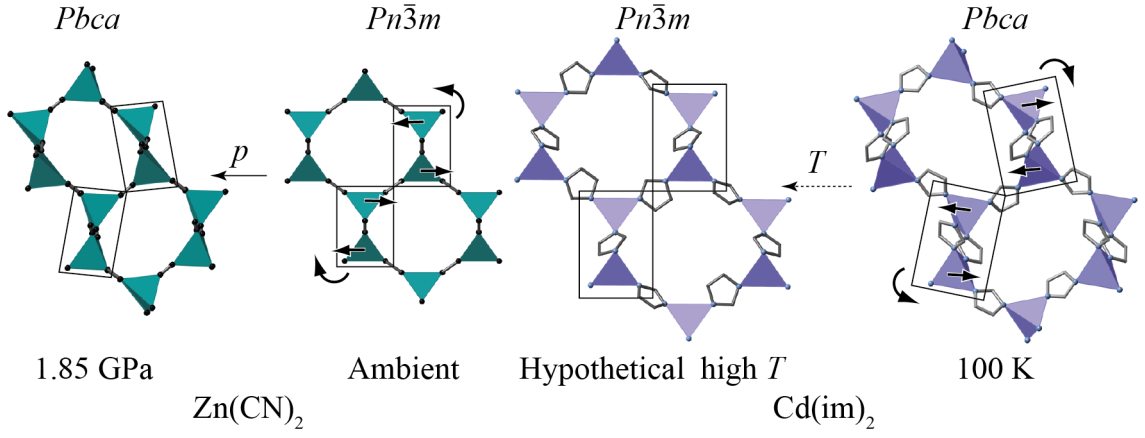

Figure 4.8: The rotations and translations of $Zn(C/N)_4$ tetrahedra observed in the $Zn(CN)_2$-I/II phase transition. Consideration of related structural changes in the distorted $Cd(im)_2$ will drive its transformation to a hypothetical $Pn\bar{3}m$ $Cd(im)_2$ phase.

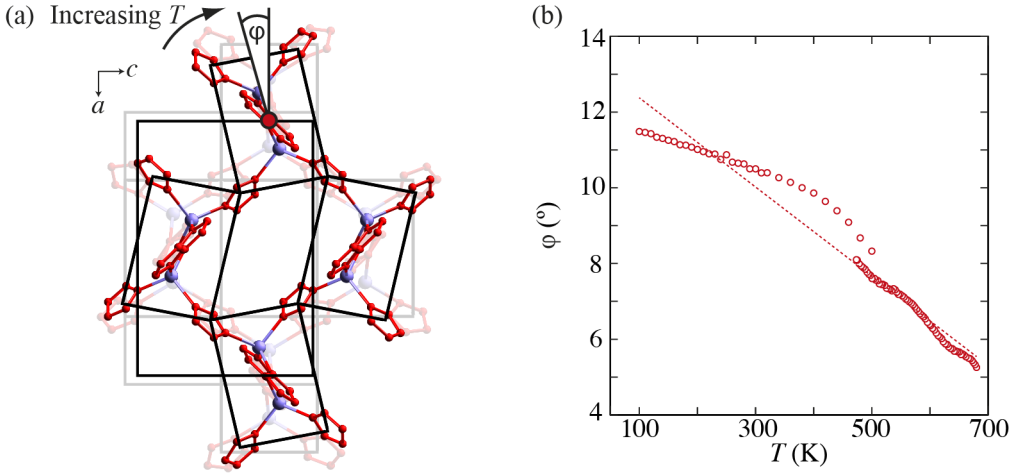

Figure 4.9: (a) The low temperature 100 K $Cd(im)_2$ crystal structure with the hypothetical $Pn\bar{3}m$ $Cd(im)_2$ phase faded in the background with the tilt angle (φ) calculated between the two structures. (b) Variation in average tilt angle as a function of increasing temperature with the straight line fit indicated by the dotted line.

To evaluate the extent to which $Cd(im)_2$ exhibits the proposed *Pbca*–$Pn\bar{3}m$ structural evolution as a function of temperature, a tilt angle φ was calculated. The tilt angle represents the degree of pairwise CdX_4 tetrahedra rotation compared to the aristotype phase, where X represents the centroid of the nitrogens on the imidazolate [Fig. 4.9(a); Fig. B.5]. Four of these φ angles are found to describe the structural evolution of the pairwise tetrahedral rotations (two in both the **ac**- and **ab**-planes) [Fig. B.6]. The average of the four φ angles is shown in Figure 4.9(b), where a continuous decrease in $\langle\varphi\rangle$ angle is observed as a function of increasing temperature, reflecting a continual 'unfolding' of both diamondoid nets. Extrapolation of the $\varphi(T)$ linear fit to $\varphi = 0$ (the point at which $Pn\bar{3}m$ symmetry would be recovered) suggests a transition temperature $T_c \simeq 1150\,\mathrm{K}$.

The φ contribution to the lattice parameter evolutions was calculated by evaluating a mean linear expansivity (α_ℓ):

$$\alpha_\ell = -\tan\varphi\frac{\mathrm{d}\varphi}{\mathrm{d}T}. \tag{4.4}$$

The derivation of this expression is found in Section B.5. Using Eq. (4.4) and the experimental values of $\langle\tan\varphi\rangle$ and $\mathrm{d}\varphi/\mathrm{d}T$, an effective $\alpha_\ell = +28.6(5)\,\mathrm{MK}^{-1}$ is obtained; the mean linear expansivity can also be calculated from the volumetric expansivity: $\alpha_\ell = \alpha_V/3 = +40.9(10)\,\mathrm{MK}^{-1}$, using the same temperature range as α_ℓ determination. The α_ℓ values indicate that up to a third

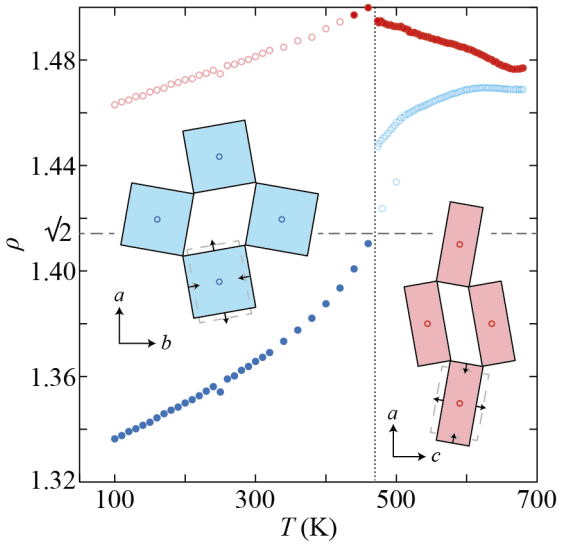

Figure 4.10: (a) The thermal variation of the corresponding aspect ratio ρ values in the rectangular units for the (001) and (010) tilt systems in $Cd(im)_2$ (blue and red data points, respectively). The inset figures represent how the schematised structure of $Cd(im)_2$ evolves to rectify the ρ values towards $\sqrt{2}$.

of the bulk thermal response of $Cd(im)_2$ is driven by correlated unfolding of the structure *via* the same mechanism that is observed in the $Zn(CN)_2$-I/II phase transition.

The anisotropy and nonlinearity observed in the thermal response of $Cd(im)_2$ do not arise from the steady decrease in φ evolutions; rather it is the reorganisation of imidazolate orientations within the CdN_4 coordination polyhedra that is the main contributor. This is seen most clearly by considering the rectangular units obtained by projection of the pairwise CdX_4 columns onto either the (010) or (001) planes, as illustrated in Figure 4.9(a). Idealised tetrahedral CdX_4 geometries would give rectangular projections with an aspect ratio (ρ) identically equal to $\sqrt{2}$; consequently, deviations from this ratio reflect geometric distortions of the tetrahedral units that arise due to either deformation of N–Cd–N bond angles or the inherent anisotropy of the imidazolate molecule. At low temperatures the ρ deviations from $\sqrt{2}$ are larger for the (001) plane (−6.0%) than for the (010) plane (+2.7%). So, on heating from 100 K the more severely distorted geometries are rectified first, which result in a contraction along **b** and an expansion along **a** [Fig. 4.10]. At 475 K, the ideal $\rho = \sqrt{2}$ is reached, but as there is no change in global symmetry—ρ cannot "lock-on" to this value as the (010) projection remains distorted. This temperature point unfortunately coincides with the extremities of the single-crystal data and the start of the powder data. Nevertheless, there is good agreement between the derived ρ values for the small overlapping temperature

range of both techniques. At temperatures higher than this point, the (010) system (which has become slightly more distorted during the first set of reorganisations) now becomes increasingly regular, resulting in expansion along **c** and reduction along **a**. Thus the unusual lattice parameter evolutions evident in Figure 4.7(a) reflect the activation of different reorganisation mechanisms at different temperatures.

Despite the nonlinearities in the lattice parameter evolutions, $Cd(im)_2$ also evolves towards an increasingly symmetric unit cell metric. This is reflected in the continuous decrease in the standard deviation of the pseudocubic lattice parameter evolutions with increasing temperature [Fig. 4.7(c)]. Extrapolation of the $\sigma(T)$ linear fit to $\sigma = 0$ gives a critical temperature of $T_c \simeq 1300\,K$ for which metrically cubic dimensions with $a' = b' = c'$ exist. This critical temperature agrees well with the one calculated from the φ evolution, however both these temperatures are well beyond the stability regime of $Cd(im)_2$ at ambient pressure.

4.6 Variable-pressure behaviour of $Cd(im)_2$

Variable-pressure diffraction measurements were performed on $Cd(im)_2$ in order to gain insight into the structural distortions that take place upon compression, and whether they could be related to the variable-temperature transformations. The single-crystal variable-pressure lattice parameter evolutions are shown in Figure 4.11(a). The increase in pressure from 0.85 to 2.1 GPa gave rise to a phase transition. However, the $Cd(im)_2$ crystal began to move during the collection of the high-pressure phase, so further high-pressure diffraction was not possible within the same experiment. The high-pressure $Cd(im)_2$ phase was first thought to be tetragonal due to the convergence of the b and c lattice parameters, however the same orthorhombic *Pbca* space group was found to best fit the data. The high-pressure phase could be refined in CRYSTALS using the previous 0.85 GPa structure refinement as a starting model. The lattice parameters obtained for this high-pressure phase are $a = 11.429(10)$ Å, $b = 10.432(10)$ Å, and $c = 10.432(8)$ Å.

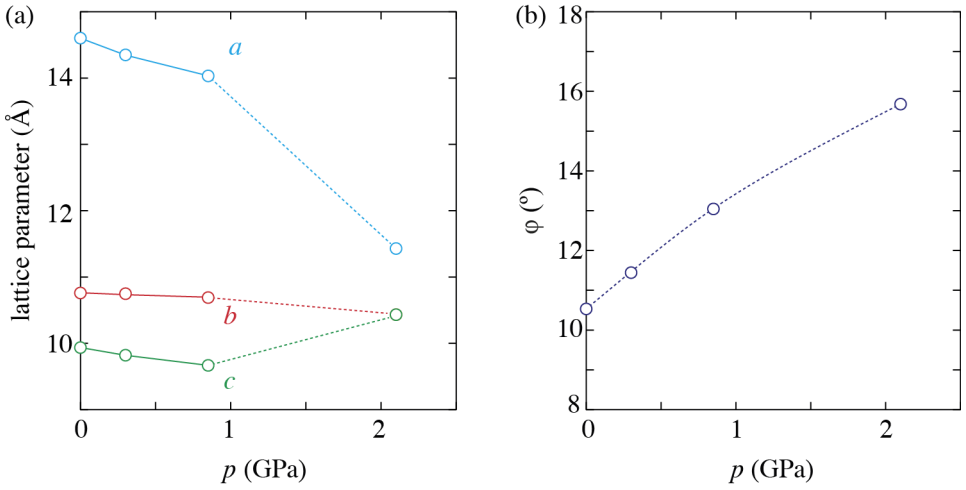

Figure 4.11: (a) Variable-pressure lattice parameter evolutions for $Cd(im)_2$, with a new phase detected at 2.1 GPa. The ambient phase pressure points are fitted with the empirical equation shown in Eq. (4.2). (b) Variation in φ as a function of increasing pressure, calculated in the same way as shown previously in the variable-temperature section. The dotted lines function as guides to the eye.

4.6.1 Phase transition mechanism

The $Cd(im)_2$ high-pressure transformation involves a shearing motion of the framework structure, in which the pairwise tetrahedra become even more tilted away from the $Pn\bar{3}m$ aristotype phase. This structural change results in a 3 Å decrease in the a lattice parameter [Fig. 4.12]. The increase in φ tilt angle as a function of pressure is shown in Figure 4.11(b). A similar shear-mode softening was observed in ZIF-8 under compression, however because of its lower density, the transition gave rise to an amorphous phase.[280] The CdN_4 coordination environments are maintained in the HP-phase, and local structural distortions involve decreases in Cd···Cd bond distances, and a divergence in Cd–im–Cd and Cd···Cd···Cd framework angles [Fig. B.4].

4.6.2 Compressibilities

A second-order Birch-Murnaghan equation of state was fitted to the 0–0.85 GPa pressure range using PASCal,[179] giving $B_0 = 10.0(3)$ GPa; the corresponding pressure derivative could not be calculated reliably, because of the low number of data points. This compares well with the B_0 determined for the dense zinc imidazolate phase (zni), with $B_0 = 11.8(9)$ in a similar pressure

Table 4.3: Linear compressibilities for $Cd(im)_2$ determined over a 0–0.85 GPa pressure range using linear fits to data for the original lattice parameters, but also for those calculated from consideration of either K_θ or K_r.

axis (Å)	K (TPa^{-1})		
	original	K due to K_θ	K due to K_r
a	46(5)	26(4)	20.4(7)
b	7.9(17)	−15(3)	22.6(13)
c	32(3)	14(3)	18.27(9)

range.[182] The linear compressibilities for each axis are shown in Table 4.3, including the compressibilities calculated due to K_θ and K_r. These were calculated in the same way as detailed for $Zn(CN)_2$-II. The deconvoluted compressibilities highlight that bond compression along the Cd–im–Cd unit dominates the bulk compressibilities observed, and explains why NLC is not exhibited along the b-axis. This contrasts to the variable-temperature behaviour of $Cd(im)_2$, which was dominated by framework angle variation. However, the phase transition mechanism of $Cd(im)_2$ is driven by framework angle changes, as illustrated in Figure 4.12 [see also Figs. B.3 and B.4].

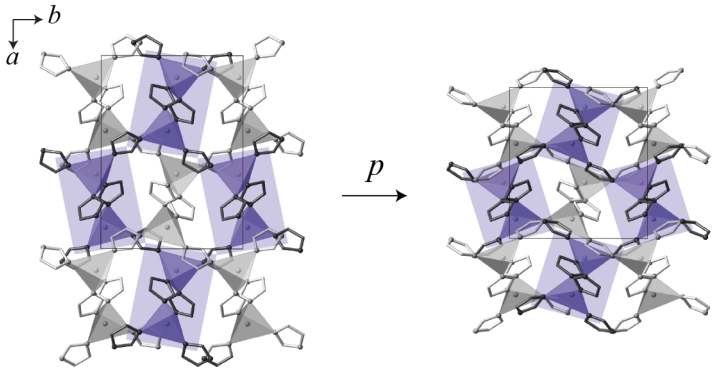

Figure 4.12: The ambient and 2.1 GPa structures are shown with the highlighted pairwise CdX_4 columns.

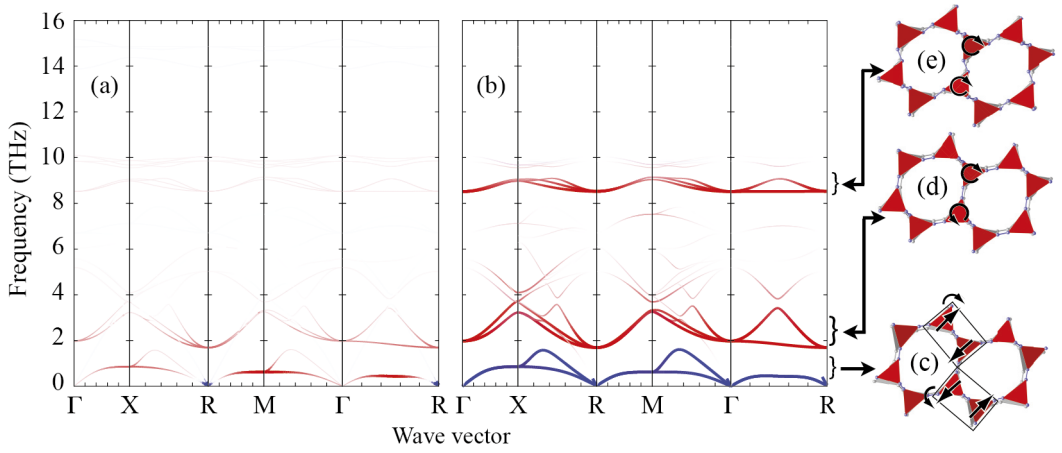

Figure 4.13: (a) Phonon dispersion curves coloured according to the corresponding value of the mode Grüneisen parameter, where red is negative, blue is positive and white represents a parameter of zero. (b) Phonon dispersion curves coloured according to the degree and type of RUM character present, where the colour strength corresponds to extent of RUMs present (white indicates no RUMs). The red colour indicates purely rotational RUM motion, while the blue colour represents purely translational RUMs. The inset figures (c–e) reveal the important RUM motions associated with the phonon modes. Figure reproduced with permission from Ref. 281, copyright 2013 by the American Physical Society.

4.7 Discussion: Homologous behaviour of $Zn(CN)_2$ and $Cd(im)_2$

4.7.1 Mechanical properties

Isotropic mechanics

The pressure-dependent behaviour of $Zn(CN)_2$ allowed the identification of the soft phonon modes responsible for NTE in its ambient phase: namely, a set of concerted tilts of pairwise $Zn(C/N)_4$ tetrahedra about the cubic $\langle 110 \rangle$ axes, giving rise to translational as well as rotational RUMs. A molecular dynamics study—published following the work detailed in this chapter—confirms the same finding: that the softest modes are translational RUMs.[281] As can be seen in Figure 4.13(a), the important NTE modes are identified by those that have negative Grüneisen parameters, and of these modes, the associated structural changes are shown in Figure 4.13(b). The lowest energy phonons correspond to the translational RUMs mentioned above [Fig. 4.13(c)].

While no $Pn\bar{3}m$ phase was observed for $Cd(im)_2$, it is expected that the aristotype $Cd(im)_2$ structure will also display NTE in the same way as $Zn(CN)_2$-I, because its thermally-induced

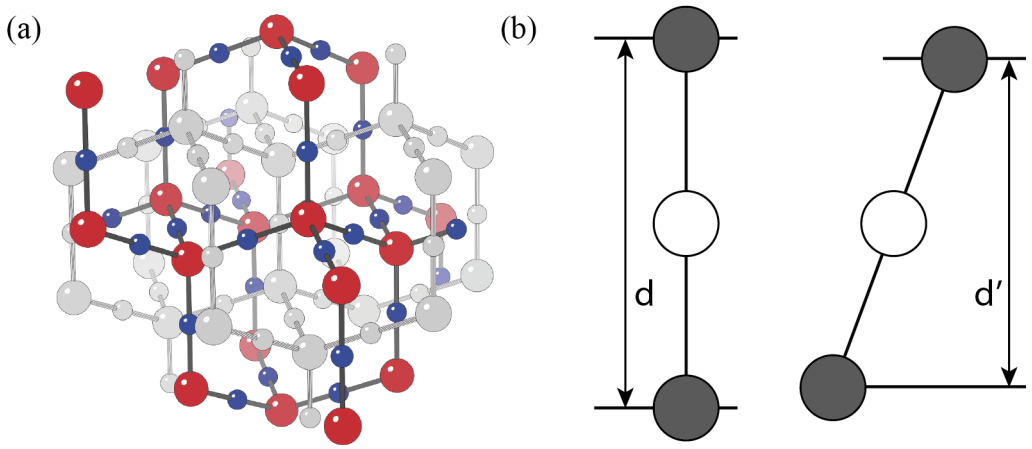

Figure 4.14: (a) The Cu_2O structure where the Cu(I) are shown as the blue atoms, and oxygen anions as the red atoms. The two-fold interpenetration is highlighted by the colouring of one net, and the grey colour in the other. (b) The translational modes activated along the O–Cu–O unit which give rise to NTE. Figure reproduced with permission from Ref. 282, copyright 2014 by the American Physical Society.

structural changes are the same soft-modes as observed in $Zn(CN)_2$-I. A recent *ab initio* lattice dynamics of cuprite [Fig. 4.14(a)]—of which $Zn(CN)_2$-I is related to the anticuprite structure—also shows that its NTE is dependent on translational acoustic modes [Fig. 4.14(b)].[282] In fact, even simple diamondoid or zincblende structures support such modes, albeit at lower temperature ranges and magnitudes.[283] This suggests that the translational mechanism which gives rise to NTE may be universal for many diamondoid topologies. By placing *molecular* linkers within this topology, the energy of the transverse acoustic mode is reduced, consequently allowing larger magnitudes of NTE. Therefore, it is likely that isoreticular MOFs will display the same soft modes inherent to the topology, but that the energy of the soft phonons, and hence magnitude of mechanics such as NTE, would vary depending on the chemical composition.

Anisotropic mechanics

The anisotropic mechanics in $Zn(CN)_2$-II and $Cd(im)_2$ were deconvoluted in terms of the strut and framework angle XBUs. It was evident for both $Zn(CN)_2$ in the low-pressure region (1.85–3.47 GPa) and $Cd(im)_2$ for the whole temperature range, that framework angle deformation was

the main mode of structural change. Yet because of the different ligands used in each case, the direction of anisotropy was not the same: $Zn(CN)_2$ displayed its negative response along the a-axis, while that of $Cd(im)_2$ was along the b-axis. In the case of high-pressure transformations of $Cd(im)_2$, there was no rapid stiffening of the structure as seen in $Zn(CN)_2$, instead continual bond compression dominated its response. This may be due to two reasons. Firstly, $Cd(im)_2$ contains bulky imidazolate ligands, which upon large framework angle changes may lead to unfavourable steric clashes, while the linear cyanide linkers allow greater framework angle deformation in $Zn(CN)_2$. Therefore framework angle variations in $Cd(im)_2$—essential for the negative response and large compressibilities—are small. Secondly, there is greater ease in deforming the Cd–im–Cd unit, which can shorten its bond lengths but also decrease the binding angle. This gives rise to large compression along the r distance ($K_r \sim 20\,\mathrm{TPa}^{-1}$), which acts to cancel out any small negative response which may have arose from framework angle changes. In $Zn(CN)_2$, the directional M–CN bonding[128] may be the reason for its smaller r compression ($K_r \sim 12\,\mathrm{TPa}^{-1}$), thus allowing the NLC to persist up to 5 GPa.

4.7.2 Critical behaviour

The similarities between the atomic displacements in $Zn(CN)_2$ and $Cd(im)_2$ are seen in their corresponding positional order parameter evolutions [Fig. 4.15]. The order parameters (Φ) for both $Zn(CN)_2$ upon increasing pressure and $Cd(im)_2$ upon decreasing temperature are obtained by considering the positions of the metal cations (M), ligand centroids (X), and comparing these to the $Pn\bar{3}m$ aristotype coordinates in an orthorhombic setting:

$$\Phi = \frac{1}{3} \sum_{i \in \{\mathrm{M,X1,X2}\}} \sqrt{[(x_{i:Pn\bar{3}m} - x_i)^2 + (y_{i:Pn\bar{3}m} - y_i)^2 + (z_{i:Pn\bar{3}m} - z_i)^2]}. \tag{4.5}$$

The corresponding i values for $Zn(CN)_2$, $Cd(im)_2$ and the aristotype phase are found in Table 4.4, with the Φ evolutions shown in Figure 4.15(a) [see Fig. B.7 for the individual Φ evolutions for M and X]. The order parameters for $Zn(CN)_2$ and $Cd(im)_2$ then reflect the degree of distortion from the aristotype $Pn\bar{3}m$ (the anticuprite phase) upon compression or cooling. For these Φ

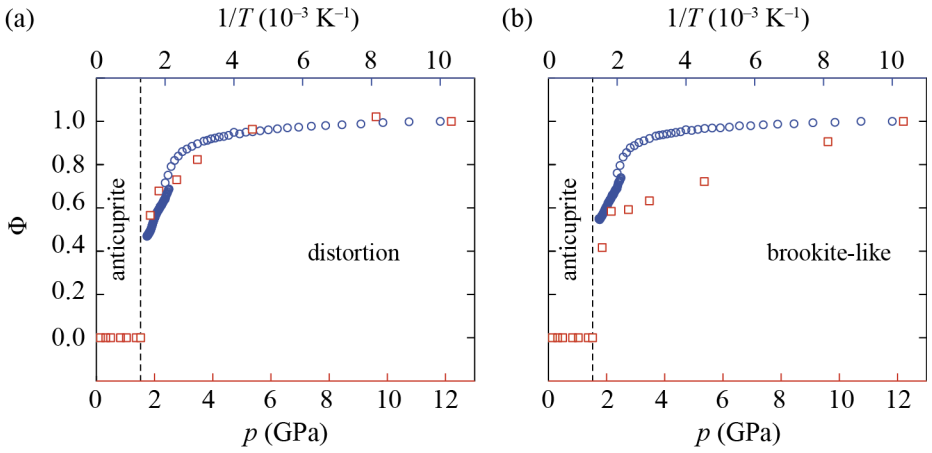

Figure 4.15: Variation of the order parameters with increasing pressure for $Zn(CN)_2$ (red squares) and decreasing temperature for $Cd(im)_2$ (blue circles). (a) The Φ parameters are calculated considering the $Pn\bar{3}m$ aristotype using Eq. (4.5). (b) The Φ parameters are obtained by calculating the distortion from $Pn\bar{3}m$ and towards brookite using Eq. (4.6).

evolutions, the values of Φ equal zero for the ideal anticuprite geometry and are normalised such that $\max(\Phi) = 1$ for each data set.

The physical driving force for the particular displacement patterns observed in the distortions of $Zn(CN)_2$ upon compression and $Cd(im)_2$ upon cooling is towards a denser packing arrangement,

Table 4.4: The coordinates of the metal and two symmetry inequivalent ligands in selected $Zn(CN)_2$ and $Cd(im)_2$ phases with reference positions of anticuprite (considered in an orthorhombic setting) and brookite structures.

	Metal (M)			Ligand 1 (X1)			Ligand 2 (X2)		
	x	y	z	x	y	z	x	y	z
Anticuprite	**0.125**	**0**	**0.75**	**0**	**0.25**	**0.25**	**0.25**	**0**	**0.5**
Brookite	**0.129**	**0.097**	**0.863**	**0.010**	**0.149**	**0.182**	**0.230**	**0.113**	**0.537**
$Zn(CN)_2$									
$p = 0$	0.125	0	0.75	0	0.25	0.25	0.25	0	0.5
$p = 12\,\mathrm{GPa}$	0.128	0.065	0.872	−0.006	0.179	0.276	0.260	0.133	0.579
$Cd(im)_2$									
$T = 680\,\mathrm{K}$	0.126	0.019	0.768	0.011	0.212	0.282	0.271	0.027	0.529
$T = 100\,\mathrm{K}$	0.191	0.036	0.808	0.034	0.179	0.292	0.283	0.041	0.585
$p = 2.1\,\mathrm{GPa}$	0.128	0.046	0.825	0.031	0.184	0.290	0.280	0.042	0.577

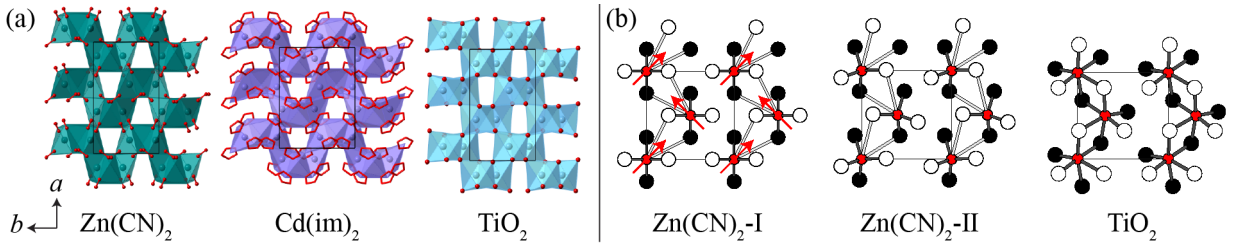

Figure 4.16: (a) Extended structures of $Zn(CN)_2$-II and $Cd(im)_2$ where the polyhedra represent 6-coordinate environments due to the addition of M–ligand bonds in order to resemble those seen in brookite. (b) Illustration of the relevant cation displacements for the anticuprite and brookite structural correspondence. Projections are shown down the *a*-axis. Cations are represented as filled red circles; anions as open and filled black circles (positive and negative out-of-plane displacements, respectively, relative to cation positions). The unit cell has been translated in each structure such that it lies underneath the metal cations; figure reproduced with permission from Andrew Cairns.

which resembles that seen in brookite. Brookite also crystallises in the *Pbca* space group; its structure can be considered as a hexagonal-close-packed array of oxide anions with Ti^{4+} cations occupying half the octahedral holes. While the brookite connectivity is clearly different to $Zn(CN)_2$ and $Cd(im)_2$, the anion and cation positions between brookite and $Zn(CN)_2$-II or $Cd(im)_2$ are similar [Table 4.4, Fig. 4.16(a)]. The larger molecular ligands in $Zn(CN)_2$ and $Cd(im)_2$ sufficiently distances the two tetrahedral nets, making the formation of a single 6-coordinate net less likely. The relationship between the anticuprite and brookite structures can be understood by considering concerted movements of the cations in the anticuprite structure. These displacements are towards a single edge of their tetrahedral coordination environment, and the resulting positions correspond to the octahedral sites of the brookite structure [Fig. 4.16(b)]. The two diamondoid nets in anticuprite then become topologically equivalent to brookite by coordination of two extra ligand anions as shown in Figure 4.16(b) by the light grey bonds. A similar mechanism is seen in reverse for framework expansion in rutile-TiO_2 under negative pressure, giving a tetrahedral TiO_2 net with the anticuprite topology;[284] likewise compression of tetrahedral SiO_2 structures eventually leads to formation of stishovite, which has the TiO_2-rutile structure.[285]

A second order parameter was then calculated, this time to quantify the distortion away from $Pn\bar{3}m$ and towards the brookite structure:

$$\Phi = \frac{1}{3} \sum_{i \in \{\mathrm{M,X1,X2}\}} \frac{(\mathbf{C}_i - \mathbf{C}_{i:Pn\bar{3}m}) \cdot (\mathbf{C}_{i:\mathrm{brookite}} - \mathbf{C}_{i:Pn\bar{3}m})}{|\mathbf{C}_{i:\mathrm{brookite}} - \mathbf{C}_{i:Pn\bar{3}m}|^2}, \tag{4.6}$$

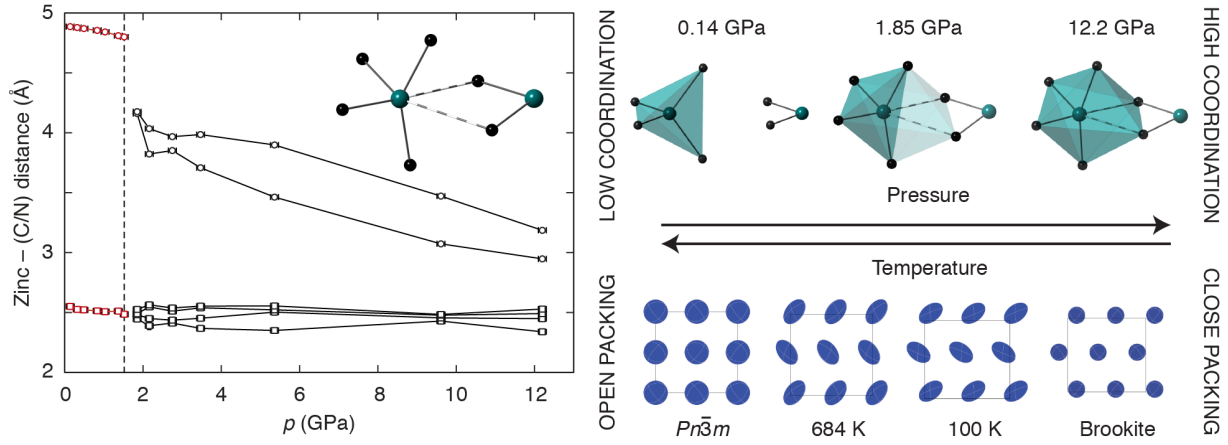

Figure 4.17: (*Left*) The evolution of the Zn–(C/N) distances as a function of pressure; figure reproduced with permission from Andrew Cairns. (*Right*) High coordination in $Zn(CN)_2$ and close packing in $Cd(im)_2$ both contribute towards denser structures, which are observed at high pressures and low temperatures, respectively, while high-symmetry arrangements are favoured at low pressures and high temperatures.

where **C** represents the x, y, z vector coordinates. Both $Zn(CN)_2$ upon compression and $Cd(im)_2$ upon cooling and compression show structural evolutions towards brookite-like arrangement [Fig. 4.15(b); see Fig. B.8 for individual Φ for the M and X]. The drive towards brookite-like packing at high pressures and low temperatures can be rationalised using the following considerations. On the one hand, there is the potential to increase the coordination number of the central cation as a means of improving packing efficiency and maximising lattice enthalpy. Analysis of the pressure-dependence of Zn–(C/N) distances in $Zn(CN)_2$-II indicates a clear progression towards sixfold coordination at high pressures, which is associated with Zn^{2+} off-centering within the $Zn(C/N)_4$ tetrahedra [Fig. 4.17]. On the other hand, there is the simple consideration of packing efficiency of bulky anions. The anion arrangement in the $Pn\bar{3}m$ aristotype phase consists of square arrays, while that in brookite is close packed [Fig. 4.17]. $Cd(im)_2$ is observed to favour close packed arrangements at low temperature, and open packing at high temperature, highlighting that the physical packing arrangements of ligands might play an important role in determining the critical response in coordination polymers.

4.8 Summary

The similarity in critical behaviour between $Zn(CN)_2$ and $Cd(im)_2$ demonstrates the potential to establish a predictive and transferable understanding of dynamical response in coordination polymers that is qualitatively independent of framework chemistry. It should be possible, for instance, to calculate generic phonon dispersion curves for aristotypic MOF topologies that highlight the existence and nature of soft modes which will likely play a dominant role in the mechanical response of all related networks. The role of framework chemistry then becomes one of tuning the energy scale and anharmonic sensitivity of these specific dynamic features. The nonlinear binding preference of the imidazolate anion, for instance, will lower the energy of transverse vibrational modes of the $Pn\bar{3}m$ $Cd(im)_2$ aristotype. Likewise, ligand substitution patterns will likely affect the periodicity with which certain low-energy displacements can most easily occur and hence favour softening at specific reciprocal lattice points. So, just as the identification of the NTE mechanism in $Zn(CN)_2$ helps understand the thermal response of $Cd(im)_2$, one can now reasonably expect to establish meaningful correspondences amongst isoreticular coordination polymers of very different chemical composition.

Chapter 5

Geometry

The framework angle XBU is seen to have a significant effect on the bulk expansivities and low-pressure compressibilities, as well as the origin of negative responses such as NTE and NLC in the coordination polymers investigated in the two previous chapters. Here, the effect of changing the framework angles on the expansivities is investigated in zinc isonicotinate, $Zn(ISN)_2$, and indium deuterium terephthalate, $InD(BDC)_2$. These MOFs were chosen because they have the same underlying topology, but the angles between connected metal nodes are quite different. As detailed in Chapter 4, the different chemical compositions of $Zn(ISN)_2$ and $InD(BDC)_2$ should not affect the general bulk response, and so it is the contrasting framework geometries that are directly investigated. The results of this chapter are found in the publication: I. E. Collings, M. G. Tucker, D. A. Keen, and A. L. Goodwin, *CrystEngComm*, 2014, **16**, 3498–3506.

Within the engineering community, it is well established that beam mechanics are determined not only by the connectivity of the network but also by the angles between connected beams, *i.e.* network geometry.[286–290] Specific beam structures—such as the "honeycomb", "re-entrant honeycomb" and "wine-rack" networks—give rise to well-known responses to temperature or pressure change, and can be predicted to show NTE, NLC or auxetic behaviour based upon the variation in connected beam geometries.[110,286–294] For example, the specific geometry of a honeycomb net

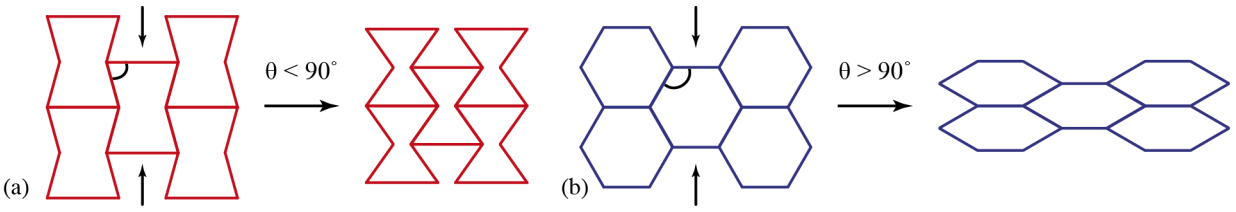

Figure 5.1: Honeycomb frameworks with different framework angles result in contrasting mechanical responses to uniaxial compression, where (a) exhibits an auxetic response, thus shrinking in the perpendicular direction of applied pressure, while (b) gives rise to normal expansion in the direction perpendicular to the axial compression.

determines whether the system has a positive or negative Poisson's ratio [Fig. 5.1]. As many coordination polymers show hinging mechanisms similar to the theoretical beam structures known in engineering, it is likely that geometry will play a significant role in their mechanical properties.

5.1 Structures of $Zn(ISN)_2$ and $InH(BDC)_2$

$Zn(ISN)_2$ and $InH(BDC)_2$ are three-dimensional MOFs composed of tetrahedral nodes (Zn^{2+} or In^{3+}) linked *via* molecular anions (ISN^- or BDC^{2-}) to form doubly-interpenetrated quartz nets [Fig. 5.2].[295,296] The initial interest in synthesising these MOFs was to mimic the quartz topology and thus synthesise inherently chiral frameworks.[297] As suggested in Ref. 295, low-temperature synthesis may be important in selecting quartz over diamondoid topologies, but that in general quartz-like coordination polymers remained rare.[295] After evacuation of the guest molecules within the $Zn(ISN)_2$ and $InH(BDC)_2$ framework pores, their structures are microporous with surface areas of $150\,m^2\,g^{-1}$ and $190\,m^2\,g^{-1}$, respectively. In the case of $Zn(ISN)_2$, the guest solvent is formed of two disordered water molecules per formula unit, while that of $InH(BDC)_2$ is thought to be 1.5 equivalents of dimethylformamide (DMF) and four equivalents of water based on the thermal analysis; the location of the H^+ in $InH(BDC)_2$ is not known.[295]

$Zn(ISN)_2$ is reported to crystallise in the chiral space groups $P3_1/P3_2$, with the lattice parameters $a = 15.256(5)$ Å and $c = 6.258(3)$ Å, while $InH(BDC)_2$ crystallises in the chiral space groups $P6_422/P6_222$ with the lattice parameters $a = 15.087(4)$ Å and $c = 12.032(5)$ Å.[295] The higher β-quartz symmetry is observed in $InH(BDC)_2$ due to its symmetric ligands. Another report of

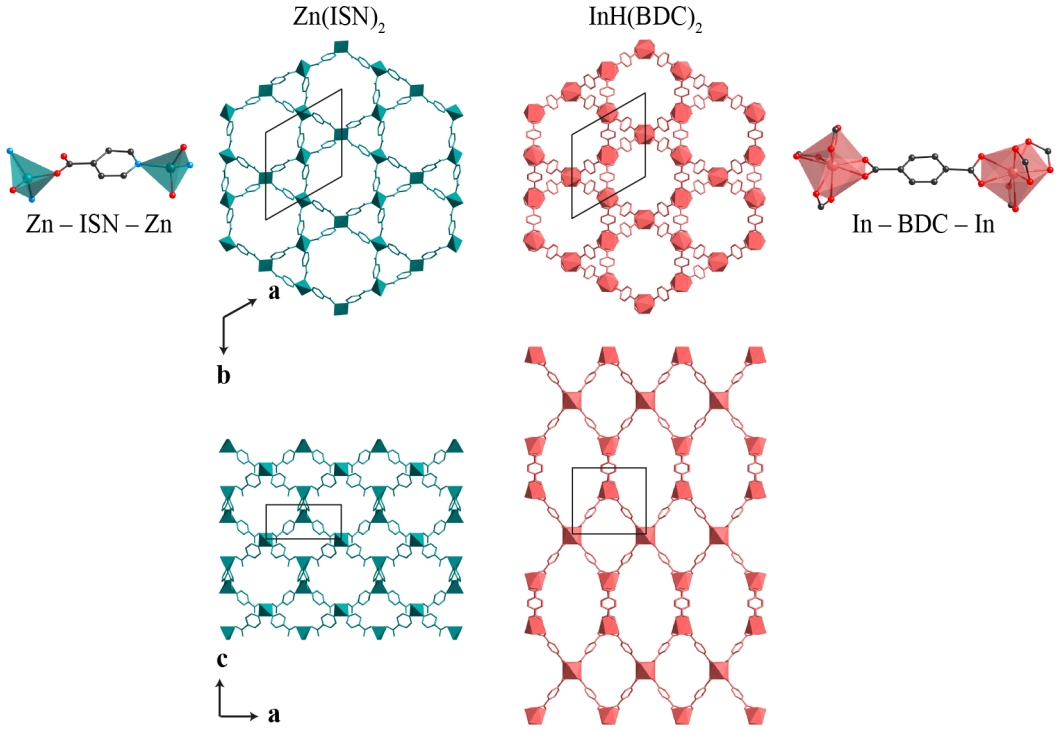

Figure 5.2: Extended framework structures of $Zn(ISN)_2$ and $InH(BDC)_2$ with metal coordination environments shown as polyhedra. The second interpenetrating net has been removed for clarity. Two views are shown: firstly to show their topological similarity to quartz, and secondly to highlight their different framework geometries, arising from their contrasting c/a ratios. The coordination environment of $Zn(ISN)_2$ and $InH(BDC)_2$ are shown at either side of the extended framework structures, where black is C, blue is N, red is O, green is Zn, and coral is In.

$Zn(ISN)_2$ was made later by Ref. 296, which had very similar lattice parameters to Ref. 295 but solved in $P6_2$.[296] For this study, variable-temperature neutron diffraction was carried out as part of a broader study into the interplay between the dynamics and flexibility of MOFs (see Appendix E),[298] thus deuterated MOFs were synthesised.

5.2 Experimental details of $Zn(ISN)_2$ and $InD(BDC)_2$

5.2.1 Synthesis

A polycrystalline sample of zinc(II) isonicotinate was prepared by mixing stoichiometric quantities of $Zn(CH_3COO)_2{\cdot}2H_2O$ (2.590 g, 11.80 mmol; Sigma-Aldrich, 98%) and isonicotinic-d^4 acid (3 g, 23.6 mmol; QMx, 98% D) each dissolved in dimethylsulfoxide (DMSO) (Sigma-Aldrich, 99.5%).

The isonicotinic-d^4 acid was warmed to 40 °C in DMSO for complete desolvation before mixing with the zinc salt solution. The white polycrystalline precipitate which was formed was filtered, washed and dried *in vacuo* (100 °C, 24 h) in order to remove solvent from the framework pores,[295] giving a total of 3.73 g of product.

Deuterium indium(III) terephthalate was prepared *via* hydrothermal synthesis. $InCl_3$ (2.60 g, 11.75 mmol; Sigma-Aldrich, 99.999%) and terephthalic-d^4 acid (4 g, 23.5 mmol; Sigma-Aldrich, 98% D) were added to 80 mL of DMF (Sigma-Aldrich, 99.9%) and heated to 120 °C for 24 hrs to encourage the reactants to dissolve. It is thought that the BDC ligand contained impurities which did not dissolve, as the addition of 120 mL of DMF and the increase of temperatures up to 145 °C were still not able to dissolve all the reactants. Consequently, the remaining powder was removed by filtration. To the dissolved solution of $InCl_3$ and ISN, 60 mL of D_2O (Sigma-Aldrich, 99.9% D) was added over gentle heating (60 °C) to allow for H^+/D^+ exchange of the mobile protons. The solution was then placed in a 300 mL teflon-lined bomb and heated in an oven at 160 °C for 3 days. The white polycrystalline gel so formed was isolated by filtration, washed and dried *in vacuo* (100 °C, 24 h) in order to remove solvent from the framework pores,[295] giving a total of 3.066 g of product. Working within a glovebox, the dried samples were ground and transferred to vanadium cans suitable for neutron scattering measurements.

5.2.2 Variable-temperature neutron powder diffraction

Neutron powder diffraction data were collected on warming at temperatures of 10 K, 50 K and then at intervals of 50 K up to 300 K for $Zn(ISN)_2$ and $InD(BDC)_2$ using the time-of-flight diffractometer GEM at ISIS.[219,221,222] These measurements were collected with Dr Matthew Tucker and Prof David Keen. For the experiment, 1.9 g of $Zn(ISN)_2$ and 1.5 g of $InD(BDC)_2$, prepared as described above, were each placed within cylindrical vanadium cans of 8.3 mm diameter and 6 cm height. Both cans were loaded at room temperature inside a closed cycle helium refrigerator (CCR) and the temperature was lowered to 10 K for the start of the measurement.

Both the $P3_1$ and $P6_2$ structural models of Refs. 295 and 296 could be used to fit the powder diffraction pattern of $Zn(ISN)_2$; consequently the $P6_2$ model was employed as the refinements did

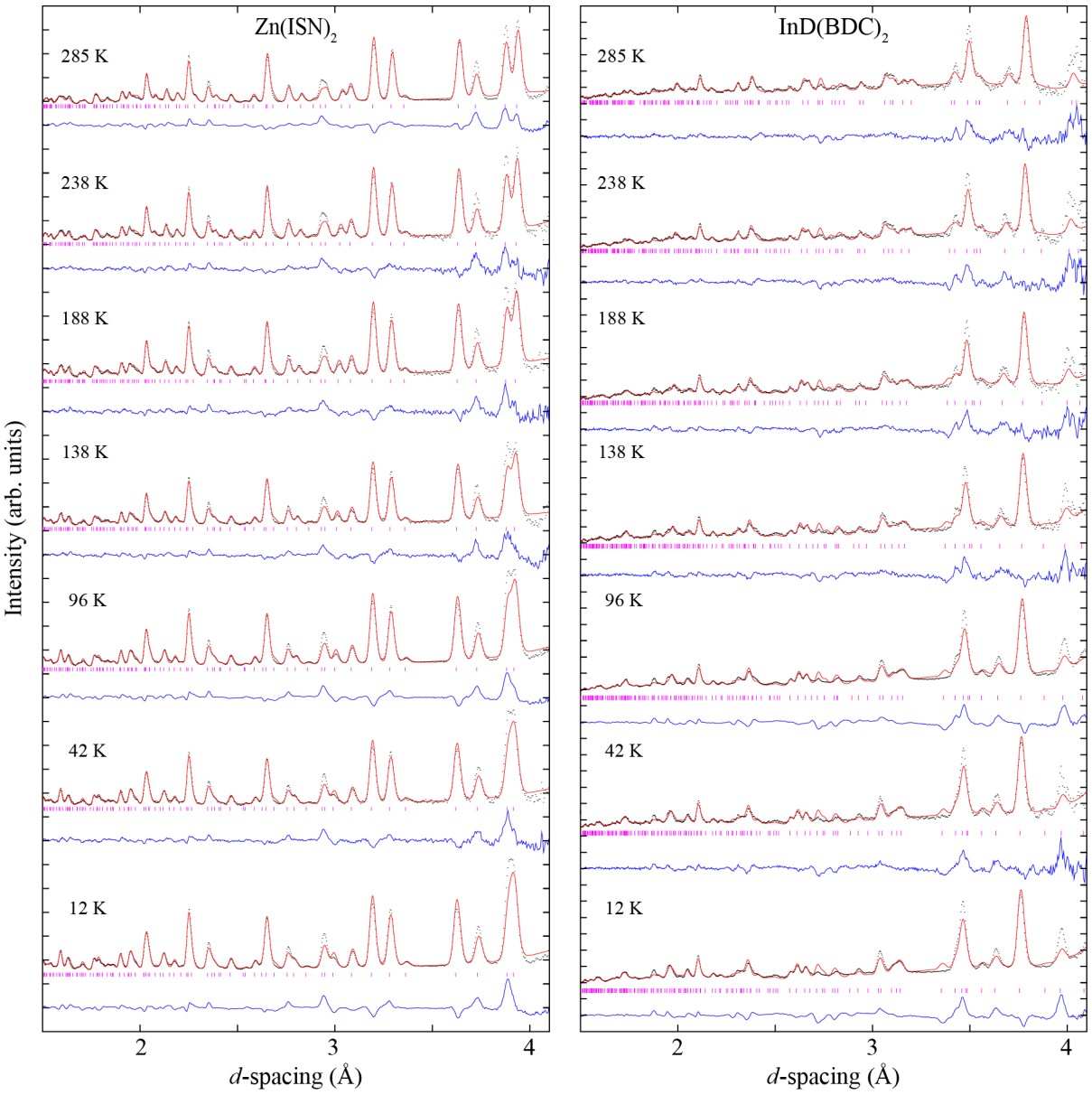

Figure 5.3: $Zn(ISN)_2$ and $InD(BDC)_2$ Rietveld fits. Experimental data are shown as points, the fitted profile as a solid red line, the difference (data−fit) as a blue line, and the *hkl* tick marks as the pink dashes.

not show any evidence of symmetry lowering. Rietveld fits for all temperatures are shown in Figure 5.3. The atomic coordinates of the isonicotinate ligand were refined using rigid body constraints in order to minimise the number of refinable parameters; likewise a single set of anisotropic thermal parameters was refined for all atoms in the isonicotinate group due to their transverse vibrational dynamics [Fig. E.3]. The zinc atom coordinates were kept fixed due to its special position in the (x,y)-plane and the lack of unique origin along the z-axis, while an isotropic displacement

parameter was freely refined. For $InD(BDC)_2$, the structure of Ref. 295 was used as a starting model. The atomic coordinates of the terephthalate moiety were refined using a combination of rigid body constraints and distance restraints, and a single set of isotropic thermal parameters was refined for all atoms in the terephthalate group. The indium atom coordinates were kept fixed due to it being on a special position in all crystallographic directions, while an isotropic displacement parameter was freely refined.

The Rietveld fits showed a slight intensity mismatch [Fig. 5.3]. The corresponding Fourier difference maps indicated that the pores of $Zn(ISN)_2$ and $InD(BDC)_2$ were not fully desolvated. Intelligent gravimetric analysis (IGA) on $Zn(ISN)_2$ revealed that the pores are mostly occupied by water molecules [Fig. C.1],[298] as is also known in the crystal structure.[295,296] Improved Rietveld fits could be obtained by modelling solvent molecules within the framework pores [Fig. C.2]. Throughout this chapter, the notation $Zn(ISN)_2$ and $InD(BDC)_2$ should therefore be taken to mean $Zn(ISN)_2$·{guest} and $InD(BDC)_2$·{guest}. For $InD(BDC)_2$, the diffraction quality was worse compared to that of $Zn(ISN)_2$, most probably owing to the large neutron absorption cross-section of indium [Table 2.1]. Despite these issues, the positions of the peaks are well defined for all temperatures in both frameworks [Tables C.1 and C.2], and it is these on which the subsequent analysis depends.

5.3 Temperature-induced mechanics of $Zn(ISN)_2$ and $InD(BDC)_2$

Relative changes in the lattice parameters extracted from the variable-temperature neutron diffraction Rietveld fits are shown in Figure 5.4(a). The corresponding expansivities were obtained by fitting an empirical equation of the form

$$\ell(T) = \ell_0 + \kappa T \left(\frac{T}{T + T_c} \right)^{\lambda}, \tag{5.1}$$

which helps capture the nonlinearity at low temperatures.[299] The derivative of Eq. (5.1) allows the calculation of the CTEs shown in Figure 5.4(b) [Eq. (A.1)]; the values of α_a and α_c extracted using linear fits to the lattice parameter evolutions are given in Table 5.1. These expansivities

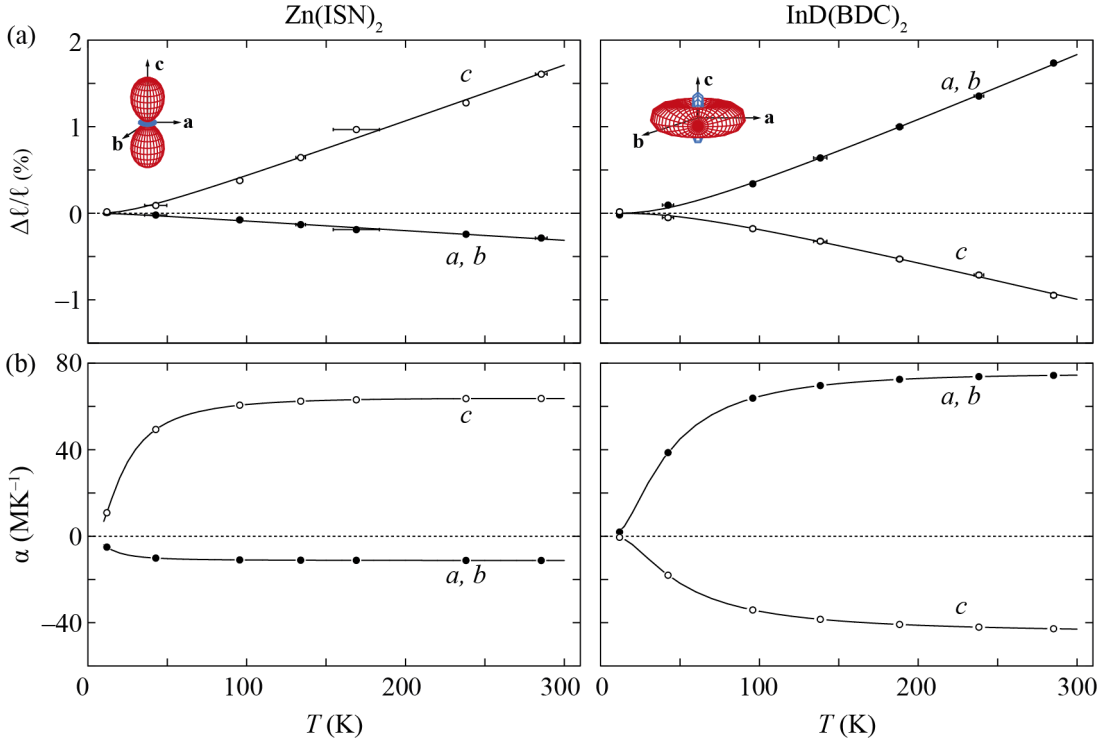

Figure 5.4: (a) Thermal variation of relative changes in lattice parameters and (b) the corresponding thermal expansivities observed for $Zn(ISN)_2$ and $InD(BDC)_2$ over the temperature range 10–300 K. The large error in the 170 K $Zn(ISN)_2$ temperature point arises from a difficulty in thermal stabilisation at this temperature for the CCR used in the experiment. Errors are substantially minimised in $InD(BDC)_2$ as equilibration time was extended. The expansivity indicatrix for each MOF is shown as an inset to (a) and indicates the spatial orientation of positive (red) and negative (blue) thermal expansion axes, obtained using PASCal.[179]

indicate large anisotropy, where PTE is exhibited in one direction and NTE in the other. The fundamental difference between the mechanical properties of the two MOFs is that the NTE is observed along different axes: $Zn(ISN)_2$ exhibits biaxial NTE in the (a, b)-plane (area expansivity $\alpha_A = 2\alpha_a = -21.8(10)\,\mathrm{MK}^{-1}$), while $InD(BDC)_2$ displays uniaxial NTE along the c-axis ($\alpha_c = -35(2)\,\mathrm{MK}^{-1}$). Biaxial NTE is a rare phenomenon having been reported in just a handful of materials: examples include (*S*,*S*)-octa-3,5-diyn-2,7-diol,[300] the MOF Cu-SIP-3,[179] $Ni(CN)_2$,[301] Zn_2(4-(1*H*-naphtho[2,3-*d*]imidazol-1-yl)benzoate)$_2(OH)_2$,[147] and silver tricyanomethanide.[166]

The evolutions of the XBUs present in $Zn(ISN)_2$ and $InD(BDC)_2$, namely the r distance (metal–ligand–metal units), and the three unique framework angles show that the framework angle variations are largest, while r distances remain essentially constant as a function of temperature

Table 5.1: Expansivities for the lattice and XBU parameters in $Zn(ISN)_2$ and $InD(BDC)_2$, calculated using linear fits to data.

i	$Zn(ISN)_2$		$InD(BDC)_2$	
	i at 285 K	α_i (MK^{-1})	i at 285 K	α_i (MK^{-1})
a, b (Å)	15.4752(6)	−10.9(5)	14.7860(17)	64(3)
c (Å)	6.2254(6)	60(3)	12.155(3)	−35(2)
V (Å^3)	1291.131	37.8(18)	2301.309	94(4)
r (Å)	8.780	4.7(4)	10.969	9.2(3)
θ_1 (°)	80.51	26.3(11)	108.58	−41(2)
θ_2 (°)	127.71	6.9(3)	140.61	−15.9(8)
θ_3 (°)	123.58	−27.0(12)	84.75	68(3)

[Fig. 5.5(a), Table 5.1]. The calculated framework angle expansivities, which make use of α_a and assume $\alpha_r = 0$, are very similar to those observed experimentally [Section C.4]. This supports the interpretation that geometric flexing of the framework dominates the bulk lattice parameter evolution [Fig. 5.5(b)]. A similar hinging mechanism has been observed in many other coordination polymers,[145,147,149,185] including Ag(mim).[299] In the case of a 2D wine-rack framework flexing—where there is only one unique framework angle—it is trivial to determine the direction of negative and positive responses depending on whether the framework changes are towards an increase in

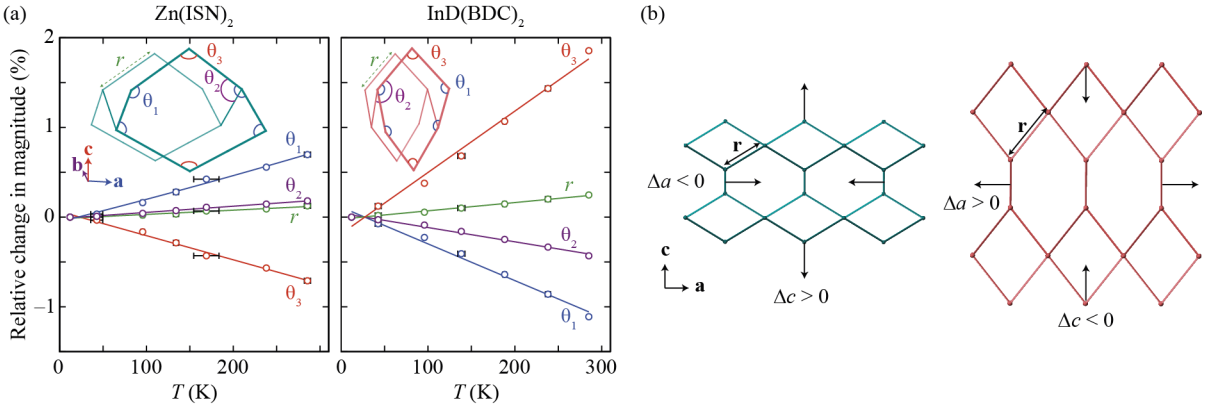

Figure 5.5: (a) Evolution of the r distance and the framework angles θ_i as a function of temperature. The inset figure shows the location of the angles in the hexagon of the framework structure. (b) Representation of $Zn(ISN)_2$ and $InD(BDC)_2$, where ligands are omitted and instead rods indicate the connectivity of the framework. The arrows indicate the direction of expansion or contraction and the linking **r** vector is indicated on both structures.

symmetry or further distortion. Yet for frameworks like $Zn(ISN)_2$ and $InD(BDC)_2$ which have three framework angles, or $Zn(CN)_2$ and $Cd(im)_2$ with six angles, the prediction of mechanical anisotropy is not straightforward from simple inspection of the structures. A geometric formalism is developed below in order to allow mechanical anisotropy to be readily predicted by considering known parameters from the crystal structure.

5.4 Geometric formalism

For this formalism, two assumptions are made: namely that $\alpha_r \simeq 0$ and that α_V is positive. Both these conditions are fulfilled in $Zn(ISN)_2$ and $InD(BDC)_2$, and are properties that are generally observed in coordination polymers which exhibit framework flexing.[145,147,299] First, the linking vector **r**—which represents the M–ligand–M unit of the framework—is defined in terms of the lattice vectors **a**, **b**, **c**. In the case of $Zn(ISN)_2$ and $InD(BDC)_2$

$$\mathbf{r} = \frac{1}{2}\mathbf{a} + \frac{1}{2}\mathbf{b} + \frac{2}{3}\mathbf{c}. \tag{5.2}$$

Conversion into orthogonal axes gives

$$\begin{aligned} \mathbf{r} &= \frac{1}{2}a\mathbf{i} + \frac{1}{2}\left(-\frac{a}{2}\mathbf{i} + \frac{\sqrt{3}}{2}a\mathbf{j}\right) + \frac{2}{3}c\mathbf{k}, \\ \mathbf{r} &= \frac{1}{4}a\mathbf{i} + \frac{\sqrt{3}}{4}a\mathbf{j} + \frac{2}{3}c\mathbf{k}. \end{aligned} \tag{5.3}$$

The magnitude of this vector

$$r = \sqrt{\frac{a^2}{4} + \frac{4c^2}{9}}, \tag{5.4}$$

corresponds to the r distance plotted in Figure 5.5(a). Taking the variation in r with T to be small (*i.e.* $\alpha_r = 0$) the following relationship is obtained:

$$\begin{aligned} \alpha_r \;=\; 0 \;&=\; \frac{1}{r}\frac{\mathrm{d}r}{\mathrm{d}T} \\ &=\; \frac{1}{2r}\left[\frac{a^2}{4}+\frac{4c^2}{9}\right]^{-\frac{1}{2}}\left[\frac{2a}{4}\frac{\mathrm{d}a}{\mathrm{d}T}+\frac{8c}{9}\frac{\mathrm{d}c}{\mathrm{d}T}\right] \\ &=\; \frac{1}{r^2}\left[\frac{a^2\alpha_a}{4}+\frac{4c^2\alpha_c}{9}\right], \end{aligned} \tag{5.5}$$

and hence

$$\begin{aligned} \frac{1}{4}a^2\alpha_a+\frac{4}{9}c^2\alpha_c \;&=\; 0 \\ \alpha_c \;&=\; -\frac{9}{16\rho^2}\alpha_a, \end{aligned} \tag{5.6}$$

where $\rho = c/a$. Equation (5.6) indicates that α_a and α_c must have opposite signs, and that the magnitude of one fixes the magnitude of the other for any given value of ρ. In hexagonal systems, $\alpha_V = 2\alpha_a + \alpha_c$, and so the constraint $\alpha_V > 0$ taken with the relationship established in Eq. (5.6) gives the crucial inequality

$$\alpha_V = \alpha_a\left[2-\frac{9}{16\rho^2}\right] > 0. \tag{5.7}$$

The importance of this equation is that α_a is predicted to be negative for values $\rho < \sqrt{\frac{9}{32}} = 0.53 = \rho_{\mathrm{crit}}$ and positive whenever ρ is larger than this value. This means that the geometry of the framework determines whether NTE is shown within the (a,b)-plane ($\rho < \rho_{\mathrm{crit}}$) or along the c-axis ($\rho > \rho_{\mathrm{crit}}$).

The experimental values of ρ for $Zn(ISN)_2$ and $InD(BDC)_2$ are given in Table 5.2, from which it is clear that these two frameworks lie on either side of the value of ρ_{crit} determined above.

Table 5.2: Lattice parameters and observed ρ values for $Zn(ISN)_2$ and $InD(BDC)_2$ at 285 K.

MOF	a (Å)	c (Å)	$\rho = c/a$
$Zn(ISN)_2$	15.4752(6)	6.2254(6)	0.40
$InD(BDC)_2$	14.7860(17)	12.155(3)	0.82

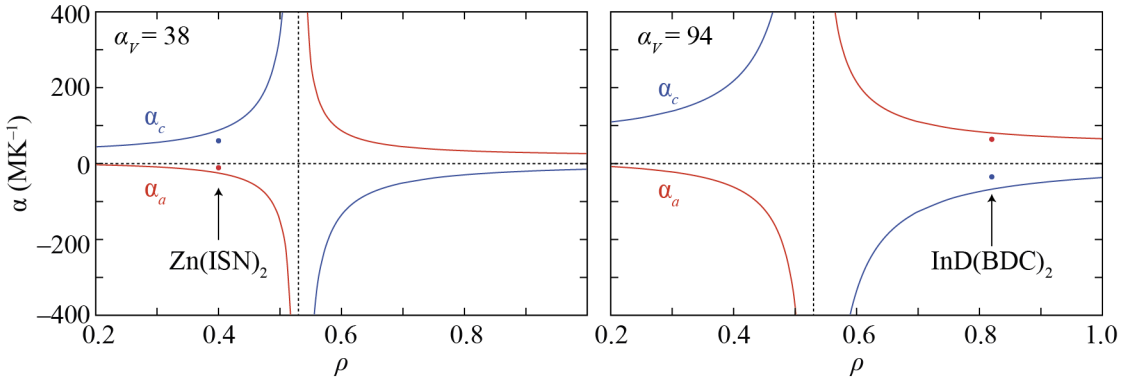

Figure 5.6: Calculated CTEs for the *a*- and *c*-axes at different ρ values for $Zn(ISN)_2$ and $InD(BDC)_2$ with constant volume expansion as determined from experiment. The points indicate the experimentally obtained CTEs. The vertical dashed line marks ρ_{crit}.

Consequently, this geometric formalism allows the prediction of the expansivity anisotropy found in $Zn(ISN)_2$ and $InD(BDC)_2$, and confirms that the reversal of anisotropic response to temperature has no real chemical origin, but is a function of framework geometry alone. Making use of the experimental values of α_V known for $Zn(ISN)_2$ and $InD(BDC)_2$, Eq. (5.7) allows calculation of the CTEs for differing lattice geometries ρ [Fig. 5.6]. The observed experimental values of CTE for $Zn(ISN)_2$ and $InD(BDC)_2$ are shown as points at the corresponding ρ values; the difference between these points and the calculated lines of CTE reflects the subtle change in the magnitude of r as a function of temperature (which is not accounted for in the geometric formalism). Hence, if α_r is sufficiently large and positive, it may negate any geometry-driven negative response, as seen in the NLC–PLC transitions in Ag(mim) and $Zn(CN)_2$.

The divergence in calculated α values near $\rho = \rho_{crit}$ reflects the fact that geometric flexing of a framework with $\rho = \rho_{crit}$ results in zero volume change to a first approximation due to the equal contributions of PTE and NTE. Consequently the magnitude of uniaxial expansivities required to give a nonzero volume CTE diverges at this point. In practice this means that the mechanical response of materials with $\rho = \rho_{crit}$ will not be dominated by geometric flexing, but rather by the intrinsic response of the framework linkers. Nevertheless the design strategy of choosing materials with values of ρ very close to ρ_{crit} may be a useful approach for identifying candidate compounds with extreme CTEs.

Table 5.3: Quartz-like frameworks with their unit cells compared to that of β-quartz, the critical and observed ρ values, and CTEs for the a- and c-axes. The calculated ρ_{crit} values are all related to the β-quartz value of 1.06 by simple ratios that reflect the relationship between the corresponding unit cells. *$Zn[Ag(CN)_2]_2$ contains AgCN within the pores.

Framework	a/a_{SiO_2}	c/c_{SiO_2}	ρ_{crit}	ρ	α_a (MK^{-1})	α_c (MK^{-1})	Ref.
β-quartz	1	1	1.06	1.09	0.12	−1.1	40
$Zn(ISN)_2$	1	0.5	0.53	0.40	−10.9	60	this work
$InD(BDC)_2$	1	0.5	0.53	0.82	64	−35	this work
$Zn[Au(CN)_2]_2$	$1/\sqrt{3}$	1	1.84	2.44	36.9	−57.6	143
$Zn[Ag(CN)_2]_2$*	$1/\sqrt{3}$	1	1.84	1.92	4.1	−21.7	143

5.5 Discussion: Generality of geometric formalism

Considering first a range of other frameworks with the quartz topology, as summarised in Table 5.3, a range of critical values of ρ are determined for these different systems by following the approach outlined above. This is perhaps counterintuitive as one might expect a unique critical c/a ratio for a given topology. The origin of this variation lies in the way interpenetration affects the relationship between the linking vector $\mathbf{r}$ and the lattice vectors. For example, the critical values of ρ in $InD(BDC)_2$ and β-quartz are related by a factor of two because two-fold interpenetration in the former gives rise to a halving of the c lattice parameter [Fig. 5.7]. For all the frameworks listed in Table 5.3, with the exception of $Zn(ISN)_2$, the observed value of ρ lies above ρ_{crit}. Consequently, based upon geometric considerations they should all show NTE along their c-axes, as is indeed found to be the case experimentally. So the differing chemistry of these frameworks would seem not to affect the anisotropy in lattice parameter evolution, but rather only the magnitude of mechanical response. The inclusion of a silica polymorph in Table 5.3 is purely for reference as it is well known that other deformation modes dominate its thermal expansion.[38,43]

The framework material $Zn[Ag(CN)_2]_2{\cdot}AgCN$ shown in Table 5.3 is a somewhat complex example because it exhibits modest volume NTE ($\alpha_V < 0$) despite the fact that its uniaxial response is as one would expect for a system with positive volume thermal expansion. This apparent discrepancy arises because the framework thermal expansion is dominated by the NTE behaviour

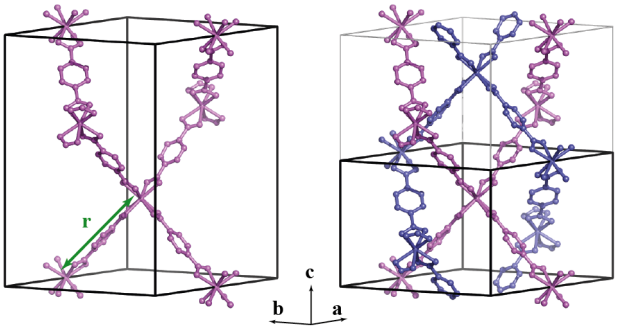

Figure 5.7: Unit cell relations between a single net of the quartz-like $InD(BDC)_2$ structure and the observed doubly-interpenetrated net. The unit cell halves along the c-axis as a result of interpenetration, which accounts for the factor of two difference in ρ_{crit} values for β-quartz and $InD(BDC)_2$.

of the linkers (strong because of low-energy transverse vibrations) rather than by geometric flexing of the lattice (weak because of the presence of AgCN chains within the framework pores). The geometric contribution to the volume expansivity

$$\begin{aligned} \alpha_{V,\text{geom}} &= \alpha_V - 3\alpha_r \\ &= -13.57(29)\,\text{MK}^{-1} - 3 \times (-5.02(14)\,\text{MK}^{-1}) \\ &= +1.5(5)\,\text{MK}^{-1} \end{aligned}$$

is positive and consequently the direction of uniaxial response, which is governed by geometry, is as expected for a system that exhibits volumetric PTE.[143] Such considerations will be of relevance to only a few of the anisotropic coordination polymers, since the NTE effect associated with transverse vibrational motion is usually much weaker than the NTE/PTE effects associated with framework flexing.[299]

So far the application of this analysis has focused on the interplay between network geometry and thermal expansivity, but the analysis here is equally applicable to understanding anisotropic compressibility. Just as geometry determines the balance between linear and area NTE, so too might geometric considerations help identify the most likely NAC candidates. Based on the results summarised in Table 5.3, $Zn(ISN)_2$ would be the most likely candidate to exhibit NAC of these quartz-like frameworks.

This approach is not limited to quartz-like frameworks. It might usefully be applied to any uniaxial

system (trigonal, hexagonal or tetragonal), where the following two considerations are satisfied: (*i*) framework angle changes are likely to dominate lattice parameter evolution, and (*ii*) all linking vectors **r** are related to each other and to the lattice vectors **a**, **b**, **c** by symmetry considerations. While in the case of $Zn(ISN)_2$ and $InD(BDC)_2$ α_V is positive, it is possible that certain frameworks will show negative volume expansion. In such cases, the anisotropy prediction will be inverted because the inequality in Eq. (5.7) will switch to fulfil $\alpha_V < 0$; the existence and value of a critical c/a ratio, however, is unaffected by the sign of the volume coefficient of thermal expansion. While volume NTE has been observed in many framework materials which exhibit transverse vibrational modes of their linkers as their main deformation mode,[127,133,134,302] frameworks which display hinging mechanisms generally exhibit positive volume CTE.[8,145,147,149,299] So it is anticipated that the condition $\alpha_V > 0$ will actually hold for the vast majority of frameworks for which geometric hinging is possible. These considerations may be affected also by the presence or otherwise of solvent within framework pores. In Section C.5, the presence of the solvent within the pores of either $Zn(ISN)_2$ or $InD(BDC)_2$ is shown not to affect the direction of anisotropy, influencing instead only the magnitude of response, as known in other MOFs.[11,147] It remains possible, if unlikely, that the inclusion of solvent within the pores of other framework materials induces a sufficiently large change in geometry that a reversal in anisotropic mechanical response arises. In this way, sorption/desorption might be used to trigger a switch from area to linear NTE or *vice versa*.

The generality of this geometric analysis is illustrated by considering several coordination polymers. The anisotropic compressibilities within the family of ammonium transition-metal formates, $[NH_4][M(HCOO)_3]$ are examined first. These frameworks have the **acs** topology, the parent of which is tungsten carbide. The zinc- and magnesium-containing members have recently been shown to exhibit NLC and NTE, respectively.[144,185] In all cases, the linking vector **r** corresponds to a M–formate–M unit [Fig. 5.8] and is related to the lattice vectors by the relationship

$$\mathbf{r} = \frac{1}{3}\mathbf{a} - \frac{1}{3}\mathbf{b} + \frac{1}{2}\mathbf{c}. \tag{5.8}$$

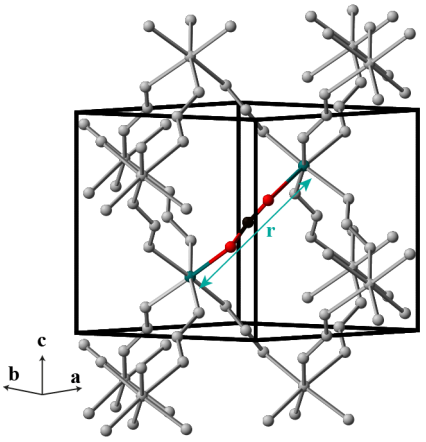

Figure 5.8: Representation of the $[NH_4][M(HCOO)_3]$ structure, with the **r** vector highlighted in the coloured M–formate–M link.

The same vector in orthogonal coordinates gives

$$\mathbf{r} = \frac{1}{2}a\mathbf{i} - \frac{\sqrt{3}}{6}a\mathbf{j} + \frac{1}{2}c\mathbf{k}. \tag{5.9}$$

Consequently the linker length is given by

$$r = \sqrt{\frac{a^2}{3} + \frac{c^2}{4}}. \tag{5.10}$$

If geometric variations dominate the mechanical response, then the approximation $K_r \simeq 0$ can be made, giving

$$\begin{aligned} K_r \simeq 0 &= -\frac{1}{r}\frac{\mathrm{d}r}{\mathrm{d}p} \\ &= -\frac{1}{2r}\left[\frac{a^2}{3} + \frac{c^2}{4}\right]^{-\frac{1}{2}}\left[\frac{2a}{3}\frac{\mathrm{d}a}{\mathrm{d}p} + \frac{2c}{4}\frac{\mathrm{d}c}{\mathrm{d}p}\right] \\ &= -\frac{1}{r^2}\left[\frac{a^2K_a}{3} + \frac{c^2K_c}{4}\right], \end{aligned} \tag{5.11}$$

and hence

$$K_c = -\frac{4}{3\rho^2}K_a. \tag{5.12}$$

This again predicts that the a and c compressibilities are of opposite signs. Since thermodynamics demand $K_V = 2K_a + K_c > 0$, the inequality

$$K_a \left[2 - \frac{4}{3\rho^2} \right] > 0 \tag{5.13}$$

is obtained, whence K_a is predicted to be negative for values $\rho < \sqrt{\frac{2}{3}} = 0.82 = \rho_{\text{crit}}$ and positive for $\rho > \sqrt{\frac{2}{3}}$. The observed ρ value for $[NH_4][Zn(HCOO)_3]$ is 1.12. As this lies above ρ_{crit}, the geometric analysis would predict $K_a > 0$ and $K_c < 0$. The experimental compressibilities given in Ref. 185 are $K_a = 15.8(9)\ \text{TPa}^{-1}$ and $K_c = -1.8(8)\ \text{TPa}^{-1}$, and so agree with what is predicted by the geometric analysis. It is expected that similar responses for the other ammonium transition-metal formates exist, as the observed ρ does not vary significantly with change in metal and is always above ρ_{crit}: $\rho = 1.10$ for $[NH_4][Ni(HCOO)_3]$ and $\rho = 1.15$ for $[NH_4][Mn(HCOO)_3]$; Ref. 303. For the $[NH_4][Mg(HCOO)_3]$ framework, the value of ρ_{crit} is the same as determined above, and thus the negative response observed along the c-axis for this structure is consistent with the observation $\rho = 1.13 > \rho_{\text{crit}}$.[144]

Likewise, the MIL-88 family—composed of metallic trimers connected *via* dicarboxylate groups—have the **acs** topology, and hence exhibit the same critical value as above ($\rho_{\text{crit}} = 0.82$; calculated by using the centre of the metal clusters as nodes).[304] Although no variable-pressure or variable-temperature studies have been carried out for these systems, adsorption of small molecules such as water and pyridine into the framework causes volume increase *via* expansion within the (a, b)-plane and contraction along the c-axis.[90,105] This mechanical response to adsorption is consistent with the geometric analysis: the observed ρ values in the MIL-88 family are above $\rho_{\text{crit}} = 0.82$, and hence negative responses are expected for the c-axis. By exploiting the tuneable chemistry of the MIL-88 family, the value of ρ can be varied between 1.31 and 2.31 using different ligands[§] while maintaining the same topology.[90] Even though these all lie above ρ_{crit}, the large variation in ρ suggests ligand substitution to be a more effective strategy for accessing different mechanical responses than is metal exchange.

[§]The ρ values were calculated using the smallest and largest differences in 'as-synthesised' lattice parameters, corresponding to the MIL-88A and MIL-88C structures, respectively.

Table 5.4: Diamondoid frameworks with their observed and critical ρ values. *Denotes frameworks which should exhibit a negative area response in the (a, b)-plane as they fulfil $\rho < \rho_{\text{crit}}$. Abbreviations used: 4-cnpy = 4-cyanopyridine, 4,4′-bipy = 4,4′-bipyridyl, D_L-cam = enantiopure camphorate, Pr_4N = tetra-*n*-propylammonium, 2,5-Me_2pyz = 2,5-dimethylpyrazine, PT = 5-propyltetrazole, 5-X-2-pymo = 5-halo-pyrimidin-2-ol (X=Br/I), mim = 2-methylimidazolate.

Framework	ρ	ρ_{crit}	Ref.
$[Ag(4\text{-cnpy})_2][BF_4]$	0.39*	0.50	305
$[Cu(4,4'\text{-bipy})_2][PF_6]$	0.57	0.50	306
$[In(D_L\text{-cam})_2][Pr_4N]$	0.60*	1.41	307
$[Cu(2,5\text{-}Me_2pyz)_2][PF_6]$	0.69*	1.41	308
$Zn(PT)_2$	1.66	1.41	309
$Co(5\text{-X-2-pymo})_2$	1.69	1.41	310
LiB(mim)	2.17	1.41	311

One particularly clear example of how MOF chemistry might be used to access a variety of geometries for a given topology is provided by the series of known diamondoid MOFs. Table 5.4 and Figure 5.9 illustrate the range of observed ρ values—above and below ρ_{crit}—which can be obtained by varying chemical composition. By identifying structures for which $\rho < \rho_{\text{crit}}$, the frameworks which are predicted to show negative area responses in the (a, b)-plane can be identified. Consequently, In(D_L-cam)$_2$, Cu(2,5-Me_2pyz)$_2$ and Ag(4-cnpy)$_2$ are all likely NAC candidates. Whether or not these materials do in fact exhibit NAC will depend on the extent to which their deformation mechanism under pressure is dominated by changes in geometry rather

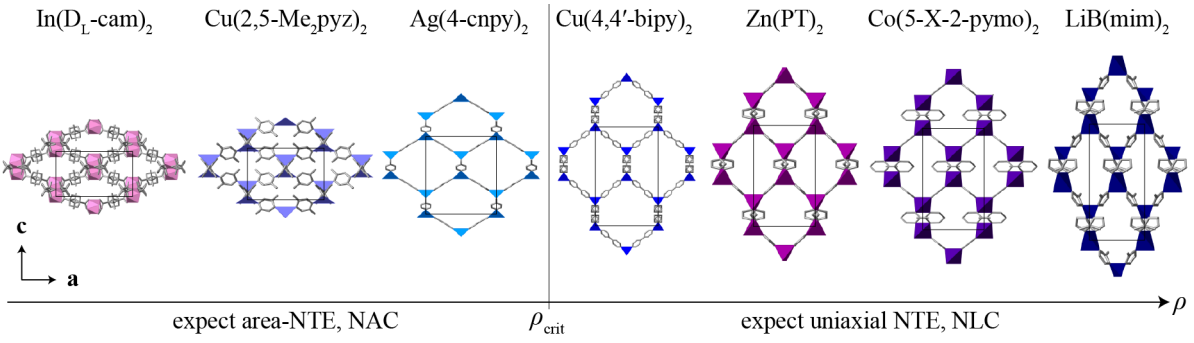

Figure 5.9: Extended diamondoid frameworks from Table 5.4 shown ordered by observed ρ with the vertical line signifying the critical ρ value. The observed ρ and unit cell dimensions of Ag(4-cnpy)$_2$ and Cu(4,4′-bipy)$_2$ are scaled by $2\sqrt{2}$ to allow comparison to the other frameworks.

than compression along the M–linker–M units. The balance between these effects has already been demonstrated in the NLC–PLC transitions in Ag(mim) and $Zn(CN)_2$.[159,299] With this in mind, in order to achieve large negative compressibility *via* framework angle deformation, linking units should be chemically engineered to be more "rigid" by using, for instance, aromatic-based ligands, and M–ligand–M struts that favour linear coordination.

5.6 Summary

A straightforward geometric formalism can be used to predict the NTE or NLC axes for flexible coordination polymers of uniaxial crystal symmetry. In particular, the contrasting geometries in $Zn(ISN)_2$ and $InD(BDC)_2$ are found to explain the switch in anisotropic expansivities. As many coordination polymers exhibit framework angle changes as the dominant form of structural variation, this analysis can be usefully applied as a predictor of mechanical property anisotropy by simply using parameters from the crystal structure.

Chapter 6

Composition

All coordination polymers contain the metal–link–metal XBU and there is a large number which can support framework-hinging XBUs. Chapter 4 highlighted the importance of the arrangement of the strut XBUs, while the anisotropic mechanical properties originating from framework hinging depend on framework geometries as shown in Chapter 5. As mentioned previously, the magnitudes of these responses are determined by the chemical components of the structure. In this chapter, the direct correspondence between the composition and the mechanical properties of the framework is investigated using variable-temperature X-ray diffraction experiments on 19 chemically varied coordination polymers. The materials of interest are based upon the $[A][M(HCOO)_3]$ family, where the chemical modifications involve the variation of the M^{2+} cations (Mg, Mn, Fe, Co, Ni, Cu, Zn, and Cd) and the A-site cations (methylammonium $[CH_3NH_3]$, dimethylammonium $[(CH_3)_2NH_2]$, ethylammonium $[CH_3CH_2NH_3]$, azetidinium $[(CH_2)_3NH_2]$, and guanidinium $[C(NH_2)_3]$). This family of materials was chosen due to its topological similarity to ABO_3 perovskites, and because the perovskite topology is maintained throughout all the different chemical compositions of $[A][M(HCOO)_3]$ mentioned above. Flexibility in these frameworks is related to the extent of framework hinging XBUs, and this chapter shows how the composition can be used to tune the magnitude of mechanics. The rules determined here are compared with other known composition-dependent mechanical properties.

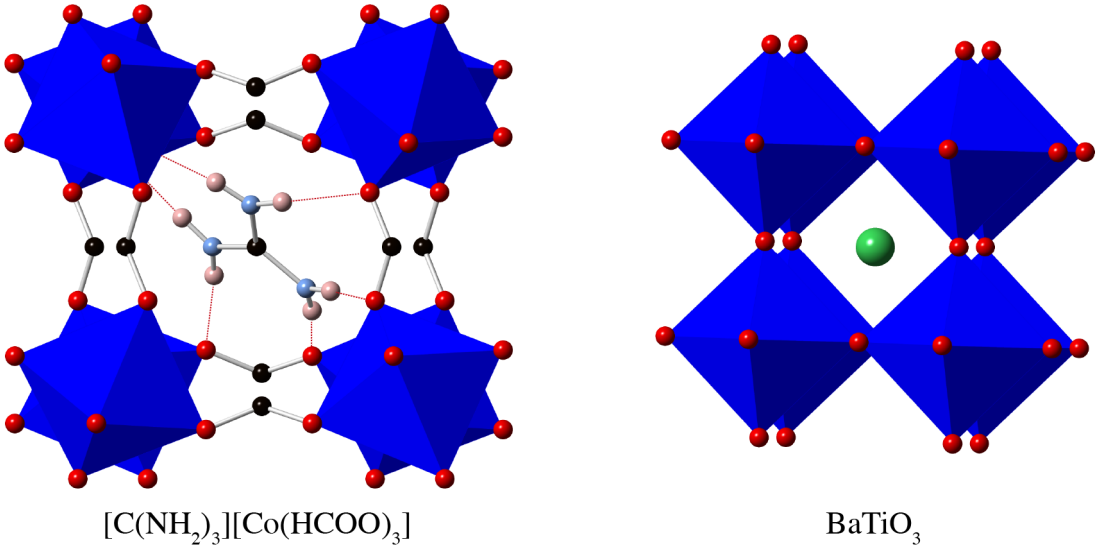

Figure 6.1: ABX_3 frameworks of $[C(NH_2)_3][Co(HCOO)_3]$ and $BaTiO_3$. The hydrogen bonding in $[C(NH_2)_3][Co(HCOO)_3]$ is shown with the dotted red line. The Co^{2+} and Ti^{4+} coordination environments are represented by polyhedra.

6.1 Structures of [A][M(HCOO)$_3$]

The $[A][M(HCOO)_3]$ framework structures are composed of octahedrally coordinated metal centres, which are linked *via* formate ligands to form an extended three-dimensional structure with the perovskite topology. Inside each framework cavity, an A-site cation is held *via* hydrogen bonds between its NH groups and the oxygens from the formate ligand [Fig. 6.1].[312,313] There are other topologies which exist for these ABX_3-type compositions. For example, the ammonium or hydroxylammonium metal formates, which contain smaller A-site cations in the pore, give rise to the denser **acs** topology [Fig. E.7].[314–316]

Many different $[A][M(HCOO)_3]$ compounds have been reported in the literature due to the increasing interest in the order–disorder ferroelectric transition observed in some of these structures. For instance, the ferroelectric transition arises in the $[(CH_3)_2NH_2][M(HCOO)_3]$ family for many different metal cations used (M^{2+} = Mg, Mn, Fe, Co, Ni, Zn), due to the rotational ordering of the dimethylammonium cation upon cooling [Fig. 6.2].[59,317–319] The denser frameworks $[NH_4][M(HCOO)_3]$ with M^{2+} = Mg, Mn, Fe, Co, Ni, and Zn are also able to exhibit a ferroelectric

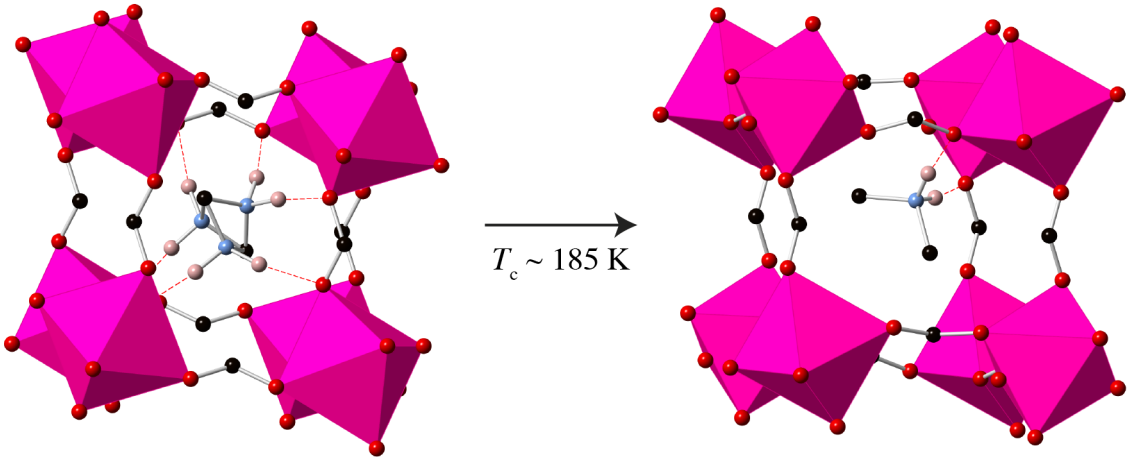

Figure 6.2: Ferroelectric phase transition in $[(CH_3)_2NH_2][Mn(HCOO)_3]$ induced upon cooling from ambient temperature to below 185 K, creating a uniaxial electric dipole as the A-site cations order from their three-site disorder. Hydrogen bonds are shown in dotted red lines, and octahedral coordination about Mn^{2+} cations are represented by polyhedra.

transition due to the rotational and translational dynamics of the ammonium cations which order within the anionic framework cavities upon cooling.[144,314,315,320] The highest T_c value for the ferroelectric transition is observed for the Mg member in both families (T_c = 270 K and 255 K) because the low polarisability of Mg^{2+} allows greater negative charge to reside on the oxygen atoms of the formate ligand. This then enhances the hydrogen bonding strength between the A-site cation and the formate.[144,318]

Within the magnetic members of $[A][M(HCOO)_3]$ (M^{2+} = Mn, Fe, Co, Ni), there is the additional promise of multiferroic properties if the magnetic order can be coupled to the ferroelectric order. So far, only weak magnetoelectric coupling has been elucidated in the paramagnetic state of $[(CH_3)_2NH_2][Mn(HCOO)_3]$.[321] The magnetic properties suggest a canted antiferromagnetic ordering within 8–36 K for the different metal cations used, giving rise to overall weak ferromagnetism.[312,322] The magnetic properties show that an increase in magnetic ordering temperature is correlated to a decrease in metal cation size,[315,322] due to the increase in magnetic coupling strength as the metal cations are brought closer together. Calculations indicate that magnetoelectric coupling should exist in guanidinium metal formates where the metal cation is Cu^{2+} or Cr^{2+}, and crucially depends on the Jahn-Teller distortion to allow the coupling.[323,324]

Table 6.1: Crystal structures of [A][Mn(HCOO)$_3$] determined at 290 K with the five different A-site cations.

	[A][Mn(HCOO)$_3$]				
A^+	CH_3NH_3	$CH_3CH_2NH_3$	$(CH_3)_2NH_2$	$(CH_2)_3NH_2$	$C(NH_2)_3$
Crystal system	Orthorhombic	Orthorhombic	Trigonal	Orthorhombic	Orthorhombic
Space group	$Pnma$	$Pna2_1$	$R\bar{3}c$	$Pnma$	$Pnna$
a (Å)	8.679(2)	9.086(1)	8.334(1)	8.688(2)	8.5211(3)
b (Å)	11.955(3)	8.215(1)	8.334(1)	12.303(3)	11.9779(4)
c (Å)	8.164(2)	12.030(2)	22.890(4)	8.875(2)	9.0593(3)
V (Å^3)	847.1(4)	897.9(2)	1376.8(3)	948.6(3)	924.64(5)
V/Z	211.8	224.5	229.5	237.2	231.2
Ref.	312	312	312,322	312	313

The known crystal structures of the [A][Mn(HCOO)$_3$] series that were used in this investigation are shown in Table 6.1. The use of other metal(II) cations in the synthesis, while employing the same A-site cation, generally formed isostructural framework structures. The exception is seen with [A][Cu(HCOO)$_3$] structures which exhibit Jahn-Teller distortions, thus usually lowering the symmetry compared to the corresponding [A][Mn(HCOO)$_3$] structures. The different syntheses which were made for this investigation are shown in Table 6.2; the grey highlighted cells indicate the compounds which were successfully synthesised and further studied. For simplicity, the [CH_3NH_3][M(HCOO)$_3$] structures will be referred to as $MeNH_3$-M, where M is the metal cation, likewise [$CH_3CH_2NH_3$][M(HCOO)$_3$] as $EtNH_3$-M, [$(CH_3)_2NH_2$][M(HCOO)$_3$] as Me_2NH_2-M, [$(CH_2)_3NH_2$][M(HCOO)$_3$] as Aze-M, and [$C(NH_2)_3$][M(HCOO)$_3$] as Gua-M. The molecular structures of the different A-site cations are shown in Figure 6.3.

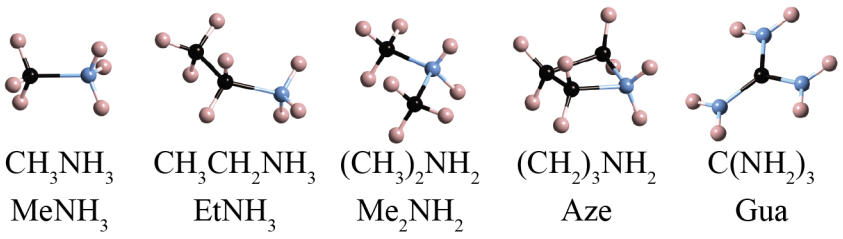

Figure 6.3: Structural representations of the different A-site cations used in this study. The colours represent the different atoms, where blue is N, black is C and pink is H.

Table 6.2: The possible combinations of A-site and metal cations, where the highlighted grey cells indicate the structures used in this investigation. The known crystal structures are associated with a reference, and the dashed cells represent unknown phases. The type of sample obtained from the synthesis is indicated, where cryst. and ppt. represent crystals and powder precipitate, respectively.

A^+	M^{2+}							
	Mg	Mn	Fe	Co	Ni	Cu	Zn	Cd
CH_3NH_3	*Pnma*	*Pnma*	*Pnma*	*Pnma*	–	$P2_1ma$	*Pnma*	*Pnma*
Ref.	here	312	here	here		here	here	here
Sample	ppt.	cryst.	ppt.	ppt.		cryst.	cryst.	ppt.
$CH_3CH_2NH_3$	$Pna2_1$	$Pna2_1$	–	–	–	–	–	–
Ref.	144	312						
Sample		cryst.						
$(CH_3)_2NH_2$	$R\bar{3}c$	$R\bar{3}c$	$R\bar{3}c$	$R\bar{3}c$	$R\bar{3}c$	$C2/c$	$R\bar{3}c$	$R\bar{3}c$
Ref.	325	322/312	59	322	322	326/327	328	329
Sample		cryst.		ppt.		cryst.	cryst.	
$(CH_2)_3NH_2$	–	*Pnma*	–	–	–	*Pnma*	–	–
Ref.		312				330		
Sample		cryst.						
$C(NH_2)_3$	–	*Pnna*	*Pnna*	*Pnna*	*Pnna*	$Pna2_1$	*Pnna*	$R\bar{3}c$
Ref.		313	313	313	313	313	313	here
Sample	ppt.	cryst.	ppt.	cryst.	cryst.	cryst.	cryst.	cryst.

6.2 Experimental details of [A][M(HCOO)$_3$]

6.2.1 Synthesis

The general synthesis procedure for growing single crystals of [A][M(HCOO)$_3$] involves a slow-diffusion reaction. A 5 mL methanol solution of 0.5 M HCOOH and 0.5 M of 'A' were placed at the bottom of a glass vial, and onto this solution 2 mL of methanol was carefully added, followed by layering 8 mL of a 0.10 M metal salt methanol solution.[312] The tube was then sealed and kept undisturbed.

The different 'A' molecules were supplied in 2 M methanol solution, thus 1.25 mL of each 'A' solution was used in the synthesis, while 94.3 μL of formic acid solution ($\geq$ 95%, Sigma-Aldrich)

was employed. The methanol used (anhydrous 99.8%, Sigma-Aldrich) should be as dry as possible due to the competing metal formate dihydrate compounds which can form if water is present. The following solutions or powders were used to obtain different A-site cations in [A][M(HCOO)$_3$]: methylamine (Acros Organics, 2 M solution in methanol), dimethylamine (Aldrich, 2 M solution in methanol), ethylamine (Aldrich, 2 M solution in methanol), azetidine (Aldrich, 98%), and guanidine carbonate (Aldrich, 99%).

For many of the manganese- and zinc-containing metal formates, single crystals would form, while the cobalt and nickel reactions often gave amorphous precipitates, which—after a couple a weeks—transformed to crystalline precipitates. Syntheses containing iron were not so successful due to the propensity for the Fe^{2+} to oxidise to Fe^{3+} in solution. In order to minimise this process, L-ascorbic acid (Sigma, 99.0%) was added to the reaction mixture,[315] in which some crystalline powders of [A][Fe(HCOO)$_3$] were formed but generally there was always a mixture of products.

6.2.2 Variable-temperature single-crystal X-ray diffraction

Variable-temperature SCXRD measurements were performed on Gua-Mn and Gua-Cd using an Agilent technologies SuperNova diffractometer (graphite-monochromated Mo Kα radiation λ = 0.71073 Å) fitted with an Oxford Cryosystems Cryosream 600 open flow cooling device. For Gua-Mn, the crystal was mounted on a glass fibre using nail polish, and diffraction was measured in the 100–300 K temperature range. In particular, the data measurement was started at 300 K, cooled to 100 K, and upon heating from 110 K to 310 K, collecting every 20 K. For Gua-Cd, the crystal was mounted on a glass fibre using araldite and diffraction data were measured at 150, 250, 300 and 450 K. The crystal was heated up to 500 K, but at this temperature only a unit cell was determined as the crystallinity of the sample was greatly reduced. These measurements were carried out with assistance from Dr Amber Thompson.

Data indexing, reduction and absorption corrections were performed using CrysAlisPRO. Structure solution was carried out with SIR92,[266] using the data collected at 100 K for Gua-Mn and 150 K for Gua-Cd. Hydrogen atoms were added geometrically and regularised using standard restraints. Structure refinement against $|F^2|$ was carried out using CRYSTALS.[210] Anisotropic

thermal parameters were refined for all non-H atoms. For Gua-Mn, the 100 K refined model was then used as a starting point for refinement against the 110 K data set. In this way, structure refinements for successive temperature points made use of the final model from the previous data set as a starting point.

6.2.3 Variable-temperature powder X-ray diffraction

Synchrotron powder diffraction data were collected on the I11 beamline at Diamond Light Source ($\lambda = 0.82715$) for the different families of [A][M(HCOO)$_3$]. The samples were loaded into 0.5 mm diameter borosilicate capillaries and were placed on the I11 carousel, allowing the robotic arm to perform sample mounting and changes. The 'Cryostream Plus' attachment on I11 was used to vary the temperature from 300 K to 110 K, and diffraction patterns were collected using the Mythen2 PSD detector. Data collection was initially started at 300 K, and then the sample was cooled to 110 K at a rate of 5 K/min while collecting patterns every ∼10 K. For data collection, two diffraction patterns were measured and subsequently merged for analysis (5 s exposure for each diffraction pattern at two angular orientations offset by 0.25°). Between collections, the shutter was closed in order to minimise radiation damage. At the lowest temperature, the capillary was translated to allow a different part of the sample to be exposed to the X-ray beam, thus minimising radiation damage. The sample was heated back to 300 K at a rate of 6 K/min and diffraction patterns were collected every ∼10 K.

The variable-temperature Rietveld refinements of the series of [A][M(HCOO)$_3$] compounds made use of the existing models in the literature,[59,312,313,317,326,327,331] and were carried out using TOPAS academic version 4.1.[216] New structures were determined for $MeNH_3$-M where M = Mg, Fe, Co, Zn, Cd, and for Gua-Cd; these structures are isostructural to the known $MeNH_3$-Mn and Me_2NH_2-Mn phases, respectively. The structure solution of Gua-Cd used SCXRD in addition to powder data in order to resolve the space group and atomic positions. After refinement of the ambient-temperature structure for all [A][M(HCOO)$_3$] compounds, subsequent diffraction patterns were refined sequentially by using the refinement model from the previous temperature as a starting model. In these sequential refinements, a polynomial background function, lattice constants,

atomic coordinates, a scale factor, and peak shapes were refined. The molecular geometries of the formate anions and the A-site cations were modelled as rigid bodies with translational and rotational degrees of freedom. Soft restraints were applied to the metal–formate bonding. In the case where there was a phase transition, as observed in Me_2NH_2-M, M = Mn, Co, Zn, then the mixture of high-temperature (HT) and low-temperature (LT) phases gave too many parameters for the sequential refinement to be performed. Therefore for these situations, the refinements were performed manually at each temperature.

6.3 Rietveld fits of [A][M(HCOO)$_3$]

Figures D.1–D.8 show representative Rietveld fits for ambient (300 K) and low-temperature diffraction (110 K) for all [A][M(HCOO)$_3$] studied. Considering first the $MeNH_3$-M family, there were no phase changes upon cooling for M = Mg, Mn, Fe, Co, and Zn [Figs. D.1 and D.2]. However, $MeNH_3$-Cd did show a phase transition as it was cooled to 110 K, evident from the extra diffraction peaks [Fig. D.9]. The new LT $MeNH_3$-Cd phase could not be indexed, as the indexing results suggested that there was a coexistence of the ambient and LT phases. The larger cell present in $MeNH_3$-Cd may be the reason for this transition, allowing additional space for the methylammonium to re-orient upon cooling. The $MeNH_3$-Cu phase could not be fitted using the structural model of the other $MeNH_3$-M family; the index of the pattern gave the lattice parameters $a = 8.57397(6)$ Å, $b = 22.92034(18)$ Å, and $c = 8.11783(6)$ Å, which are related to the $MeNH_3$-M lattice parameters by the doubling of the cell along the b-axis [Table 6.1]. The index of this powder pattern suggests a space group symmetry of $P2_1ma$, which would agree well with a symmetry-lowered version of the parent $Pnma$ $MeNH_3$-Mn structure, arising from the Jahn-Teller distortions of the copper formate framework [Fig. D.3]. The large lattice parameters obtained suggest that a coordination polymer has formed (as opposed to a simple salt), but the structure solution of this phase was not possible. Amongst the samples of the $MeNH_3$-M family, it was the $MeNH_3$-Mg and $MeNH_3$-Co phases which formed the additional metal formate dihydrate impurity.

The $EtNH_3$-Mn phase showed unusually high background due to the low sample content present within the capillary [Fig. D.4]. Indeed, upon capillary translation, there was not enough sample to obtain a heating run from 110 K to 300 K.

The Aze-Mn phase exhibited a ferroelastic phase transition at ∼250 K [Fig. D.3]; the symmetry change was from the ambient orthorhombic $Pnma$ to monoclinic $P2_1/n$ at lower temperatures. This transition is associated with the orientational ordering of the azetidinium cation within the $Mn(HCOO)_3$ framework cavities, and has been documented in detail by Ref. 332.

The Me_2NH_2-M phases are well known to exhibit a ferroelectric transition due to the ordering of the dimethylammonium cation, as mentioned previously.[59,317] This transition is evident from the diffraction patterns, which display peak splitting at low temperatures [Fig. D.9]. However, the transitions in Me_2NH_2-M, for M = Mn, Co, and Zn are observed at much lower temperatures than those reported in the literature, and furthermore, the HT phases ($R\bar{3}c$) do not fully convert to the LT ferroelectric phases (Cc) upon cooling [Fig. D.9]. For Me_2NH_2-Mn, the coexistence of HT and LT phases was observed in the temperature range: 159–119 K for the cooling run, and 111–175 K for the heating run, while the reported transition temperature is at 180–190 K.[59,317] The coexistence of HT and LT phases for Me_2NH_2-Co and Me_2NH_2-Zn was observed in the temperature range 111–149 K, but for the heating run only (*cf.* 165 K from Ref. 59 for Me_2NH_2-Co and 156 K from Ref. 331 for Me_2NH_2-Zn). The different experimental conditions, heating/cooling rates, sample type and sample quantity may have all contributed to the differences in transition temperatures between this investigation and reported values (the reported values were determined using dielectric constant and specific heat measurements on single crystals).[59] The diffraction experiments would have to be repeated with a standard and using different heating and cooling rates in order to obtain more conclusive phase transition temperatures.

The Me_2NH_2-Cu structure crystallises in a similar LT-phase to the other Me_2NH_2-M phases but with a centrosymmetric space group ($C2/c$) instead, thus exhibiting antiferroelectric order of the dimethylammonium cations. This structure was originally solved in the non-standard crystal setting ($I2/c$),[326] and later in the conventional $C2/c$ setting.[327] The ambient structure is reported

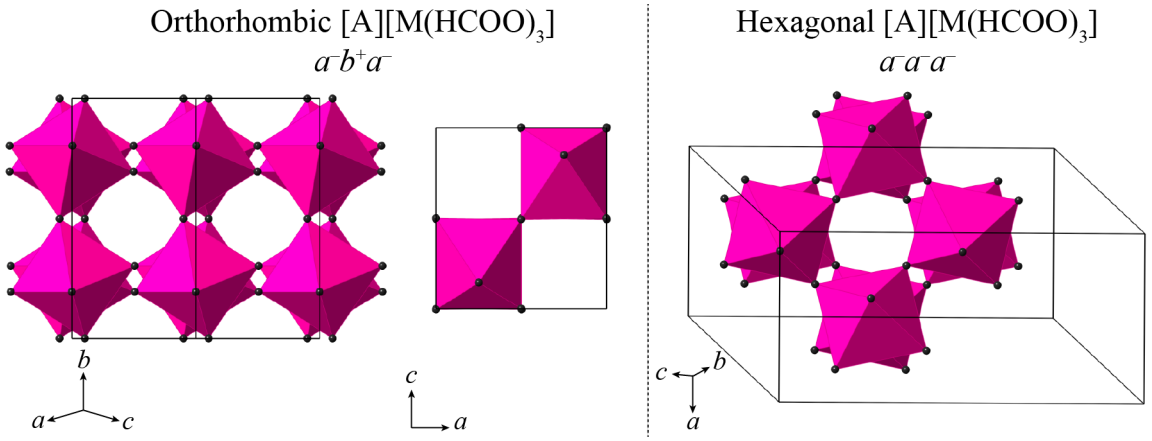

Figure 6.4: The different tilts observed in [A][M(HCOO)$_3$], categorised by their different symmetry. The polyhedra are generated by using metal coordination to the centroid of the formate ligand.

to have the same $R\bar{3}c$ symmetry as the other Me_2NH_2-M members;[333] however, the powder data up to 300 K does not show any evidence for this high-symmetry phase [Fig. D.4].

The Gua-M family was the most successful in crystallising for a wide variety of M cations due to the stronger hydrogen bonding provided by the guanidinium cation.[334] No phase transitions were observed upon cooling for all metal cations: M = Mn, Fe, Co, Ni, Cu, Zn, and Cd [Figs. D.6–D.8]. Only the Gua-Ni powder sample contained the corresponding metal formate dihydrate impurity. Gua-Cd did not crystallise in the same orthorhombic *Pnna* structure as the rest of the Gua-M family. Instead it adopted $R\bar{3}c$ symmetry, with similar atomic coordinates to the ambient phase of Me_2NH_2-Mn [Fig. D.8]. This is driven by the different octahedral tilt system displayed by Gua-Cd compared to the other Gua-M orthorhombic members [Fig. 6.4]. The guanidinium cation—already possessing an inherent three-fold molecular symmetry—does not show any cation disorder as seen in Me_2NH_2-Mn. A new phase is observed for Gua-Mg, which could be fitted using the same *Pnna* structure as Gua-Mn, but with additional peaks unaccounted for [Fig. D.8].

For the subsequent analysis, only lattice parameters and metal cation positions (many of which lie on special positions) are used as the basis for the conclusions of this work. The $MeNH_3$-Cu and Gua-Mg structures are not included in the analysis as they could not be refined using the Rietveld method.

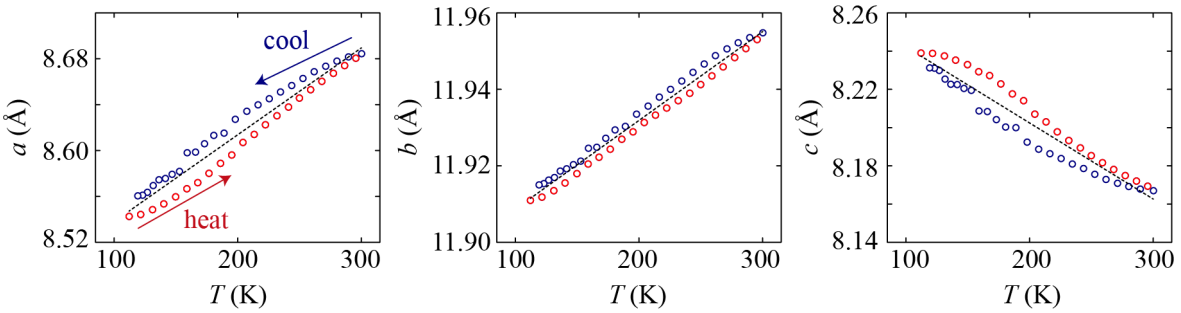

Figure 6.5: Lattice parameter evolutions for $MeNH_3$-Mn. The data collections were started at 300 K and continued during cooling to 110 K (blue circles). The data collection was paused at low temperature, and the capillary translated before performing a heating run (red circles). The dotted black lines indicate the straight-line fits to heating and cooling data for the calculation of the CTEs; the error on the CTEs are based upon these fits to the data.

6.4 Temperature-induced mechanics of [A][M(HCOO)$_3$]

The lattice parameters extracted from the Rietveld fits of heating and cooling data are used to calculate the linear expansivities for all [A][M(HCOO)$_3$] compounds which could be solved; the corresponding errors for the expansivities are determined from these linear fits [Table 6.3]. Figure 6.5 shows the extracted lattice parameter evolutions as a function of temperature for $MeNH_3$-Mn; the corresponding lattice parameter evolutions for all of the compounds are shown in Figures D.10–D.13. The magnitudes of these expansivities vary over the range 54.5–102 MK^{-1} by changing the metal cation within an isostructural group; likewise, by using different A-site cations one accesses the expansivity range 42.2–104 MK^{-1} [Table 6.3]. The origins of these variations with respect to the chemical composition of the framework are the primary focus of this chapter.

For the orthorhombic $MeNH_3$-M and Gua-M families, the CTEs are shown as a function of metal cation size in Figure 6.6. It can be seen that the magnitudes of CTE increase as the metal cation size is also increased. This observation could be due to three effects. Firstly, the strength of the metal–formate coordination bond may be decreasing as larger metal cations are used, which then facilitates the movement of this bond and enhances the framework flexibility. Secondly, the larger unit cells obtained with larger metal cations may allow greater structural freedom. This is found for the IRMOFs series, where the MOFs with the longer linkers exhibit greater magnitudes of NTE, although this phenomenon is also associated with the greater structural freedom of the extended

Table 6.3: The lattice and volume parameters at 300 K, and their corresponding CTEs over the 110–300 K temperature range, calculated using linear fits to data for the [A][M(HCOO)$_3$] studied here. The crystal symmetry is orthorhombic for all compounds apart from those indicated by symbols, where † represents hexagonal, and * indicates monoclinic with a $\beta = 123.8649(6)$ and its CTEs calculated using PASCal.[179] The superscript ^{a} indicates that the CTEs were calculated using the data upon cooling only. For orthorhombic and hexagonal structures: $\alpha_1 = \alpha_a$, $\alpha_2 = \alpha_b$, $\alpha_3 = \alpha_c$. The expansivities for Aze-Mn shown here are determined for an orthorhombic cell throughout the temperature range (see Table D.1 for the principal-axis expansivities of the monoclinic structure).

A^+	M^{2+}	a	α_1	b	α_2	c	α_3	V	α_V
$MeNH_3$	Mg	8.5078(2)	54.5(13)	11.7248(2)	22.1(5)	8.0585(2)	−20.0(5)	803.85(3)	56.7(13)
	Mn	8.68444(6)	88(3)	11.95480(8)	19.5(4)	8.16700(6)	−49(2)	847.904(10)	58.8(15)
	Fe	8.53325(6)	74(2)	11.84574(6)	14.7(4)	8.11808(6)	−25.1(12)	820.597(9)	63.5(16)
	Co	8.39751(9)	68.7(13)	11.71476(10)	22.3(4)	8.10591(9)	−28.8(6)	797.417(14)	62.2(11)
	Zn	8.42480(7)	69(3)	11.71688(8)	18.9(9)	8.10176(7)	−34.6(10)	799.744(11)	54(3)
	Cd	8.84786(3)	102(7)	12.15981(4)	15.0(14)	8.26861(3)	−61(7)	889.606(6)	56(2)
$EtNH_3$	Mn^a	9.08800(14)	44.2(4)	12.04075(13)	33.2(4)	8.21464(11)	4.14(13)	898.90(2)	81.5(9)
Me_2NH_2	Mn†	8.33404(2)	4.5(5)	8.33404(2)	4.5(5)	22.89428(12)	60.4(13)	1377.111(11)	69.4(15)
	Co†	8.19785(3)	10.6(2)	8.19785(3)	10.6(2)	22.22016(13)	46.5(10)	1293.235(11)	67.7(13)
	Cu*	13.67232(13)	−14.3(10)	8.72425(8)	45.7(17)	8.85366(7)	57(3)	876.91(2)	100(5)
	Zn†	8.20056(3)	8.3(9)	8.20056(3)	8.3(9)	22.2607(2)	36.4(4)	1296.453(13)	53(5)
Aze	Mn	8.70053(10)	104(8)	12.31449(7)	15.3(12)	8.86705(11)	−21(6)	950.039(17)	98(4)
Gua	Mn	8.52412(6)	42.2(6)	11.98914(7)	30.0(4)	9.05465(8)	−10.6(3)	925.356(12)	61.5(10)
	Fe	8.42185(12)	33.1(4)	11.87427(13)	31.6(3)	8.92920(15)	−1.5(2)	892.95(2)	63.2(7)
	Co	8.33334(4)	36.6(6)	11.75230(5)	25.8(5)	8.91080(5)	−6.7(2)	872.687(8)	55.8(10)
	Ni	8.26049(9)	27.1(8)	11.65324(10)	22.4(6)	8.82540(11)	3.59(16)	849.546(16)	53.2(15)
	Cu	8.52285(8)	45.9(18)	9.03234(10)	21.4(9)	11.34927(9)	1.4(8)	873.681(15)	69(3)
	Zn	8.34623(4)	30.7(19)	11.73260(5)	21.9(9)	8.92279(5)	−5.3(6)	873.746(7)	47.4(2)
	Cd†	9.19263(3)	−16.8(9)	9.19263(3)	−16.8(9)	19.60561(8)	106(3)	1434.797(10)	71.9(14)

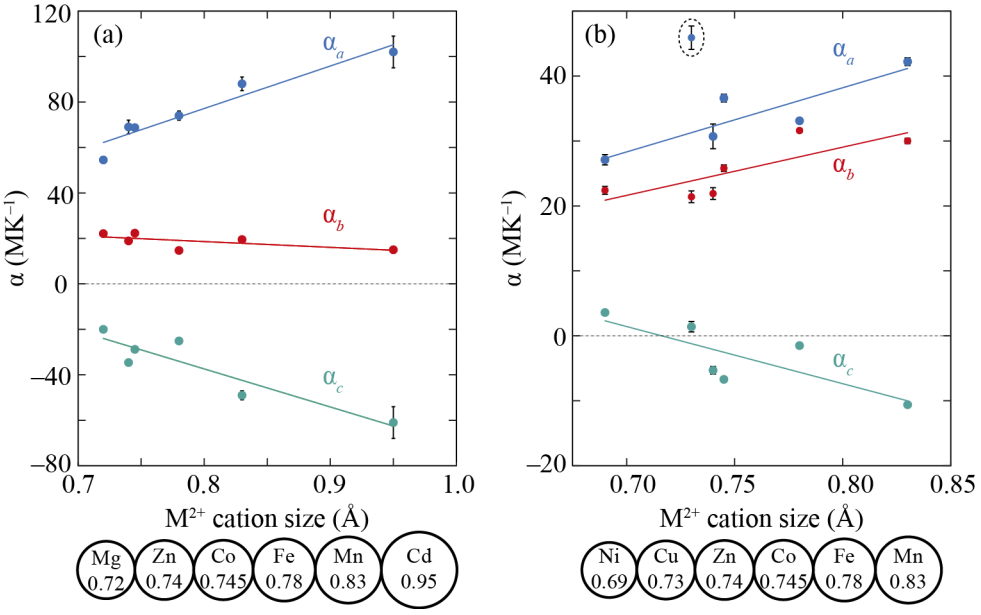

Figure 6.6: CTEs for the *a*-, *b*- and *c*-axes as a function of metal cation size for (a) $MeNH_3$-M and (b) Gua-M families (the hexagonal Gua-Cd is considered later on). The dotted ellipse in (b) indicates α_a of Gua-Cu, which is not included in the visual linear fit of the *a*-axis expansivities. The ionic radii for each M^{2+} is shown in Å, and were obtained from Ref. 19 for octahedrally coordinated high-spin M^{2+} cations.

linkers.[204] Thirdly, the A–formate hydrogen bonding strength, which is affected by the change in metal cation, may also contribute to the framework flexibility. Figure 6.7(a) shows that the U_{iso} thermal parameters for the formate ligand and metal cation in the $MeNH_3$-M family increase as a function of increasing metal size. This supports the theory that weaker coordination bonds are formed, allowing greater displacements of metal and formate ions, a phenomenon that is also found within the variation of NTE magnitude in Prussian Blue analogues (discussed in more detail in Section 6.5).[205] The effect of the metal cation size on the value of T_c in the $[NH_4][M(HCOO)_3]$ and $[(CH_3)_2NH_2][M(HCOO)_3]$ families is shown in Figure 6.7(b). While there is certainly a dependence with the choice of metal cation, there is not a clear trend with metal cation size.

The Gua-Cu structure is now considered in more detail due to its greater-than-anticipated expansivity observed along the *a*-axis [Fig. 6.6(b)]. The Gua-Cu structure (space group $Pna2_1$) is

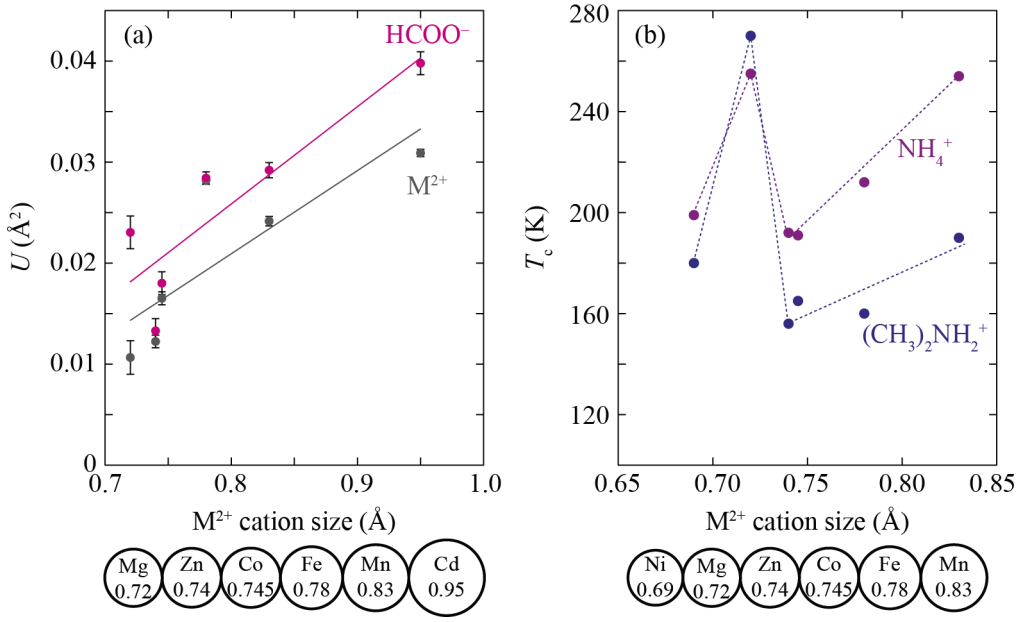

FIGURE 6.7: (a) Variation of the U_{iso} thermal parameter for the metal and formate ions in the $MeNH_3$-M family as a function of metal cation size (U_{iso} values were taken at 300 K for all compounds). (b) Ferroelectric transition T_c for the $[NH_4][M(HCOO)_3]$ and $[(CH_3)_2NH_2][M(HCOO)_3]$ families with M = Ni, Mg, Zn, Co, Fe, and Mn, as a function of metal cation size (T_c values obtained from Refs. 59,144,315,318, 331).

related to the parent Gua-Mn structure by the matrix transformation

$$\begin{bmatrix} \mathbf{a} \\ \mathbf{b} \\ \mathbf{c} \end{bmatrix}_{\text{Gua-Cu}} = \begin{bmatrix} 1 & 0 & 0 \\ 0 & 0 & -1 \\ 0 & 1 & 0 \end{bmatrix} \begin{bmatrix} \mathbf{a} \\ \mathbf{b} \\ \mathbf{c} \end{bmatrix}_{\text{Gua-Mn}} . \tag{6.1}$$

Table 6.3 shows the lattice parameters of Gua-Cu following this transformation, and from this point on, the cell of Gua-Cu will be referred to as the transformed Gua-Cu cell in order to be comparable to the other Gua-M structures. The large expansivity observed along the a-axis may be rationalised by considering the Jahn-Teller distortion present in the **ac**-plane of Gua-Cu [Fig. 6.8(a)]. This distortion gives rise to longer Cu–formate coordination bonds which require less energy for their deformation, thus giving rise to greater structural flexibility in the **ac**-plane of Gua-Cu.

For both $MeNH_3$-M and Gua-M families, the a and c expansivities are anisotropic, such that

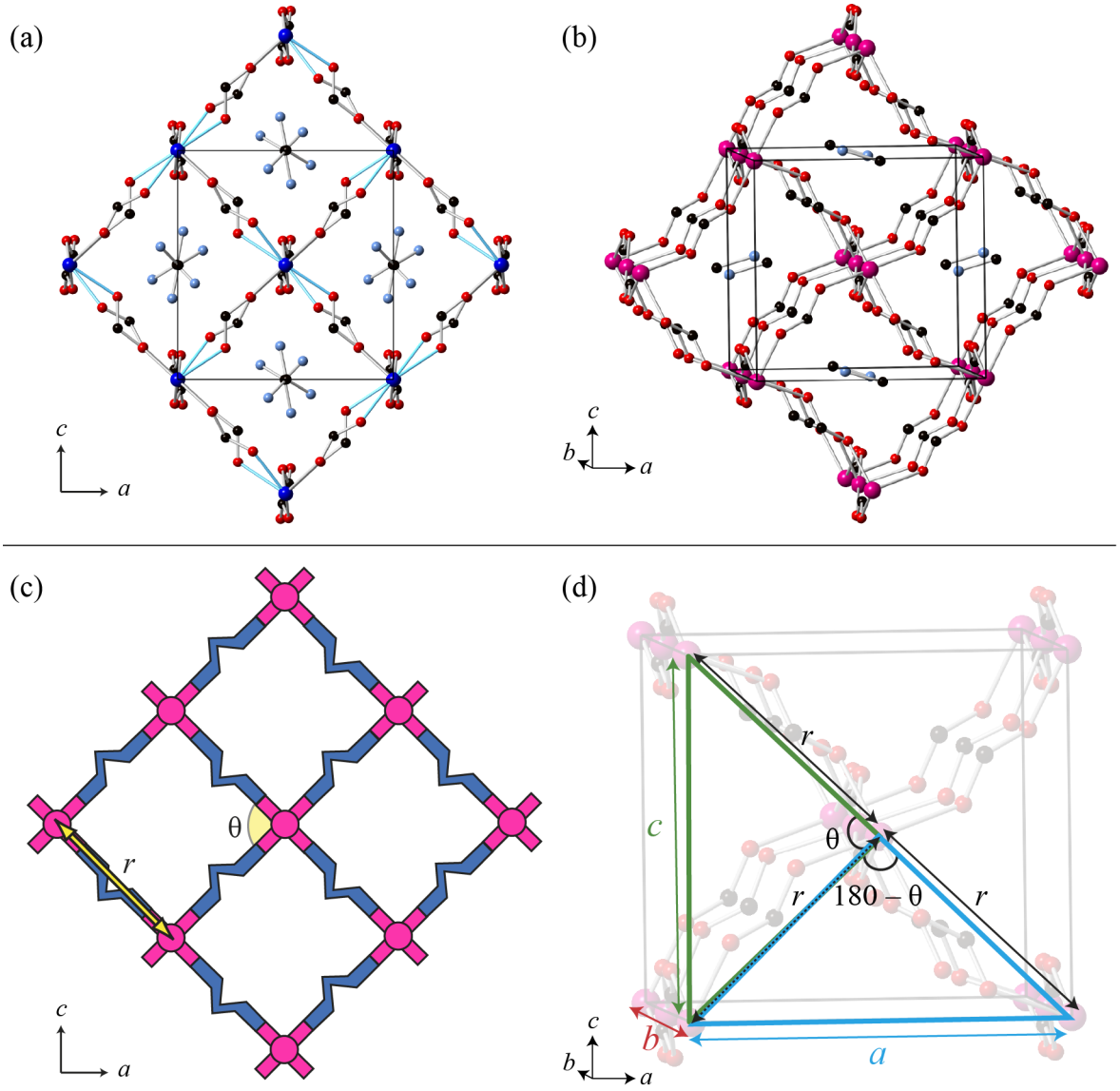

Figure 6.8: (a) Extended structure of Gua-Cu viewed in the **ac**-plane, with its longer bonds highlighted in light blue. (b) Extended structure of $MeNH_3$-Mn, with (d) its XBU relation to the unit cell parameters, allowing simple trigonometry to be used for calculation of the *a*- and *c*-lattice parameters from the XBUs. (c) Schematic wine-rack motif in the **ac**-plane giving rise to the anisotropic expansivities in these directions.

PTE is observed along the *a*-axis and NTE along the *c*-axis (with the exception of Gua-Ni and Gua-Cu). The *b*-axis also shows PTE, although the magnitude is lower than that of α_a; in the case of the $MeNH_3$-M family, α_b is more than half the magnitude of α_a. These CTEs can be directly correlated to the XBUs in the orthorhombic $[A][M(HCOO)_3]$ structures [Fig. 6.8(c,d)]. In the **ac**-plane, the *a*-lattice parameter depends on the change in M$\cdots$M formate-connected centres (*r* distance), and by the corresponding angle connecting the two *r* lengths. Equally the *c*-lattice

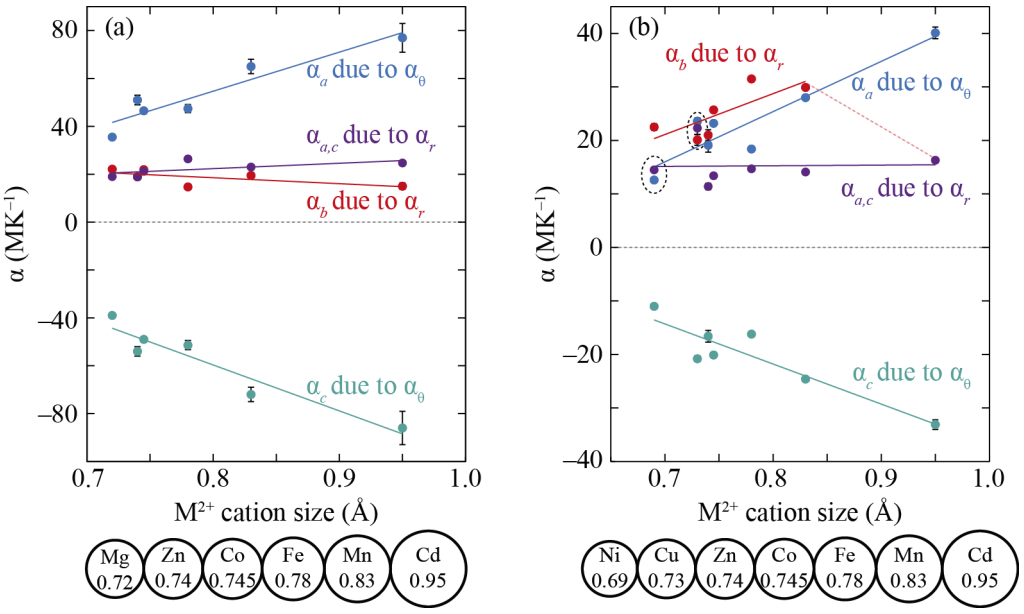

Figure 6.9: Expansivities calculated for lattice parameters in (a) $MeNH_3$-M and (b) Gua-M families by considering only framework angle changes (due to α_θ) and those from only M$\cdots$M distance changes (due to α_r). The dotted ellipses indicate the Gua-Ni and Gua-Cu structures.

parameter depends on the same XBU relationships. Along the b-lattice parameter, two r distances make up its length [Fig. 6.8(d)]. So while the **ac**-plane depends on r and framework angle variation [Fig. 6.8(c)], the b-axis is only affected by r changes.

The lattice parameter evolutions are recalculated based upon these XBUs, and the effects of framework angle and M$\cdots$M distances variations (α_θ and α_r, respectively) are deconvoluted by calculating lattice parameter evolutions which consider purely θ or r changes. From these calculations, it is apparent that framework angle changes dominate the resulting α_a and α_c values in the $MeNH_3$-M family, while the two r XBUs found in the **ac**-plane and along the b-axis show similar expansivities at $\alpha_r \simeq 20\,\mathrm{MK}^{-1}$ [Fig. 6.9(a)]. The combination of a positive α_r and the anisotropic NTE/PTE produced by the θ variation gives rise to greater PTE and reduced NTE responses than if framework hinging was the sole structural change, and thus explains the subtle differences between these calculated CTEs and the observed CTEs in $MeNH_3$-M [Fig. 6.6(a)].

Considering the XBUs in the Gua-M family, the θ variation is much smaller compared to the $MeNH_3$-M family, yet anisotropic lattice parameter evolutions are still observed experimentally when the lattice parameters changes due to α_r in the **ac**-plane are less than those generated

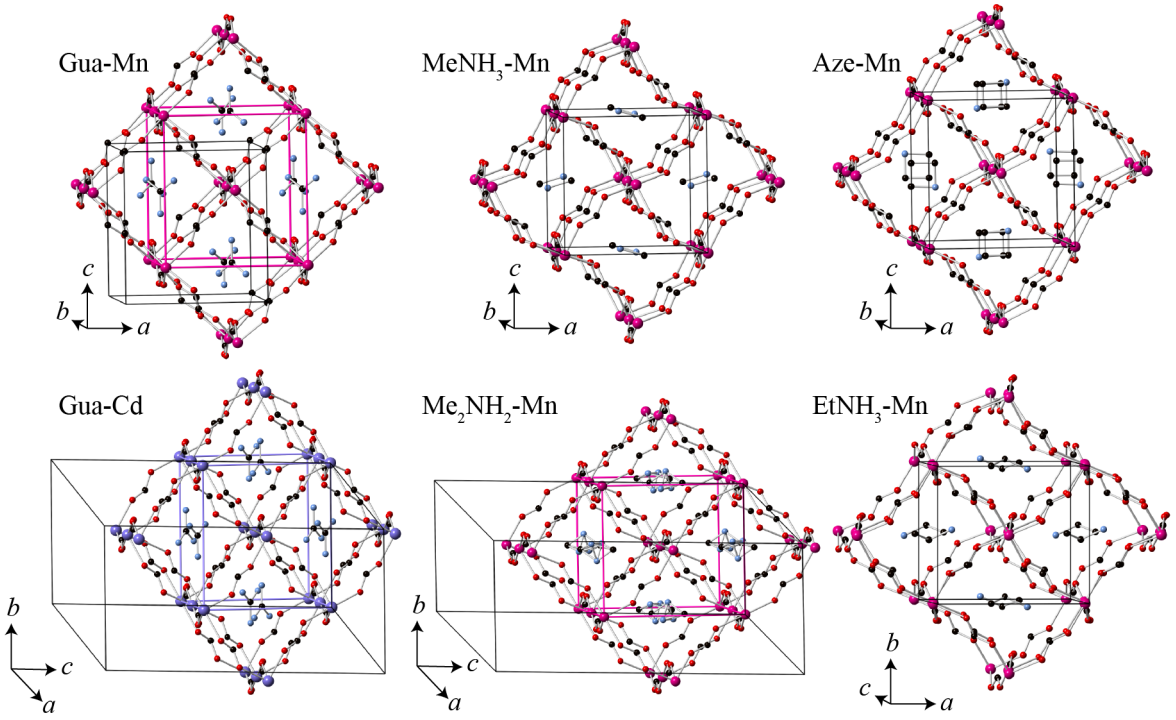

Figure 6.10: Equivalent XBU cells (coloured pink or purple) for all the different structure symmetries observed. In the orthorhombic Aze-Mn, Gua-M and $MeNH_3$-M families, the XBU cell corresponds to the crystallographic unit cell (in black). In $EtNH_3$-Mn, a simple matrix transformation of its crystallographic unit cell gives the XBU cell [Eq. (6.1)]. The XBU cells in Gua-Cd and the Me_2NH_2-M family have a more complex relation to their crystallographic unit cells, thus these are calculated purely for comparison with the other orthorhombic $[A][M(HCOO)_3]$ structures.

from α_θ [Fig. 6.9(b)]. Gua-Ni and Gua-Cu are examples where the r expansion in the **ac**-plane is greater than the framework hinging in the same plane. In the case of Gua-Ni, the small cation size restricts the magnitude of framework hinging, thus giving rise to low α_θ values, while the Jahn-Teller distortion in Gua-Cu allows greater-than-anticipated r expansion. Consequently, these structures exhibit PTE along the c-axis instead of NTE as observed in the other Gua-M members [Fig. 6.6(b)]. While the CTEs of the hexagonal Gua-Cd structure could not be directly compared to those of the Gua-M orthorhombic structures, using the XBUs it is possible to calculate equivalent CTEs [Fig. 6.10]. The higher symmetry in the Gua-Cd structure gives a unique r distance in all directions, hence the apparent decrease in α_b in Figure 6.9(b). The values and expansivities of the XBUs are given for all compounds in Table 6.4.

Table 6.4: XBU parameters r and framework angle θ and their corresponding expansivities. The symbols have the same meaning as those in Table 6.3. The $EtNH_3$-Mn and Gua-Cu have lower crystal symmetries, giving rise to two unique r distances in the **ac**-plane. The average of these is used for the Figures 6.9 and 6.11.

		ac-plane				*b*-axis	
A^+	M^{2+}	r	α_r	θ	α_θ	r	α_r
$MeNH_3$	Mg	5.859	19.0(4)	86.89	−48.8(12)	5.862	22.1(5)
	Mn	5.961	23.0(7)	86.48	−90(4)	5.977	19.5(4)
	Fe	5.889	26.4(7)	87.14	−65(2)	5.923	14.7(4)
	Co	5.836	21.2(4)	87.98	−61.8(15)	5.857	21.9(4)
	Zn	5.844	18.9(13)	87.76	−67(3)	5.858	18.9(9)
	Cd	6.055	24.7(7)	86.12	−107(9)	6.080	15.0(14)
$EtNH_3$	Mn[a]	6.093, 6.157	49(2), 3(2)	84.22	−26.52(15)	6.041	28.5(4)
Me_2NH_2	Mn†	6.141	25.9(6)	85.46	−26.6(7)	6.141	25.9(6)
	Co†	6.010	24.2(5)	86.01	−16.9(4)	6.010	24.2(5)
	Zn†	6.015	18.9(19)	85.95	−13.3(13)	6.015	18.9(19)
$(CH_2)_3NH_2$	Mn	6.211	39.8(11)	91.09	−78(9)	6.157	15.3(1.2)
$C(NH_2)_3$	Mn	6.218	14.1(3)	93.46	−32.1(5)	5.995	29.9(4)
	Fe	6.137	14.7(2)	93.35	−21.2(3)	5.937	31.5(3)
	Co	6.100	13.4(3)	93.84	−26.3(5)	5.876	25.7(5)
	Ni	6.044	14.5(4)	93.79	−14.3(4)	5.827	22.5(6)
	Cu	6.222, 6.197	14.6(16), 30(3)	93.32	−27.1(7)	5.675	20.1(10)
	Zn	6.110	11.4(6)	93.82	−21.7(15)	5.866	21.0(10)
	Cd†	6.233	16.3(3)	95.03	−43.7(13)	6.233	16.3(3)

As already seen in the $MeNH_3$-M and Gua-M families, the use of different A-site cations does modify the extent of framework hinging observed. To investigate this in more detail, the expansivities of the [A][Mn(HCOO)$_3$] compounds with $A^+ = CH_3NH_3$, $CH_3CH_2NH_3$, $(CH_3)_2NH_2$, $(CH_2)_3NH_2$, and $C(NH_2)_3$ were compared. To allow equivalent comparisons (despite differences in symmetry), the unit cells were calculated based upon the XBUs shown in Figure 6.8(d). The relevant cells used for the different compounds are shown in Figure 6.10. The sizes of the different A-site cations were estimated in CRYSTALS by calculating the principal axis lengths and directions of the A-site cation centroid, forming an ellipsoid around all atoms within the A-site cation.[336] The minimum, medium and maximum components of this ellipsoid, as well as its equivalent isotropic sizes are

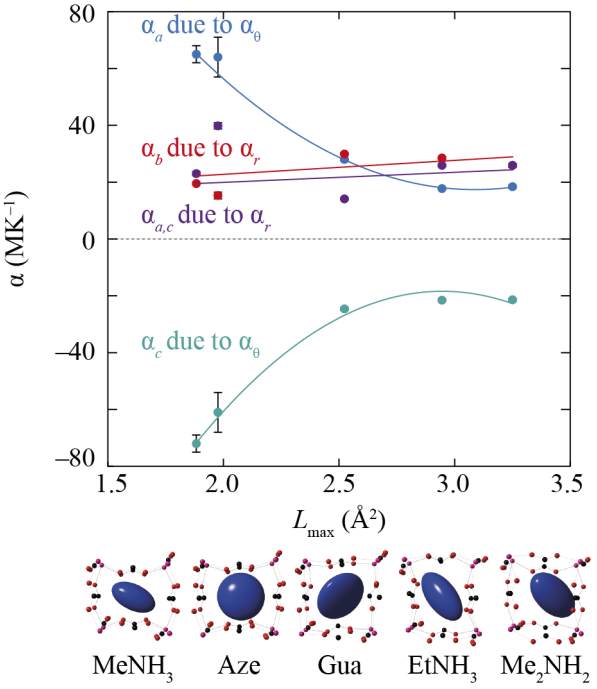

Figure 6.11: Expansivities calculated for $MeNH_3$-Mn, Aze-Mn, Gua-Mn, $EtNH_3$-Mn, and Me_2NH_2-Mn by considering only framework angle changes (due to α_θ) and those arising from only M$\cdots$M distance changes (due to α_r), as a function of effective maximum A-site cation length. The A-site cation ellipse generated from CRYSTALS is shown below the graph for each compound. The values for the Aze-Mn structure were calculated by refining the HT orthorhombic phase throughout the whole temperature range (despite being monoclinic at LT), thus there are large error bars associated with its expansivities. The solid lines are guides to the eye, and exclude the Aze-Mn compound for the fit.

shown in Table 6.5. Figure 6.11 shows the lattice expansivities calculated from the variations in XBU for $MeNH_3$-Mn, $EtNH_3$-Mn, Me_2NH_2-Mn, Aze-Mn, and Gua-Mn as a function of maximum effective length of A-site cation. It can be seen that the framework-hinging lattice expansivities are smallest for the larger A-site cations within the manganese formate framework. This may be due to a steric effect between the A-site cation and the host framework, preventing large changes in framework angles. The different H-bonding strengths of the various A-site cations may also impact the framework flexibility, however, this could not be reliably investigated from the X-ray

Table 6.5: Computed principal axis effective lengths (Å^2) and directions for each of the A-site cation centroids in the host manganese formate, calculated within CRYSTALS. The calculation of the isotropic sizes (Å^2) are as follows: $L_{\text{arith}} = (L_{\text{min}} + L_{\text{med}} + L_{\text{max}})/3$; $L_{\text{geom}} = (L_{\text{min}} \times L_{\text{med}} \times L_{\text{max}})^{\frac{1}{3}}$; $L_{\text{prime}} = (L_{\text{med}} \times (L_{\text{max}}/L_{\text{min}})$.[335] The $L_{\text{max}}/L_{\text{med}}$ term represents the anisotropy in the maximum and medium effective lengths of the A-site cation.

A^+	L_{min}	L_{med}	L_{max}	L_{arith}	L_{geom}	L_{prime}	$L_{\text{max}}/L_{\text{med}}$
CH_3NH_3	0.54	0.57	1.88	1.00	0.84	1.98	3.29
$CH_3CH_2NH_3$	0.65	0.88	2.95	1.49	1.19	3.98	3.36
$(CH_3)_2NH_2$	0.71	1.21	3.25	1.72	1.41	5.54	2.68
$(CH_2)_3NH_2$	0.82	1.92	1.98	1.57	1.46	4.62	1.03
$C(NH_2)_3$	0.48	2.39	2.52	1.80	1.42	12.62	1.06

powder diffraction data. Furthermore, Figure 6.11 shows that the manganese formates containing bulky A-site cations give rise to mechanics which are dominated by α_r; thus negative responses are not likely to be displayed in these structures. This explains the PTE observed along all axes in $EtNH_3$-Mn and Me_2NH_2-Mn, which contain the largest A-site cations [Table 6.3].

6.4.1 Geometric formalism in uniaxial [A][M(HCOO)$_3$]

For the hexagonal symmetry present in the Me_2NH_2-M family and Gua-Cd, the relation between the XBUs and their unit cells is shown in Figure 6.12. In the same way as detailed previously, lattice parameter evolutions were calculated by considering either only framework angle changes or M$\cdots$M distance variations (α due to α_θ or α due to α_r, respectively) [Table 6.6]. From these calculations, it can be seen that changes in framework angles give rise to negative responses in the **ab**-plane for all compounds; yet because of large α_r values in the Me_2NH_2-M compounds, overall PTE is observed in this plane experimentally. As these uniaxial structures contain a unique **r** vector which relates to the lattice vectors **a** and **c** by symmetry considerations, a ρ_{crit} value could be calculated. Even though it is clear that framework angle variation does not dominate the mechanical properties of the Me_2NH_2-M family, the ρ_{crit} evaluated would predict the anisotropy

Table 6.6: Expansivities for Me_2NH_2-Mn, Me_2NH_2-Co, Me_2NH_2-Zn, and Gua-Cd, calculated using linear fits to the original lattice parameter data, and those calculated due to α_θ or due to α_r.

Compound	Axis	α (MK^{-1})		
		original	α due to α_θ	α due to α_r
Me_2NH_2-Mn	a	4.5(5)	−21.3(6)	25.8(6)
	c	60.4(13)	34.3(9)	25.8(6)
Me_2NH_2-Co	a	10.6(2)	−13.6(3)	24.2(5)
	c	46.5(10)	22.3(5)	24.2(5)
Me_2NH_2-Zn	a	8.3(9)	−10.7(10)	18.9(19)
	c	36.4(4)	17.5(17)	18.9(19)
Gua-Cd	a	−16.8(9)	−33.1(9)	16.3(3)
	c	106(3)	89(3)	16.3(3)

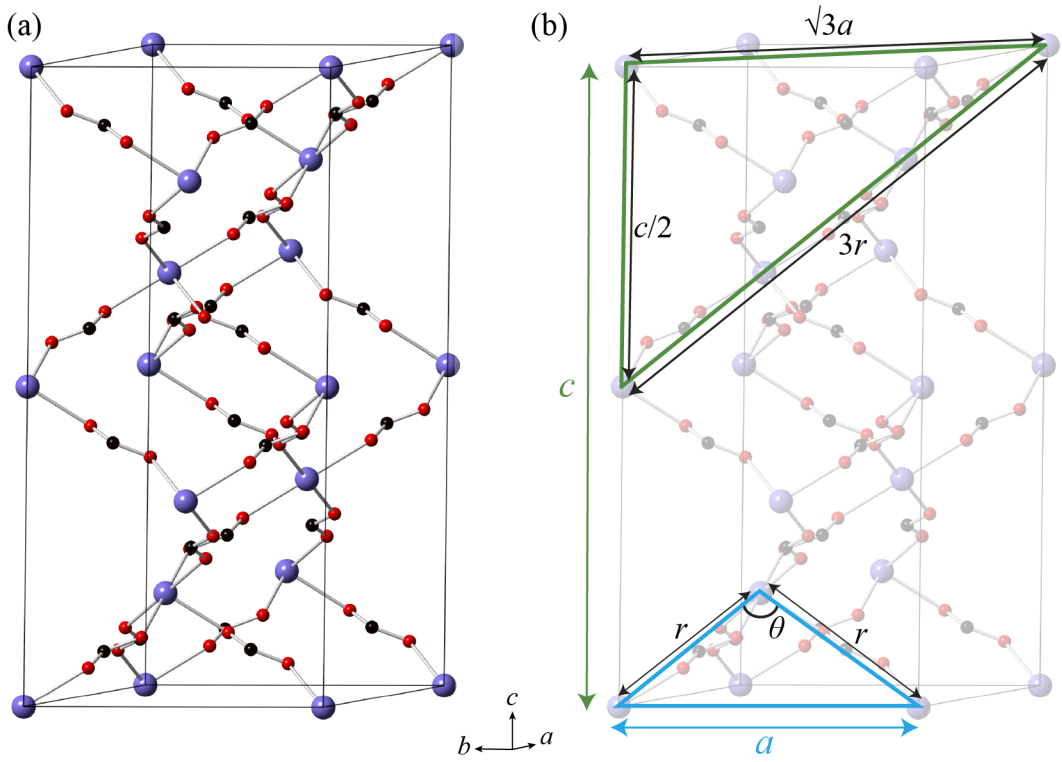

Figure 6.12: (a) Extended structure of Gua-Cd within its unit cell (guanidinium cations and hydrogen atoms are omitted for clarity). (b) The same structural representation of Gua-Cd with its r and framework angle θ XBUs shown with the relevant trigonometric parameters used to calculate the lattice parameters a and c.

seen in lattice expansivities when $\alpha_r = 0$ is implied (*i.e.* α due to α_θ). The method of performing this calculation was introduced in Chapter 5.

The linking **r** vector for both Me_2NH_2-M and Gua-Cd structures is

$$\mathbf{r} = \frac{2}{3}\mathbf{a} + \frac{1}{3}\mathbf{b} - \frac{1}{6}\mathbf{c}. \tag{6.2}$$

Conversion to orthogonal coordinates gives

$$\mathbf{r} = \frac{1}{2}a\mathbf{i} + \frac{\sqrt{3}}{6}a\mathbf{j} - \frac{1}{6}c\mathbf{k}, \tag{6.3}$$

thus the magnitude of the **r** vector is given by

$$r = \sqrt{\frac{a^2}{3} + \frac{c^2}{36}}. \tag{6.4}$$

When $\alpha_r = 0$ is imposed, the following relationship is obtained

$$\begin{aligned} \alpha_r = 0 &= \frac{1}{r}\frac{\mathrm{d}r}{\mathrm{d}T} \\ &= \frac{1}{2r}\left[\frac{a^2}{3}+\frac{c^2}{36}\right]^{-\frac{1}{2}}\left[\frac{2a}{3}\frac{\mathrm{d}a}{\mathrm{d}T}+\frac{2c}{36}\frac{\mathrm{d}c}{\mathrm{d}T}\right] \\ &= \frac{1}{r^2}\left[\frac{a^2\alpha_a}{3}+\frac{c^2\alpha_c}{36}\right], \end{aligned} \tag{6.5}$$

and hence

$$\begin{aligned} \frac{1}{3}a^2\alpha_a + \frac{1}{36}c^2\alpha_c &= 0 \\ \alpha_c &= -\frac{12}{\rho^2}\alpha_a, \end{aligned} \tag{6.6}$$

where $\rho = c/a$. The inequality

$$\alpha_V = \alpha_a\left[2-\frac{12}{\rho^2}\right] > 0 \tag{6.7}$$

gives a $\rho_{\mathrm{crit}} = \sqrt{6} = 2.45$. For the Me_2NH_2-M compounds, their ρ value lies above ρ_{crit} at 2.75 (Me_2NH_2-Mn) and 2.71 (Me_2NH_2-Co and Me_2NH_2-Zn), while that of Gua-Cd is below ρ_{crit} at $\rho = 2.13$. Hence, the negative response is predicted to be along the c-axis for the Me_2NH_2-M structures, and in the **ab**-plane for Gua-Cd. However, while the mechanical anisotropy is correctly predicted for the Gua-Cd expansivities, this is not the case for the Me_2NH_2-M structures, which exhibit negative responses due to framework hinging in the **ab**-plane [Table 6.6].

The reason for the discrepancy between the geometry-predicted mechanical anisotropy and the calculated expansivities due to α_θ for the Me_2NH_2-M family is because their structures become more anisotropic upon heating. In particular, their framework angles diverge away from 90° upon heating (the ideal angle for a 2D wine-rack), while the geometric formalism assumes an increasing regularity in structure with increasing temperature. The two types of 2D framework hinging are drawn schematically to represent increasing regularity (type 1) or divergence (type 2) in framework angles upon increasing temperature [Fig. 6.13]. Normally, an anisotropic framework material would flex in order to increase its volume upon heating, so that greater vibrational motion of the ligands can be accommodated, thus maximising the entropy of the system. In order to ensure

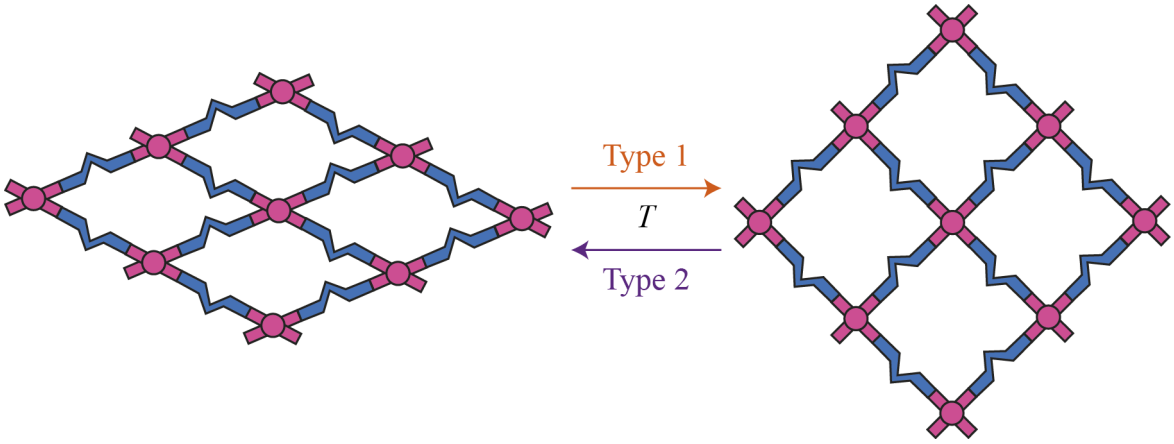

Figure 6.13: Two types of 2D framework hinging observed in [A][M(HCOO)$_3$] materials upon heating. Type 1 gives rise to variation in framework angles towards 90°, whereas type 2 shows further divergence of framework angles away from 90°.

greater entropy of the framework, the separation between connected ligands should be increased towards the maximum separation of 90° (for a 2D wine-rack), as observed in the case of type 1 framework hinging. Yet, for [A][M(HCOO)$_3$] compounds, there is the additional consideration of the A-site cation vibrational motion, which will also contribute to the entropy term. In the Me_2NH_2-M family, the entropy of the system is increased by type 2 framework hinging, because although the ligands are brought closer together by the framework hinging, the anisotropic pore shape allows greater vibrational motion of the A-site cation, which is itself anisotropic in shape. The $MeNH_3$-M family and $EtNH_3$-Mn structure also show type 2 hinging due to their anisotropic A-site cation, as seen by the decrease in framework angle away from 90° upon heating [Table 6.4]. The Gua-M family and Aze-Mn structure contain an isotropic-shaped guanidinium and azetidinium cations, respectively, which consequently favours an isotropic pore shape to maximise their vibrational motions, thus type 1 framework hinging is observed for these compounds. The degree of A-site cation anisotropy is estimated by calculating L_{max}/L_{med} values, where deviations from one have greatest anisotropy and exhibit type 2 framework hinging [Table 6.5].

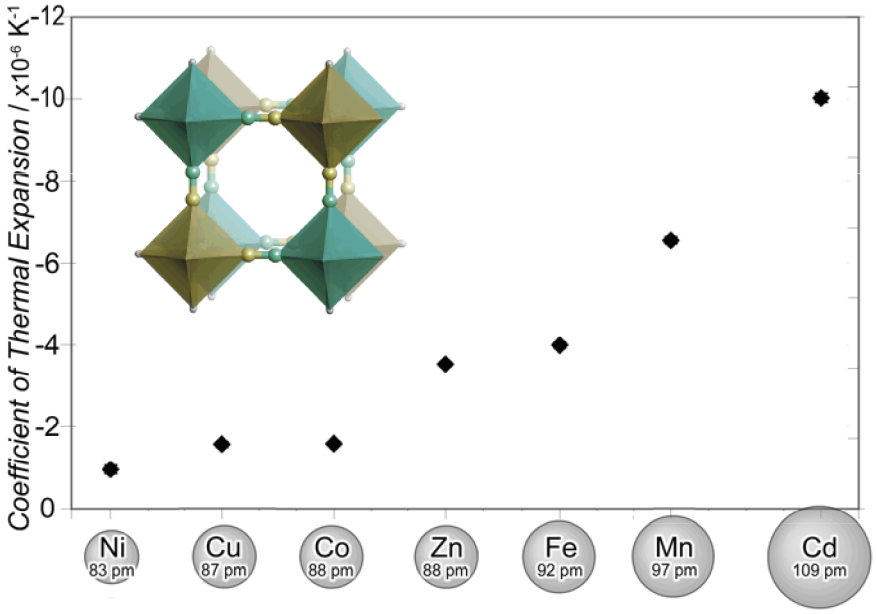

Figure 6.14: CTE for the Prussian Blue analogues of the composition $M^{II}Pt^{IV}(CN)_6$, as a function of M^{2+} crystal radii (in this chapter, ionic radii were quoted instead); figure reproduced from Ref. 205 with permission from the Journal of the American Society, copyright 2006 American Chemical Society.

6.5 Discussion: Composition-dependent mechanics

Three main conclusions can be summarised from this work. Firstly, magnitudes of thermal expansion depend on metal–ligand coordination bond strength, which can be regulated by using metal cations of different ionic radii. Within the cubic Prussian Blue family, the magnitude of isotropic NTE was also found to correlate with ionic radii size [Fig. 6.14].[205] The tetragonal expansivities of the $CuPt(CN)_6$ Prussian Blue were included in the analysis by averaging the NTE and PTE observed: $(\alpha_a+\alpha_a+\alpha_c)/3 = (-5.01 + -5.01 + 5.26)/3 = -1.59\,MK^{-1}$.[205] Therefore, from Figure 6.14 there is no indication that the $CuPt(CN)_6$ structure shows any increased flexibility due to the Jahn-Teller distortion, yet it is evident from the magnitudes of the individual lattice expansivities. The correspondence between CTEs and metal cation size is also found in the series of $LnCo(CN)_6$ materials.[141] Another study on hydrated Prussian Blues shows similar results,[132] however, due to the differing water content within the framework pores, comparison of CTEs becomes more difficult, in particular as water content is seen to affect the magnitudes of expansivities.[129]

A nanoindentation study of the Me_2NH_2-M family indicated that their Young's moduli along

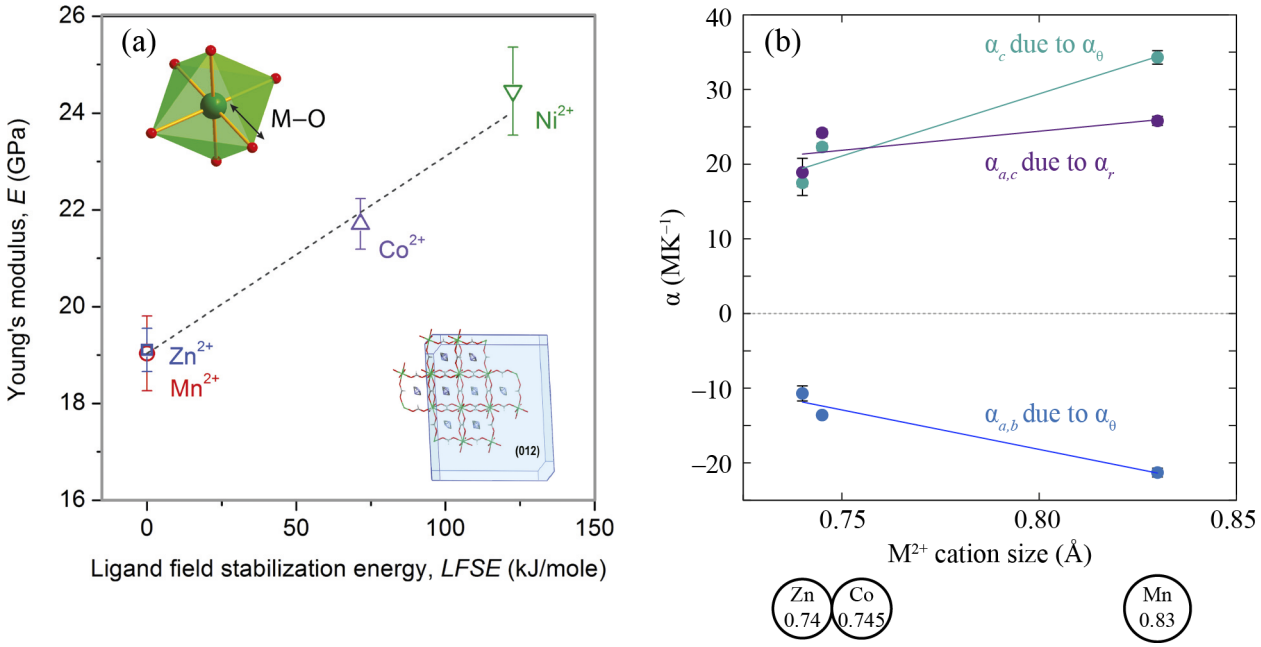

Figure 6.15: (a) Young's moduli for the Me_2NH_2-M structures as a function of LFSE, measured down the {012} plane; figure reproduced from Ref. 195 with permission from the Royal Society of Chemistry. (b) Expansivities calculated for Me_2NH_2-Mn, Me_2NH_2-Co, and Me_2NH_2-Zn by considering only framework angle changes (due to α_θ) and those from r distance variation (due to α_r), as a function of metal cation ionic radii.

the {012} crystal orientation were correlated with ligand field stabilisation energy (LFSE) of the metal(II) cations [Fig. 6.15(a)]. The LFSE magnitude was proposed to represent a resistance against distortion of the MO_6 octahedra in the metal formate framework, and so high values of LFSE consequently gave rise to an increased elastic stiffness of the framework. However, this finding is not supported by the expansivities calculated here for the same family, which instead show a trend with metal cation size [Fig. 6.15(b)]. In particular, Me_2NH_2-Mn and Me_2NH_2-Zn show near identical Young's moduli, while their expansivities due to framework hinging have a factor-of-two difference. A Brillioun scattering study on $[NH_4][Mn(HCOO)_3]$ and $[NH_4][Zn(HCOO)_3]$ supports the importance of ionic radii for mechanical properties, as $[NH_4][Zn(HCOO)_3]$ exhibits stiffer mechanics compared to $[NH_4][Mn(HCOO)_3]$, despite their identical LFSE.[337] The discrepancy could be due to the different experimental methods used; in the case of nanoindentation, a uniaxial force is exerted upon the crystal, while upon temperature variation, an isotropic external stimulus is applied. Although in other studies, there are reports of a correlation between the Young's moduli and metal cation sizes, such as are found in perovskites,[338] and glass materials.[339] Further studies

using both techniques would be needed to confirm the role of LFSE in determining the mechanical properties.

A second conclusion is associated with the correspondence between the A-site cation size and the lattice expansivities, where longer A-site cations cause a significant decrease in the framework hinging observed. Thus these structures are not expected to give rise to anomalous mechanics, such as NTE, instead their mechanics will be dominated by the behaviour of the M–linker–M units. Thirdly, the direction of framework hinging can be switched by using anisotropic-shaped A-site cations within the framework pores. In the case of isotropic A-site cations present, the framework hinging is directed towards a convergence of framework angles (such as 90° for a 2D wine-rack) as would be expected upon heating, whereas there is a divergence of framework angles in the case where anisotropic A-site cations are used.

6.6 Summary

This chapter highlights that metal cation size correlates well with expansivity magnitudes, in particular for the expansivities derived from framework hinging. Specifically, the smallest metal cations, with the strongest metal–ligand bonding, give rise to stiffer frameworks, while the larger metal cations are associated with the more extreme framework flexibility. The A-site cation size is also found to significantly dampen framework hinging when long A-site cations are present within the framework pore. Moreover, the anisotropic-shaped A-site cations direct framework hinging towards diverging framework angles in order to accommodate the A-site cation. This is most likely to be observed only in dense coordination polymers, where the vibrational motion of the anisotropic A-site cation induces the reversal of the mechanical properties of the framework, as predicted through the general geometric formalism. The most readily applicable rule involves that of the metal cations, where simple evaluation of its size within different oxidation states or coordination environments can provide a scale of flexibility within a series of isostructural frameworks.

Chapter 7

Conclusions

The range of structural, chemical and mechanical diversity in coordination polymers is staggering, yet it is the control and understanding of these that is of fundamental importance for the design of functional materials. While there have been great advances in designing chemical and structural aspects of these materials, the design principles concerning the mechanical properties have not been so well established. In this thesis, the link between the mechanical properties and the common structural features of coordination polymers is explored, allowing structure–property relationships to be derived. These rules are applied to many families of coordination polymers in order to rationalise and predict their potential flexibility, rigidity, or anomalous mechanics.

The two main mechanical building units, namely the r distance (ligand-connected M$\cdots$M) and framework angle θ XBUs, were first identified in Ag(mim). The variations of the XBUs to external stimuli were used to comprehend the anomalous mechanical properties of Ag(mim) as well as those of $Zn(CN)_2$-I/II, $Cd(im)_2$, $Zn(ISN)_2$, $InD(BDC)_2$ and a family of $[A][M(HCOO)_3]$ materials. In many of the studied structures, temperature-induced structural changes were dominated by variations in the framework angles, due to their relatively small energy penalties compared to those of r changes ($100\,\mathrm{J\,mol^{-1}}$ *vs* $270\,\mathrm{J\,mol^{-1}}$).[299] Moreover, the direction of framework hinging could be predicted based upon the framework geometries present, using a formalism developed here for uniaxial framework materials.[340] Exceptions to these rules were observed in the denser

[A][M(HCOO)$_3$] structures with large A-site cations, which (*i*) impeded framework hinging mechanisms, giving rise to mechanics dominated largely by r variation, and (*ii*) reversed the direction of framework hinging based upon the shape of the A-site cation within the pores. The pressure- and temperature-induced responses are likely to be related in structures which exhibit coupled strains, as usually occurs in materials with high dimensionality. Yet, upon compression, the framework hinging mechanism is reduced at higher pressures, consequently giving rise to a more subtle interplay between r- and θ-driven mechanics. This leads to NLC–PLC transitions, as observed in Ag(mim) and Zn(CN)$_2$-II, which arise from the increasing compression of r compared to the framework hinging. In the case of Cd(im)$_2$, the decrease in r dominated the mechanics and thus no negative response was observed under pressure.

Design principles for directing flexibility or rigidity in coordination polymers include the following considerations. Firstly, for large anomalous mechanics to be mediated *via* transverse vibrational modes in isotropic materials, or *via* framework hinging in anisotropic structures, an unconstrained topology must be present. In the former structures, unconstrained topologies allow correlation of transverse vibrations using RUMs,[125] and many tetrahedral nets have the right balance between the degrees of translational freedom and the number of bonding constraints to exhibit RUMs.[45] Framework hinging relies on the topological flexibility to allow the framework angle variations in the first instance, and is observed in many wine-rack and honeycomb lattices. To ensure large negative responses from framework hinging, three considerations should be made. Firstly, framework pores which are empty will encourage greater framework angle variations as seen for Zn(ISN)$_2$ and InD(BDC)$_2$. Secondly, the possible steric clashes from framework hinging upon compression should be minimised to ensure prolonged framework angle variation, and hence negative mechanics, at high pressure. This will likely depend on the shape and size of the ligands, as seen in the small framework angle variation in Cd(im)$_2$ compared to Zn(CN)$_2$ under pressure. Thirdly, α_r should be negative, or at the very least have small positive magnitudes, which also applies to K_r. Small variations in r could be engineered by selecting rigid linkers, as found in ligands with aromatic cores or triple/double bonds. Linear M–linker–M binding geometries are particularly important for encouraging NLC or NAC responses, as non-linear geometries are able to readily decrease r by decreasing its binding angle, as found for the compressible Cd–im–Cd units.

Large metal cations, such as strontium, manganese, and indium could be employed to increase framework flexibility, either by greater transverse vibrational motion, or framework hinging. This has been illustrated using DFT calculations, where the MIL-53(Ga) is much more compressible than MIL-53(Al).[14] To enhance magnitudes of anisotropic response, weak interactions between the linkers should be present,[9,10] which can be chemically designed by using metallophilic, $\pi \cdots \pi$ or van der Waals interactions.

Secondly, rigid structures, with small magnitudes of expansivity and compressibility, will depend on a constrained topology. This can be achieved through use of triangular connectivities, tri- or tetra-dentate ligands that bind to different metal coordination environments, giving rise to high metal connectivity. The same considerations as above apply for obtaining small variations in r. Likewise, small metal cations, such as magnesium, nickel or aluminium may be used to further constrain movement of the framework by increasing the coordination bond strength.

In both cases, the topology is the principal directing tool for the mechanical properties.[206] Identifying a suitable topology is therefore important for the appropriate mechanics to be selected, but may not always be possible by simple inspection. Calculation of phonon dispersion curves will prove useful as future work for selecting flexible topologies that have a propensity for exhibiting soft phonon modes, and hence anomalous mechanics. Rigid topologies will be characterised by their higher energy phonons, associated with bond deformations. The identified flexible or rigid topologies will then be likely to exhibit their characteristic mechanical properties regardless of the choice of chemical components, as highlighted by the homologous critical behaviour seen in $Zn(CN)_2$ and $Cd(im)_2$.[159] The changes in chemistry will simply vary the energy scale of the phonons, and allow the magnitudes of the topologically-inherent mechanics to be tuned.

The coexistence of flexibility and structural regularity gives coordination polymers a unique standing for many sophisticated applications.[64] In particular, useful physical properties such as ferroelectricity and piezoelectricity in flexible coordination polymers will allow, in principle, an amplification of these desirable properties if they can be coupled to the large structural changes. The coupling of these physical properties with chemical stimuli can also be envisaged in MOFs, in

which host–guest interactions provide a signal to a ferroelectric MOF.[341] Certainly, the anomalous mechanics present in coordination polymers does make them particularly attractive for precise sensing capabilities of external stimuli such as temperature, chemicals, and especially pressure.

While the investigations in this thesis have considered the mechanical properties of crystals, the next step is to understand bulk mechanical response. In particular, the implementation of coordination polymers within devices is most commonly achieved by using thin-films.[114] Recent work on the mechanical properties of thin-films does show promise for flexible MOFs, as they are able to retain high crystallinity under applied force.[116] Yet the denser frameworks will give additional beneficial properties such as high stiffness, elastic recoveries and abrasion resistance.[116] There will also be great challenges in the incorporation of anisotropic responses within thin films, as the crystallites would need to be aligned. This is likely to be highly dependent on crystal morphology, but it is not something that has yet been investigated.

Finally, for industrial viability, the cost and toxicity of materials play a large role. Now that the important XBUs have been identified, chemical substitutions could be made with greater success in maintaining similar framework mechanics. For example, the large NLC response of $Zn[Au(CN)_2]_2$ relies on the helical aurophilic interactions; if these are replaced by cheaper copper ions, cuprophilic interactions may allow the NLC to be preserved. Similarly, while the use of large cadmium cations does enhance framework flexibility, less toxic cations of even greater size such as calcium and strontium could be employed instead. The same sort of considerations could be also made with the ligands. As long as the topology, and the important weak interactions are maintained, similar mechanical properties in coordination polymers can be expected by chemical substitutions.

Bibliography

[1] B. F. Hoskins and R. Robson. Design and construction of a new class of scaffolding-like materials comprising infinite polymeric frameworks of 3D-linked molecular rods. A reappraisal of the $Zn(CN)_2$ and $Cd(CN)_2$ structures and the synthesis and structure of the diamond-related frameworks $[N(CH_3)_4][CuZn(CN)_4]$ and $Cu[4,4',4'',4'''$-tetracyanotetraphenylmethane$]BF_4{\cdot}xC_6H_5NO_2$. *J. Am. Chem. Soc.*, **112**, 1546–1554 (1990).

[2] R. Robson. A net-based approach to coordination polymers. *J. Chem. Soc., Dalton Trans.*, **21**, 3735–3744 (2000).

[3] O. M. Yaghi, M. O'Keeffe, N. W. Ockwig, H. K. Chae, M. Eddaoudi and J. Kim. Reticular synthesis and the design of new materials. *Nature*, **423**, 705–714 (2003).

[4] S. L. James. Metal–organic frameworks. *Chem. Soc. Rev.*, **32**, 276–288 (2003).

[5] A. K. Cheetham, G. Férey and T. Loiseau. Open-framework inorganic materials. *Angew. Chem. Int. Ed.*, **38**, 3268–3292 (1999).

[6] S. Kitagawa, R. Kitaura and S. Noro. Functional porous coordination polymers. *Angew. Chem. Int. Ed.*, **43**, 2334–2375 (2004).

[7] E. V. Alexandrov, V. A. Blatov, A. V. Kochetkov and D. M. Proserpio. Underlying nets in three-periodic coordination polymers: topology, taxonomy and prediction from a computer-aided analysis of the Cambridge Structural Database. *CrystEngComm*, **13**, 3947–3958 (2011).

[8] A. L. Goodwin, M. Calleja, M. J. Conterio, M. T. Dove, J. S. O. Evans, D. A. Keen, L. Peters and M. G. Tucker. Colossal positive and negative thermal expansion in the framework material $Ag_3[Co(CN)_6]$. *Science*, **319**, 794–797 (2008).

[9] A. B. Cairns, J. Catafesta, C. Levelut, J. Rouquette, A. van der Lee, L. Peters, A. L. Thompson, V. Dmitriev, J. Haines and A. L. Goodwin. Giant negative linear compressibility in zinc dicyanoaurate. *Nat. Mater.*, **12**, 212–216 (2013).

[10] S. Henke, A. Schneemann and R. A. Fischer. Massive anisotropic thermal expansion and thermo-responsive breathing in metal–organic frameworks modulated by linker functionalization. *Adv. Funct. Mater.*, **23**, 5990–5996 (2013).

[11] Y.-S. Wei, K.-J. Chen, P.-Q. Liao, B.-Y. Zhu, R.-B. Lin, H.-L. Zhou, B.-Y. Wang, W. Xue, J.-P. Zhang and X.-M. Chen. Turning on the flexibility of isoreticular porous coordination frameworks for drastically tunable framework breathing and thermal expansion. *Chem. Sci*, **4**, 1539–1546 (2013).

[12] K. W. Chapman, G. J. Halder and P. J. Chupas. Pressure-induced amorphization and porosity modification in a metal–organic framework. *J. Am. Chem. Soc.*, **131**, 17546–17547 (2009).

[13] T. D. Bennett, A. L. Goodwin, M. T. Dove, D. A. Keen, M. G. Tucker, E. R. Barney, A. K. Soper, E. G. Bithell, J.-C. Tan and A. K. Cheetham. Structure and properties of an amorphous metal–organic framework. *Phys. Rev. Lett.*, **104**, 115503 (2010).

[14] A. U. Ortiz, A. Boutin, A. H. Fuchs and F.-X. Coudert. Anisotropic elastic properties of flexible metal–organic frameworks: how soft are soft porous crystals? *Phys. Rev. Lett.*, **109**, 195502 (2012).

[15] K. D. Hammonds, M. T. Dove, A. P. Giddy, V. Heine and B. Winkler. Rigid-unit phonon modes and structural phase transitions in framework silicates. *Am. Mineral.*, **81**, 1057–1079 (1996).

[16] W. Zhong and D. Vanderblit. Competing structural instabilities in cubic perovskites. *Phys. Rev. Lett.*, **74**, 2587–2590 (1995).

[17] R. Mittal, S. L. Chaplot and N. Choudhury. Modeling of anomalous thermodynamic properties using lattice dynamics and inelastic neutron scattering. *Prog. Mater. Sci*, **51**, 211–286 (2006).

[18] V. M. Goldschmidt. Die gesetze der krystallochemie. *Naturwissenschaften*, **14**, 477–485 (1926).

[19] R. D. Shannon. Revised effective ionic radii and systematic studies of interatomic distances in halides and chaleogenides. *Acta Cryst. A*, **32**, 751–767 (1976).

[20] J. P. Attfield. 'A' cation control of perovskite properties. *Cryst. Eng.*, **5**, 427–438 (2002).

[21] G. King and P. M. Woodward. Cation ordering in perovskites. *J. Mater. Chem.*, **20**, 5785–5796 (2010).

[22] M. Azuma, K. Takata, T. Saito, S. Ishiwata, Y. Shimakawa and M. Takano. Designed ferromagnetic, ferroelectric Bi_2NiMnO_6. *J. Am. Chem. Soc.*, **127**, 8889–8892 (2005).

[23] T. Qian, P. Tong, B. Kim, S.-I. Lee, N. Shin, S. Park and B. G. Kim. Enhancement of ferromagnetism by decreasing tolerance factor in electron-doped manganites. *Phys. Rev. B*, **77**, 094423 (2008).

[24] G. Shirane, S. Hoshino and K. Suzuki. X-ray study of the phase transition in lead titanate. *Phys. Rev.*, **80**, 1105–1106 (1950).

[25] G. Shirane, J. D. Axe, J. Harada and J. P. Remeika. Soft ferrelectric modes in lead titanate. *Phys. Rev. B*, **2**, 155–159 (1970).

[26] I. Tomeno, J. A. Fernandez-Baca, K. J. Marty, K. Oka and Y. Tsunoda. Simultaneous softening of acoustic and optical modes in cubic $PbTiO_3$. *Phys. Rev. B*, **86**, 134306 (2012).

[27] S. A. Hayward and E. K. H. Salje. Cubic-tetragonal phase transition in $SrTiO_3$ revisited: landau theory and transition mechanism. *Phase Transit.*, **63**, 501–522 (1999).

[28] J. L. Bettis, M.-H. Whangbo, J. Köhler, A. Bussmann-Holder and A. R. Bishop. Lattice dynamical analogies and differences between $SrTiO_3$ and $EuTiO_3$ revealed by phonon-dispersion relations and double-well potentials. *Phys. Rev. B*, **84**, 184114 (2011).

[29] M. T. Dove. *Structure and Dynamics: An Atomic View of Materials* (Oxford University Press, Oxford, 2003).

[30] M. W. Lufaso and P. M. Woodward. Prediction of the crystal structures of perovskites using the software program SPuDS. *Acta Cryst. B*, **57**, 725–738 (2001).

[31] A. M. Glazer. The classification of tilted octahedra in perovskites. *Acta Cryst. B*, **28**, 3384–3392 (1972).

[32] C. J. Howard and H. T. Stokes. Group-theoretical analysis of octahedral tilting in perovskites. *Acta Cryst. B*, **54**, 782–789 (1998).

[33] B. Magyari-Köpe, L. Vitos, B. Johansson and J. Kollár. Origin of octahedral tilting in orthorhombic perovskites. *Phys. Rev. B*, **66**, 092103 (2002).

[34] R. J. Angel, J. Zhao and N. L. Ross. General rules for predicting phase transitions in perovskites due to octahedral tilting. *Phys. Rev. Lett.*, **95**, 025503 (2005).

[35] N. R. Keskar and J. R. Chelikowsky. Structural properties of nine silica polymorphs. *Phys. Rev. B*, **46**, 1–13 (1992).

[36] M. G. Tucker, M. P. Squires, M. T. Dove and D. A. Keen. Dynamic structural disorder in

cristobalite: neutron total scattering measurement and reverse monte carlo modelling. *J. Phys.: Condens. Matter*, **13**, 403–423 (2001).

[37] P. R. L. Welche, V. Heine and M. T. Dove. Negative thermal expansion in beta-quartz. *Phys. Chem. Miner.*, **26**, 63–77 (1998).

[38] L. Huang and J. Kieffer. Structural origin of negative thermal expansion in high-temperature silica polymorphs. *Phys. Rev. Lett.*, **95**, 215901 (2005).

[39] E. Bourova and P. Richet. Quartz and cristobalite: high-temperature cell parameters and volumes of fusion. *Geophys. Res. Lett.*, **25**, 2333–2336 (1998).

[40] M. A. Carpenter, E. K. H. Salje, A. Graeme-Barber, B. Wruck, M. T. Dove and K. S. Knight. Calibration of excess thermodynamic properties and elastic constant variations associated with the α to β phase transition in quartz. *Am. Mineral.*, **83**, 2–22 (1998).

[41] W. W. Schmahl, I. P. Swainson, M. T. Dove and A. Graeme-Barber. Landau free energy and order parameter behaviour of the α/β phase transition in cristobalite. *Z. Kristallogr.*, **201**, 125–145 (1992).

[42] M. T. Dove. Theory of displacive phase transitions in minerals. *Am. Mineral.*, **82**, 213–244 (1997).

[43] F. S. Tautz, V. Heine, M. T. Dove and X. Chen. Rigid unit modes in the molecular dynamics simulation of quartz and the incommensurate phase transition. *Phys. Chem. Miner.*, **18**, 326–336 (1991).

[44] I. P. Swainson and M. T. Dove. Molecular dynamics simulation of α- and β-cristobalite. *J. Phys.: Condens. Matter*, **7**, 1771–1788 (1995).

[45] M. T. Dove, V. Heine and K. D. Hammonds. Rigid unit modes in framework silicates. *Mineral. Mag.*, **59**, 629–639 (1993).

[46] P. Sollich, V. Heine and M. T. Dove. The Ginzburg interval in soft-mode phase transitions: Consequences of the rigid unit mode picture. *J. Phys.: Condens. Matter*, **6**, 3171–3196 (1994).

[47] A. K. A. Pryde, K. D. Hammonds, M. T. Dove, V. Heine, J. D. Gale and M. C. Warren. Origin of the negative thermal expansion in ZrW_2O_8 and ZrV_2O_7. *J. Phys.: Condens. Matter*, **8**, 10973–10982 (1996).

[48] K. D. Hammonds, M. T. Dove, A. P. Giddy and V. Heine. Crush: a Fortran program for the analysis of the rigid-unit mode spectrum of a framework structure. *Am. Mineral.*, **79**, 1207–1209 (1994).

[49] A. L. Goodwin. Rigid unit modes and intrinsic flexibility in linearly bridged framework structures. *Phys. Rev. B*, **74**, 134302 (2006).

[50] Y. Liu and R. L. Withers. Rigid unit modes (RUMs) of distortion, local crystal chemistry and the inherent displacive flexibility of microporous $AlPO_4$-11. *J. Solid State Chem.*, **172**, 431–437 (2003).

[51] M. T. Dove, M. Gambhir and V. Heine. Anatomy of a structural phase transition: theoretical analysis of the displacive phase transition in quartz and other silicates. *Phys. Chem. Miner.*, **26**, 344–353 (1999).

[52] A. P. Giddy, M. T. Dove, G. S. Pawley and V. Heine. The determination of rigid-unit modes as potential soft modes for displacive phase transitions in framework crystal structures. *Acta Cryst. A*, **49**, 697–703 (1993).

[53] M. T. Dove, K. O. Trachenko, M. G. Tucker and D. A. Keen. Rigid unit modes in framework structures: theory, experiment and applications. *Rev. Mineral. Geochem.*, **39**, 1–33 (2000).

[54] M. T. Dove, A. K. A. Pryde, V. Heine and K. D. Hammonds. Exotic distributions of rigid unit modes in the reciprocal spaces of framework aluminosilicates. *J. Phys.: Condens. Matter*, **19**, 275209 (2007).

[55] G. Férey. Hybrid porous solids: past, present, future. *Chem. Soc. Rev.*, **37**, 191–214 (2008).

[56] C. N. R. Rao, A. K. Cheetham and A. Thirumurugan. Hybrid inorganic–organic materials: a new family in condensed matter physics. *J. Phys.: Condens. Matter*, **20**, 083202 (2008).

[57] Y. Cui, Y. Yue, G. Qian and B. Chen. Luminescent functional metal–organic frameworks. *Chem Rev.*, **112**, 1126–1162 (2012).

[58] W. Zhang and R.-G. Xiong. Ferroelectric metal–organic frameworks. *Chem. Rev.*, **112**, 1163–1195 (2012).

[59] P. Jain, V. Ramachandran, R. J. Clark, H. D. Zhou, B. H. Toby, N. S. Dalal, H. W. Kroto and A. K. Cheetham. Multiferroic behaviour associated with an order–disorder hydrogen bonding transition in metal–organic frameworks (MOFs) with the perovskite ABX_3 architecture. *J. Am. Chem. Soc.*, **131**, 13625–13627 (2009).

[60] E. Coronado and G. Mínguez Espallargas. Dynamic magnetic MOFs. *Chem. Soc. Rev.*, **42**, 1525–1539 (2013).

[61] M. Kurmoo. Magnetic metal–organic frameworks. *Chem. Soc. Rev.*, **38**, 1353–1379 (2009).

[62] O. R. Evans and W. Lin. Crystal engineering of NLO materials based on metal–organic coordination networks. *Acc. Chem. Res.*, **35**, 511–522 (2002).

[63] C. Wang, T. Zhang and W. Lin. Rational synthesis of noncentrosymmetric metal–organic frameworks for second-order nonlinear optics. *Chem. Rev.*, **112**, 1084–1104 (2012).

[64] S. Horike, S. Shimomura and S. Kitagawa. Soft porous crystals. *Nat. Chem.*, **1**, 695–704 (2009).

[65] S. R. Batten, N. R. Champness, X.-M. Chen, J. Garcia-Martinez, S. Kitagawa, L. Öhrström, M. O'Keeffe, M. Paik Suh and J. Reedijk. Terminology of metal–organic frameworks and coordination polymers (IUPAC recommendations 2013). *Pure Appl. Chem.*, **85**, 1715–1724 (2013).

[66] C. S. Cundy and P. A. Cox. The hydrothermal synthesis of zeolites: history and development from the earliest days to the present time. *Chem. Rev.*, **103**, 663–701 (2003).

[67] J. S. Seo, D. Whang, H. Lee, S. I. Jun, J. Oh, Y. J. Jeon and K. Kim. A homochiral metal–organic porous material for enantioselective separation and catalysis. *Nature*, **404**, 982–986 (2000).

[68] S. Hasegawa, S. Horike, R. Matsuda, S. Furukawa, K. Mochizuki, Y. Kinoshita and S. Kitagawa. Three-dimensional porous coordination polymer functionalized with amide groups based on tridentate ligand: Selective sorption and catalysis. *J. Am. Chem. Soc.*, **129**, 2607–2614 (2007).

[69] L. Ma, J. M. Falkowski, C. Abney and W. Lin. A series of isoreticular chiral metal–organic frameworks as a tunable platform for asymmetric catalysis. *Nat. Chem.*, **2**, 838–846 (2010).

[70] P. Horcajada, T. Chalati, C. Serre, B. Gillet, C. Sebrie, T. Baati, J. F. Eubank, D. Heurtaux, P. Clayette, C. Kreuz, J.-S. Chang, Y. K. Hwang, V. Marsaud, P.-N. Bories, L. Cynober, S. Gil, G. Férey, P. Couvreur and R. Gref. Porous metal-organic-framework nanoscale carriers as a potential platform for drug delivery and imaging. *Nat. Mater.*, **9**, 172–178 (2010).

[71] P. Horcajada, C. Serre, G. Maurin, N. A. Ramsahye, F. Balas, M. Vallet-Regí, M. Sebban, F. Taulelle and G. Férey. Flexible porous metal–organic frameworks for a controlled drug delivery. *J. Am. Chem. Soc.*, **130**, 6774–6780 (2008).

[72] R. C. Huxford, K. E. deKrafft, W. S. Boyle, D. Liu and W. Lin. Lipid-coated nanoscale coordination polymers for targeted delivery of antifolates to cancer cells. *Chem. Sci.*, **3**, 198–204 (2012).

[73] L. E. Kreno, K. Leong, O. K. Farha, M. Allendorf, R. P. Van Duyne and J. T. Hupp. Metal–organic framework materials as chemical sensors. *Chem. Rev.*, **112**, 1105–1125 (2012).

[74] Z. Xie, L. Ma, K. E. DeKrafft, A. Jin and W. Lin. Porous phosphorescent coordination polymers for oxygen sensing. *J. Am. Chem. Soc.*, **132**, 922–923 (2010).

[75] M. D. Allendorf, R. J. T. Houk, L. Andruszkiewicz, A. A. Talin, J. Pikarsky, A. Choudhury, K. A. Gall and P. J. Hesketh. Stress-induced chemical detection using flexible metal–organic frameworks. *J. Am. Chem. Soc.*, **130**, 14404–14405 (2008).

[76] M. Eddaoudi, J. Kim, N. Rosi, D. Vodak, J. Wachter, M. O'Keeffe and O. M. Yaghi. Systematic design of pore size and functionality in isoreticular MOFs and their application in methane storage. *Science*, **295**, 469–472 (2002).

[77] L. J. Murray, M. Dincă and J. R. Long. Hydrogen storage in metal–organic frameworks. *Chem. Soc. Rev.*, **38**, 1294–1314 (2009).

[78] K. Sumida, D. L. Rogow, J. A. Mason, T. M. McDonald, E. D. Bloch, Z. R. Herm, T.-H. Bae and J. R. Long. Carbon dioxide capture in metal–organic frameworks. *Chem. Rev.*, **112**, 724–781 (2012).

[79] K. Konstas, T. Osl, Y. Yang, M. Batten, N. Burke, A. J. Hill and M. R. Hill. Methane storage in metal organic frameworks. *J. Mater. Chem.*, **22**, 16698–16708 (2012).

[80] R. Sabouni, H. Kazemian and S. Rohani. Carbon dioxide capturing technologies: a review focusing on metal organic framework materials (MOFs). *Environ. Sci. Pollut. Res.*, **21**, 5427–5449 (2014).

[81] J.-R. Li, J. Sculley and H.-C. Zhou. Metal–organic frameworks for separations. *Chem. Rev.*, **112**, 869–932 (2012).

[82] Z. R. Herm, B. M. Wiers, J. A. Mason, J. M. van Baten, M. R. Hudson, P. Zajdel, C. M. Brown, N. Masciocchi, R. Krishna and J. R. Long. Separation of hexane isomers in a metal–organic framework with triangular channels. *Science*, **340**, 960–964 (2013).

[83] M. I. H. Mohideen, B. Xiao, P. S. Wheatley, A. C. McKinlay, Y. Li, A. M. Z. Slawin, D. W. Aldous, N. F. Cessford, T. Düren, X. Zhao, R. Gill, K. M. Thomas, J. M. Griffin, S. E. Ashbrook and R. E. Morris. Protecting group and switchable pore-discriminating adsorption properties of a hydrophilic–hydrophobic metal–organic framework. *Nat. Chem.*, **3**, 304–310 (2011).

[84] J. F. Keggin and F. D. Miles. Structures and formulae of the Prussian Blues and related compounds. *Nature*, **137**, 577–578 (1936).

[85] H. J. Buser, D. Schwarzenbach, W. Petter and A. Ludi. The crystal structure of Prussian Blue: $Fe_4[Fe(CN)_6]_3 \cdot xH_2O$. *Inorg. Chem.*, **16**, 2704–2710 (1977).

[86] T. R. Cook, Y.-R. Zheng and P. J. Stang. Metal–organic frameworks and self-assembled supramolecular coordination complexes: comparing and contrasting the design, synthesis, and functionality of metal–organic materials. *Chem. Rev.*, **113**, 734–777 (2013).

[87] L. Pauling and P. Pauling. A trireticulate crystal structure: trihydrogen cobalticyanide and trisilver cobalticyanide. *Proc. Natl. Acad. Sci. U.S.A.*, **60**, 362–367 (1968).

[88] B. F. Hoskins, R. Robson and N. V. Y. Scarlett. Six interpenetrating quartz-like nets in the structure of $ZnAu_2(CN)_4$. *Angew. Chem. Int. Ed.*, **34**, 1203–1204 (1995).

[89] J. L. Korčok, M. J. Katz and D. B. Leznoff. Impact of metallophilicity on "colossal" positive and negative thermal expansion in a series of isostructural dicyanometallate coordination polymers. *J. Am. Chem. Soc.*, **131**, 4866–4871 (2009).

[90] S. Surblé, C. Serre, C. Mellot-Draznieks, F. Millange and G. Férey. A new isoreticular class of metal–organic-frameworks with the MIL-88 topology. *Chem. Commun.*, 284–286 (2006).

[91] H. Deng, S. Grunder, K. E. Cordova, C. Valente, H. Furukawa, M. Hmadeh, F. Gándara, A. C. Whalley, Z. Liu, S. Asahina, H. Kazumori, M. O'Keeffe, O. Terasaki, J. F. Stoddart and O. M. Yaghi. Large-pore apertures in a series of metal–organic frameworks. *Science*, **336**, 1018–1023 (2012).

[92] H. Furukawa, K. E. Cordova, M. O'Keeffe and O. M. Yaghi. The chemistry and applications of metal–organic frameworks. *Science*, **341**, 1230444 (2013).

[93] Y.-Q. Tian, C.-X. Cai, X.-M. Ren, C.-Y. Duan, Y. Xu, S. Gao and X.-Z. You. The silica-like extended polymorphism of cobalt(II) imidazolate three-dimensional frameworks: X-ray single-crystal structures and magnetic properties. *Chem. Eur. J.*, **9**, 5673–5685 (2003).

[94] K. S. Park, Z. Ni, A. P. Côté, J. Y. Choi, R. Huang, F. J. Uribe-Romo, H. K. Chae, M. O'Keeffe and O. M. Yaghi. Exceptional chemical and thermal stability of zeolitic imidazolate frameworks. *Proc. Natl. Acad. Sci. U.S.A.*, **103**, 10186–10191 (2006).

[95] R. Banerjee, A. Phan, B. Wang, C. Knobler, H. Furukawa, M. O'Keeffe and O. M. Yaghi. High-throughput synthesis of zeolitic imidazolate frameworks and application to CO_2 capture. *Science*, **319**, 939–943 (2008).

[96] T. D. Bennett, D. A. Keen, J.-C. Tan, E. R. Barney, A. L. Goodwin and A. K. Cheetham. Thermal amorphization of zeolitic imidazolate frameworks. *Angew. Chem. Int. Ed.*, **50**, 3067–3071 (2011).

[97] S. Cao, T. D. Bennett, D. A. Keen, A. L. Goodwin and A. K. Cheetham. Amorphization of the prototypical zeolitic imidazolate framework ZIF-8 by ball-milling. *Chem. Commun.*, **48**, 7805–7807 (2012).

[98] K. W. Chapman, D. F. Sava, G. J. Halder, P. J. Chupas and T. M. Nenoff. Trapping guests within a nanoporous metal–organic framework through pressure-induced amorphization. *J. Am. Chem. Soc.*, **133**, 18583–18585 (2011).

[99] T. D. Bennett, P. J. Saines, D. A. Keen, J.-C. Tan and A. K. Cheetham. Ball-milling-induced amorphization of zeolitic imidazolate frameworks (ZIFs) for the irreversible trapping of iodine. *Chem. Eur. J.*, **19**, 7049–7055 (2013).

[100] K. Uemura, R. Matsuda and S. Kitagawa. Flexible microporous coordination polymers. *J. Solid State Chem.*, **178**, 2420–2429 (2005).

[101] S. Kitagawa and K. Uemura. Dynamic porous properties of coordination polymers inspired by hydrogen bonds. *Chem. Soc. Rev.*, **34**, 109–119 (2005).

[102] G. Férey and C. Serre. Large breathing effects in three-dimensional porous hybrid matter: facts, analyses, rules and consequences. *Chem. Soc. Rev.*, **38**, 1380–1399 (2009).

[103] C. Serre, F. Millange, C. Thouvenot, M. Noguès, G. Marsolier, D. Louër and G. Férey. Very large breathing effect in the first nanoporous chromium(III)-based solids: MIL-53 or $Cr^{III}(OH)\cdot\{O_2C–C_6H_4–CO_2\}\cdot\{HO_2C–C_6H_4–CO_2H\}_x\cdot H_2O_y$. *J. Am. Chem. Soc.*, **124**, 13519–13526 (2002).

[104] F. Millange, N. Guillou, R. I. Walton, J.-M. Grenèche, I. Margiolaki and G. Férey. Effect of the nature of the metal on the breathing steps in MOFs with dynamic frameworks. *Chem. Commun.*, 4732–4734 (2008).

[105] C. Serre, C. Mellot-Draznieks, S. Surblé, N. Audebrand, Y. Filinchuk and G. Férey. Role of solvent-host interactions that lead to very large swelling of hybrid frameworks. *Science*, **315**, 1828–1831 (2007).

[106] M. A. Meyers, A. Mishra and D. J. Benson. Mechanical properties of nanocrystalline materials. *Prog. Mater. Sci.*, **51**, 427–556 (2006).

[107] J.-C. Tan and A. K. Cheetham. Mechanical properties of hybrid inorganic–organic framework materials: establishing fundamental structure–property relationships. *Chem. Soc. Rev.*, **40**, 1059–1080 (2011).

[108] A. Schneemann, S. Henke, I. Schwedler and R. A. Fischer. Targeted manipulation of metal–organic frameworks to direct sorption properties. *ChemPhysChem*, **15**, 823–838 (2014).

[109] S. Shimomura, S. Horike, R. Matsuda and S. Kitagawa. Guest-specific function of a flexible undulating channel in a 7,7,8,8-tetracyano-*p*-quinodimethane dimer-based porous coordination polymer. *J. Am. Chem. Soc.*, **129**, 10990–10991 (2007).

[110] R. H. Baughman, S. Stafström, C. Cui and S. O. Dantas. Materials with negative compressibilities in one or more dimensions. *Science*, **279**, 1522–1524 (1998).

[111] J. J. Purewal, D. Liu, J. Yang, A. Sudik, D. J. Siegel, S. Maurer and U. Müller. Increased volumetric hydrogen uptake of MOF-5 by powder densification. *Int. J. Hydrogen Energ.*, **37**, 2723–2727 (2012).

[112] R. Zacharia, D. Cossement, L. Lafi and R. Chahine. Volumetric hydrogen sorption capacity of monoliths prepared by mechanical densification of MOF-177. *J. Mater. Chem.*, **20**, 2145–2151 (2010).

[113] G. Lu and J. T. Hupp. Metal–organic frameworks as sensors: a ZIF-8 based Fabry–Pérot device as a selective sensor for chemical vapors and gases. *J. Am. Chem. Soc.*, **132**, 7832–7833 (2010).

[114] O. Shekhah, J. Liu, R. A. Fischer and Ch. Wöll. MOF thin films: existing and future applications. *Chem. Soc. Rev.*, **40**, 1081–1106 (2011).

[115] S. Eslava, L. Zhang, S. Esconjauregui, J. Yang, K. Vanstreels, M. R. Baklanov and E. Saiz. Metal–organic framework ZIF-8 films as low-κ dielectrics in microelectronics. *Chem. Mater.*, **25**, 27–33 (2013).

[116] B. Van de Voorde, R. Ameloot, I. Stassen, M. Everaert, D. De Vos and J.-C. Tan. Mechanical properties of electrochemically synthesised metal–organic framework thin films. *J. Mater. Chem. C*, **1**, 7716–7724 (2013).

[117] R. M. Hazen and C. T. Prewitt. Effects of temperature and pressure on interatomic distances in oxygen-based minerals. *Am. Mineral.*, **62**, 309–315 (1977).

[118] J. S. O. Evans. Negative thermal expansion materials. *J. Chem. Soc., Dalton Trans.*, 3317–3326 (1999).

[119] K. Takenaka. Negative thermal expansion materials: technological key for control of thermal expansion. *Sci. Technol. Adv. Mater.*, **13**, 013001 (2012).

[120] E. Grüneisen. *Handbuch Der Physik*, vol. X (Springer, Berlin, 1926).

[121] M. T. Dove. *Introduction to Lattice Dynamics* (Cambridge University Press, Cambridge, 1993).

[122] K. Röttger, A. Endriss, J. Ihringer, S. Doyle and W. F. Kuhs. Lattice constants and thermal expansion of H_2O and D_2O ice I*h* between 10 and 265 K. *Acta Cryst. B*, **50**, 644–648 (1994).

[123] M. Gambhir, M. T. Dove and V. Heine. Rigid unit modes and dynamic disorder: SiO_2 cristobalite and quartz. *Phys. Chem. Miner.*, **26**, 484–495 (1999).

[124] T. A. Mary, J. S. O. Evans, T. Vogt and A. W. Sleight. Negative thermal expansion from 0.3 to 1050 Kelvin in ZrW_2O_8. *Science*, **272**, 90–92 (1996).

[125] A. K. A. Pryde, K. D. Hammonds, M. T. Dove, V. Heine, J. D. Gale and M. C. Warren. Rigid unit modes and the negative thermal expansion in ZrW_2O_8. *Phase Transit.*, **61**, 141–153 (1997).

[126] M. G. Tucker, A. L. Goodwin, M. T. Dove, D. A. Keen, S. A. Wells and J. S. O. Evans. Negative thermal expansion in ZrW_2O_8: mechanisms, rigid unit modes, and neutron total scattering. *Phys. Rev. Lett.*, **95**, 255501 (2005).

[127] K. W. Chapman, P. J. Chupas and C. J. Kepert. Direct observation of a tranverse vibrational mechanism for negative thermal expansion in $Zn(CN)_2$: an atomic pair distribution function analysis. *J. Am. Chem. Soc.*, **127**, 15630–15636 (2005).

[128] A. L. Goodwin and C. J. Kepert. Negative thermal expansion and low-frequency modes in cyanide-bridged framework materials. *Phys. Rev. B*, **71**, 140301 (2005).

[129] A. L. Goodwin, K. W. Chapman and C. J. Kepert. Guest-dependent negative thermal expansion in nanoporous Prussian Blue analogues $M^{II}Pt^{IV}(CN)_6{\cdot}xH_2O$ ($0 \leq x \leq 2$; M = Zn, Cd). *J. Am. Chem. Soc.*, **127**, 17980–17981 (2005).

[130] K. W. Chapman, M. Hagen, C. J. Kepert and P. Manuel. Low energy phonons in the NTE compounds $Zn(CN)_2$ and $ZnPt(CN)_6$. *Physica B*, **385-386**, 60–62 (2006).

[131] A. E. Phillips, A. L. Goodwin, G. J. Halder, P. D. Southon and C. J. Kepert. Nanoporosity and exceptional negative thermal expansion in single-network cadmium cyanide. *Angew. Chem. Int. Ed.*, **47**, 1396–1399 (2008).

[132] S. Adak, L. L. Daemen, M. Hartl, D. Williams, J. Summerhill and H. Nakotte. Thermal expansion in 3d-metal prussian blue analogs—a survey study. *J. Solid State Chem.*, **184**, 2854–2861 (2011).

[133] W. Zhou, H. Wu, T. Yildirim, J. R. Simpson and A. R. Hight Walker. Origin of the exceptional negative thermal expansion in metal-organic framework-5 Zn_4O(1,4-benzenedicarboxylate)$_3$. *Phys. Rev. B*, **78**, 054114 (2008).

[134] Y. Wu, A. Kobayashi, G. J. Halder, V. K. Peterson, K. W. Chapman, N. Lock, P. D. Southon and C. J. Kepert. Negative thermal expansion in the metal–organic framework material Cu_3(1,3,5-benzenetricarboxylate)$_2$. *Angew. Chem.*, **120**, 9061–9064 (2008).

[135] N. Lock, Y. Wu, M. Christensen, L. J. Cameron, V. K. Peterson, A. J. Bridgeman, C. J. Kepert and B. B. Iversen. Elucidating negative thermal expansion in MOF-5. *J. Phys. Chem. C*, **114**, 16181–16186 (2010).

[136] N. Lock, M. Christensen, Y. Wu, V. K. Peterson, M. K. Thomsen, R. O. Piltz, A. J. Ramirez-Cuesta, G. J. McIntyre, K. Norén, R. Kutteh, C. J. Kepert, G. J. Kearley and B. B. Iversen. Scrutinizing negative thermal expansion in MOF-5 by scattering techniques and *ab initio* calculations. *Dalton Trans.*, **42**, 1996–2007 (2013).

[137] J. S. O. Evans, W. I. F. David and A. W. Sleight. Structural investigation of the negative-thermal-expansion material ZrW_2O_8. *Acta Cryst. B*, **55**, 333–340 (1999).

[138] A. Sanson, F. Rocca, G. Dalba, P. Fornasini, R. Grisenti, M. Dapiaggi and G. Artioli. Negative thermal expansion and local dynamics in Cu_2O and Ag_2O. *Phys. Rev. B*, **73**, 214305 (2006).

[139] M. P. Attfield and A. W. Sleight. Strong negative thermal expansion in siliceous faujasite. *Chem. Commun.*, 601–602 (1998).

[140] M. P. Attfield and A. W. Sleight. Exceptional negative thermal expansion in $AlPO_4$-17. *Chem. Mater.*, **10**, 2013–2019 (1998).

[141] S. G. Duyker, V. K. Peterson, G. J. Kearley, A. J. Ramirez-Cuesta and C. J. Kepert. Negative thermal expansion in $LnCo(CN)_6$ (Ln=La, Pr, Sm, Ho, Lu, Y): mechanisms and compositional trends. *Angew. Chem. Int. Ed.*, **52**, 5266–5270 (2013).

[142] A. L. Goodwin, D. A. Keen, M. G. Tucker, M. T. Dove, L. Peters and J. S. O. Evans. Argentophilicity-dependent colossal thermal expansion in extended prussian blue analogues. *J. Am. Chem. Soc*, **130**, 9660–9661 (2008).

[143] A. L. Goodwin, B. J. Kennedy and C. J. Kepert. Thermal expansion matching *via* framework flexibility in zinc dicyanometallates. *J. Am. Chem. Soc.*, **131**, 6334–6335 (2009).

[144] R. Shang, G.-C. Xu, Z.-M. Wang and S. Gao. Phase transitions, prominent dielectric anomalies, and negative thermal expansion in three high thermally stable ammonium magnesium–formate frameworks. *Chem. Eur. J.*, **20**, 1146–1158 (2014).

[145] L. D. DeVries, P. M. Barron, E. P. Hurley, C. Hu and W. Choe. "Nanoscale lattice fence" in a metal–organic framework: interplay between hinged topology and highly anisotropic thermal response. *J. Am. Chem. Soc.*, **133**, 14848–14851 (2011).

[146] C. Yang, X. Wang and M. A. Omary. Crystallographic observation of dynamic gas adsorption sites and thermal expansion in a breathable fluorous metal–organic framework. *Angew. Chem. Int. Ed.*, **48**, 2500–2505 (2009).

[147] I. Grobler, V. J. Smith, P. M. Bhatt, S. A. Herbert and L. J. Barbour. Tunable anisotropic thermal expansion of a porous zinc(II) metal–organic framework. *J. Am. Chem. Soc.*, **135**, 6411–6414 (2013).

[148] H.-L. Zhou, R.-B. Lin, C.-T. He, Y.-B. Zhang, N. Feng, Q. Wang, F. Deng, J.-P. Zhang and X.-M. Chen. Direct visualization of a guest-triggered crystal deformation based on a flexible ultramicroporous framework. *Nat. Commun.*, **4**, 1–8 (2013).

[149] Y. Liu, J.-H. Her, A. Dailly, A. J. Ramirez-Cuesta, D. A. Neumann and C. M. Brown. Reversible structural transition in MIL-53 with large temperature hysteresis. *J. Am. Chem. Soc.*, **130**, 11813–11818 (2008).

[150] A. L. Goodwin. The crystallography of flexibility: local structure and dynamics in framework materials. *Z. Kristallogr. Suppl.*, **30**, 1–11 (2009).

[151] D. C. Wallace. *Thermodynamics of crystals* (John Wiley & Sons, New York, 1972).

[152] R. Gatt and J. N. Grima. Negative compressibility. *Phys. Stat. Sol. RRL*, **2**, 236–238 (2008).

[153] R. Lakes and K. W. Wojciechowski. Negative compressibility, negative Poisson's ratio, and stability. *Phys. Stat. Sol. B*, **245**, 545–551 (2008).

[154] Z. G. Nicolaou and A. E. Motter. Mechanical metamaterials with negative compressibility transitions. *Nat. Mater.*, **11**, 608–613 (2012).

[155] R. E. Newnham. *Properties of Materials* (Oxford University Press, Oxford, 2005).

[156] F. D. Murnaghan. The compressibility of media under extreme pressures. *Proc. Natl. Acad. Sci. U.S.A.*, **30**, 244–247 (1944).

[157] P. Vinet, J. R. Smith, J. Ferrante and J. H. Rose. Temperature effects on the universal equation of state of solids. *Phys. Rev. B*, **35**, 1945–1953 (1987).

[158] K. W. Chapman and P. J. Chupas. Pressure enhancement of negative thermal expansion behavior and induced framework softening in zinc cyanide. *J. Am. Chem. Soc.*, **129**, 10090–10091 (2007).

[159] I. E. Collings, A. B. Cairns, A. L. Thompson, J. E. Parker, C. C. Tang, M. G. Tucker, J. Catafesta, C. Levelut, J. Haines, V. Dmitriev, P. Pattison and A. L. Goodwin. Homologous critical behavior in the molecular frameworks $Zn(CN)_2$ and $Cd(imidazolate)_2$. *J. Am. Chem. Soc.*, **135**, 7610–7620 (2013).

[160] S. H. Lapidus, G. J. Halder, P. J. Chupas and K. W. Chapman. Exploiting high pressures to generate porosity, polymorphism, and lattice expansion in the nonporous molecular framework $Zn(CN)_2$. *J. Am. Chem. Soc*, **135**, 7621–7628 (2013).

[161] C. A. Perottoni and J. A. H. da Jornada. Pressure-induced amorphization and negative thermal expansion in ZrW_2O_8. *Science*, **280**, 886–889 (1998).

[162] Y. H. Hu and L. Zhang. Amorphization of metal-organic framework MOF-5 at unusually low applied pressure. *Phys. Rev. B*, **81**, 174103 (2010).

[163] Y. Lee, T. Vogt, J. A. Hriljac, J. B. Parise and G. Artioli. Pressure-induced volume expansion of zeolites in the natrolite family. *J. Am. Chem. Soc*, **124**, 5466–5475 (2002).

[164] S. A. Moggach, T. D. Bennett and A. K. Cheetham. The effect of pressure on ZIF-8: increasing pore size with pressure and the formation of a high-pressure phase at 1.47 GPa. *Angew. Chem.*, **121**, 7221–7223 (2009).

[165] A. J. Graham, D. R. Allan, A. Muszkiewicz, C. A. Morrison and S. A. Moggach. The effect of high pressure on MOF-5: guest-induced modification of pore size and content at high pressure. *Angew. Chem. Int. Ed.*, **50**, 11138–11141 (2011).

[166] S. A. Hodgson, J. Adamson, S. J. Hunt, M. J. Cliffe, A. B. Cairns, A. L. Thompson, M. G. Tucker, N. P. Funnell and A. L. Goodwin. Negative area compressibility in silver(I) tricyanomethanide. *Chem. Commun.*, **50**, 5264–5266 (2014).

[167] A. E. Aliev, J. Oh, M. E. Kozlov, A. A. Kuznetsov, S. Fang, A. F. Fonseca, R. Ovalle, M. D. Lima, M. H. Haque, Y. N. Gartstein, M. Zhang, A. A. Zakhidov and R. H. Baughman. Giant-stroke, superelastic carbon nanotube aerogel muscles. *Science*, **323**, 1575–1578 (2009).

[168] K. E. Evans and A. Alderson. Auxetic materials: functional materials and structures from lateral thinking! *Adv. Mater.*, **12**, 617–628 (2000).

[169] R. H. Baughman. Avoiding the shrink auxetic. *Nature*, **425**, 667 (2003).

[170] G. N. Greaves, A. L. Greer, R. S. Lakes and T. Rouxel. Poisson's ratio and modern materials. *Nat. Mater.*, **10**, 823–837 (2011).

[171] A. L. Goodwin, D. A. Keen and M. G. Tucker. Large negative linear compressibility of $Ag_3[Co(CN)_6]$. *Proc. Natl. Acad. Sci. U.S.A*, **105**, 18708–18713 (2008).

[172] A. B. Cairns, A. L. Thompson, M. G. Tucker, J. Haines and A. L. Goodwin. Rational design of materials with extreme negative compressibility: selective soft-mode frustration in $KMn[Ag(CN)_2]_3$. *J. Am. Chem. Soc.*, **134**, 4454–4456 (2012).

[173] R. W. Munn. Rôle of the elastic constants in negative thermal expansion of axial solids. *J. Phys. C: Solid State Phys.*, **5**, 535–542 (1972).

[174] G. D. Barerra, J. A. O. Bruno, T. H. K. Barron and N. L. Allan. Negative thermal expansion. *J. Phys.: Condens. Matter*, **17**, R217–R252 (2005).

[175] A. C. Bailey and B. Yates. Anisotropic thermal expansion of pyrolytic graphite at low temperatures. *J. Appl. Phys.*, **41**, 5088–5091 (1970).

[176] P. G. Yot, Q. Ma, J. Haines, Q. Yang, A. Ghoufi, T. Devic, C. Serre, V. Dmitriev, G. Férey, C. Zhong and G. Maurin. Large breathing of the MOF MIL-47(V^{IV}) under mechanical pressure: a joint experimental–modelling exploration. *Chem. Sci.*, **3**, 1100–1104 (2012).

[177] I. Beurroies, M. Boulhout, P. L. Llewellyn, B. Kuchta, G. Férey, C. Serre and R. Denoyel. Using pressure to provoke the structural transition of metal–organic frameworks. *Angew. Chem. Int. Ed.*, **49**, 7526–7529 (2010).

[178] A. Ghoufi, A. Subercaze, Q. Ma, P. G. Yot, Y. Ke, I. Puente-Orench, T. Devic, V. Guillerm, C. Zhong, C. Serre, G. Férey and G. Maurin. Comparative guest, thermal, and mechanical breathing of the porous metal organic framework MIL-53(Cr): a computational exploration supported by experiments. *J. Phys. Chem. C*, **116**, 13289–13295 (2012).

[179] M. J. Cliffe and A. L. Goodwin. PASCal: a principal-axis strain calculator for thermal expansion and compressibility determination. *J. Appl. Cryst.*, **45**, 1321–1329 (2012).

[180] J. S. O. Evans, Z. Hu, J. D. Jorgensen, D. N. Argyriou, S. Short and A. W. Sleight. Compressibility, phase transitions, and oxygen migration in zirconium tungstate, ZrW_2O_8. *Science*, **275**, 61–65 (1997).

[181] Y.-N. Jang, C.-C. Kao, T. Vogt and Y. Lee. Anisotropic compression of a synthetic potassium aluminogermanate zeolite with gismondine topology. *J. Solid State Chem.*, **183**, 2305–2308 (2010).

[182] E. C. Spencer, R. J. Angel, N. L. Ross, B. E. Hanson and J. A. K. Howard. Pressure-induced cooperative bond rearrangement in a zinc imidazolate framework: a high-pressure single-crystal X-ray diffraction study. *J. Am. Chem. Soc.*, **131**, 4022–4026 (2009).

[183] T. D. Bennett, J.-C. Tan, S. A. Moggach, R. Galvelis, C. Mellot-Draznieks, B. A. Reisner, A. Thirumurugan, D. R. Allan and A. K. Cheetham. Mechanical properties of dense zeolitic imidazolate frameworks (ZIFs): a high-pressure X-ray diffraction, nanoindentation and computational study of the zinc framework $Zn(Im)_2$, and its lithium-boron analogue, $LiB(Im)_4$. *Chem. Eur. J.*, **16**, 10684–10690 (2010).

[184] K. W. Chapman, G. J. Halder and P. J. Chupas. Guest-dependent high pressure phenomena in a nanoporous metal–organic framework material. *J. Am. Chem. Soc.*, **130**, 10524–10526 (2008).

[185] W. Li, M. R. Probert, M. Kosa, T. D. Bennett, A. Thirumurugan, R. P. Burwood, M. Parinello, J. A. K. Howard and A. K. Cheetham. Negative linear compressibility of a metal–organic framework. *J. Am. Chem. Soc.*, **134**, 11940–11943 (2012).

[186] E. C. Spencer, N. L. Ross and R. J. Angel. The high pressure behaviour of the 3D copper carbonate framework $\{[Cu(CO_3)_2](CH_6N_3)_2\}_n$. *J. Mater. Chem.*, **22**, 2074–2080 (2012).

[187] L. Glasser. Volume-based thermoelasticity: Compressibility of mineral-structured materials. *J. Phys. Chem. C*, **114**, 11248–11251 (2010).

[188] J. F. Nye. *Physical Properties of Crystals* (Oxford University Press, Oxford, 1985).

[189] Z. Li, M. V. Nevitt and S. Ghose. Elastic constants of sodalite $Na_4Al_3Si_3O_{12}Cl$. *Appl. Phys. Lett.*, **55**, 1730–1731 (1989).

[190] C. Sanchez-Valle, S. V. Sinogeikin, Z. A. D. Lethbridge, R. I. Walton, C. W. Smith, K. E. Evans and J. D. Bass. Brillouin scattering study on the single-crystal elastic properties of natrolite and analcime zeolites. *J. Appl. Phys.*, **98**, 053508 (2005).

[191] J. J. Williams, C. W. Smith, K. E. Evans, Z. A. D. Lethbridge and R. I. Walton. Off-axis elastic properties and the effect of extraframework species on structural flexibility of the NAT-type zeolites: simulations of structure and elastic properties. *Chem. Mater.*, **19**, 2423–2434 (2007).

[192] J.-C. Tan, B. Civalleri, C.-C. Lin, L. Valenzano, R. Galvelis, P.-F. Chen, T. D. Bennett, C. Mellot-Draznieks, C. M. Zicovich-Wilson and A. K. Cheetham. Exceptionally low shear modulus in a prototypical imidazole-based metal–organic framework. *Phys. Rev. Lett.*, **108**, 095502 (2012).

[193] A. U. Ortiz, A. Boutin, A. H. Fuchs and F.-X. Coudert. Metal–organic frameworks with wine-rack motif: what determines their flexibility and elastic properties? *J. Chem. Phys.*, **138**, 174703 (2013).

[194] J.-C. Tan, T. D. Bennett and A. K. Cheetham. Chemical structure, network topology, and porosity effects on the mechanical properties of zeolitic imidazolate frameworks. *Proc. Natl. Acad. Sci. U.S.A*, **107**, 9938–9943 (2010).

[195] J.-C. Tan, P. Jain and A. K. Cheetham. Influence of ligand field stabilization energy on the elastic properties of multiferroic MOFs with the perovskite architecture. *Dalton Trans.*, **41**, 3949–3952 (2012).

[196] C. Sanchez-Valle, Z. A. D. Lethbridge, S. V. Sinogeikin, J. J. Williams, R. I. Walton, K. E. Evans and J. D. Bass. Negative Poisson's ratios in siliceous zeolite MFI-silicalite. *J. Chem. Phys.*, **128**, 184503 (2008).

[197] A. Yeganeh, D. J. Weidner and J. B. Parise. Elasticity of α-cristobalite: a silicon dioxide with a negative Poisson's ratio. *Science*, **257**, 650–652 (1992).

[198] D. F. Bahr, J. A. Reid, W. M. Mook, C. A. Bauer, R. Stumpf, A. J. Skulan, N. R. Moody, B. A. Simmons, M. M. Shindel and M. D. Allendorf. Mechanical properties of cubic zinc carboxylate IRMOF-1 metal–organic framework crystals. *Phys. Rev. B*, **76**, 184106 (2007).

[199] C. Volkringer, T. Loiseau, N. Guillou, G. Férey and E. Elkaïm. Syntheses and structures of the MOF-type series of metal 1,4,5,8,-naphthalenetetracarboxylates $M_2(OH)_2[C_{14}O_8H_4]$ (Al, Ga, In) with infinite *trans*-connected M–OH–M chains (MIL-122). *Solid State Sci.*, **11**, 1507–1512 (2009).

[200] V. Guillerm, F. Ragon, M. Dan-Hardi, T. Devic, M. Vishnuvarthan, B. Campo, A. Vimont, G. Clet, Q. Yang, G. Maurin, G. Férey, A. Vittadini, S. Gross and C. Serre. A series of isoreticular, highly stable, porous zirconium oxide based metal–organic frameworks. *Angew. Chem. Int. Ed.*, **51**, 9267–9271 (2012).

[201] K. Barthelet, J. Marrot, D. Riou and G. Férey. A breathing hybrid organic-inorganic solid with very large pores and high magnetic characteristics. *Angew. Chem. Int. Ed.*, **41**, 281–284 (2002).

[202] A. E. Phillips, G. J. Halder, K. W. Chapman, A. L. Goodwin and C. J. Kepert. Zero thermal expansion in a flexible, stable framework: tetramethylammonium copper(I) zinc(II) cyanide. *J. Am. Chem. Soc.*, **132**, 10–11 (2010).

[203] S. Margadonna, K. Prassides and A. N. Fitch. Zero thermal expansion in a prussian blue analogue. *J. Am. Chem. Soc.*, **126**, 15390–15391 (2004).

[204] D. Dubbeldam, K. S. Walton, D. E. Ellis and R. Q. Snurr. Exceptional negative thermal expansion in isoreticular metal–organic frameworks. *Angew. Chem. Int. Ed.*, **46**, 4496–4499 (2007).

[205] K. W. Chapman, P. J. Chupas and C. J. Kepert. Compositional dependence of negative thermal expansion in the Prussian Blue analogues M(II)Pt(IV)$(CN)_6$ (M = Mn, Fe, Co, Ni, Cu, Zn, Cd). *J. Am. Chem. Soc.*, **128**, 7009–7014 (2006).

[206] L. Sarkisov, R. L. Martin, M. Haranczyk and B. Smit. On the flexibility of metal–organic frameworks. *J. Am. Chem. Soc.*, **136**, 2228–2231 (2014).

[207] C. Giacovazzo, H. L. Monaco, G. Artioli, D. Viterbo, M. Milanesio, G. Ferraris, G. Gilli, P. Gilli, G. Zanotti and M. Catti. *Fundamentals of Crystallography* (Oxford University Press, Oxford, 2011).

[208] V. K. Pecharsky and P. Y. Zavalij. *Fundamentals of Powder Diffraction and Structural Characterization of Materials* (Springer, New York, 2008).

[209] A. J. Blake, W. Clegg, J. M. Cole, J. S. O. Evans, P. Main, S. Parsons and D. J. Watkin. *Crystal Structure Analysis: Principles and Practice* (Oxford University Press, Oxford, 2009).

[210] P. W. Betteridge, J. R. Carruthers, R. I. Cooper, K. Prout and D. J. Watkin. *CRYSTALS* version 12: software for guided crystal structure analysis. *J. Appl. Cryst.*, **36**, 1487 (2003).

[211] S. A. Moggach, D. R. Allan, S. Parsons and J. E. Warren. Incorporation of a new design of backing seat and anvil in a Merrill-Bassett diamond anvil cell. *J. Appl. Cryst.*, **41**, 249–251 (2008).

[212] G. J. Piermarini, S. Block, J. D. Barnett and R. A. Forman. Calibration of pressure-dependence of R1 ruby fluorescence line to 195 Kbar. *J. Appl. Phys.*, **46**, 2774–2780 (1975).

[213] G. S. Pawley. Unit-cell refinement from powder diffraction scans. *J. Appl. Cryst.*, **14**, 357–361 (1981).

[214] H. M. Rietveld. Line profiles of neutron powder-diffraction peaks for structure refinement. *Acta Cryst.*, **22**, 151–152 (1967).

[215] H. M. Rietveld. A profile refinement method for nuclear and magnetic structures. *J. Appl. Cryst.*, **2**, 65–71 (1969).

[216] A. A. Coelho. TOPAS-Academic, version 4.1 (computer software), Coelho Software, Brisbane (2007).

[217] S. P. Thompson, J. E. Parker, J. Potter, T. P. Hill, A. Birt, T. M. Cobb, F. Yuan and C. C. Tang. Beamline I11 at Diamond: a new instrument for high resolution powder diffraction. *Rev. Sci. Instrum.*, **80**, 075107 (2009).

[218] S. P. Thompson, J. E. Parker, J. Marchal, J. Potter, A. Birt, F. Yuan, R. D. Fearn, A. R. Lennie, S. R. Street and C. C. Tang. Fast X-ray powder diffraction on I11 at Diamond. *J. Synchrotron Rad.*, **18**, 637–648 (2011).

[219] A. C. Hannon. Results on disordered materials from the GEneral Materials diffractometer, GEM, at ISIS. *Nucl. Instrum. Meth. A*, **551**, 88–107 (2005).

[220] V. F. Sears. Neutron scattering lengths and cross sections. *Neutron News*, **3**, 29–37 (1992).

[221] W. G. Williams, R. M. Ibberson, P. Day and J. E. Enderby. GEM − General materials diffractometer at ISIS. *Physica B*, **241-243**, 234–236 (1997).

[222] P. Day, J. Enderby, W. Williams, L. Chapon, A. Hannon, P. Radaelli and A. Soper. Scientific reviews: GEM: the general materials diffractometer at ISIS-multibank capabilities for studying crystalline and disordered materials. *Neutron News*, **15**, 19–23 (2004).

[223] ISIS Facility, STFC Rutherford Appleton Laboratory, UK. http://wwwisis2.isis.rl.ac.uk/disordered/gem/gem_home.htm.

[224] S. A. McLain, D. T. Bowron, A. C. Hannon and A. K. Soper. *Gudrun A Computer Program Developed for Analysis of Neutron Diffraction Data.* ISIS Facility, Rutherford-Appleton Laboratory, UK (2012).

[225] D. A. Keen. A comparison of various commonly used correlation functions for describing total scattering. *J. Appl. Cryst.*, **34**, 172–177 (2001).

[226] M. G. Tucker, D. A. Keen, M. T. Dove, A. L. Goodwin and Q. Hui. RMCProfile: Reverse Monte Carlo for polycrystalline materials. *J. Phys.: Condens. Matter*, **19**, 335218 (2007).

[227] R. L. McGreevy and L. Pusztai. Reverse Monte Carlo simulation: a new technique for the determination of disordered structures. *Mol. Simul.*, **1**, 359–367 (1988).

[228] M. G. Tucker, M. T. Dove and D. A. Keen. Application of the reverse Monte Carlo method to crystalline materials. *J. Appl. Cryst.*, **34**, 630–638 (2001).

[229] X. C. Huang, D. Li and X. M. Chen. Solvent-induced supramolecular isomerism in silver(I) 2-methylimidazolate. *CrystEngComm*, **8**, 351–355 (2006).

[230] M. Jansen. Homoatomic d^{10}–d^{10} interactions: their effects on structure and chemical and physical properties. *Angew. Chem. Int. Ed. Engl.*, **26**, 1098–1110 (1987).

[231] M. A. Omary, T. R. Webb, Z. Assefa, G. E. Shankle and H. H. Patterson. Crystal structure, electronic structure, and temperature-dependent Raman spectra of $Tl[Ag(CN)_2]$: evidence for ligand-unsupported argentophilic interactions. *Inorg. Chem.*, **37**, 1380–1386 (1998).

[232] K. Doll, P. Pyykkö and H. Stoll. Closed-shell interaction in silver and gold chlorides. *J. Chem. Phys.*, **109**, 2339–2345 (1998).

[233] L. Pan, E. B. Woodlock, X. T. Wang, K. C. Lam and A. L. Rheingold. Novel silver(I)-organic coordination polymers: conversion of extended structures in the solid state as driven by argentophilic interactions. *Chem. Commun.*, 1762–1763 (2001).

[234] X. Liu, G. C. Guo, M. L. Fu, X. H. Liu, M. S. Wang and J. S. Huang. Three novel silver complexes with ligand-unsupported argentophilic interactions and their luminescent properties. *Inorg. Chem.*, **45**, 3679–3685 (2006).

[235] P. Pyykkö. Relativistic effects in structural chemistry. *Chem. Rev.*, **88**, 563–594 (1988).

[236] K. Singh, J. R. Long and P. Stavropoulos. Ligand-unsupported Metal–Metal (M = Cu, Ag) interactions between closed-shell d^{10} trinuclear systems. *J. Am. Chem. Soc.*, **119**, 2942–2943 (1997).

[237] S. Sculfort and P. Braunstein. Intramolecular d^{10}–d^{10} interactions in heterometallic clusters of the transition metals. *Chem. Soc. Rev.*, **40**, 2741–2760 (2011).

[238] Y. Wang, C.-T. He, Y.-J. Liu, T.-Q. Zhao, X.-M. Lu, W.-X. Zhang, J.-P. Zhang and X.-M. Chen. Copper(I) and silver(I) 2-methylimidazolates: extended isomerism, isomerization, and host–guest properties. *Inorg. Chem.*, **51**, 4772–4778 (2012).

[239] K. Nomiya, K. Tsuda, T. Sudob and M. Oda. Ag(I)–N bond-containing compound showing wide spectra in effective antimicrobial activities: polymeric silver(I) imidazolate. *J. Inorg. Biochem.*, **68**, 39–44 (1997).

[240] M. D. Allendorf, C. A. Bauer, R. K. Bhakta and R. J. T. Houk. Luminescent metal–organic frameworks. *Chem. Soc. Rev.*, **38**, 1330–1352 (2009).

[241] J. Cosier and A. M. Glazer. Oxford Cryosystems CryoStream. *J. Appl. Cryst.*, **19**, 105–107 (1986).

[242] Bruker. *SAINT* (2007). Bruker-AXS Inc., Madison, Wisconsin, USA.

[243] Bruker. *SADABS* (2001). Bruker-AXS Inc., Madison, Wisconsin, USA.

[244] G. M. Sheldrick. A short history of *SHELX*. *Acta Cryst. A*, **64**, 112–122 (2008).

[245] A. Dawson, D. R. Allan, S. Parsons and M. Ruf. Use of a CCD diffractometer in crystal structure determinations at high pressure. *J. Appl. Cryst.*, **37**, 410–416 (2004).

[246] S. Parsons. *SHADE. Program for empirical absorption corrections to high pressure data* (2004).

[247] R. I. Cooper, A. L. Thompson and D. J. Watkin. *CRYSTALS* enhancements: dealing with hydrogen atoms in refinement. *J. Appl. Cryst.*, **43**, 1100–1107 (2010).

[248] A. C. Larson and R. B. Von Dreele. *General Structure Analysis System (GSAS)*. Los Alamos National Laboratory Report LAUR 86-748 (2000).

[249] B. H. Toby. EXPGUI, a graphical user interface for GSAS. *J. Appl. Cryst.*, **34**, 210–213 (2001).

[250] A. Stein, S. W. Keller and T. E. Mallouk. Turning down the heat: design and mechanism in solid-state synthesis. *Science*, **259**, 1558–1564 (1993).

[251] C. M. Che, M. C. Tse, M. C. W. Chan, K. K. Cheung, D. L. Phillips and K. H. Leung. Spectroscopic evidence for argentophilicity in structurally characterized luminescent binuclear silver(I) complexes. *J. Am. Chem. Soc.*, **122**, 2464–2468 (2000).

[252] M. A. Rawashdeh-Omary, M. A. Omary, H. H. Patterson and J. P. Fackler. Excited-state interactions for $[Au(CN)_2^-]_n$ and $[Ag(CN)_2^-]_n$ oligomers in solution. Formation of luminescent gold-gold bonded excimers and exciplexes. *J. Am. Chem. Soc.*, **123**, 11237–11247 (2001).

[253] M. Calleja, A. L. Goodwin and M. T. Dove. Origin of the colossal positive and negative thermal expansion in $Ag_3[Co(CN)_6]$: an *ab initio* density functional theory study. *J. Phys.:*

Condens. Matter, **20**, 255226 (2008).

[254] F. Millange, C. Serre and G. Férey. Synthesis, structure determination and properties of MIL-53as and MIL-53ht: The first Cr^{III} hybrid inorganic–organic molecular solids: $Cr^{III}(OH)\cdot\{O_2C–C_6H_4–CO_2\}\cdot\{HO_2C–C_6H_4–CO_2H\}_x$. *Chem. Commun.*, 822–823 (2002).

[255] P. Serra-Crespo, A. Dikhtiarenko, E. Stavitski, J. Juan-Alcañiz, F. Kapteijn, F.-X. Coudert and J. Gascon. Experimental evidence of negative linear compressibility in the MIL-53 metal–organic framework family. *CrystEngComm*, DOI: 10.1039/c4ce00436a (2014).

[256] S. Scheiner. Comparison of proton transfers in heterodimers and homodimers of NH_3 and OH_2. *J. Chem. Phys.*, **77**, 4039–4050 (1982).

[257] F. Shugam and H. Zhdanov. The crystal structure of cyanides. The structure of $Cd(CN)_2$. *Acta Physiochim. URSS*, **20**, 247–252 (1945).

[258] D. J. Williams, D. E. Partin, F. J. Lincoln, J. Kouvetakis and M. O'Keeffe. The disordered crystal structures of $Zn(CN)_2$ and $Ga(CN)_3$. *J. Solid State Chem.*, **134**, 164–169 (1997).

[259] T. R. Ravindran, A. K. Arora and T. N. Sairam. A spectroscopic resolution of the structure of $Zn(CN)_2$. *J. Raman Spectrosc.*, **38**, 283–287 (2007).

[260] S. J. Hibble, A. M. Chippindale, E. Marelli, S. Kroeker, V. K. Michaelis, B. J. Greer, P. M. Aguiar, E. J. Bilbé, E. R. Barney and A. C. Hannon. Local and average structure in zinc cyanide: toward an understanding of the atomistic origin of negative thermal expansion. *J. Am. Chem. Soc.*, **135**, 16478–16489 (2013).

[261] N. Masciocchi, G. A. Ardizzoia, S. Brenna, F. Castelli, S. Galli, A. Maspero and A. Sironi. Synthesis and *ab-initio* XRPD structure of group 12 imidazolato polymers. *Chem. Commun.*, 2018–2019 (2003).

[262] I. A. Baburin and S. Leoni. Modelling polymorphs of metal–organic frameworks: a systematic study of diamondoid zinc imidazolates. *CrystEngComm*, **12**, 2809–2816 (2010).

[263] Y.-Q. Tian, L. Xu, C. C.-X., J.-C. Wei, Y.-Z. Li and X.-Z. You. Determination of the solvothermal synthesis mechanism of metal imidazolates by X-ray single-crystal studies of photoluminescent cadmium(II) imidazolate and its intermediate involving piperazine. *Eur. J. Inorg. Chem.*, 1039–1044 (2004).

[264] Y.-Q. Tian, S.-Y. Yao, D. Gu, K.-H. Cui, D.-W. Guo, G. Zhang, Z.-X. Chen and D.-Y. Zhao. Cadmium imidazolate frameworks with polymorphism, high thermal stability, and a large surface area. *Chem. Eur. J.*, **16**, 1137–1141 (2010).

[265] CrysAlisPRO. Oxford Diffraction/Agilent Technologies UK Ltd, Yarnton, England.

[266] A. Altomare, G. Cascarano, C. Giacovazzo, A. Guagliardi, M. Burla, G. Polidori and M. Camalli. SIR 92—a program for automatic solution of crystal structures by direct methods. *J. Appl. Cryst.*, **27**, 435 (1994).

[267] A. P. Hammersley. FIT2D: an introduction and overview. ESRF (1997).

[268] A. P. Hammersley, S. O. Svensson, M. Hanfland, A. N. Fitch and D. Häusermann. Two-dimensional detector software: from real detector to idealised image or two-theta scan. *High Press. Res.*, **14**, 235–248 (1996).

[269] S. Klotz, J.-C. Chervin, P. Munsch and G. Le Marchand. Hydrostatic limits of 11 pressure transmitting media. *J. Phys. D: Appl. Phys.*, **42**, 075413 (2009).

[270] A. C. Larson and R. B. Von Dreele. General structure analysis system (GSAS). Los Alamos National Laboratory Report LAUR 86-748 (1994).

[271] J. W. Zwanziger. Phonon dispersion and Grüneisen parameters of zinc dicyanide and cadmium dicyanide from first principles: Origin of negative thermal expansion. *Phys. Rev. B*, **76**, 052102 (2007).

[272] P. Ding, E. J. Liang, Y. Jia and Z. Y. Du. Electronic structure, bonding and phonon modes in the negative thermal expansion materials of $Cd(CN)_2$ and $Zn(CN)_2$. *J. Phys.: Condens. Matter*, **20**, 275224 (2008).

[273] R. Mittal, M. Zbiri, H. Schober, E. Marelli, S. J. Hibble, A. M. Chippindale and S. L. Chaplot. Relationship between phonons and thermal expansion in $Zn(CN)_2$ and $Ni(CN)_2$ from inelastic neutron scattering and *ab initio* calculations. *Phys. Rev. B*, **83**, 024301 (2011).

[274] H. K. Poswal, A. K. Tyagi, A. Lausi, S. K. Deb and M. Sharma. Structural phase transitions in $Zn(CN)_2$ under high pressures. *J. Solid State Chem.*, **182**, 136–140 (2009).

[275] T. R. Ravindran, A. K. Arora, S. Chandra, M. C. Valsakumar and N. V. Chandra Shekar. Soft modes and negative thermal expansion in $Zn(CN)_2$ from raman spectroscopy and first-principles calculations. *Phys. Rev. B*, **76**, 054302 (2007).

[276] J. D. Jorgensen, Z. Hu, S. Teslic, D. N. Argyriou, S. Short, J. S. O. Evans and A. W. Sleight. Pressure-induced cubic-to-orthorhombic phase transition in ZrW_2O_8. *Phys. Rev. B*, **59**, 215–225 (1999).

[277] J. D. Jorgensen, Z. Hu, S. Short, A. W. Sleight and J. S. O. Evans. Pressure-induced cubic-to-orthorhombic phase transformation in the negative thermal expansion material HfW_2O_8. *J. Appl. Phys.*, **89**, 3184–3188 (2001).

[278] C. Lind, D. G. VanDerveer, A. P. Wilkinson, J. Chen, M. T. Vaughan and D. J. Weidner.

New high-pressure form of the negative thermal expansion materials zirconium molybdate and hafnium molybdate. *Chem. Mater.*, **13**, 487–490 (2001).

[279] S. Rath, M. Kunz and R. Miletich. Pressure-induced phase transition in malayaite, $CaSnOSiO_4$. *Am. Mineral.*, **88**, 293–300 (2003).

[280] A. U. Ortiz, A. Boutin, A. H. Fuchs and F.-X. Coudert. Investigating the pressure-induced amorphization of zeolitic imidazolate framework ZIF-8: mechanical instability due to shear mode softening. *J. Phys. Chem. Lett.*, **4**, 1861–1865 (2013).

[281] H. Fang, M. T. Dove, L. H. N. Rimmer and A. J. Misquitta. Simulation study of pressure and temperature dependence of the negative thermal expansion in $Zn(CN)_2$. *Phys. Rev. B*, **88**, 104306 (2013).

[282] L. H. N. Rimmer, M. T. Dove, B. Winkler, D. J. Wilson, K. Refson and A. L. Goodwin. Framework flexibility and the negative thermal expansion mechanism of copper(I) oxide, Cu_2O. *Phys. Rev. B*, **89**, 214115 (2014).

[283] G. K. White. Solids: thermal expansion and contraction. *Contemp. Phys.*, **34**, 193–204 (1993).

[284] Y. Liu, L. Ni, Z. Ren, G. Xu, C. Song and G. Han. Negative pressure induced ferroelectric phase transition in rutile TiO_2. *J. Phys.: Condens. Matter*, **21**, 275901 (2009).

[285] S. M. Stishov and S. V. Popova. A new modification of silica. *Geokhimiya*, **10**, 837–839 (1961).

[286] N. Gaspar, X. J. Ren, C. W. Smith, J. N. Grima and K. E. Evans. Novel honeycombs with auxetic behaviour. *Acta Mater.*, **53**, 2439–2445 (2005).

[287] W. Miller, D. S. Mackenzie, C. W. Smith and K. E. Evans. A generalised scale-independent mechanism for tailoring of thermal expansivity: positive and negative. *Mech. Mater.*, **40**, 351–361 (2008).

[288] J. N. Grima, D. Attard, R. Caruana-Gauci and R. Gatt. Negative linear compressibility of hexagonal honeycombs and related systems. *Scripta Mater.*, **65**, 565–568 (2011).

[289] J. C. A. Elipe and A. D. Lantada. Comparative study of auxetic geometries by means of computer-aided design and engineering. *Smart Mater. Struct.*, **21**, 105004 (2012).

[290] D. L. Barnes, W. Miller, K. E. Evans and A. Marmier. Modelling negative linear compressibility in tetragonal beam structures. *Mech. Mater.*, **46**, 123–128 (2012).

[291] J. N. Grima, D. Attard and R. Gatt. Truss-type systems exhibiting negative compressibility. *Phys. Stat. Sol. B*, **245**, 2405–2414 (2008).

[292] J. Schwerdtfeger, F. Wein, G. Leugering, R. F. Singer, C. Körner, M. Stingl and F. Schury. Design of auxetic structures *via* mathematical optimization. *Adv. Mater.*, **23**, 2650–2654 (2011).

[293] J. N. Grima, R. Caruana-Gauci, D. Attard and R. Gatt. Three-dimensional cellular structures with negative Poisson's ratio and negative compressibility properties. *Proc. R. Soc. A*, **468**, 3121–3138 (2012).

[294] T.-C. Lim. Negative thermal expansion structures constructed from positive thermal expansion trusses. *J. Mater. Sci.*, **47**, 368–373 (2012).

[295] J. Sun, L. Weng, Y. Zhou, J. Chen, Z. Chen, Z. Liu and D. Zhao. QMOF-1 and QMOF-2: three-dimensional metal–organic open frameworks with a quartzlike topology. *Angew. Chem. Int. Ed.*, **41**, 4471–4473 (2002).

[296] Y. Wu, D. Li, F. Fu, L. Tang, J. Wang and X. G. Yang. Microporous 3-D chiral metal-organic framework with a quartzlike topology based on an achiral building unit. *J. Coord. Chem.*, **62**, 2665–2674 (2009).

[297] R. E. Morris and X. Bu. Induction of chiral porous solids containing only achiral building blocks. *Nat. Chem.*, **2**, 353–361 (2010).

[298] I. E. Collings, M. G. Tucker, D. A. Keen and A. L. Goodwin. Static disorder and local structure in zinc(II) isonicotinate, a quartz-like metal-organic framework. *Z. Kristallogr.*, **227**, 313–320 (2012).

[299] J. M. Ogborn, I. E. Collings, S. A. Moggach, A. L. Thompson and A. L. Goodwin. Supramolecular mechanics in a metal–organic framework. *Chem. Sci.*, **3**, 3011–3017 (2012).

[300] D. Das, T. Jacobs and L. J. Barbour. Exceptionally large positive and negative anisotropic thermal expansion of an organic crystalline material. *Nat. Mater.*, **9**, 36–39 (2010).

[301] S. J. Hibble, A. M. Chippindale, A. H. Pohl and A. C. Hannon. Surprises from a simple material—the structure and properties of nickel cyanide. *Angew. Chem. Int. Ed.*, **46**, 7116–7118 (2007).

[302] D. A. Woodcock, P. Lightfoot, P. A. Wright, L. A. Villaescusa, M.-J. Dìaz-Cabañas and M. A. Camblor. Strong negative thermal expansion in the siliceous zeolites ITQ-1, ITQ-3 and SSZ-23. *J. Mater. Chem.*, **9**, 349–351 (1999).

[303] Z. Wang, B. Zhang, K. Inoue, H. Fujiwara, T. Otsuka, H. Kobayashi and M. Kurmoo. Occurrence of a rare $4^9.6^6$ structural topology, chirality, and weak ferromagnetism in the $[NH_4][M^{II}(HCOO)_3]$ (M = Mn, Co, Ni) frameworks. *Inorg. Chem.*, **46**, 437–445 (2007).

[304] C. Mellot-Draznieks, C. Serre, S. Surblé, N. Audebrand and G. Férey. Very large swelling in hybrid frameworks: a combined computational and powder diffraction study. *J. Am. Chem. Soc.*, **127**, 16273–16278 (2005).

[305] L. Carlucci, G. Ciani, D. M. Proserpio and A. Sironi. Interpenetrating Diamondoid Frameworks. *J. Chem. Soc., Chem. Commun.*, 2755–2756 (1994).

[306] L. R. MacGillivray, S. Subramanian and M. J. Zaworotko. Interwoven two- and three-dimensional coordination polymers through self-assembly of Cu^{I} cations with linear bidentate ligands. *J. Chem. Soc., Chem. Commun.*, 1325–1326 (1994).

[307] J. Zhang, S. Chen and X. Bu. Multiple functions of ionic liquids in the synthesis of three-dimensional low-connectivity homochiral and achiral frameworks. *Angew. Chem. Int. Ed.*, **47**, 5434–5437 (2008).

[308] T. Otieno, S. J. Rettig, R. C. Thompson and J. Trotter. Complex polymeric cations of copper(I) with graphite- and diamond-related lattices: crystal structures of poly-tris(μ-2,5-dimethylpyrazine)dicopper(I) hexafluorophosphate and poly-bis(μ-2,5-dimethylpyrazine)copper(I) hexafluorophosphate. *Inorg. Chem.*, **32**, 1607–1611 (1993).

[309] L. Ma, Y.-C. Qiu, G. Peng, J.-B. Cai and H. Deng. *In Situ* tetrazole ligand synthesis of two-fold interpenetrating zinc coordination frameworks. *Eur. J. Inorg. Chem.*, **2011**, 3446–3453 (2011).

[310] N. Masciocchi, S. Galli, A. Sironi, E. Cariati, M. A. Galindo, E. Barea, M. A. Romero, J. M. Salas, J. A. R. Navarro and F. Santoyo-González. Tuning the structural and magnetic properties of thermally robust coordination polymers. *Inorg. Chem.*, **45**, 7612–7620 (2006).

[311] J. Zhang, T. Wu, C. Zhou, S. Chen, P. Feng and X. Bu. Zeolitic boron imidazolate frameworks. *Angew. Chem. Int. Ed.*, **48**, 2542–2545 (2009).

[312] Z. Wang, B. Zhang, T. Otsuka, K. Inoue, H. Kobayashi and M. Kurmoo. Anionic NaCl-type frameworks of $[Mn^{II}(HCOO)_3{}^-]$, templated by alkylammonium, exhibit weak ferromagnetism. *Dalton Trans.*, 2209–2216 (2004).

[313] K.-L. Hu, M. Kurmoo, Z. Wang and S. Gao. Metal–organic perovskites: synthesis, structures, and magnetic properties of $[C(NH_2)_3][M^{II}(HCOO)_3]$ (M = Mn, Fe, Co, Ni, Cu, and Zn; $C(NH_2)_3$ = guanidinium). *Chem Eur. J.*, **15**, 12050–12064 (2009).

[314] G.-C. Xu, X.-M. Ma, L. Zhang, Z.-M. Wang and S. Gao. Disorder–order ferroelectric transition in the metal formate framework of $[NH_4][Zn(HCOO)_3]$. *J. Am. Chem. Soc.*, **132**, 9588–9590 (2010).

[315] G.-C. Xu, W. Zhang, X.-M. Ma, Y.-H. Chen, L. Zhang, H.-L. Cai, Z.-M. Wang, R.-G. Xiong

and S. Gao. Coexistence of magnetic and electric orderings in the metal–formate frameworks of $[NH_4][M(HCOO)_3]$. *J. Am. Chem. Soc.*, **133**, 14948–14951 (2011).

[316] B. Liu, R. Shang, K.-L. Hu, Z.-M. Wang and S. Gao. A new series of chiral metal formate frameworks of $[HONH_3][M^{II}(HCOO)_3]$ (M = Mn, Co, Ni, Zn, and Mg): synthesis, structures, and properties. *Inorg. Chem.*, **51**, 13363–13372 (2012).

[317] M. Sánchez-Andújar, S. Presedo, S. Yáñez-Vilar, S. Castro-García, J. Shamir and M. A. Señarís Rodríguez. Characterization of the order–disorder dielectric transition in the hybrid organic–inorganic perovskite-like formate $Mn(HCOO)_3[(CH_3)_2NH_2]$. *Inorg. Chem.*, **49**, 1510–1516 (2010).

[318] B. Pato-Doldán, M. Sánchez-Andújar, L. C. Gómez-Aguirre, S. Yáñez-Vilar, J. López-Beceiro, C. Gracia-Fernández, A. A. Haghighirad, F. Ritter, S. Castro-García and M. A. Señarís Rodríguez. Near room temperature dielectric transition in the perovskite formate framework $[(CH_3)_2NH_2][Mg(HCOO)_3]$. *Phys. Chem. Chem. Phys.*, **14**, 8498–8501 (2012).

[319] M. Mączka, A. Gągor, B. Macalik, A. Pikul, M. Ptak and J. Hanuza. Order–disorder transition and weak ferromagnetism in the perovskite metal formate frameworks of $[(CH_3)_2NH_2][M(HCOO)_3]$ and $[(CH_3)_2ND_2][M(HCOO)_3]$ (M = Ni, Mn). *Inorg. Chem.*, **53**, 457–467 (2014).

[320] M. Mączka, A. Pietraszko, B. Macalik and K. Hermanowicz. Structure, phonon properties, and order–disorder transition in the metal formate framework of $[NH_4][Mg(HCOO)_3]$. *Inorg. Chem.*, **53**, 787–794 (2014).

[321] W. Wang, L.-Q. Yan, J.-Z. Cong, Y.-L. Zhao, F. Wang, S.-P. Shen, T. Zou, D. Zhang, S.-G. Wang, X.-F. Han and Y. Sun. Magnetoelectric coupling in the paramagnetic state of a metal–organic framework. *Scientific Reports*, **3**, 2024 (2013).

[322] X.-Y. Wang, L. Gan, S.-W. Zhang and S. Gao. Perovskite-like metal formates with weak ferromagnetism and as precursors to amorphous materials. *Inorg. Chem.*, **43**, 4615–4625 (2004).

[323] A. Stroppa, P. Jain, P. Barone, M. Marsman, J. M. Perez-Mato, A. K. Cheetham, H. W. Kroto and S. Picozzi. Electric control of magnetization and interplay between orbital ordering and ferroelectricity in a multiferroic metal–organic framework. *Angew. Chem. Int. Ed.*, **50**, 5847–5850 (2011).

[324] A. Stroppa, P. Barone, P. Jain, J. M. Perez-Mato and S. Picozzi. Hybrid improper ferroelectricity in a multiferroic and magnetoelectric metal–organic framework. *Adv. Mater.*, **25**, 2284–2290 (2013).

[325] A. Rossin, A. Ienco, F. Costantino, T. Montini, B. Di Credico, M. Caporali, L. Gonsalvi,

P. Fornasiero and M. Peruzzini. Phase transitions and CO_2 adsorption properties of polymeric magnesium formate. *Cryst. Growth Des.*, **8**, 3302–3308 (2008).

[326] E. Sletten and L. H. Jensen. The crystal structure of dimethylammonium copper(II) formate, $NH_2(CH_3)_2[Cu(OOCH)_3]$. *Acta Cryst. B*, **29**, 1752–1756 (1973).

[327] D. Kong, J. Zoñ, J. McBee and A. Clearfield. Rational design and synthesis of porous organic–inorganic hybrid frameworks constructed by 1,3,5-benzenetriphosphonic acid and pyridine synthons. *Inorg. Chem.*, **45**, 977–986 (2006).

[328] H. F. Clausen, R. D. Poulsen, A. D. Bond, M. A. S. Chevallier and B. B. Iversen. Solvothermal synthesis of new metal organic framework structures in the zinc-terephthalic acid-dimethyl formamide system. *J. Solid State Chem.*, **178**, 3342–3351 (2005).

[329] S. Gao and S. W. Ng. Poly[dimethylammonium [tris(μ_2-formato-κ^2O:O')cadmate(II)]]. *Acta Cryst. E*, **66**, m1599 (2010).

[330] B. Zhou, Y. Imai, A. Kobayashi, Z.-M. Wang and H. Kobayashi. Giant dielectric anomaly of a metal–organic perovskite with four-membered ring ammonium cations. *Angew. Chem. Int. Ed.*, **50**, 11441–11445 (2011).

[331] P. Jain, N. S. Dalal, B. H. Toby, H. W. Kroto and A. K. Cheetham. Order–disorder antiferroelectric phase transition in a hybrid inorganic–organic framework with the perovskite architecture. *J. Am. Chem. Soc.*, **130**, 10450–10451 (2008).

[332] W. Li, Z. Zhang, E. G. Bithell, A. S. Batsanov, P. T. Barton, P. J. Saines, P. Jain, C. J. Howard, M. A. Carpenter and A. K. Cheetham. Ferroelasticity in a metal–organic framework perovskite; towards a new class of multiferroics. *Acta Mater.*, **61**, 4928–4938 (2013).

[333] S.-Q. Xu and J.-M. Li. Crystal structure of *catena*-(dimethylammonium) tris(μ_2-formato)copper(II), $[C_2H_8N][Cu(CHO_2)_3]$. *Z. Kristallogr. NCS*, **224**, 383–384 (2009).

[334] Z. Wang, K. Hu, S. Gao and H. Kobayashi. Formate-based magnetic metal–organic frameworks templated by protonated amines. *Adv. Mater.*, **22**, 1526–1533 (2010).

[335] D. Watkin. U_{equiv}: its past, present and future. *Acta Cryst. B*, **56**, 747–749 (2000).

[336] R. I. Cooper, B. M. Foxman and L. Yang. CIF applications. XVI. CIF2CRY: for CIF input into the CRYSTALS program. *J. Appl. Cryst.*, **37**, 669–671 (2004).

[337] M. Mączka, M. Ptak and S. Kojima. Brillouin scattering study of ferroelectric transition mechanism in multiferroic metal–organic frameworks of $[NH_4][Mn(HCOO)_3]$ and $[NH_4][Zn(HCOO)_3]$. *Appl. Phys. Lett.*, **104**, 222903 (2014).

[338] G. Lalitha and P. V. Reddy. Elastic behavior of some manganite-based orthorhombic $RMnO_3$ (R = Sm, Eu, Gd, Dy) multiferroics. *J. Magn. Magn. Mater.*, **320**, 754–759 (2008).

[339] C.-C. Lin, S.-F. Chen, L.-g. Liu and C.-C. Li. Size effects of modifying cations on the structure and elastic properties of Na_2O-MO-SiO_2 glasses (M = Mg, Ca, Sr, Ba). *Mater. Chem. Phys.*, **123**, 569–580 (2010).

[340] I. E. Collings, M. G. Tucker, D. A. Keen and A. L. Goodwin. Geometric switching of linear to area negative thermal expansion in uniaxial metal–organic frameworks. *CrystEngComm*, **16**, 3498–3506 (2014).

[341] X.-Y. Dong, B. Li, B.-B. Ma, S.-J. Li, M.-M. Dong, Y.-Y. Zhu, S.-Q. Zang, Y. Song, H.-W. Hou and T. C. W. Mak. Ferroelectric switchable behavior through fast reversible de/adsorption of water spirals in a chiral 3D metal–organic framework. *J. Am. Chem. Soc.*, **135**, 10214–10217 (2013).

[342] M. G. Tucker, M. T. Dove and D. A. Keen. Simultaneous analysis of changes in long-range and short-range structural order at the displacive phase transition in quartz. *J. Phys.: Condens. Matter*, **12**, L723–L730 (2000).

[343] A. L. Goodwin, S. A. T. Redfern, M. T. Dove, D. A. Keen and M. G. Tucker. Ferroelectric nanoscale domains and the 905 K phase transition in $SrSnO_3$: a neutron total-scattering study. *Phys. Rev. B*, **76**, 174114 (2007).

[344] A. K. Soper. Inelasticity corrections for time-of-flight and fixed wavelength neutron diffraction experiments. *Mol. Phys.*, **107**, 1667–1684 (2009).

[345] Manipulation and Analysis Toolkit for Instrument Data.; Mantid Project. http://dx.doi.org/10.5286/SOFTWARE/MANTID.

[346] C. L. Farrow, P. Juhas, J. W. Liu, D. Bryndin, E. S. Božin, J. Bloch, Th. Proffen and S. J. L. Billinge. PDFfit2 and PDFgui: computer programs for studying nanostructure in crystals. *J. Phys.: Condens. Matter*, **19**, 335219 (2007).

[347] S. A. Wells, M. T. Dove and M. G. Tucker. Finding best-fit polyhedral rotations with geometric algebra. *J. Phys.: Condens. Matter*, **14**, 4567–4584 (2002).

[348] S. A. Wells, M. T. Dove, M. G. Tucker and K. Trachenko. Real-space rigid-unit-mode analysis of dynamic disorder in quartz, cristobalite and amorphous silica. *J. Phys.: Condens. Matter*, **14**, 4645–4657 (2002).

[349] S. Wells, M. Dove and M. Tucker. Reverse Monte Carlo with geometric analysis – RMC+GA. *J. Appl. Cryst.*, **37**, 536–544 (2004).

[350] W. Zhou and T. Yildirim. Lattice dynamics of metal–organic frameworks: neutron inelastic scattering and first-principles calculations. *Phys. Rev. B*, **74**, 180301 (2006).

[351] O. R. Evans, R. G. Xiong, Z. Y. Wang, G. K. Wong and W. B. Lin. Crystal engineering of acentric diamondoid metal–organic coordination networks. *Angew. Chem. Int. Ed.*, **38**, 536–538 (1999).

[352] S. Horiuchi and Y. Tokura. Organic ferroelectrics. *Nat. Mater.*, **7**, 357–366 (2008).

[353] N. L. Allinger, Y. H. Yuh and J.-H. Lii. Molecular mechanics. The MM3 force field for hydrocarbons 1. *J. Am. Chem. Soc.*, **8**, 8551–8566 (1989).

[354] M. G. Tucker, M. T. Dove, A. L. Goodwin and D. A. Keen. *RMCProfile User Manual code version 6.5.0.* www.rmcprofile.org/Manuals (2012).

[355] D. Di Sante, A. Stroppa, P. Jain and S. Picozzi. Tuning the ferroelectric polarization in a multiferroic metal–organic framework. *J. Am. Chem. Soc.*, **135**, 18126–18130 (2013).

Appendix A

Supporting information for Chapter 3

A.1 Principal axes

There is close resemblance between the monoclinic axes and those of the principal axes in Ag(mim), as the monoclinic β angle is close to 90° and largely invariant. Precisely, the principal and lattice axes are related by the transformation

$$\begin{bmatrix} \mathbf{x}_1 \\ \mathbf{x}_2 \\ \mathbf{x}_3 \end{bmatrix} = \begin{bmatrix} 0.9892 & 0 & -0.1467 \\ 0 & 1 & 0 \\ -0.1085 & 0 & -0.9941 \end{bmatrix} \begin{bmatrix} \mathbf{a} \\ \mathbf{b} \\ \mathbf{c} \end{bmatrix},$$

in the case of the variable-temperature data, and by

$$\begin{bmatrix} \mathbf{x}_1 \\ \mathbf{x}_2 \\ \mathbf{x}_3 \end{bmatrix} = \begin{bmatrix} 0.9875 & 0 & 0.1573 \\ 0 & -1 & 0 \\ 0.2414 & 0 & -0.9704 \end{bmatrix} \begin{bmatrix} \mathbf{a} \\ \mathbf{b} \\ \mathbf{c} \end{bmatrix},$$

in the case of the variable-pressure data. In both instances, the deviation of $\mathbf{x}_1$ and $\mathbf{x}_3$ away from the a- and c-axes is less than 3%.

A.2 Empirical equation derivatives for T and p

The differentiation of Eq. (3.1):

$$\frac{\mathrm{d}\ell}{\mathrm{d}T} = \kappa \left(\frac{T}{T + T_\mathrm{c}} \right)^{\lambda} + \kappa T \lambda \left(\frac{T}{T + T_\mathrm{c}} \right)^{\lambda - 1} \left(\frac{T_\mathrm{c}}{(T + T_\mathrm{c})^2} \right), \tag{A.1}$$

allows the calculation of α.

Similarly, the differentiation of Eq. (3.2):

$$\frac{\mathrm{d}\ell}{\mathrm{d}p} = \eta \nu (p - p_\mathrm{c})^{\nu - 1}, \tag{A.2}$$

allows the calculation of K.

A.3 Energy cost of transverse vibrations

The trigonometry which gives rise to the 0.78° change following a 1% strain is shown in Figure A.1. By displacing both zinc atoms by 0.5%, an overall 1% strain is achieved; the calculation in Figure A.1 shows the calculation for one of the Zn displacements.

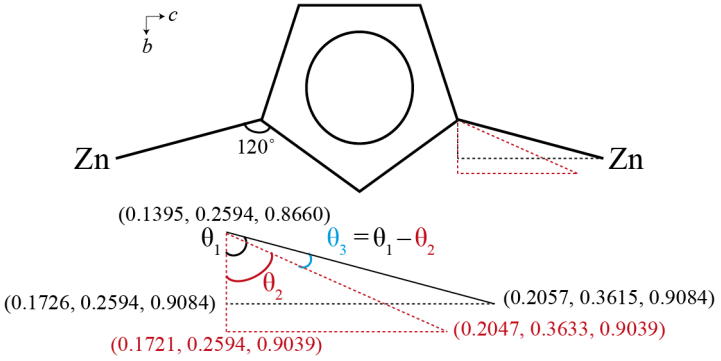

Figure A.1: The Zn–im–Zn binding geometry found in ZIF-4. Using a 0.5% change in coordinates for one of the zinc atoms, the relevant angles can be calculated.

Appendix B

Supporting information for Chapter 4

B.1 Absorption correction for $Cd(im)_2$

Absorption was added for $Cd(im)_2$ Rietveld refinements because of the high absorption of Cd, which was confirmed by the online X-ray absorption calculator (http://11bm.xray.aps.anl.gov/absorb/absorb.php) [Fig. B.1].

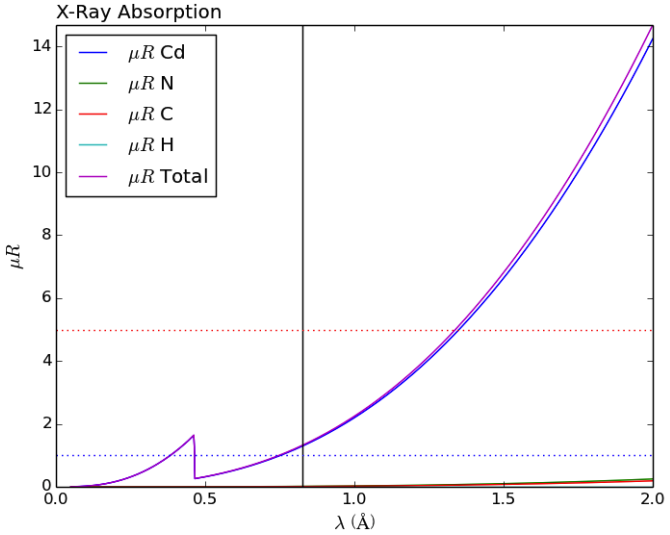

Figure B.1: Computed X-ray absorption as a function of X-ray wavelength for a 0.5 mm capillary and at a packing efficiency of 0.6 for $Cd(im)_2$. The black vertical line indicates the wavelength used for the experiment; ideally the sample absorption should be below one (dotted blue line). This calculation was performed using the online program: http://11bm.xray.aps.anl.gov/absorb/absorb.php.

B.2 Empirical equation derivative for p

The differentiation of Eq. (4.3):

$$\frac{\mathrm{d}\ell}{\mathrm{d}p} = \eta\nu(p - p_\mathrm{c})^{\nu-1} - \beta, \tag{B.1}$$

allows the calculation of K_a.

B.3 XBU-driven lattice parameter evolutions for $Zn(CN)_2$-II and $Cd(im)_2$

The lattice parameter evolutions which were calculated from either θ or r variations, while keeping the other XBU parameter fixed at its initial value, are shown in Figure B.3 for $Zn(CN)_2$-II and $Cd(im)_2$. The original lattice parameter evolutions and those calculated from θ variations look very similar, indicating that framework angle changes dominate the expansivities or compressibilities of $Zn(CN)_2$-II and $Cd(im)_2$ in general. The XBU relationships to the *Pbca* unit cell were used for the calculation of the XBU-driven lattice parameter evolutions [Figs. 4.6 and B.2].

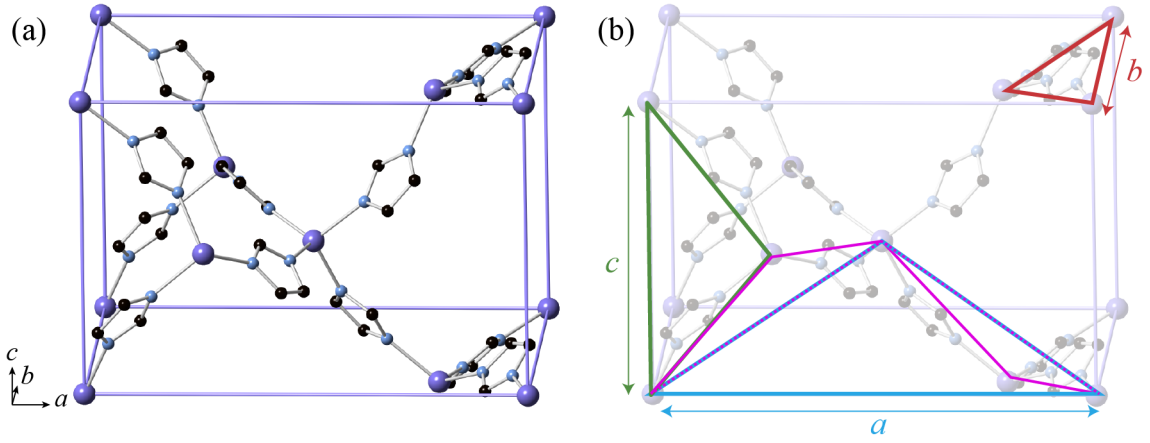

Figure B.2: (a) Extended structure of a single net of $Cd(im)_2$ with its unit cell translated so that Cd cations sit at its corners. (b) The same extended structure of $Cd(im)_2$ with the XBU relationships to the lattice parameters shown. The same trigonometric calculations given for $Zn(CN)_2$-II are used for $Cd(im)_2$.

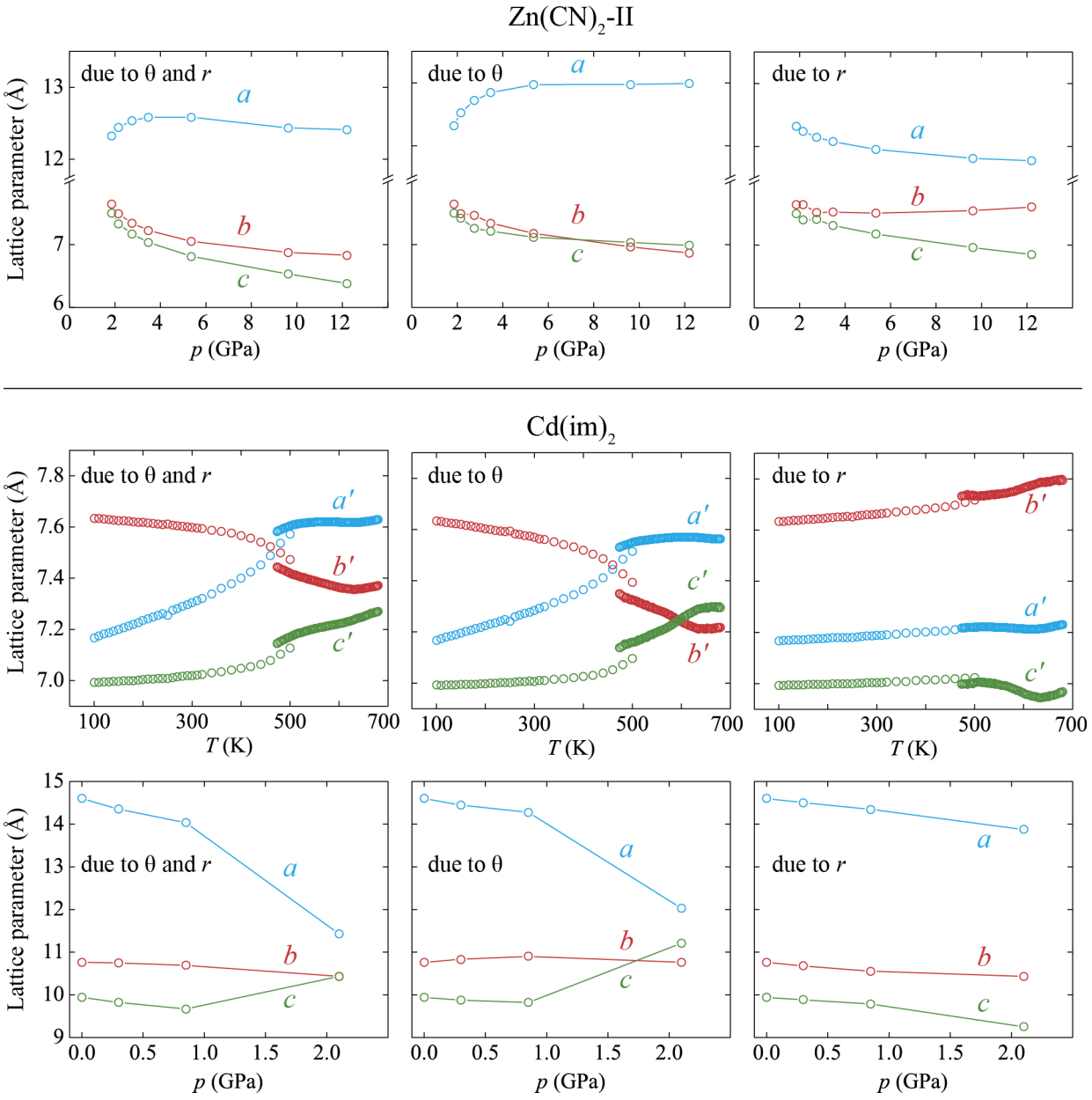

Figure B.3: Lattice parameter evolutions for $Zn(CN)_2$-II and $Cd(im)_2$ as a function of pressure, and $Cd(im)_2$ as a function of temperature (pseudocubic lattice parameters shown). The first column of graphs corresponds to the original lattice parameters observed (due to θ and r), while the middle column represents the lattice parameters calculated from purely framework angle changes (due to θ). In the third column of graphs, the lattice parameters are calculated by considering only r changes (due to r). The lines joining the lattice parameters in $Cd(im)_2$ and $Zn(CN)_2$ on compression function as guides to the eye.

B.4 Local structure evolutions for $Zn(CN)_2$-II and $Cd(im)_2$

The local structure parameters in $Zn(CN)_2$-II and $Cd(im)_2$ are shown in Figure B.4 as a function of temperature and pressure. The relevant parameters are illustrated in $Cd(im)_2$.

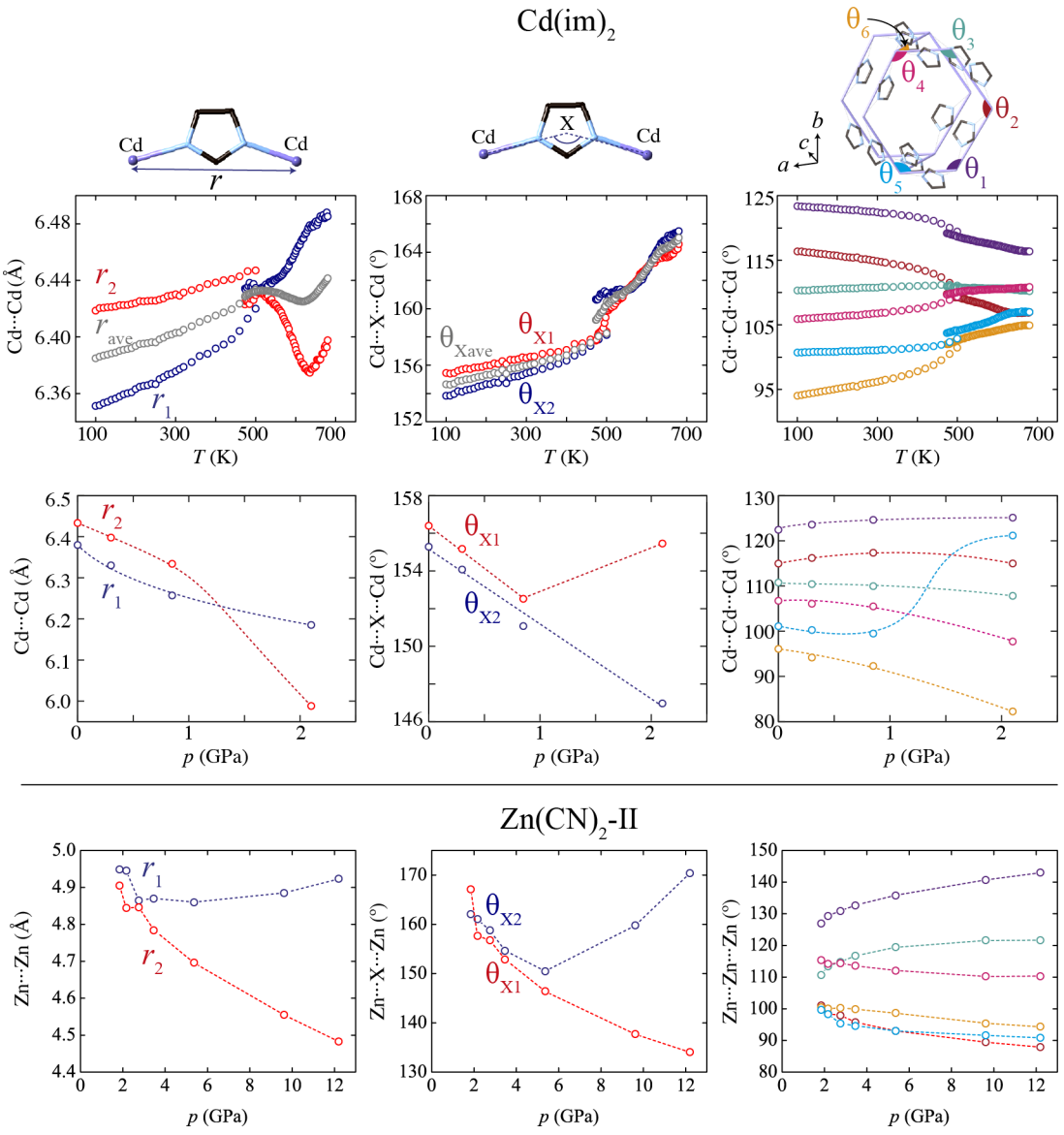

Figure B.4: Variation in ligand-connected M···M distances, M···X···M angles and all ligand-connected M···M···M framework angles as a function of temperature or pressure, where X represents the centroid of the nitrogens within the imidazolate anion, or the centroid of the cyanide anion. The average of the two Cd···Cd distances and Cd···X···Cd angles for the variable-temperature data set are shown in grey. The six different framework angles are represented by different colours and their positions are highlighted in the $Cd(im)_2$ structure at the top of the graphs.

B.5 Polyhedral tilt parameter for $Cd(im)_2$

The polyhedral tilts are defined in terms of a mean angle φ, calculated using equations $\varphi_1 = \tan^{-1}\{[4(z_X - 0.5)c]/a\}$ and $\varphi_2 = \tan^{-1}\{[4(x_X - 0.25)a]/c\}$ for the two unique φ angles shown in Figure B.5. The z_X and x_X correspond to the z- and x-coordinates of the centroid of the nitrogens from the imidazolate anion, respectively. Similar calculations were performed for the **ab**-plane, and the four φ angles, shown in Figure B.6, were averaged to give the $\langle\varphi\rangle$ values. The mean lattice expansivity is calculated using the relationship between the lattice parameters and the φ angles, such as $a = 2s_1 \cos\varphi_1$ for the a-axis [Fig. B.5]; equivalent equations are present for the b- and c-axes. The following equations, shown here with the a-axis relation to φ, give the mean lattice expansivity:

$$\begin{aligned}
\alpha_a = \frac{1}{a}\frac{\mathrm{d}a}{\mathrm{d}T} &= \frac{1}{a}\frac{\mathrm{d}}{\mathrm{d}T}[2s\cos\varphi] \\
&= \frac{2s}{a}\frac{\mathrm{d}}{\mathrm{d}T}\cos\varphi \\
&= -\frac{2s}{a}\sin\varphi\frac{\mathrm{d}\varphi}{\mathrm{d}T} \\
&= -\frac{2s\sin\varphi}{2s\cos\varphi}\frac{\mathrm{d}\varphi}{\mathrm{d}T} \\
\alpha_\ell &= -\tan\varphi\frac{\mathrm{d}\varphi}{\mathrm{d}T}.
\end{aligned}$$

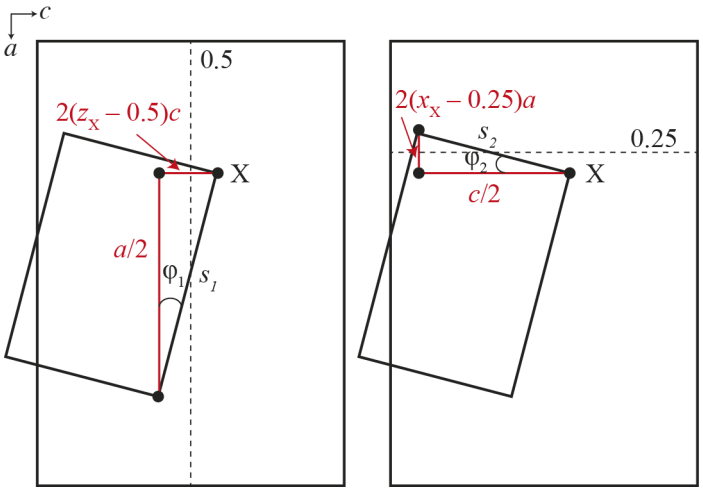

Figure B.5: Projection of a pairwise CdX_4 column in the **ac**-plane, illustrating how the φ angles are calculated.

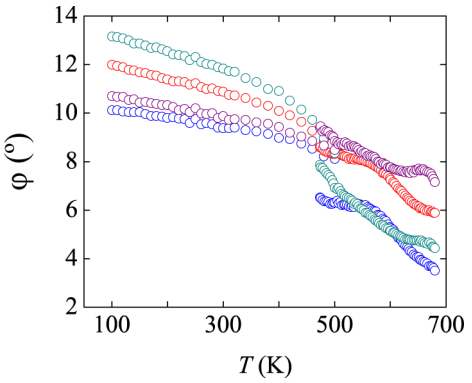

Figure B.6: The four individual φ evolutions as a function of temperature, highlighted by their different colours.

B.6 Individual order parameters for $Cd(im)_2$ and $Zn(CN)_2$

The individual order parameters for the metal and the ligand centroids calculated for $Cd(im)_2$ and $Zn(CN)_2$ are shown in Figure B.7. These evolutions were averaged to obtain the order parameter shown in Figure 4.15(a).

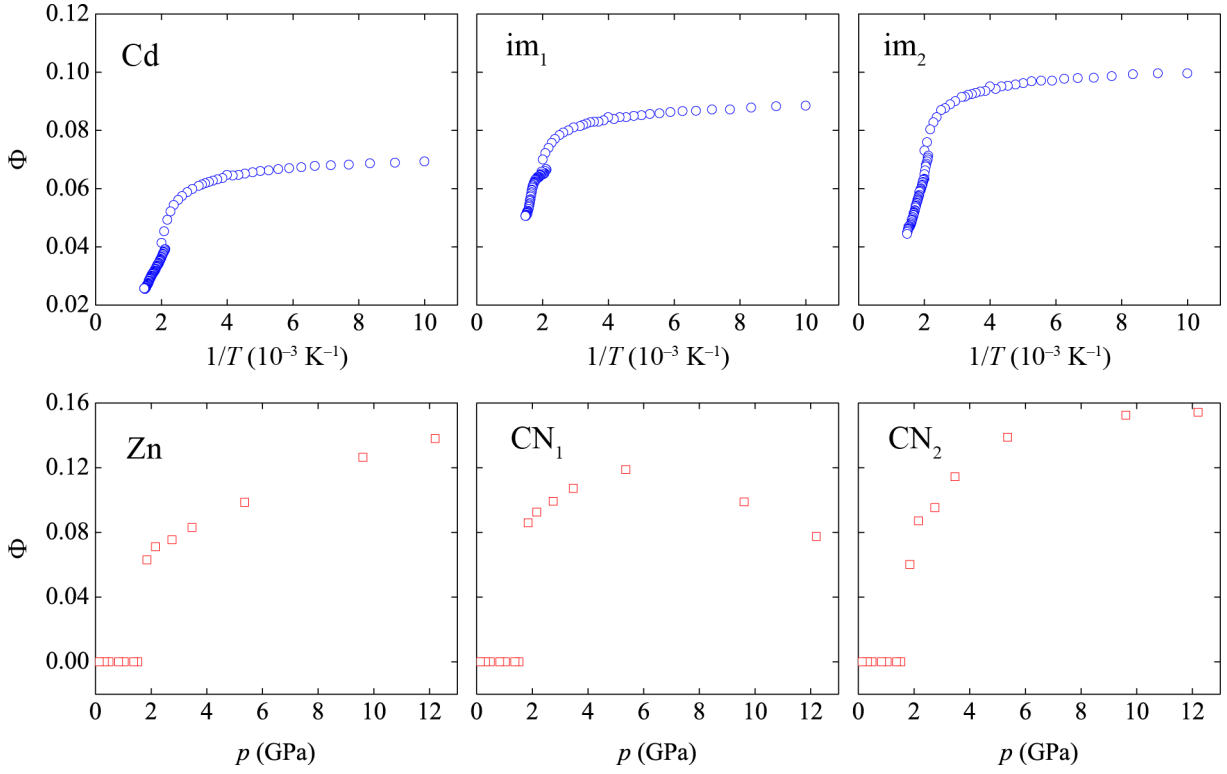

Figure B.7: Individual positional order parameters for the metal and two ligand centroids in $Cd(im)_2$ and $Zn(CN)_2$.

The individual order parameters for the brookite-like displacements are shown in Figure B.8; the average of these order parameters are shown in Figure 4.15(b). Additionally, the drive towards brookite-like packing is shown for $Cd(im)_2$ upon compression.

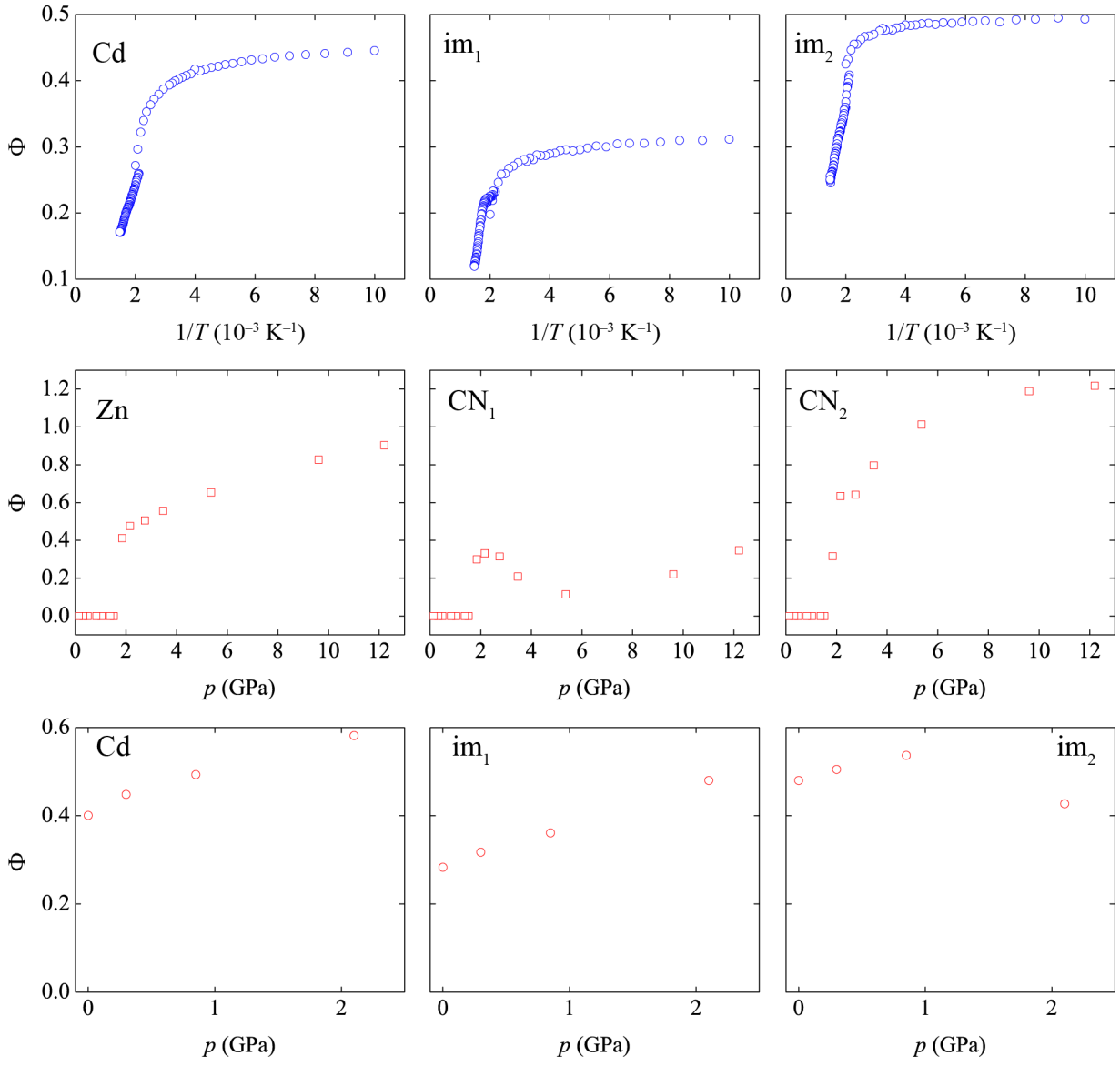

Figure B.8: Individual positional order parameters towards brookite, for the metal and two ligand centroids in $Cd(im)_2$ and $Zn(CN)_2$.

Appendix C

Supporting information for Chapter 5

C.1 IGA measurement of $Zn(ISN)_2$

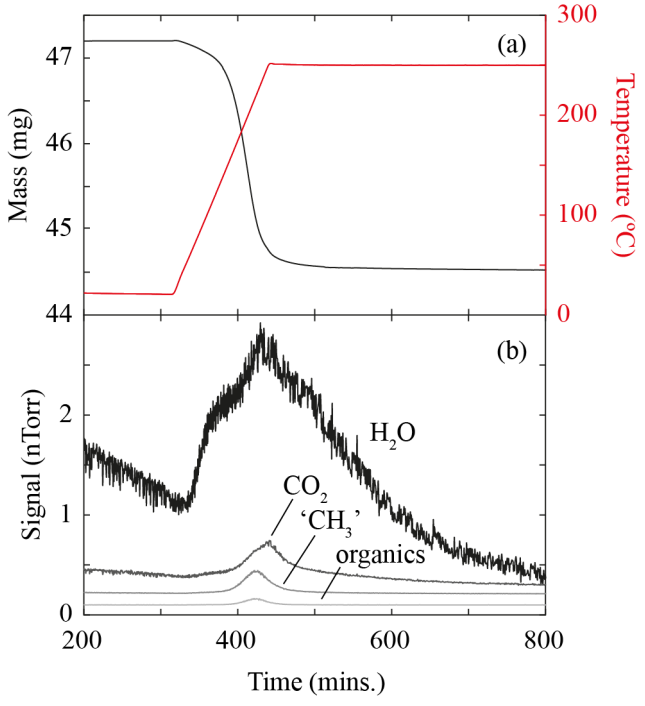

Figure C.1: Intelligent Gravimetric Analysis (IGA) spectrum. (a) The weight loss of $Zn(ISN)_2$ as it is heated from room temperature to 250 °C. (b) The relative quantities of detected solvents and gases due to the evacuation of the framework pores. This measurement was performed by Josh Makepeace.

C.2 Rietveld fits for $Zn(ISN)_2$·guest and $InD(BDC)_2$·guest

The intensity fit for $Zn(ISN)_2$ and $InD(BDC)_2$ could be improved by modelling solvent within the pores [Fig. C.2]. The extra pore density in $Zn(ISN)_2$ was modelled using water molecules, referred to as $Zn(ISN)_2$·guest. In the case of $InD(BDC)_2$, the pore density was modelled using oxygen atoms ($InD(BDC)_2$·guest) because the nature and quantity of the disordered solvent was not well determined.

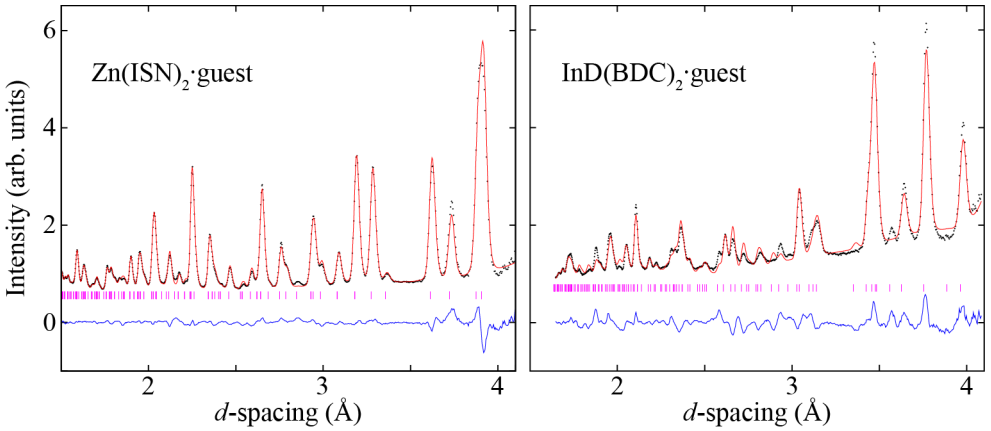

Figure C.2: Rietveld fits of $Zn(ISN)_2$ and $InD(BDC)_2$ at 12 K, modelled with guests in the framework pores. Experimental data are shown as points, the fitted profile as a solid red line, and the difference (data−fit) as a blue line.

C.3 Variable-temperature lattice parameter data

Variable-temperature lattice parameter data for $Zn(ISN)_2$ and $InD(BDC)_2$ with and without modelled solvent are given in Tables C.1 and C.2. As expected, the lattice parameters obtained from both the empty and solvent-containing Rietveld models are the same within error. The errors for each temperature were calculated using the difference between the temperature at the start and end of the corresponding measurement.

Table C.1: Variable-temperature lattice parameter data for $Zn(ISN)_2$ and $Zn(ISN)_2$·guest (marked by asterisks) as determined using Rietveld fits to powder neutron diffraction upon warming from 10 K to 300 K.

T (K)	a (Å)	c (Å)	V (Å^3)
11.970(14)	15.5190(6)	6.1280(5)	1278.12(14)
11.970(14)*	15.5190(5)*	6.1282(5)*	1278.16(13)*
43(7)	15.5164(6)	6.1325(6)	1278.65(15)
43(7)*	15.5163(5)*	6.1327(5)*	1278.67(13)*
96(2)	15.5078(5)	6.1500(5)	1280.88(14)
96(2)*	15.5076(5)*	6.1501(5)*	1280.85(13)*
134(3)	15.4994(6)	6.1664(6)	1282.89(15)
134(3)*	15.4984(5)*	6.1667(5)*	1282.79(14)*
169(15)	15.4906(6)	6.1862(6)	1285.55(16)
169(15)*	15.4892(5)*	6.1868(5)*	1285.44(14)*
238.1(14)	15.4821(6)	6.2051(6)	1288.05(16)
238.1(14)*	15.4811(5)*	6.2059(6)*	1288.05(14)*
285(4)	15.4753(6)	6.2251(6)	1291.08(16)
285(4)*	15.4748(5)*	6.2257(5)*	1291.13(13)*

Table C.2: Variable-temperature lattice parameter data for $InD(BDC)_2$ and $InD(BDC)_2$·guest (marked by asterisks) as determined using Rietveld fits to powder neutron diffraction upon warming from 10 K to 300 K.

T (K)	a (Å)	c (Å)	V (Å^3)
11.96(7)	14.5310(15)	12.273(2)	2244.2(6)
11.96(7)*	14.5291(11)*	12.2738(17)*	2243.8(5)*
42(3)	14.5474(15)	12.265(2)	2247.8(6)
42(3)*	14.5475(12)*	12.2628(19)*	2247.5(5)*
95.8(8)	14.5831(15)	12.249(2)	2256.0(6)
95.8(8)*	14.5838(11)*	12.2472(17)*	2255.8(5)*
138(4)	14.6266(15)	12.231(2)	2266.2(7)
138(4)*	14.6285(12)*	12.2296(19)*	2266.4(5)*
188(2)	14.6788(16)	12.206(2)	2277.7(7)
188(2)*	14.6818(12)*	12.2035(19)*	2278.1(5)*
238(3)	14.7304(16)	12.183(2)	2289.5(7)
238(3)*	14.7335(12)*	12.1809(19)*	2289.9(5)*
285.2(5)	14.7859(17)	12.154(3)	2301.3(7)
285.2(5)*	14.7900(13)*	12.152(2)*	2302.0(5)*

C.4 Framework angle expansivity derivation

The three unique framework angles (θ_1, θ_2, θ_3) can be expressed in terms of the lattice parameter a and the M–link–M unit distance r. This derivation uses the relationship between the dot product of two vectors

$$\mathbf{r}_1 \cdot \mathbf{r}_2 = r^2 \cos\theta, \tag{C.1}$$

and so the framework angle is given by

$$\theta = \cos^{-1}\left(\frac{\mathbf{r}_1 \cdot \mathbf{r}_2}{r^2}\right). \tag{C.2}$$

The **r** vectors used for calculating the three framework angles are given here in cartesian vectors **i**, **j**, **k**:

$$\begin{aligned}
\mathbf{r}_1 &= \frac{1}{2}a\mathbf{i} + \frac{2}{3}c\mathbf{k}, \\
\mathbf{r}_2 &= -\frac{1}{4}a\mathbf{i} + \frac{\sqrt{3}}{4}a\mathbf{j} - \frac{2}{3}c\mathbf{k}, \\
\mathbf{r}_3 &= -\frac{1}{2}a\mathbf{i} + \frac{2}{3}c\mathbf{k}, \\
\mathbf{r}_4 &= -\frac{1}{4}a\mathbf{i} + \frac{\sqrt{3}}{4}a\mathbf{j} - \frac{2}{3}c\mathbf{k},
\end{aligned}$$

and their locations are shown in Figure C.3. The magnitude of these **r** vectors is given by

$$r = \sqrt{\frac{a^2}{4} + \frac{4c^2}{9}}. \tag{C.3}$$

Using the equations above, the framework angles can be defined with respect to the lattice parameter a and r distance [Table C.3].

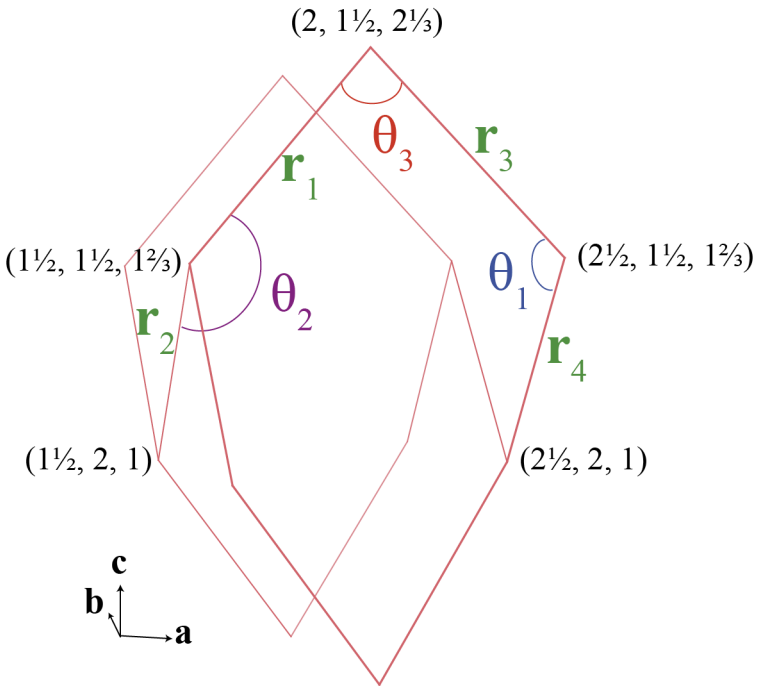

Figure C.3: Framework structure of $InD(BDC)_2$ with the ligands replaced by rods, where the **r** vectors and the three unique framework angles are shown. The fractional coordinates of the metal sites which are used for **r** vector calculations are shown in brackets.

Table C.3: Derivation of θ_i in terms of its lattice parameter a and r distance.

θ_1	θ_2	θ_3
$\mathbf{r}_3 \cdot \mathbf{r}_4 = \frac{1}{8}a^2 - \frac{4}{9}c^2$	$\mathbf{r}_1 \cdot \mathbf{r}_2 = -\frac{1}{8}a^2 - \frac{4}{9}c^2$	$\mathbf{r}_1 \cdot \mathbf{r}_3 = -\frac{1}{4}a^2 + \frac{4}{9}c^2$
$\mathbf{r}_3 \cdot \mathbf{r}_4 = -\left(r^2 - \frac{3}{8}a^2\right)$	$\mathbf{r}_1 \cdot \mathbf{r}_2 = -\left(r^2 - \frac{1}{8}a^2\right)$	$\mathbf{r}_1 \cdot \mathbf{r}_3 = \left(r^2 - \frac{1}{2}a^2\right)$
$\theta_1 = \cos^{-1}\left[-\frac{\left(r^2-\frac{3}{8}a^2\right)}{r^2}\right]$	$\theta_2 = \cos^{-1}\left[-\frac{\left(r^2-\frac{1}{8}a^2\right)}{r^2}\right]$	$\theta_3 = \cos^{-1}\left[\frac{\left(r^2-\frac{1}{2}a^2\right)}{r^2}\right]$
$\theta_1 = \cos^{-1}\left(-1 + \frac{3a^2}{8r^2}\right)$	$\theta_2 = \cos^{-1}\left(-1 + \frac{a^2}{8r^2}\right)$	$\theta_3 = \cos^{-1}\left(1 - \frac{a^2}{2r^2}\right)$

The framework angles are differentiated with respect to temperature in order to obtain a relationship which relates α_θ to α_a by approximating that $\alpha_r = 0$ [Eqs. (C.4), (C.5), (C.6)].

$$\begin{aligned}
\theta_1 &= \cos^{-1}\left(-1 + \frac{3a^2}{8r^2}\right) \\
\frac{\mathrm{d}\theta_1}{\mathrm{d}T} &= -\frac{1}{\sqrt{1 - \left(-1 + \frac{3a^2}{8r^2}\right)^2}} \frac{\mathrm{d}}{\mathrm{d}T}\left(\frac{3a^2}{8r^2}\right) \\
&= -\frac{8r^2}{\sqrt{48r^2 - 9a^2}} \frac{6a}{8r^2} \frac{\mathrm{d}a}{\mathrm{d}T} \\
&= -\frac{6a\alpha_a}{\sqrt{48r^2 - 9a^2}} \\
\alpha_{\theta_1} &= -\frac{6a\alpha_a}{\theta_1\sqrt{48r^2 - 9a^2}}
\end{aligned} \tag{C.4}$$

$$\begin{aligned}
\theta_2 &= \cos^{-1}\left(-1 + \frac{a^2}{8r^2}\right) \\
\frac{d\theta_2}{\mathrm{d}T} &= -\frac{1}{\sqrt{1 - \left(-1 + \frac{a^2}{8r^2}\right)^2}} \frac{\mathrm{d}}{\mathrm{d}T}\left(\frac{a^2}{8r^2}\right) \\
&= -\frac{8r^2}{a\sqrt{16r^2 - a^2}} \frac{2a}{8r^2} \frac{\mathrm{d}a}{\mathrm{d}T} \\
&= -\frac{2a\alpha_a}{\sqrt{16r^2 - a^2}} \\
\alpha_{\theta_2} &= -\frac{2a\alpha_a}{\theta_2\sqrt{16r^2 - a^2}}
\end{aligned} \tag{C.5}$$

$$
\begin{aligned}
\theta_3 &= \cos^{-1}\left(1-\frac{a^2}{2r^2}\right) \\
\frac{d\theta_3}{\mathrm{d}T} &= -\frac{1}{\sqrt{1-\left(1-\frac{a^2}{2r^2}\right)^2}}\frac{\mathrm{d}}{\mathrm{d}T}\left(-\frac{a^2}{2r^2}\right) \\
&= \frac{2r^2}{a\sqrt{4r^2-a^2}}\frac{2a}{2r^2}\frac{\mathrm{d}a}{\mathrm{d}T} \\
&= \frac{2a\alpha_a}{\sqrt{4r^2-a^2}} \\
\alpha_{\theta_3} &= \frac{2a\alpha_a}{\theta_3\sqrt{4r^2-a^2}}
\end{aligned}
\tag{C.6}
$$

The expansivities for the three framework angles are calculated by using the Eqs. (C.4), (C.5), (C.6) and the known values of a, r, and α_a. By implying $\alpha_r = 0$, the angle expansivities can be determined without any effects from bond deformation. For $Zn(ISN)_2$ at 285 K: $a = 15.4752$ Å, $r = 8.78$ Å, and $\alpha_a = -10.9\,\mathrm{MK}^{-1}$. For $InD(BCD)_2$ at 285 K: $a = 14.786$ Å, $r = 10.969$ Å, and $\alpha_a = 64\,\mathrm{MK}^{-1}$. Table C.4 compares the angle expansivities when $\alpha_r = 0$ is implied with the experimental values measured from the structures. The calculated and experimental α_θ values are very similar, indicating that bond deformation along the **r** vector does not change the geometric hinging of the framework substantially.

Table C.4: Framework angle expansivities calculated from the derivations above and compared to the experimentally obtained values in $Zn(ISN)_2$ and $InD(BDC)_2$.

i	calculated α_i (MK^{-1})		experimental α_i (MK^{-1})	
	$Zn(ISN)_2$	$InD(BDC)_2$	$Zn(ISN)_2$	$InD(BDC)_2$
r	0	0	4.7(4)	9.2(3)
θ_1	18	−49	26.3(11)	−41(2)
θ_2	5	−19	6.9(3)	−15.9(8)
θ_3	−19	80	−27.0(12)	68(3)

C.5 Lattice parameter evolutions for desolvated $Zn(ISN)_2$ and $InD(BDC)_2$

In order to clarify the effect of solvent on the thermal expansivities for both MOFs, the powdered samples of $Zn(ISN)_2$ and $InD(BDC)_2$ were each heated up to 520 K while collecting diffraction data using a Siemens D5000 diffractometer. X-ray diffraction patterns were collected using heating and cooling cycles while maintaining a helium flow in the sample chamber. Figure C.4 shows the relative changes in lattice parameters for $Zn(ISN)_2$ and $InD(BDC)_2$ during sequential heating and cooling cycles. The dehydration of $InD(BDC)_2$ can be clearly seen in the first heating cycle, while the change in peak intensities indicate dehydration in $Zn(ISN)_2$. Further heating of $InD(BDC)_2$ above 520 K gave rise to an irreversible phase transition (the lattice parameters in Fig. C.4 are for the ambient $InD(BDC)_2$ phase).

The CTEs for the desolvated $Zn(ISN)_2$ and $InD(BDC)_2$ samples are shown in Table C.5; these calculations made use of the lattice parameters after the first heating cycle in both MOFs. It can be seen that the anisotropy of thermal expansion is the same as solvated phases of $Zn(ISN)_2$ and $InD(BDC)_2$, while the magnitudes are slightly modified. The geometric parameters were calculated as detailed in section C.4, and again show that the α_θ have the same anisotropy as

Table C.5: Lattice and XBU expansivities of desolvated $Zn(ISN)_2$ and $InD(BDC)_2$, calculated using linear fits to X-ray diffraction data. The lattice and XBU expansivities for the solvated phases detailed in the main chapter are also shown for comparison. The asterisks denote the α_θ values that are calculated assuming $\alpha_r = 0$ as detailed in section C.4.

Parameter, i	α_i (MK^{-1})		α_i (MK^{-1})	
	$Zn(ISN)_2$	$InD(BDC)_2$	$Zn(ISN)_2$·{guest}	$InD(BDC)_2$·{guest}
a, b	−16.1(4)	75.2(17)	−10.9(5)	64(3)
c	52.3(10)	−47(5)	60(3)	−35(2)
V	20.1(3)	103(4)	37.8(18)	94(4)
r	−0.55(12)	10(2)	4.7(4)	9.2(3)
θ_1*	27	−56	18	−49
θ_2*	7	−22	5	−19
θ_3*	−28	92	−19	80

the solvated phases [Table C.5]. Consequently, the analysis presented in Chapter 5—which relies on the direction of mechanical anisotropy in $Zn(ISN)_2$ and $InD(BDC)_2$—is clearly unaffected by framework guest occupancy. It is interesting to note that the magnitudes of α_θ values are greater in the desolvated phases, which means that these phases show greater geometric hinging. In the case of $Zn(ISN)_2$, the desolvated phase favours additionally greater transverse vibrational modes of the linker (giving rise to negative α_r values).

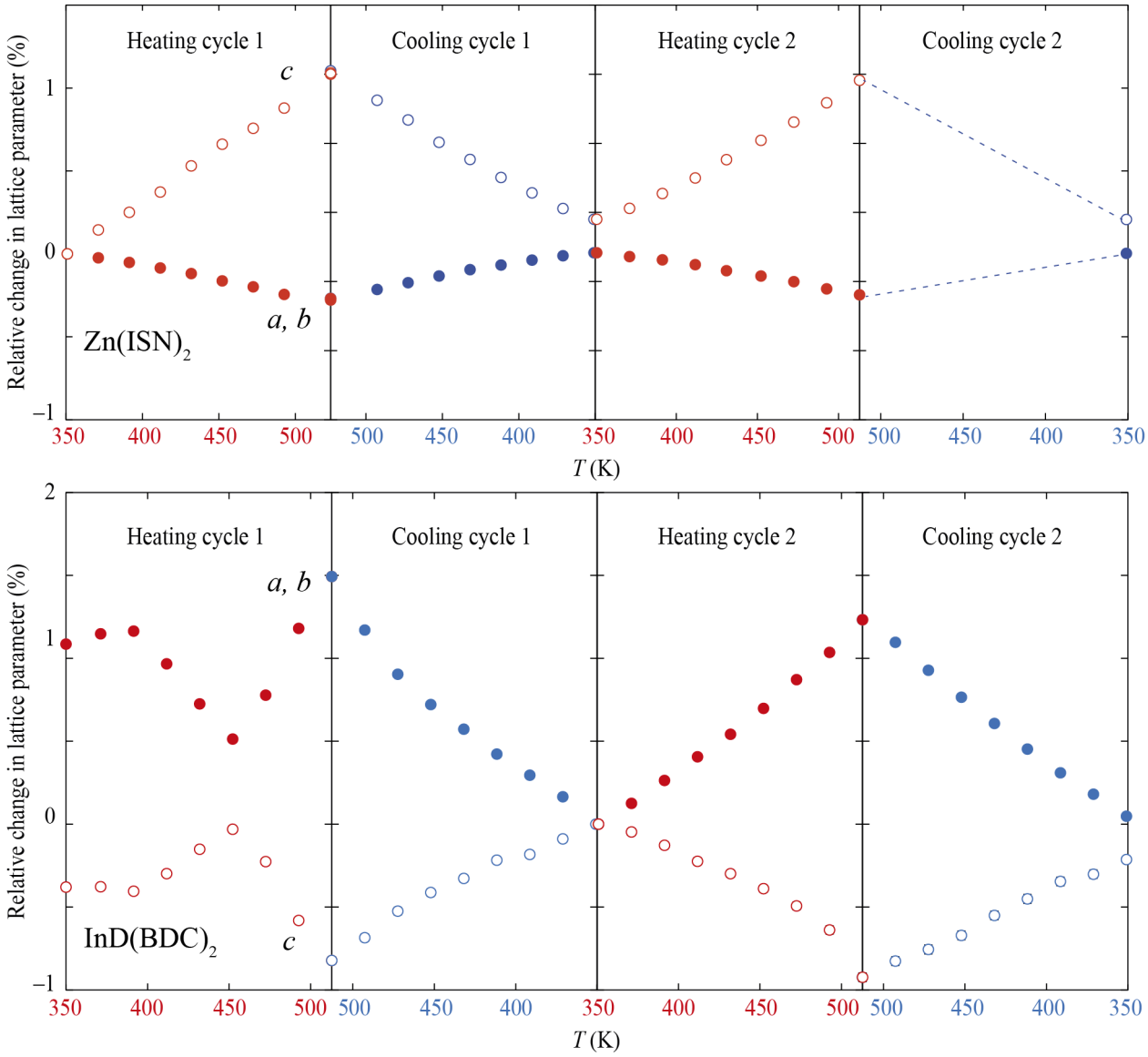

Figure C.4: Relative changes in lattice parameters for $Zn(ISN)_2$ and $InD(BDC)_2$ for heating (red) and cooling (blue) cycles in the temperature range of 350–520 K. The (a, b)-lattice parameters are represented by filled circles, while open circles symbolise the c-lattice parameter. For $Zn(ISN)_2$, the lattice parameters from the first 350 K temperature point were used for normalisation, whereas in $InD(BDC)_2$, the lattice parameters from the second 350 K point were used. The dotted lines in the cooling cycle of $Zn(ISN)_2$ function as guides to the eye only.

Appendix D

Supporting information for Chapter 6

D.1 Rietveld fits for [A][M(HCOO)$_3$]

For all Rietveld or Pawley fits, experimental data are given as points, the fitted profile as a solid red line, and the difference (data−fit) as a blue line. The pink *hkl* tick marks represent the [A][M(HCOO)$_3$] phase and green *hkl* tick marks indicate the metal formate dihydrate phase.

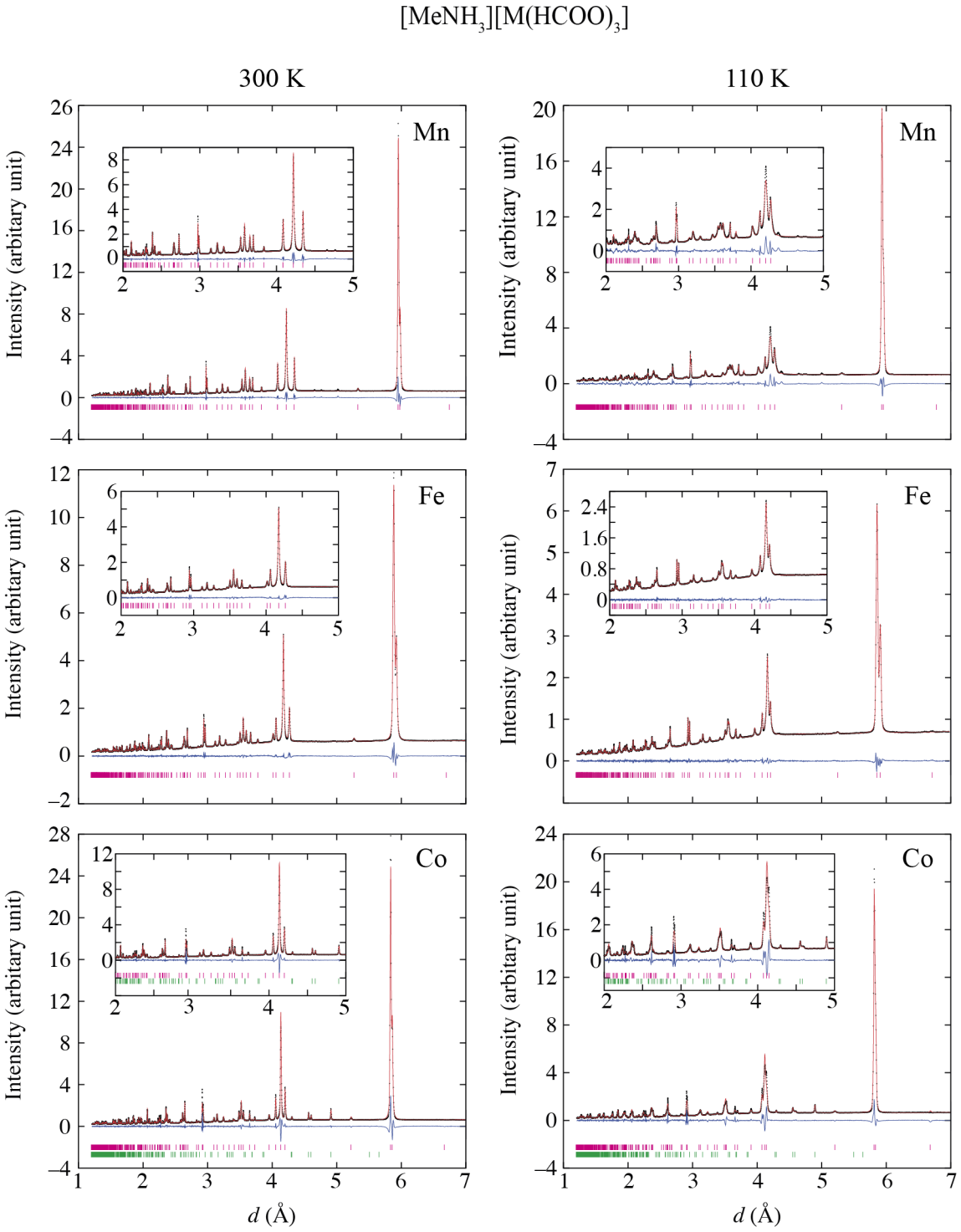

Figure D.1: Rietveld fits for $[CH_3NH_3][M(HCOO)_3]$ with M = Mn, Fe, and Co at 300 and 110 K.

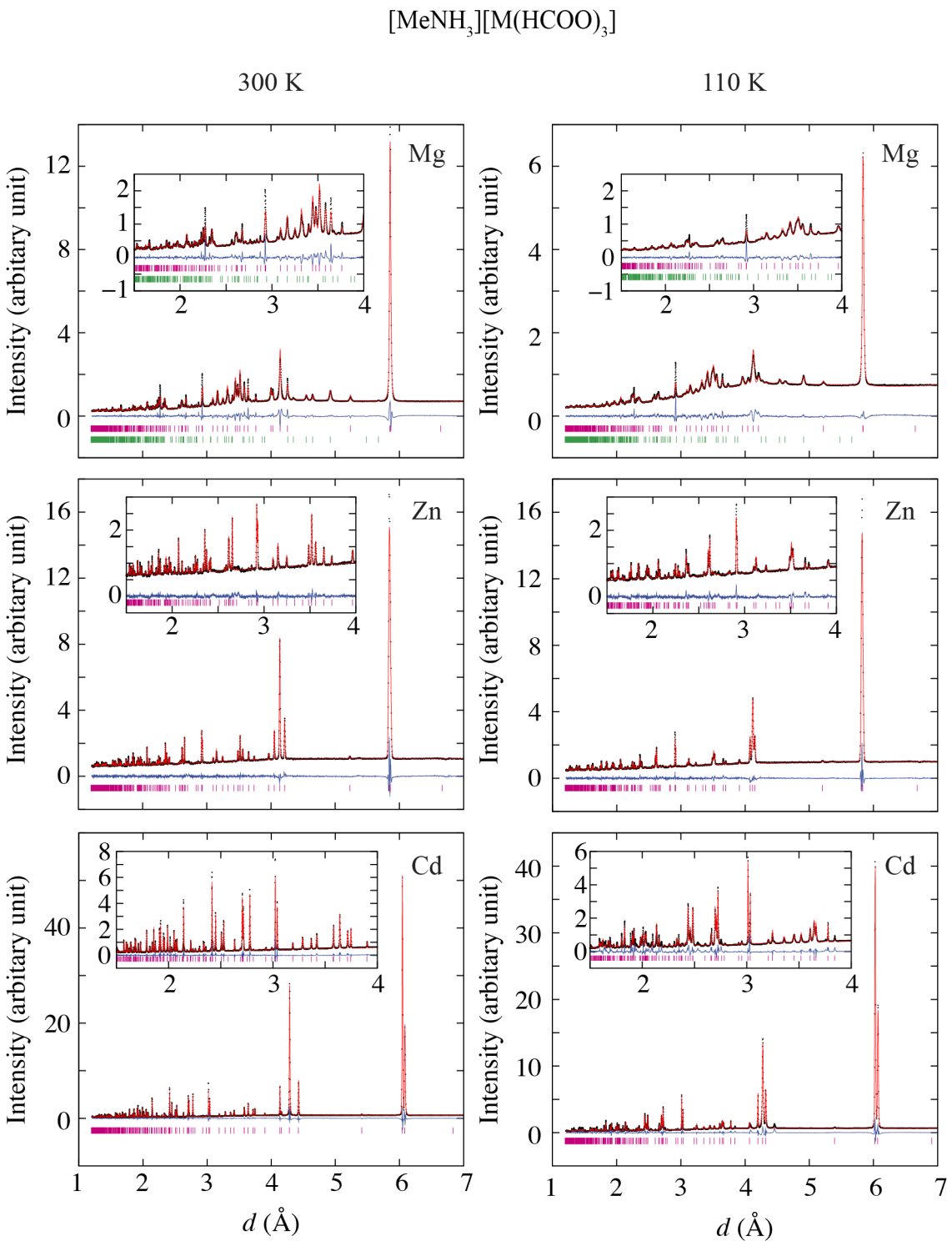

Figure D.2: Rietveld fits for $[CH_3NH_3][M(HCOO)_3]$ with M = Mg, Zn, and Cd at 300 and 110 K.

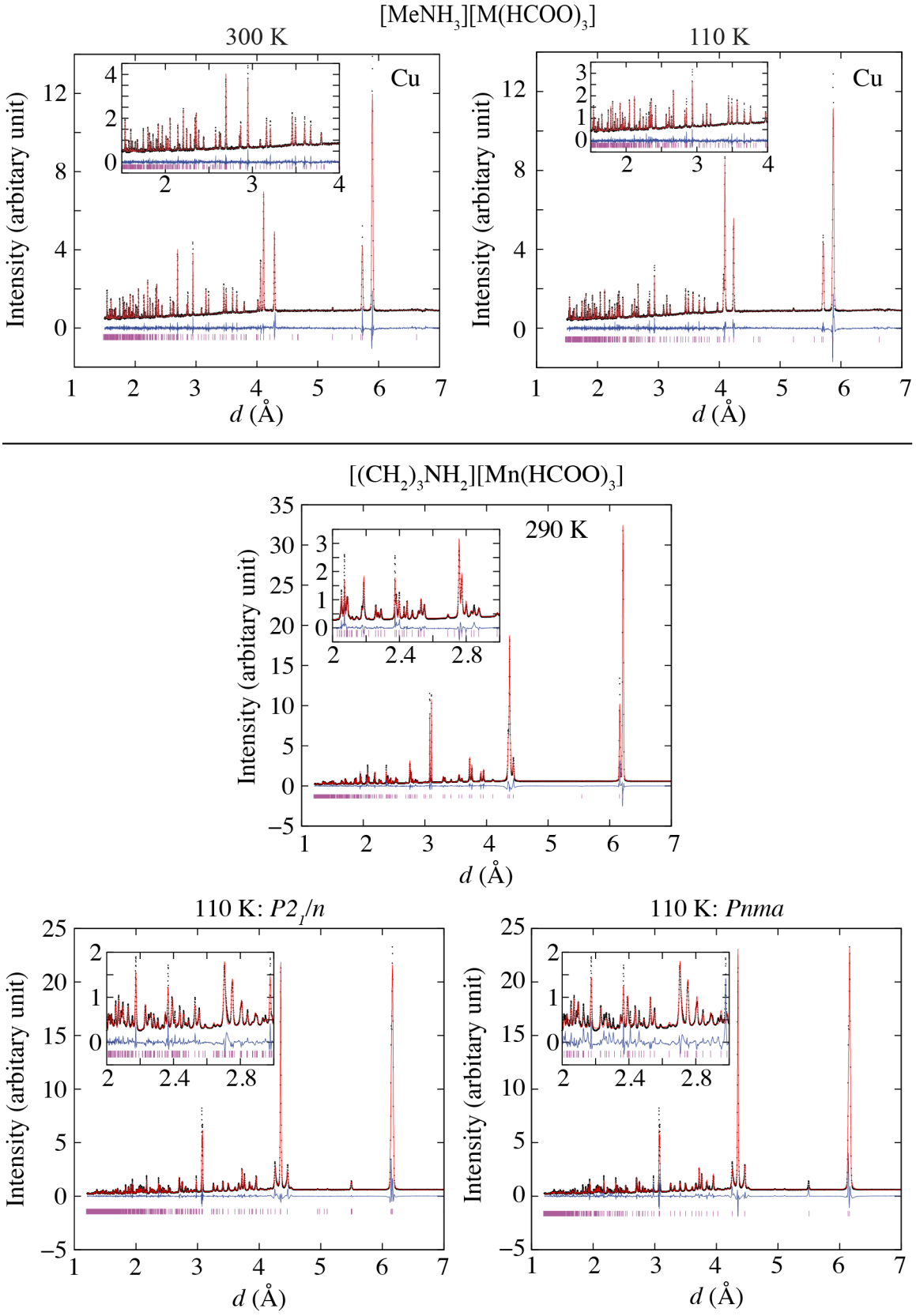

Figure D.3: (*Top*) Pawley fits for the $[CH_3NH_3][Cu(HCOO)_3]$ compound at 300 and 110 K. (*Bottom*) Rietveld fits for $[(CH_2)_3NH_2][Mn(HCOO)_3]$ at 290 and 110 K. The low-temperature diffraction is shown fitted with the monoclinic phase ($P2_1/n$) and the ambient phase (*Pnma*).

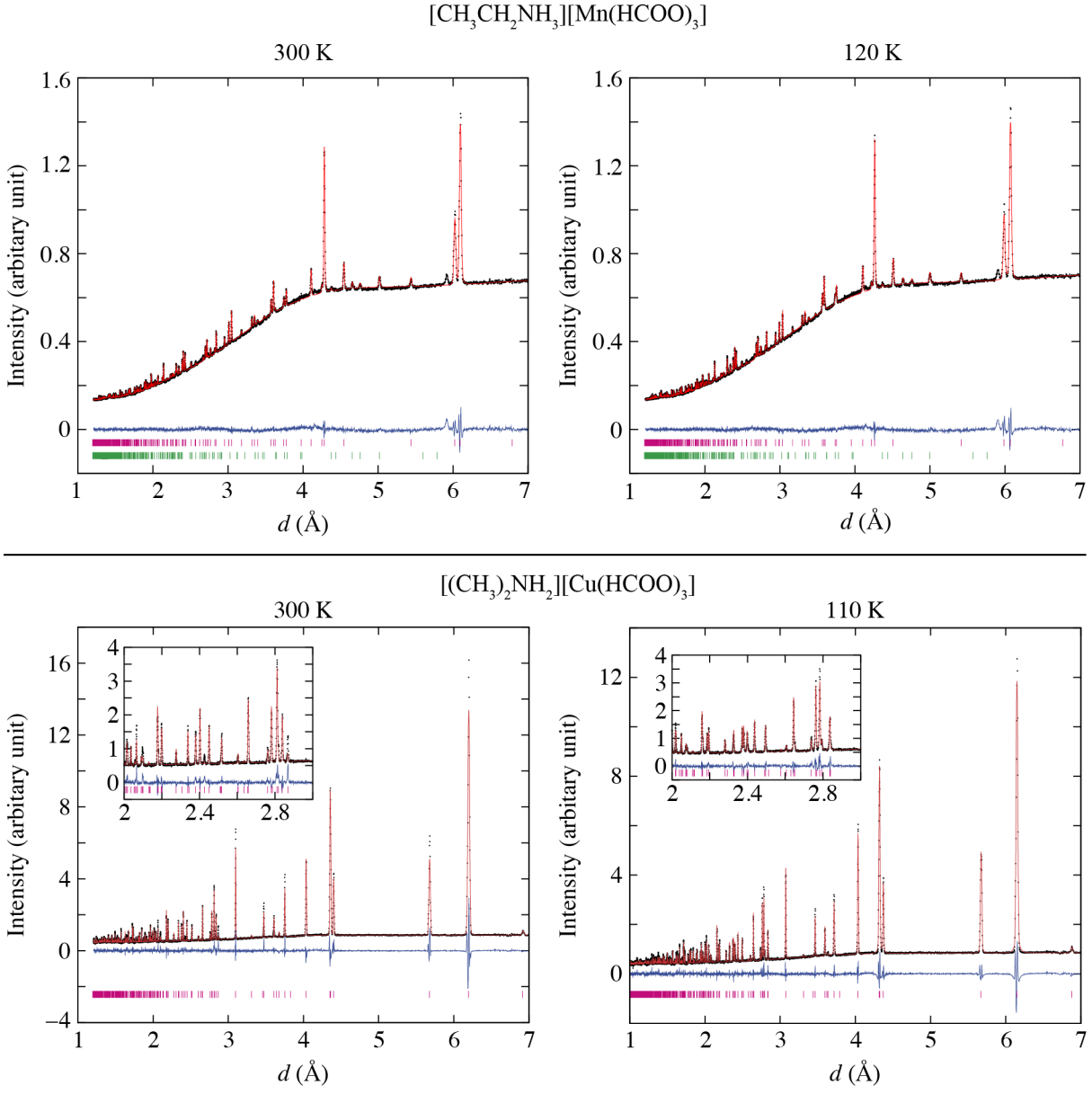

Figure D.4: (*Top*) Rietveld fits for $[CH_3CH_2NH_3][Mn(HCOO)_3]$ at 300 and 120 K. The high background is due to the low sample content in the capillary. (*Bottom*) Rietveld fits for $[(CH_3)_2NH_2][Cu(HCOO)_3]$ at 300 and 100 K, both refined in the monoclinic $C2/c$ symmetry.

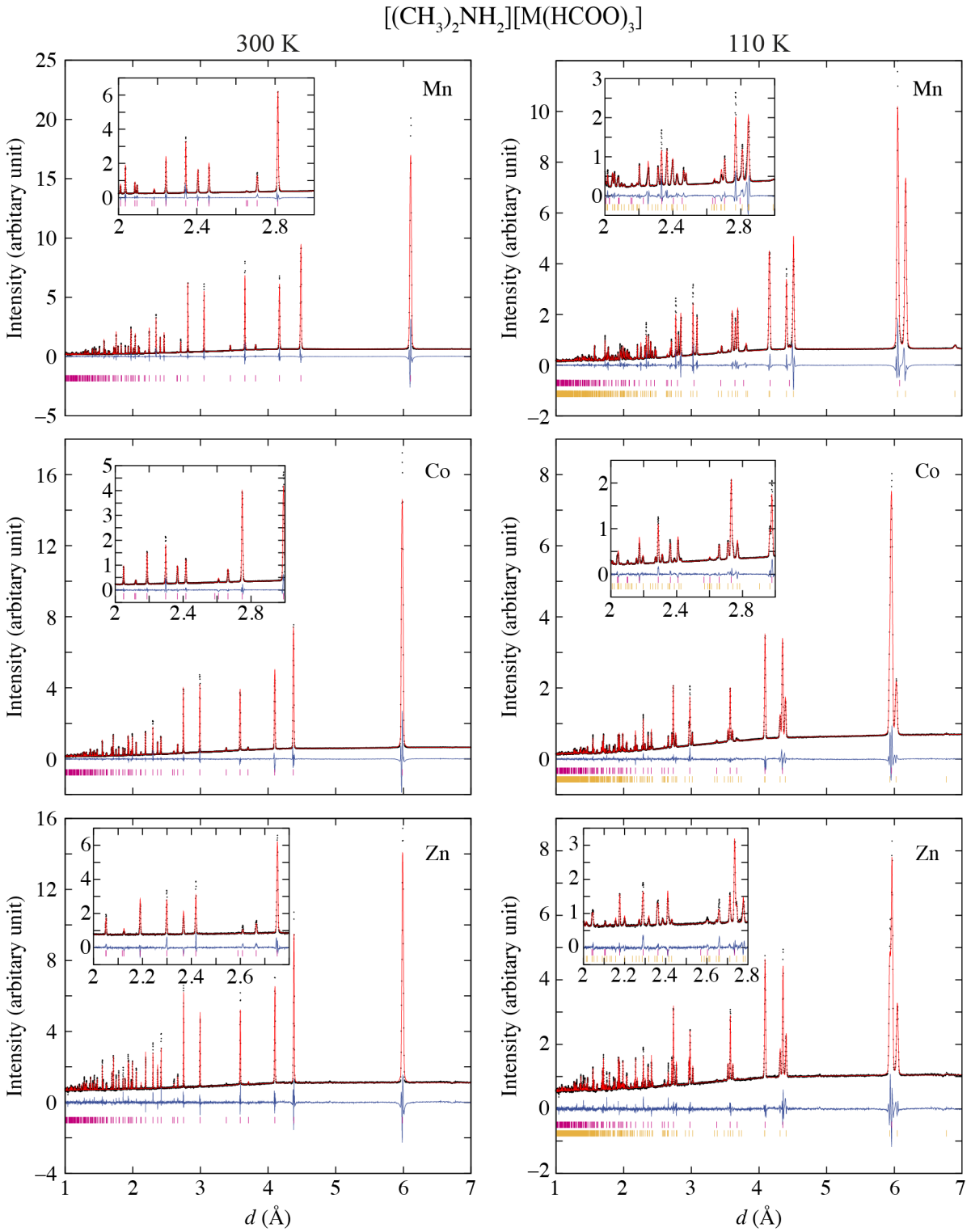

Figure D.5: Rietveld fits for $[(CH_3)_2NH_2][M(HCOO)_3]$ with M = Mn, Co, Zn at 300 and 110 K. The HT phase is indicated by pink *hkl* tick marks, while the LT phase is represented by orange *hkl* tick marks.

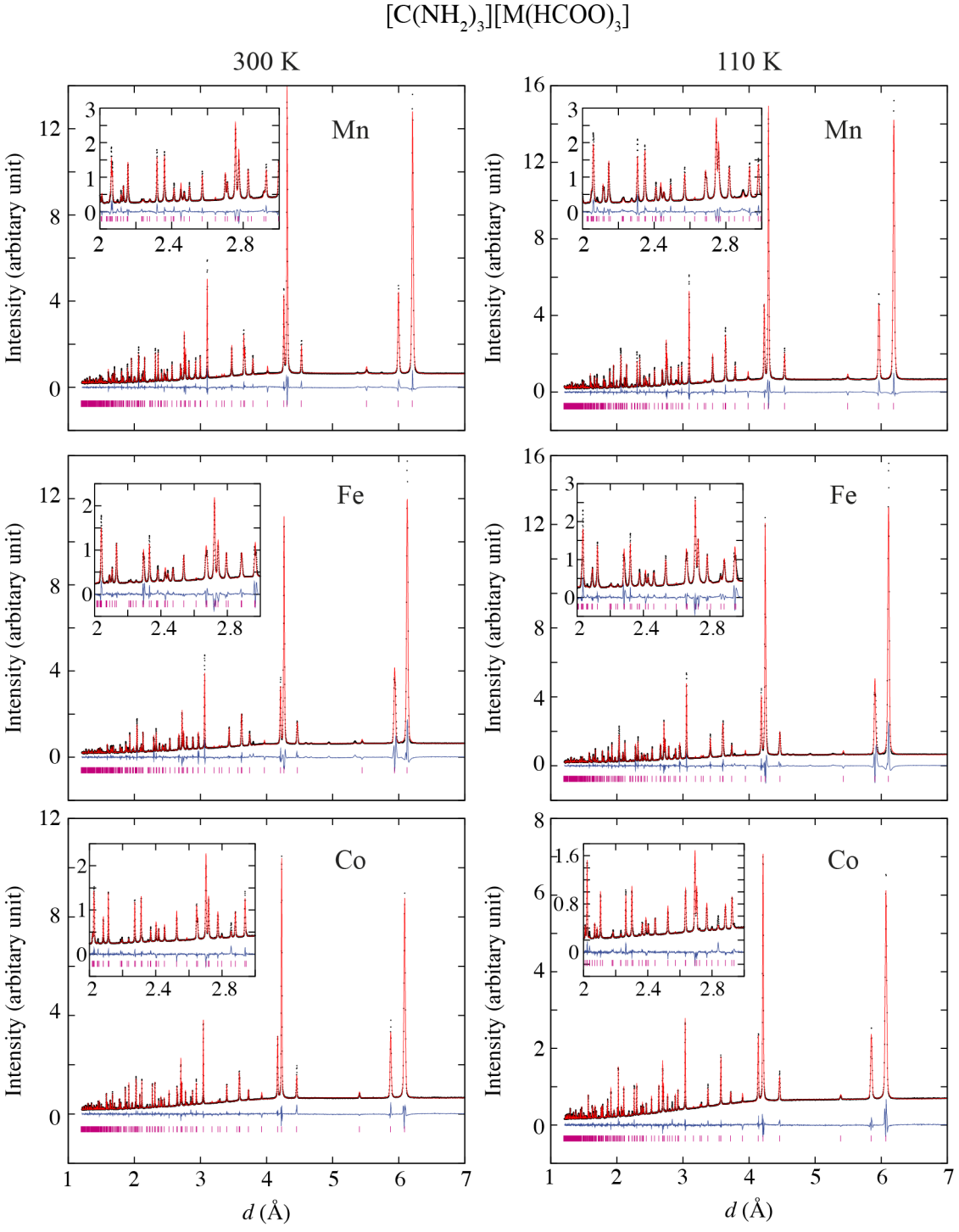

Figure D.6: Rietveld fits for $[C(NH_2)_3][M(HCOO)_3]$ with M = Mn, Fe, Co at 300 and 110 K.

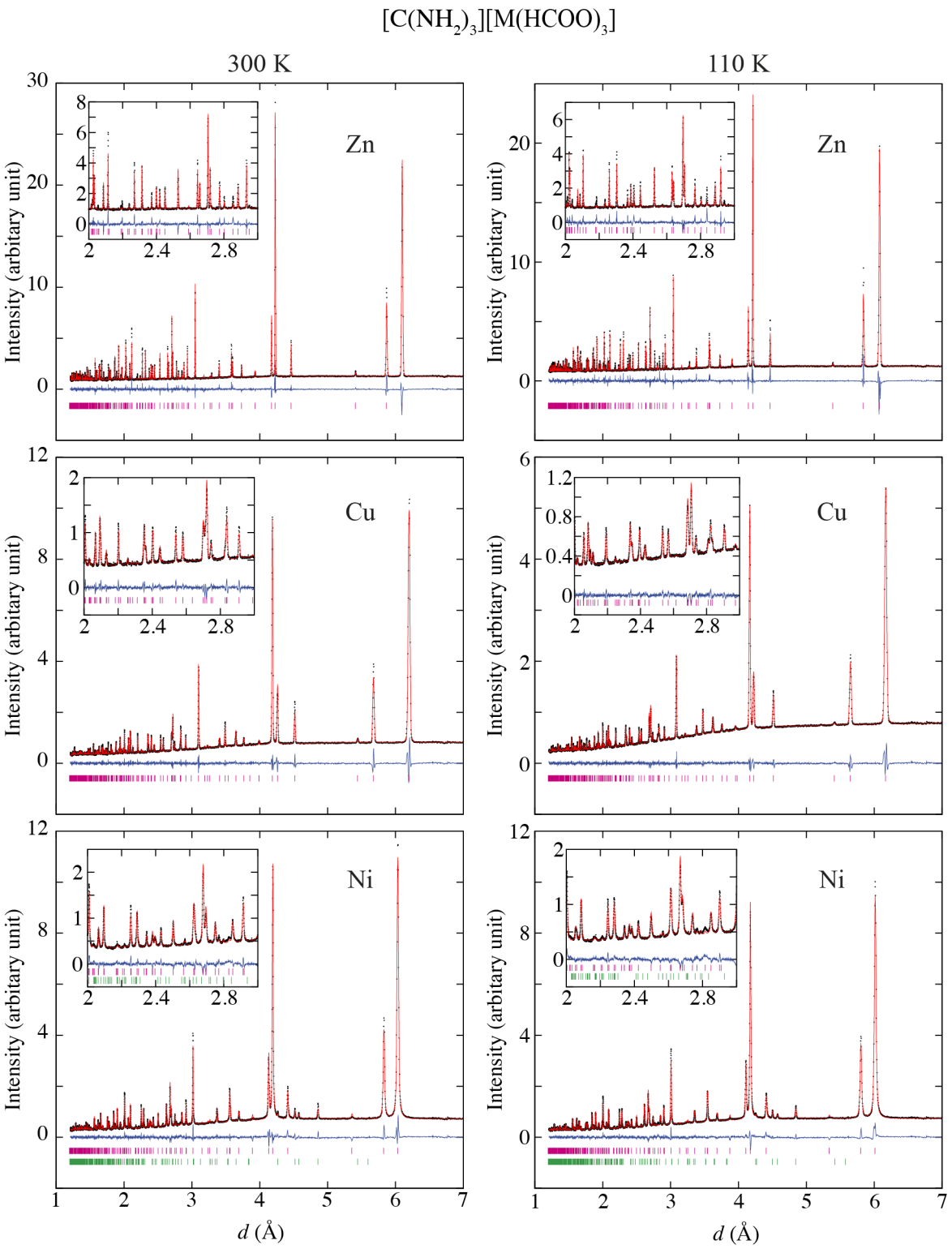

Figure D.7: Rietveld fits for $[C(NH_2)_3][M(HCOO)_3]$ with M = Ni, Cu, Zn at 300 and 110 K.

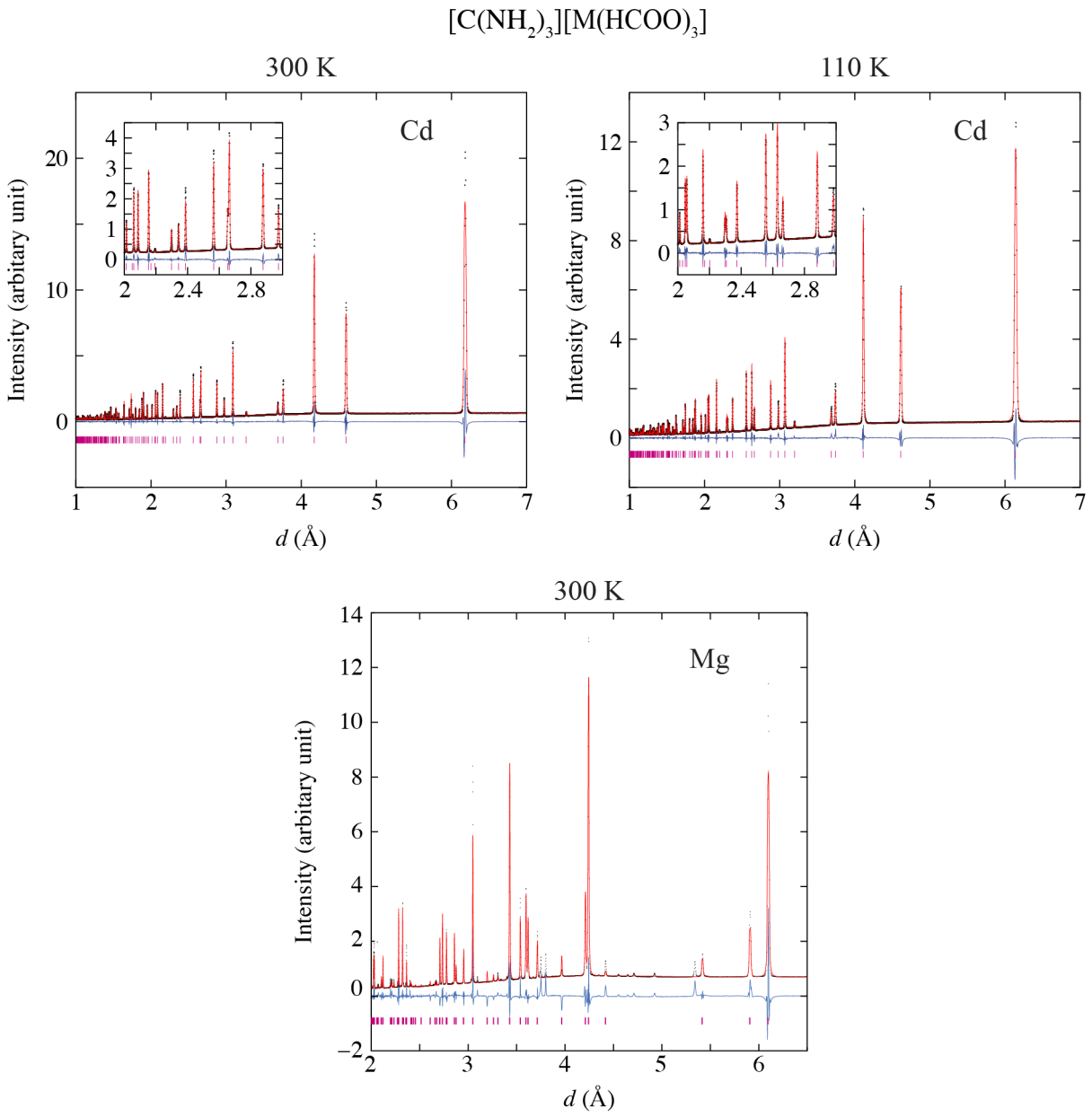

Figure D.8: Rietveld fits for $[C(NH_2)_3][M(HCOO)_3]$ with M = Cd at 300 and 110 K, and M = Mg at 300 K fitted with the *Pnna* structure of Gua-Mn.

D.1.1 Phase transitions

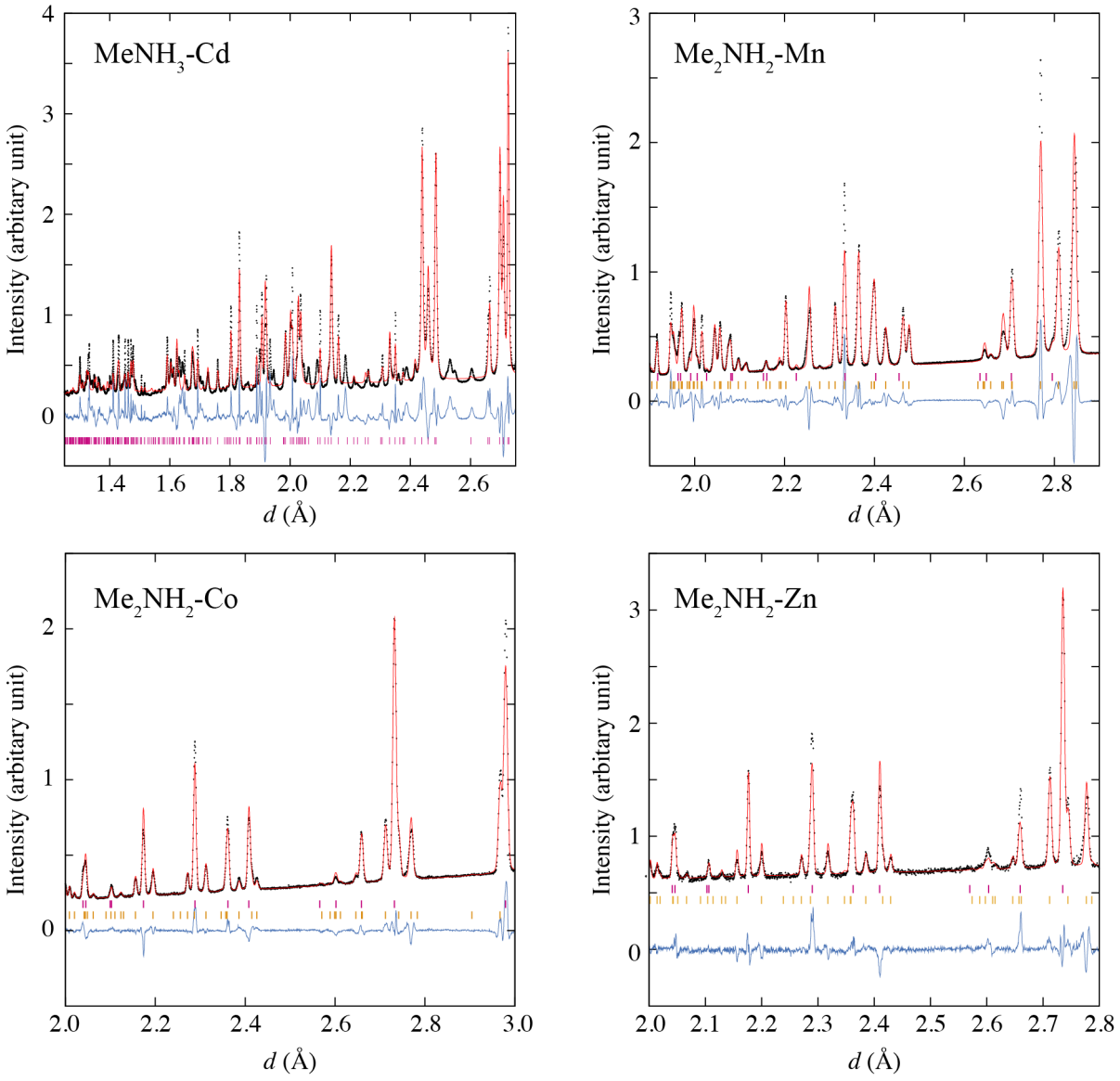

Figure D.9: Rietveld fits for $[CH_3NH_3][Cd(HCOO)_3]$ and $[(CH_3)_2NH_2][M(HCOO)_3]$ with M = Mn, Co, and Zn at 110 K, in a low *d*-spacing zoom. The diffraction patterns show the extra unfitted peaks for $MeNH_3$-Cd and the coexistence of the HT and LT phases (pink and orange *hkl* tick marks, respectively) for Me_2NH_2-M.

D.2 Lattice parameter evolutions for [A][M(HCOO)$_3$]

The lattice parameter evolutions as a function of temperature (110–300 K) for the [A][M(HCOO)$_3$] compounds investigated are found in Figures D.10–D.13. In all figures, the cooling data are indicated by the blue circles, and the heating data by red circles. The black dotted lines indicate the linear fits used to calculate the CTEs; the error on each of the CTEs is then calculated based upon the discrepancy between the linear fit and the data. Table D.1 gives the CTEs for the monoclinic and orthorhombic phases of [$(CH_2)_3NH_2$][Mn(HCOO)$_3$].

Table D.1: Calculated linear expansivities for the HT phase of Aze-Mn (*Pnna* symmetry), and the LT-phase arising below ∼250 K. In the HT-phase, the $\mathbf{x}_1$, $\mathbf{x}_2$, and $\mathbf{x}_3$ directions correspond to **a**, **b**, and **c** lattice vectors, respectively, while for the LT phase: $\mathbf{x}_1 = -0.6793\mathbf{a}+0.7339\mathbf{c}$, $\mathbf{x}_2 = \mathbf{b}$, and $\mathbf{x}_3 = 0.7326\mathbf{a}+0.6807\mathbf{c}$.

Symmetry	T range (K)	α (MK^{-1})		
		$\mathbf{x}_1$	$\mathbf{x}_2$	$\mathbf{x}_3$
Pnna	110–300	104(8)	15.3(1.2)	−21(6)
$P2_1/n$	110–260	109(11)	11.5(16)	−27(8)

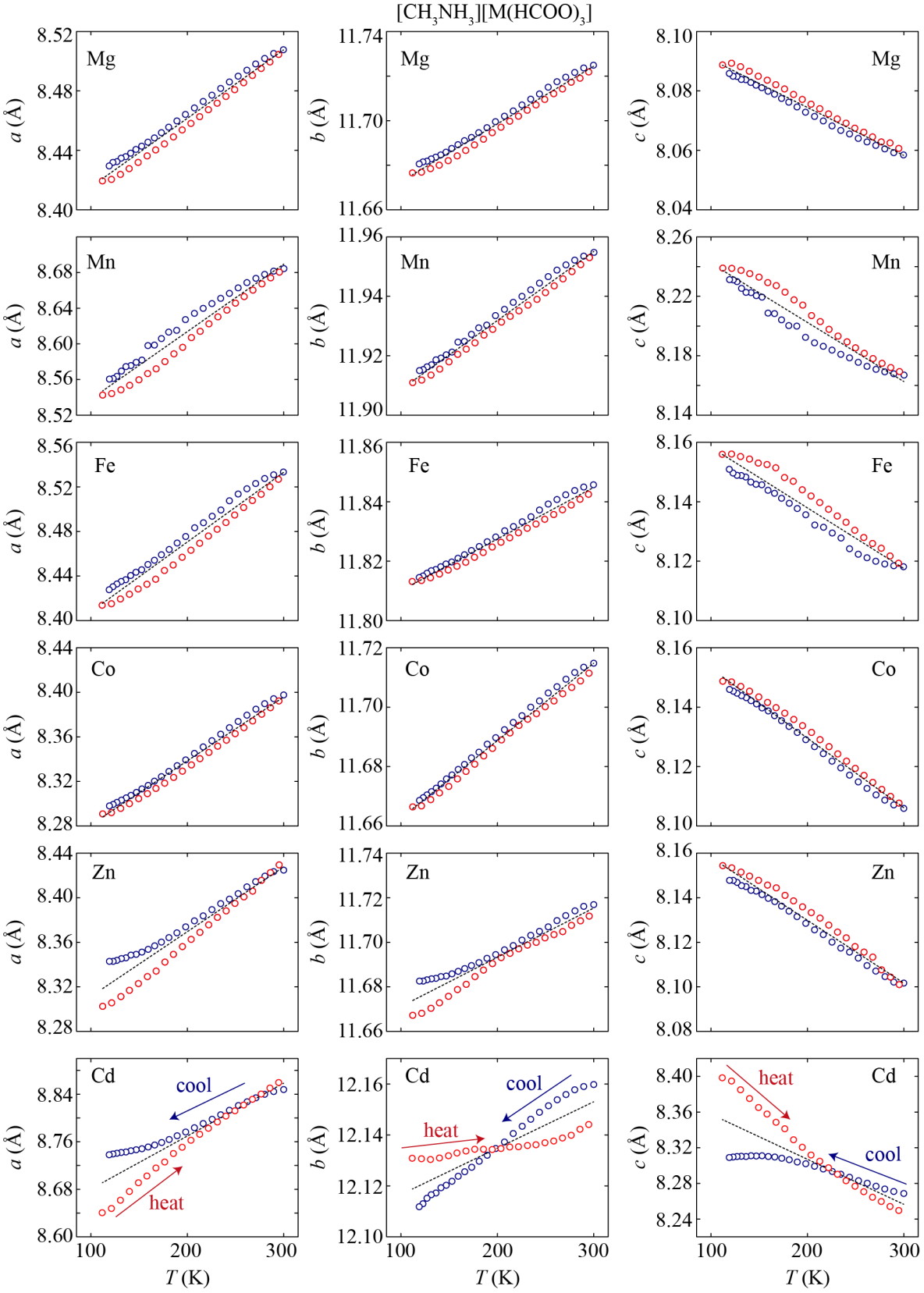

Figure D.10: Lattice parameter evolutions as a function of temperature for the $[CH_3NH_3][M(HCOO)_3]$ family.

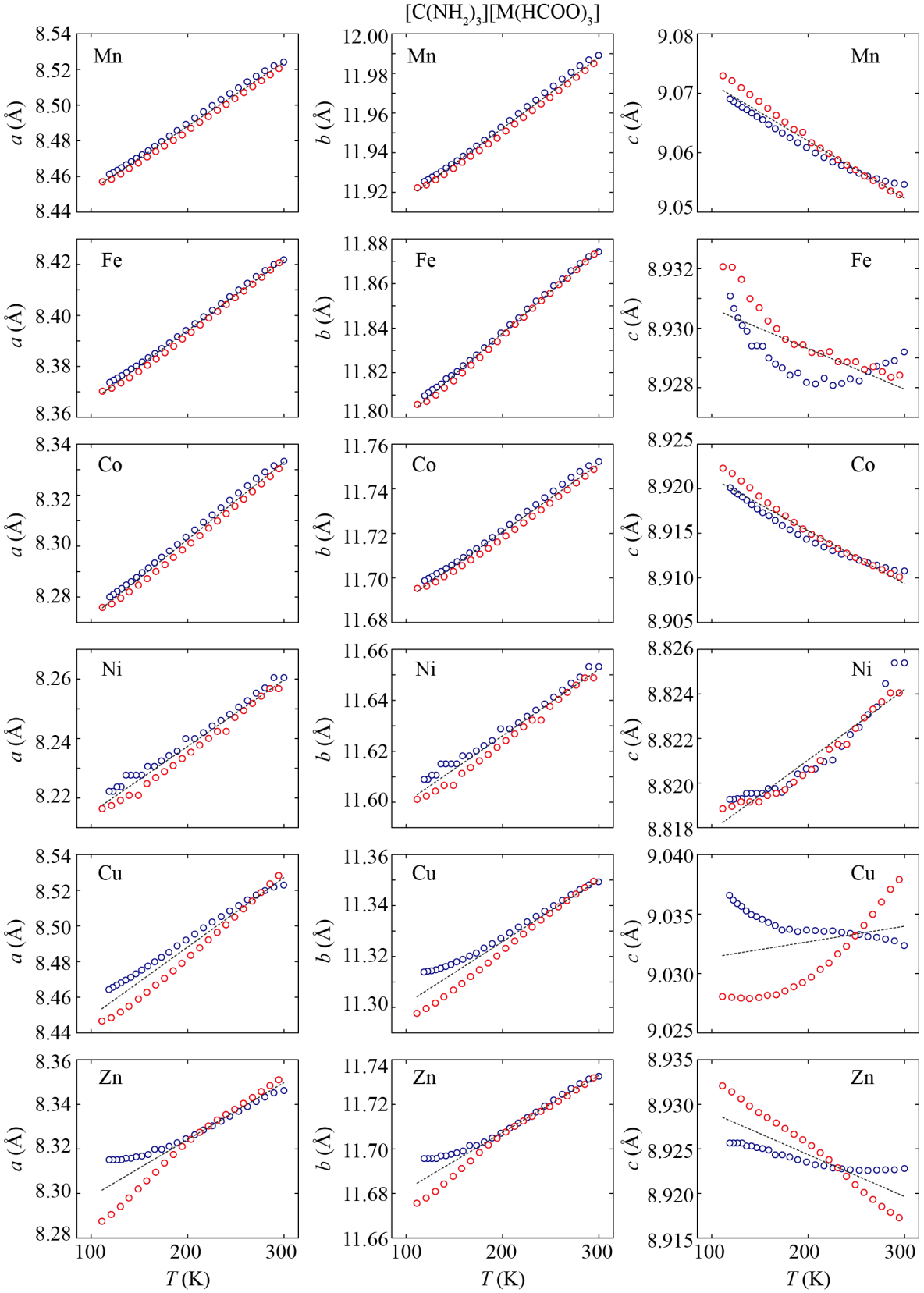

Figure D.11: Lattice parameter evolutions as a function of temperature for the $[C(NH_2)_3][M(HCOO)_3]$ family.

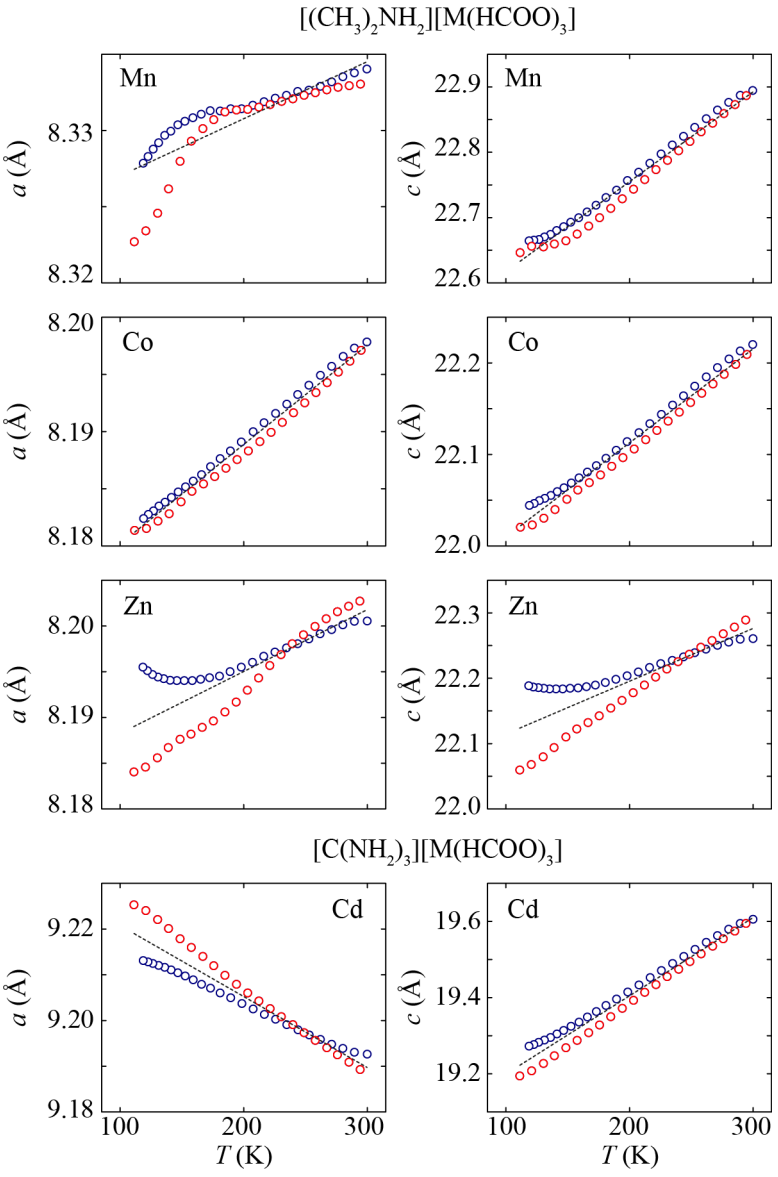

Figure D.12: Lattice parameter evolutions as a function of temperature for the $[(CH_3)_2NH_2][M(HCOO)_3]$ family and $[C(NH_2)_3][Cd(HCOO)_3]$.

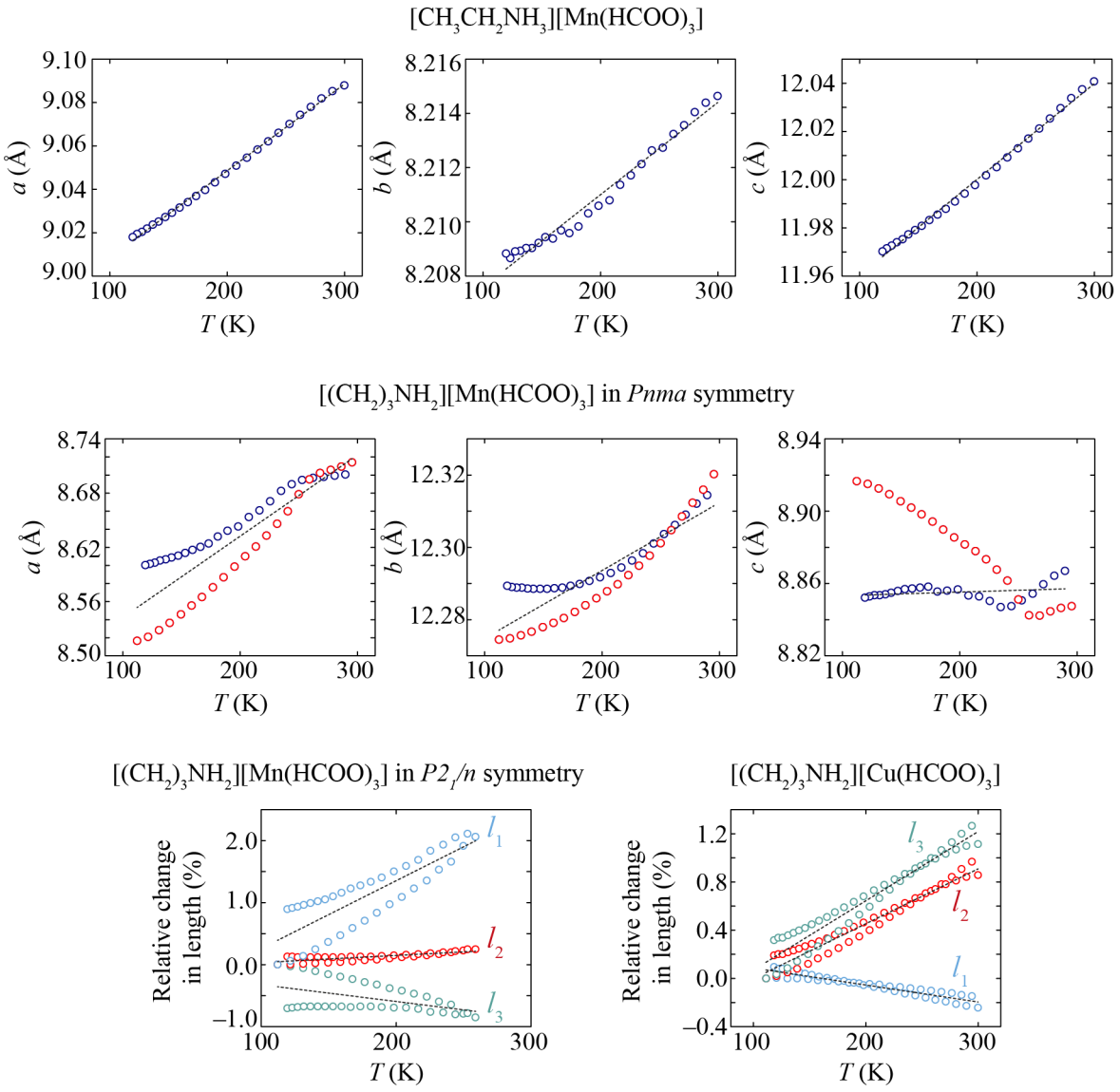

Figure D.13: (*Top*) Lattice parameter evolutions as a function of temperature for $[CH_3CH_2NH_3][Mn(HCOO)_3]$, and $[(CH_2)_3NH_2][Mn(HCOO)_3]$ refined in orthorhombic *Pnma* symmetry. (*Bottom*) The relative changes in principal axes for the monoclinic structures: LT $[(CH_2)_3NH_2][Mn(HCOO)_3]$ and $[(CH_3)_2NH_2][Cu(HCOO)_3]$.

Appendix E

Local structure and dynamics in MOFs

From the transverse vibrational modes identified in MOF-5 and HKUST-1,[133–136] to the amorphisation processes of ZIFs,[12,13,96,97] there are many examples that suggest low-energy phonons and rich dynamical properties are inherent properties of flexible coordination polymers. In this appendix chapter, the dynamics of two coordination polymers are investigated, namely $Zn(ISN)_2$ (already introduced in Chapter 5) and ammonium zinc formate $[NH_4][Zn(HCOO)_3]$, which is a denser version of the perovskite $[A][M(HCOO)_3]$ structures discussed in Chapter 6. The purpose of studying the former quartz-like MOF was to characterise the low-temperature dynamics of the framework and compare these to the known dynamics in quartz.[342] The results from this work can be found in the publication: I. E. Collings, M. G. Tucker, D. A. Keen, and A. L. Goodwin, *Z. Kristallogr.*, 2012, **227**, 313–320. The ammonium zinc formate was studied because it exhibits an order–disorder ferroelectric transition that arises from collective reorientations of the ammonium cations.[314] This phenomenon is known to occur for the average crystal structures, but the local structure associated with this transition is not known.

Neutron total scattering was used as the experimental technique for these investigations, allowing the local and average structures of the frameworks to be examined. Traditionally, neutron total scattering was applied to liquid and amorphous systems, but is now increasingly used to understand disorder in powdered crystalline materials. For instance, total scattering was used to elucidate

disorder in β-cristobalite,[36] the origin of NTE in ZrW_2O_8,[126] and the nanoscale ferroelectric domains in $SrSnO_3$.[343]

This appendix chapter is divided into two parts. The first is dedicated to the dynamics of $Zn(ISN)_2$ at 10 K, and the second to the order–disorder ferroelectric phase transition in ammonium zinc formate.

E.1 Low-temperature dynamics of $Zn(ISN)_2$

E.1.1 Experimental

Many of the relevant experimental details have already been covered in Chapter 5. Additional details are provided here.

E.1.1.1 Neutron total scattering measurements

Total-scattering data were collected at 10, 100, and 300 K over a large range of scattering vectors of magnitudes $0.52 \leq Q \leq 40$ Å^{-1}, giving a real-space resolution of the order

$$\Delta r \simeq 3.791/Q_{\max} \simeq 0.095\,\text{Å}. \tag{E.1}$$

E.1.1.2 Total scattering data correction

As discussed in Section 2.2.4.1, total scattering data normalisation relies on an accurate knowledge of sample composition. However, the unquantified amounts of solvent in the framework pores of $Zn(ISN)_2$ [Section 5.2.2 and Fig. C.1] meant that there was ambiguity concerning its chemical composition. In addition to the uncertainty in the sample composition, the presence of the hydrogen-containing solvent molecules gave rise to large backgrounds in the collected data. These are due to the incoherent scattering of neutrons by hydrogen atoms [Table 2.1]. The hydrogen-affected backgrounds are apparent by inspection of the measured differential cross-section data

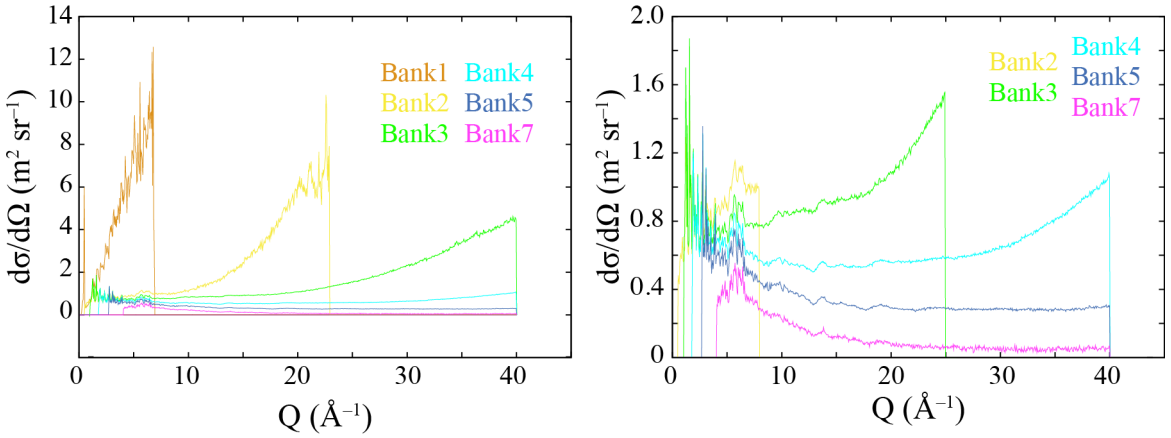

Figure E.1: (*Left*) Differential cross-section data for $Zn(ISN)_2$ in the full data range for all GEM detector banks, represented by the different colours to match those defined in Figure 2.5. (*Right*) The differential cross-section data ranges that were used for correcting the total scattering data of $Zn(ISN)_2$.

from the different GEM detector banks, where these data are expected to overlap in an ideal case [Fig. E.1].

A top hat convolution method was used in GUDRUN in order to subtract the background associated with each detector bank.[§] This allowed the data to be merged into a single structure factor.[344] Still, the ambiguity in sample composition meant that additional considerations were taken for the RMC fitting procedure, discussed in greater detail in Section E.1.1.4.

E.1.1.3 Rietveld refinement

The corresponding Bragg profile functions for all data were obtained using the Mantid program.[345] The experimental Bragg diffraction patterns of four detector banks, centred on scattering angles $2\theta = 34.96°, 63.62°, 91.30°$, and $154.40°$, were fitted simultaneously with the GSAS Rietveld refinement program.[248,249] Both the published $P3_1$ and $P6_2$ structural models were used, but as there was no evidence for symmetry lowering, the $P6_2$ model was employed.[295,296] Atomic coordinates of the organic ligand were refined using rigid body constraints in order to minimise the number of refinable parameters; likewise a single set of anisotropic displacement parameters was refined for all atoms in the isonicotinate group. Zn atom coordinates were refined while fixing the z-coordinate (there being no unique origin in z for either $P3_1$ or $P6_2$) and an isotropic displacement

[§]The total scattering data correction for $Zn(ISN)_2$ was carried out by Prof David Keen.

parameter was allowed to refine freely. Solvent occupancy within the pore network was tested for a number of different values, and the best fit was obtained using a model containing four water molecules per formula unit, discussed in more detail in Section E.1.2.

E.1.1.4 Reverse Monte Carlo refinement

The starting configurations for RMC were based on an orthogonal supercell related to the crystallographic cell of $Zn(ISN)_2$ by the transformation

$$\begin{bmatrix} \mathbf{a} \\ \mathbf{b} \\ \mathbf{c} \end{bmatrix}_{\mathrm{RMC}} = \begin{bmatrix} 4 & 0 & 0 \\ 2 & 4 & 0 \\ 0 & 0 & 10 \end{bmatrix} \times \begin{bmatrix} \mathbf{a} \\ \mathbf{b} \\ \mathbf{c} \end{bmatrix}_{P6_2} . \tag{E.2}$$

The use of orthogonal axes in RMC maximises the pair distribution cut-off value r_{max} for a given number of atoms, and thus minimises unnecessary computational expense. This supercell had dimensions: 60.14 Å × 53.82 Å × 61.36 Å, and contained 18 720 atoms, of which 12 960 were part of the framework and 5 760 were part of the included water molecules. The configuration contained six different atom types (C, D, H, N, O, Zn), giving rise to a total of 21 partial $g_{ij}(r)$ contributions (which is the largest number refined to date using the RMCPROFILE code). A number of soft constraints and restraints were applied throughout the refinement process: closest-approach constraints prevented atom pairs from being separated by unphysically short distances; 'distance-window' constraints maintained the framework connectivity without prejudicing the bond-bending and bond-stretching terms [Table E.1]; and, finally, a set of empirical geometric restraints were applied to maintain the geometry of the isonicotinate ligand.[13]

The refinement process was driven by fitting to the experimental $F(Q)$ ($0.6 \leq Q \leq 40\,\text{Å}^{-1}$), $I(t)$ ($5350 \leq t \leq 19370\,\mu\text{s}$; equivalent to the d-spacing range 1.1–4 Å) and $G(r)$ ($1.7 \leq r \leq 25.2\,\text{Å}$) functions. A total of five independent RMC refinements were performed in parallel; each refinement was allowed to continue until no further improvements in the fits to data were observed. The five independent RMC refinements originated from the same average-structure model, which was

Table E.1: 'Distance-window' parameters $d_{\min}$, $d_{\max}$ used in the RMC refinements and the corresponding mean pair separations $\bar{d}$ and their standard deviations σ after a converged RMC refinement.

Atom pair	$d_{\min}$ (Å)	$d_{\max}$ (Å)	$\bar{d}$ (Å)	σ (Å)
O–H	0.8	1.1	1.006	0.076
C–D	0.9	1.2	1.039	0.072
C–C	1.1	1.7	1.431	0.062
C–N	1.1	1.7	1.321	0.055
C–O	1.1	1.7	1.268	0.040
Zn–O	1.8	2.4	2.004	0.128
Zn–N	1.8	2.4	2.081	0.104

then randomised by allowing each atomic configuration to move without fitting to any data. After this process, the five random configurations were fitted to the $F(Q)$, $G(r)$ and $I(t)$ functions. The absolute atomic coordinates differ amongst the five final configurations, but the corresponding fits to data, average positions, and pairwise correlation functions are essentially identical. Wherever possible, the results presented are averaged over all five configurations.

Due to the uncertainty in the sample composition of $Zn(ISN)_2$, three particular adjustments were made for the RMC fitting procedures. Firstly, the calculated $G(r)$ and $F(Q)$ functions from the RMC configuration were allowed to refine an overall scaling parameter to fit the experimental $G(r)$ and $F(Q)$. While refinement of a scale factor is not usually used for the RMC technique, it is an approach that is applied commonly in other PDF fitting procedures.[346] Secondly, because the water molecules in the RMC model are a simplification of the actual solvent present [Fig. C.1], the low-r region was excluded from RMC fitting in order to preserve the local structure of the ISN ligands. In particular, $r \leq 1.7$ Å was excluded because the local structure of the likely solvents, as well as that of the ISN, all have nearest-bonding distances below 1.7 Å. Thirdly, a smoothly-varying function was subtracted from the normalised data [Fig. E.4(c,d)]. This did not affect the final model but improved visually the quality of the fits to data, and was applied due to the difficulty in quantitative normalisation of the $G(r)$ function.

Table E.2: Crystallographic parameters, atomic coordinates and isotropic equivalent displacement parameters determined using Rietveld refinement of neutron scattering data for $Zn(ISN)_2$. The ISN coordinates are given as the centre-of-mass of the ligand. The water coordinates are represented by those of the oxygen atoms. The first set of positional and displacement parameters corresponds to the final structural model containing four H_2O molecules per formula unit; the second (marked with an asterisk) corresponds to the solvent-free model discussed in the text.

Crystal system	Hexagonal			
Space group	$P6_2$			
a (Å)	15.5362(3)			
c (Å)	6.1356(3)			
V (Å^3)	1282.54(6)			
Z	3			
T (K)	10			
Atom	x	y	z	U_{eq} (Å^2)
Zn	0.5	0	0	0.016(2)
ISN	0.26254(8)	0.79743(9)	0.3603(11)	0.0231(3)
H_2O	0.7630(9)	0.8004(7)	0.125(4)	0.352(6)
H_2O	0.8143(8)	1.0300(8)	0.2087(16)	0.352(6)
Zn*	0.5	0	0	0.017(4)
ISN*	0.26315(15)	0.79512(17)	0.381(3)	0.0193(7)

E.1.2 Average structure of $Zn(ISN)_2$

Both crystal structures of Refs. 295 and 296 were used as starting models for the Rietveld refinement; in both cases the corresponding models include two water molecules per formula unit within the framework pore structure. The first set of refinements involved simply removing the solvent component and refining framework coordinates. Essentially identical fits were obtained for both $P3_1$ and $P6_2$ models, neither of which fitted the peak intensities well [Fig. E.2(a), $wR_p = 0.255$]. A considerable improvement to the quality of these fits was obtained by including scattering density within the framework pores. A number of different ways of modelling this scattering density were tested—including the H_2O coordinates of Refs. 295 and 296—but the best fits were obtained for a slightly different model containing four H_2O molecules per formula unit [Fig. E.2(b), $wR_p = 0.0156$]. The corresponding crystallographic details are summarised in Table E.2.

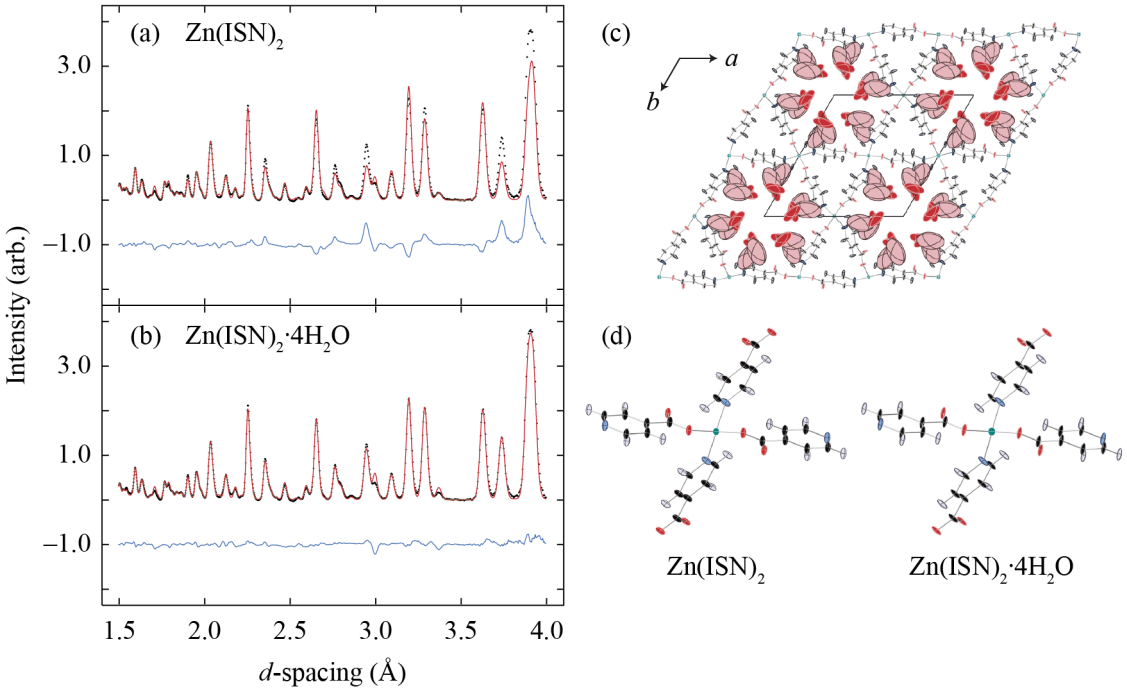

Figure E.2: Representative Rietveld fits to the 10 K neutron diffraction pattern of $Zn(ISN)_2$: (a) using an empty-framework model, and (b) using a model containing four water molecules per formula unit. In both cases, the $P6_2$ symmetry was applied. Experimental data are given as points, the fitted profile as a solid red line, and the difference (data−fit) as a blue line shifted downwards by one unit. Fits are shown for the data obtained from the detector centred on $2\theta = 63.62°$. (c) Extended structure of $Zn(ISN)_2{\cdot}4H_2O$ with thermal ellipsoids shown in 50% probability. (d) Local coordination environment around Zn(II) as found in $Zn(ISN)_2$ and $Zn(ISN)_2{\cdot}4H_2O$. Atom colours represent the different atom types, where green is Zn, blue is N, red is O, black is C, grey is D, and pink is H.

It is certainly feasible that the $Zn(ISN)_2$ sample absorbed atmospheric H_2O during setup of the GEM experiment or that residual H_2O or DMSO (used in the synthesis) remained following incomplete desolvation during sample preparation. As all of the various solvent-containing models that were tested exhibited large displacement parameters and fractional occupancies of multiple equivalent sites, the diffraction intensities alone were not sufficiently sensitive to identify the chemical composition of the solvent. Instead, the extent to which the structural parameters of the framework itself were affected by the different models was assessed. The positions and atomic displacement parameters obtained for the $Zn(ISN)_2{\cdot}4H_2O$ and solvent-free models are given in Table E.2 and visualised in Figure E.2(d); their close correspondence illustrates that the framework geometry is robustly defined by the diffraction data, even if those of the solvent component are

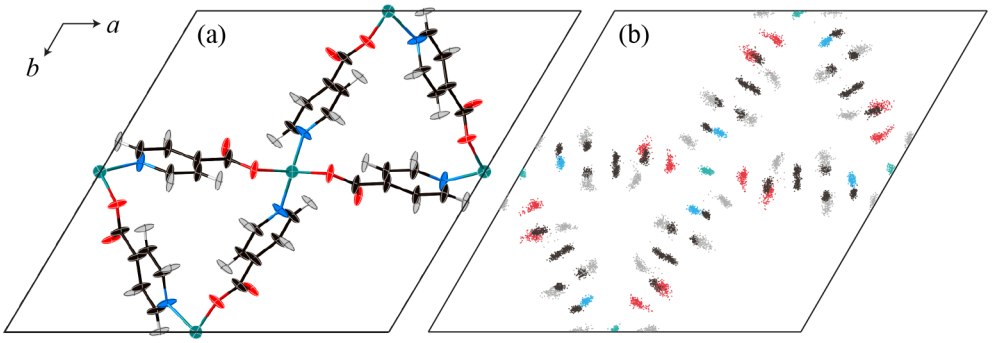

Figure E.3: Unit cell projections of $Zn(ISN)_2$ viewed down the *c*-axis, showing (a) the Rietveld model and (b) the atomic distributions obtained by collapsing the RMC configuration onto a single unit cell. Atom colours describe atom types as detailed in Figure E.2; water molecules have been omitted for clarity.

not.

It was possible to refine reliably a set of anisotropic displacement parameters for the ISN ligand. The values obtained correspond to thermal ellipsoids that are strongly elongated in a direction perpendicular to the plane of the ligand itself [Fig. E.3(a)]. This sort of behaviour is not uncommon for coordination polymers, since the lowest-energy vibrational modes usually involve transverse displacements of the bridging ligand.[128,135] However, the magnitude of the thermal ellipsoids is unusual given that the data were collected at 10 K. The wide range of GEM detector banks used in the Rietveld refinement, including data at sufficiently low *d*-spacing values, does allow reliable determination of thermal displacement parameters. The origin of the large displacement parameters is discussed in more detail in Section E.1.4.

E.1.3 Local structure of $Zn(ISN)_2$

With the strong preference for a structural model containing four water molecules per formula unit in Rietveld refinements, this same model was used as a starting point for RMC. RMC refinement gave fits to the Bragg diffraction pattern that were essentially identical to those obtained by Rietveld refinement [Fig. E.4(a)]. As anticipated, the water molecules were strongly disordered in the final RMC configurations and consequently the analysis focusses on the local structure of the $Zn(ISN)_2$ framework itself.

By 'collapsing' the atomic coordinates of each refined RMC configuration onto a single unit cell, it is possible to visualise the average structure model to which these configurations correspond. The 'collapsed' RMC configuration of $Zn(ISN)_2$ shows a clear similarity to its structural model from the Rietveld refinement [Fig. E.3(b)]. In particular, there are large anisotropic displacements of the ISN ligand that reflect well the displacement parameters determined from the Rietveld fits. Whereas the Rietveld refinement employed rigid-body constraints and a single set of displacement parameters for all atoms within the ISN ligand, the RMC refinement allows the scattering distribution for each atomic site to assume whatever form is demanded by the data. There are small differences amongst the atomic distributions for the various atoms in the ISN ligand, but for all ISN atoms the displacements are much stronger in a direction perpendicular to the ligand plane.

The absence of pronounced features in the PDF beyond $r \simeq 5\,\text{Å}$ is unusual, especially so for data collected at 10 K [Fig. E.4(b–d)]. Even for a structure with a disordered component, the framework itself would be expected to give rise to a well-structured $G(r)$ function: the superposition of two functions—one strongly varying and the other weakly varying—still varies strongly. Consequently, the broad $G(r)$ function suggests a large degree of disorder in the framework geometry of $Zn(ISN)_2$.

The local disorder in $Zn(ISN)_2$ was investigated by calculating two different polyhedral angles from the RMC configurations. The first corresponds to the angles within the $[ZnN_2O_2]$ coordination tetrahedra [Fig. E.5(a)]. The second type of angle is based on the centres of mass of the ISN ligands (represented by the symbol 'X') [Fig. E.5(b)]. The X–Zn–X angle distributions are analogous to the O–Si–O tetrahedral angle distribution in α-quartz itself. The distributions in both cases are very broad, suggesting that $Zn(ISN)_2$ is flexible both on the scale of the framework itself and also in terms of the individual coordination tetrahedra.

The degree of structural distortion can be quantified further using the language of geometric algebra (GA).[347] Analysis of RMC configurations using the GA-based code GASP[347–349] allows the atomic displacements of $[ZnN_2O_2]$ and $[ZnX_4]$ tetrahedra [Fig. E.5(c)] to be understood in terms of (*i*) rigid-unit translations, (*ii*) rigid-unit rotations, and (*iii*) distortions. The latter involve bond stretching and coordination angle changes (referred to as 'bending'). The first two displacements are known as RUMs, and are low-energy, while the distortions are usually considered as higher

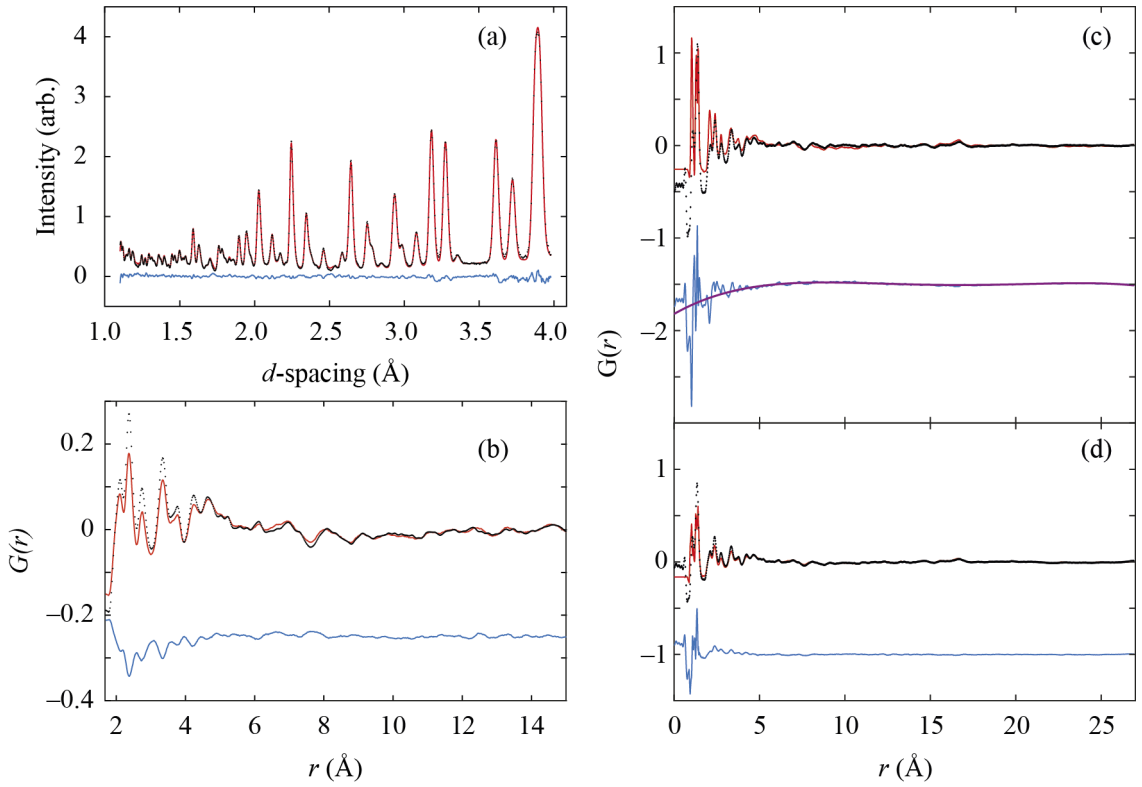

Figure E.4: (a) RMC fit (solid red line) to the experimental Bragg diffraction pattern (points). The difference curve (fit−data) is shown beneath the fit. (b) Experimental $G(r)$ data (points) and RMC fit (solid red line) with the corresponding difference curve below. Full range of the $G(r)$ functions and their fits: (c) without any modifications and (d) with a smooth function subtracted from the experimental $G(r)$ using a quadratic fit to the difference curve from (c) (the purple line) of the form $y = (v_1 - v_2)(r - v_3)(r - v_4)(r - v_5)(r - v_6)$, where v are variables. The experimental and calculated $G(r)$ functions (with their corresponding scale factors) were averaged over the five configurations in figures (b, c, d).

energy penalties. Using the five RMC configurations, the $[ZnN_2O_2]$ and $[ZnX_4]$ tetrahedra were compared and displaced according to the geometric algebra routine [Fig. E.5(d)]. The results from this analysis highlight that the largest structural changes are propagated as translational RUMs of $[ZnN_2O_2]$ coordination tetrahedra. The next largest displacements are associated with the X–Zn–X angle variation, indicating movement of the ISN ligands. Both these observation support transverse vibrational modes of ISN ligand, which is also seen in the form of the thermal ellipsoid of the Rietveld model and atomic distributions of the collapsed RMC configuration [Fig. E.3]. The rotational RUMs are much less frequently observed, showing similar occurrence to the bond stretching displacements.

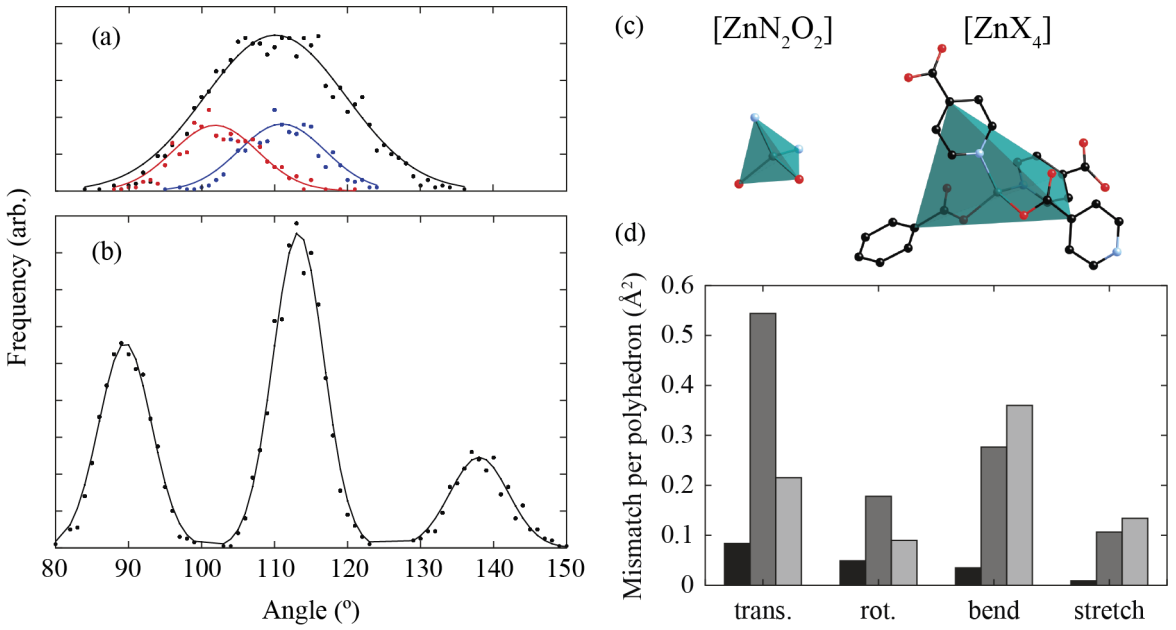

Figure E.5: RMC bond angle distributions calculated from a single RMC configuration for (a) intratetrahedral angles within the $[ZnN_2O_2]$ coordination environment (N–Zn–N in blue, O–Zn–O in red, and N–Zn–O in black) and (b) intratetrahedral X–Zn–X angles. (c) Structural representations of the $[ZnN_2O_2]$ and $[ZnX_4]$ tetrahedra. (d) Average mismatch scores obtained using GASP for α-quartz (black), the $[ZnN_2O_2]$ coordination environment in $Zn(ISN)_2$ (dark grey), and the $[ZnX_4]$ framework geometry of $Zn(ISN)_2$ (light grey), where large mismatch scores indicate large displacements. The bar chart shows the type of distortions present in the polyhedra: (left–right) translations, rotations, bond angle bending and bond stretching.

The same analysis was performed on α-quartz for comparison with $Zn(ISN)_2$. A RMC configuration of α-quartz was used, which had also been fitted to 10 K total scattering data; this RMC configuration was supplied by Dr Matthew Tucker (based upon the work from Ref. 342) [Fig. E.5(d)]. As expected, all displacements are much larger for $Zn(ISN)_2$ than for α-quartz, a result that is consistent with the general increased flexibility seen in coordination polymers. In α-quartz, the frequency of the different types of displacements are found to be correlated with the energy terms of the displacements, where low-energy RUMs are the favoured type of tetrahedral movement.

E.1.4 Discussion

Static disorder

Both the average- and local-structure analyses seem to indicate large transverse displacements of the ISN ligands in $Zn(ISN)_2$ even at 10 K. The origin of these displacements could either be from dynamical transverse vibrational modes or static disorder of the ISN ligands. In order to investigate the possible contributions of the ISN displacements, atomic displacement parameters were calculated using the following lattice dynamical formalism[29]

$$\langle u_j^2 \rangle = \frac{\hbar}{m_j \omega} \left[\frac{1}{2} + n(\omega, T) \right], \tag{E.3}$$

where $n(\omega, T) = 1/\{\exp[\hbar\omega/k_B T] - 1\}$ is the Bose-Einstein occupation number, m_j the atomic mass of species j, and ω is the phonon frequency. As the measurement of $Zn(ISN)_2$ was performed at low temperature, the displacements in Eq. (E.3) are likely to be dominated by low-energy phonons. While phonon frequencies have not been determined for $Zn(ISN)_2$, those of MOF-5 are available. As MOF-5 contains a similar ligand (terephthalate) connected *via* Zn^{2+} centres, its lowest phonon energy observed at $\omega \simeq 3$ meV was used to allow an approximate $\langle u_j^2 \rangle$ to be calculated for $Zn(ISN)_2$.[350] This ω value corresponds to an angular frequency of $\omega = 2\pi \times 0.242 \times 3 = 4.6$ THz. Substituting this ω value into into Eq. (E.3) with the appropriate molecular weights (126 $g mol^{-1}$ for ISN and 65 $g mol^{-1}$ for Zn) one obtains $\langle u_{Zn}^2 \rangle = 0.0113$ Å^2 and $\langle u_{ISN}^2 \rangle = 0.0059$ Å^2. Comparing these values to the U_{iso} values in Table E.2, it is clear that the experimental Zn and ISN displacements are, respectively, approximately 1.4 and four times larger than can be accounted for by thermal motion alone. This suggests that the displacements observed in $Zn(ISN)_2$ involve static disorder of the framework, especially the ISN ligands.

As a further check, the program PDFGUI[346] was used to calculate the $G(r)$ functions expected from the Rietveld model of Section E.1.2. First, the $G(r)$ functions were calculated for the as-refined U_{ij} and U_{iso} parameters (*i.e.* with static disorder). This gives the expected $G(r)$ corresponding to the Rietveld model. Second, the $G(r)$ was re-calculated using the displacement parameters of Eq. (E.3). This new $G(r)$ corresponds to an ordered model where displacements are only due to

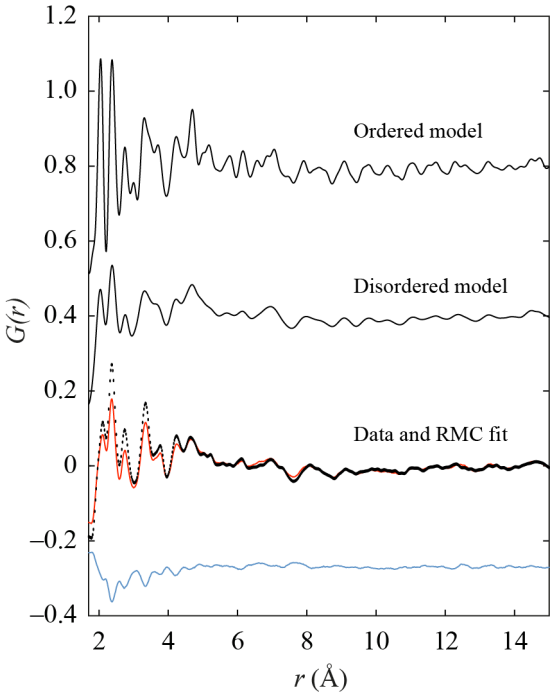

Figure E.6: Calculated and experimental $G(r)$ functions for $Zn(ISN)_2$. (*Bottom*) Experimental $G(r)$ data (filled black circles) and RMC fit (red line). (*Middle*) Calculated $G(r)$ function for the static disordered model obtained from Rietveld refinement. (*Top*) Calculated $G(r)$ function for a low-energy dynamical model.

low-energy vibrational motion. The results of both calculations are shown in Figure E.6, from which it is clear that (*i*) the ordered model gives a PDF that is much more typical of 10 K data, and (*ii*) the statically disordered model reflects well the experimental $G(r)$.

Thermal-induced mechanics

As detailed in Chapter 5, the thermal-induced mechanics of $Zn(ISN)_2$ involve framework angle variation. This variation can either occur through rigid coordination geometries, where the ligands accommodate the framework hinging or through coordination angle changes. The local structure of $Zn(ISN)_2$, even down to 10 K, does show greater tetrahedral angle variation than it does rigid tetrahedral tilting [Fig. E.5]. This suggests that the thermal response of $Zn(ISN)_2$ is brought about by direct coordination angle variation.

E.1.5 Summary

A combination of Rietveld and RMC refinement of neutron total scattering data was used to study the local and average structure of zinc(II) isonicotinate. While this study has unquestionably been complicated by the inclusion of hydrogen-containing solvent molecules within the pore structure of the framework, there is evidence for the existence of large-scale static disorder in the material at 10 K. This disorder involves displacements of the Zn tetrahedral environment and uncorrelated displacements of the ISN ligands, which give rise to a large variation in coordination angles.

Future work of this nature would be most successful with non-porous coordination polymers, ensuring no ambiguities on the structure density. Characterisation of possible local disorder in the non-porous diamondoid $Zn(ISN)_2$ (Ref. 351) will allow more conclusive evidence on any static disorder present, especially as the effect of disordered solvent on the framework dynamics is not well understood. Local structure analysis using the GA-based code on a coordination polymer which has constrained coordination, such as a Ni-containing framework structure, would be interesting to help clarify the effect of LFSE remarked in Chapter 6.

E.2 Ferroelectric ordering in $[NH_4][Zn(HCOO)_3]$

Ammonium zinc formate, $[NH_4][Zn(HCOO)_3]$, was studied as a function of temperature in order to characterise the nature of the ferroelectric ordering of the ammonium cations within the framework cavities. The transition between the low-temperature ordered phase ($P6_3$, LT) and the high-temperature disordered phase ($P6_322$, HT) corresponds to orientational order–disorder of the three NH_4^+ cations per formula unit $\left(\mathrm{N1} : \frac{2}{3}, \frac{1}{3}, z\right)$, $\left(\mathrm{N2} : \frac{1}{3}, \frac{2}{3}, z\right)$, and $(\mathrm{N3} : 0, 0, z)$ [Fig. E.7]. The relation between the $P6_3$ and $P6_322$ unit cells is given by the transformation

$$\begin{bmatrix} \mathbf{a} \\ \mathbf{b} \\ \mathbf{c} \end{bmatrix}_{P6_3} = \begin{bmatrix} 1 & -1 & 0 \\ 1 & 2 & 0 \\ 0 & 0 & 1 \end{bmatrix} \times \begin{bmatrix} \mathbf{a} \\ \mathbf{b} \\ \mathbf{c} \end{bmatrix}_{P6_322} . \tag{E.4}$$

In the LT-phase, the three crystallographically unique NH_4^+ ions are shifted by $-0.36\,\text{Å}$, $-0.38\,\text{Å}$, and $+0.4\,\text{Å}$ along the c-direction with respect to the anionic framework, giving an overall polarisation along that direction of $0.96\,\mu\text{C}\,\text{cm}^{-2}$; Refs. 314,315. This value is typical for hydrogen-bonded ferroelectrics, such as KH_2PO_4 at $5\,\mu\text{C}\,\text{cm}^{-2}$ and Rochelle salt at $0.25\,\mu\text{C}\,\text{cm}^{-2}$.[352] A recent Raman and IR study on a related structure, $[NH_4][Mg(HCOO)_3]$, indicated that the transition is due to orientational ordering of the NH_4^+ ions, but that the rotational and translational motions do not freeze completely at the phase transition.[320]

The transition temperature of $[NH_4][Zn(HCOO)_3]$ is measured at 191–192 K.[314] Single-crystal structures have been determined at either side of the transition at 110 K and 290 K [Fig. E.7], but there are no structural models in-between this temperature range to allow the transition to be fully characterised. In order to elucidate the mechanism of the ferroelectric ordering in $[NH_4][Zn(HCOO)_3]$, RMC refinements were performed on neutron total scattering data collected over the temperature range 50–300 K at intervals of 50 K.

The use of neutron diffraction is particularly advantageous in order to locate the NH_4^+ cations, especially as N has the highest neutron scattering length compared to all other elements found

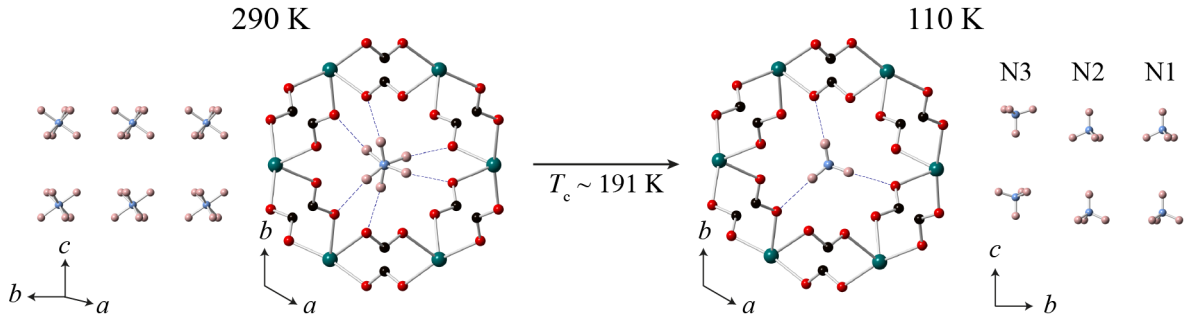

Figure E.7: Order–disorder phase transition of the ammonium in $[NH_4][Zn(HCOO)_3]$ induced by cooling from ambient temperature to below 191 K. The different heights of the three ammonium cations in the LT-phase can be seen along the *c*-axis, while in the HT-phase, the ammonium cations are at the same height with the hydrogens disordered onto six sites. The dotted blue lines indicate the hydrogen bonding. Hydrogens on the formate have been omitted for clarity.

in ammonium zinc formate [Table 2.1]. Yet to minimise the inelastic scattering from H, the ammonium zinc formate should be prepared in deuterated form.

E.2.1 Experimental

E.2.1.1 Synthesis

A deuterated polycrystalline sample of ammonium zinc formate was synthesised by mixing $ZnCl_2$ (3.548 g, 26.03 mmol; Aldrich, 99.999%) and $DCOOND_4$ (7.085 g, 104.112 mmol; QMx, 98% D) with DCOOD (2.5 g, 52.06 mmol; QMx, 95% w/w in D_2O) in 520.56 mL of CH_3OD (Sigma-Aldrich, 98% D). The synthesis was performed under inert atmospheres with the help of Alex Corkett, and was kept undisturbed for a week to allow polycrystals to form. The powder formed was filtered and washed with deuterated methanol. This powder, however, had a considerable amount of zinc formate dihydrate impurity. A pure sample of ammonium zinc formate was obtained by mixing the as-synthesised powder with 1 g of $DCOOND_4$ in methanol [Fig. E.8]. It is thought that the deuterated methanol was not completely anhydrous and contaminated the deuterated sample with water and hydrogen. Hence, the sample will be referred to as $[N(D/H)_4][Zn(DCOO)_3]$, because it was found subsequently from Rietveld refinements that the ammonium deuterium positions were contaminated with hydrogen, discussed in greater detail in Section E.2.3. The pure

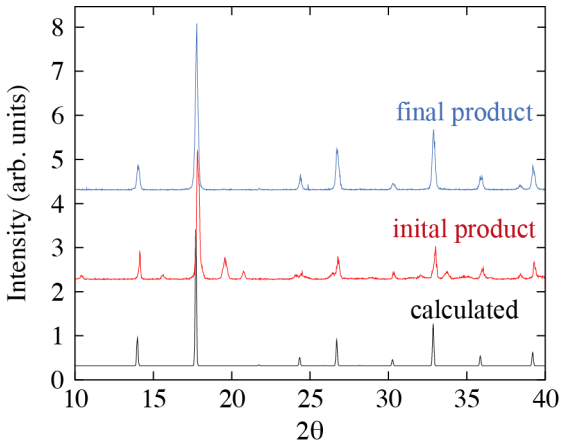

Figure E.8: X-ray diffraction pattern of the initially synthesised $[N(D/H)_4][Zn(DCOO)_3]$ (red profile), and after subsequent exposure to excess $DCOOND_4$ (blue profile). The calculated diffraction from the single-crystal structure of 290 K $[NH_4][Zn(HCOO)_3]$ from Ref. 314 is shown in black.

$[N(D/H)_4][Zn(DCOO)_3]$ was dried *in vacuo* at 60°C for 24 h prior to the GEM experiment. The total product weighed 1.8718 g, thus giving a yield of 32% for the synthesis.

E.2.1.2 Neutron total scattering measurements

Two types of variable-temperature neutron powder scattering measurements were performed on $[N(D/H)_4][Zn(DCOO)_3]$. The first, involved quick diffraction runs every 10 K from 10–300 K for Rietveld refinement and lattice parameter extraction. Secondly, long collection runs were carried out on cooling from 300 K down to 50 K every 50 K in order to obtain variable-temperature total scattering data. For the experiment, 1.812 g of $[N(D/H)_4][Zn(DCOO)_3]$ were placed within a cylindrical vanadium can of 8.3 mm diameter and 6 cm height. A closed cycle helium refrigerator on the GEM beamline was used to control the sample temperature.

E.2.1.3 Total scattering data correction

The presence of hydrogen in $[N(D/H)_4][Zn(DCOO)_3]$ was evidenced in the different background levels of the GEM detector banks [Fig. E.9]. Therefore, the top hat convolution method was applied to $[N(D/H)_4][Zn(DCOO)_3]$ as part of the data normalisation procedure.

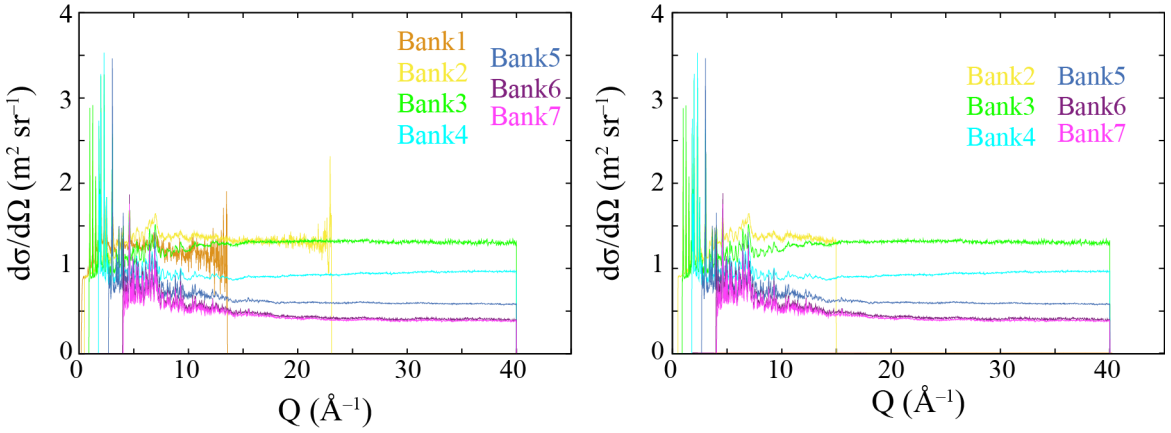

Figure E.9: (*Left*) Differential cross-section data for $[N(H/D)_4][Zn(DCOO)_3]$ in the full data range for all GEM detector banks, represented by the different colours to match those defined in Figure 2.5. (*Right*) The differential cross-section data ranges that were used for correcting the data of $[N(H/D)_4][Zn(DCOO)_3]$.

E.2.1.4 Rietveld refinement

The short diffraction runs were analysed in TOPAS academic version 4.1 using the detector bank centred on the scattering angle $2\theta = 63.62°$. Rietveld refinements made use of the LT-model from Ref. 314 and were performed sequentially, where the previous temperature model was used as a starting model for the next temperature. Lattice parameters were extracted from these fits.

For the total scattering data, the Rietveld model fitted to the data from five detector banks (centred on $2\theta = 17.98°, 34.96°, 63.62°, 91.37°, 154.46°$) simultaneously in TOPAS. For all temperatures, the LT-phase from Ref. 314 was used as a starting model. For the Rietveld refinements, the formate ligands were refined as rigid bodies and restraints were applied for the Zn–O and N–H bonding distances. The position of the Zn atom was freely refined in the (x, y)-plane, and kept fixed along z-axis due to the lack of unique origin in $P6_3$ symmetry. The N positions, being fixed in the (x, y)-plane due to their special positions, were refined freely along the z-axis. Isotropic thermal parameters were refined for Zn, formate and ammonium ions.

In order to obtain the Bragg profile parameters for RMCPROFILE, the refined models from TOPAS were used to refine the same data in GSAS. In these GSAS refinements, background, scale factors, peak shapes, lattice parameters, atomic and thermal parameters were refined. Thermal similarity restraints within the formate and ammonium ions were applied.

Table E.3: Distance-window parameters $d_{\min}$ and $d_{\max}$ used in the RMC refinements.

Atom pair	$d_{\min}$ (Å)	$d_{\max}$ (Å)
C–D	0.87	1.15
C–O	1.15	1.4
N–H	0.87	1.15
Zn–O	1.8	2.5

E.2.1.5 Reverse Monte Carlo refinement

A large atomistic configuration suitable for RMC refinements was prepared as a supercell of the model obtained from Rietveld refinements. In order to maximise the pair distribution cut-off value $r_{\max}$, the hexagonal cell was converted to an orthogonal one using the transformation

$$\begin{bmatrix} \mathbf{a} \\ \mathbf{b} \\ \mathbf{c} \end{bmatrix}_{\text{ortho}} = \begin{bmatrix} 1 & 0 & 0 \\ 1 & 2 & 0 \\ 0 & 0 & 1 \end{bmatrix} \times \begin{bmatrix} \mathbf{a} \\ \mathbf{b} \\ \mathbf{c} \end{bmatrix}_{\text{hexa}} . \tag{E.5}$$

This orthogonalised cell was then used as a basis to produce a $6 \times 4 \times 10$ supercell, giving the dimensions of $75.47\,\text{Å} \times 87.15\,\text{Å} \times 82.06\,\text{Å}$ at 50 K and a total of 51 840 atoms. The configuration contained six different atoms types (C, D, H, N, O, Zn), where H refers to the H/D mix found for the ammonium cations. A number of soft constraints and restraints were applied to the refinements through distance-window constraints [Table E.3] and geometric restraints of the zinc formate framework and the ammonium cations [Table E.4]. These allowed framework connectivity to be maintained and molecular geometry to be restrained within sensible values. The soft coordination restraints for Zn were applied only to configurations that were not constrained by data, allowing so-called RMC 'randomised' models to be produced with reasonable Zn coordination environments.

The refinement process was driven by fitting to the experimental $D(r)$ ($0.02 \leq r \leq 37.72$ Å), $F(Q)$ ($0.52 \leq Q \leq 40$ Å^{-1}), and $I(t)$ ($4870 \leq t \leq 19590\,\mu$s; equivalent to the d-spacing range 1–4 Å) functions for the six different temperatures (50, 100, 150, 200, 250 and 300 K). Four different starting models were used to test the robustness and reproducibility of the final RMC configurations.

Table E.4: Soft restraints on the bonding distances and bonding angles used in the RMC refinements based upon the published MM3 potentials.[353,354] The first atom within the angle terms refers to the central atom.

Atom pair stretch	energy (eV)	distance (Å)
C–D	2.272	1.096
C–O	4.847	1.208
N–H	3.081	1.015
Zn–O	4.0	2.121
Atoms within angle	**energy (eV)**	**angle (°)**
C–D–O	7.989	120.5
C–O–O	17.876	129.8
N–H–H	7.552	106.4
Zn–O–O	4.0	90.1
Zn–O–O	4.0	171.1

The first model involved using the crystalline configuration obtained from Rietveld refinements for each temperature. The second and third models used the same starting configuration of atomic coordinates for the 50 K and 300 K models, respectively, for all temperatures (the corresponding

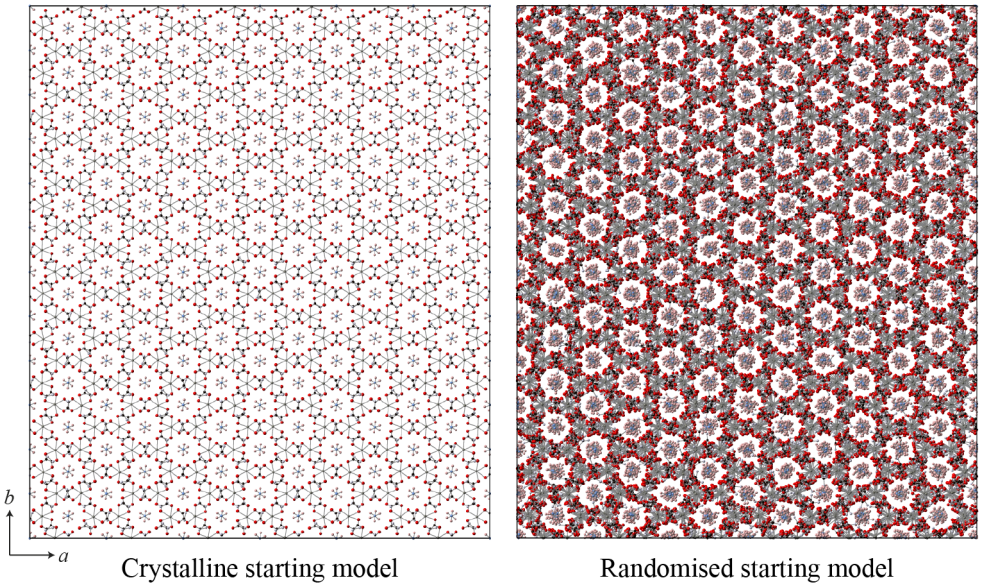

Figure E.10: The crystalline starting model shown for 50 K and its corresponding randomised model obtained through an effective Monte Carlo refinement.

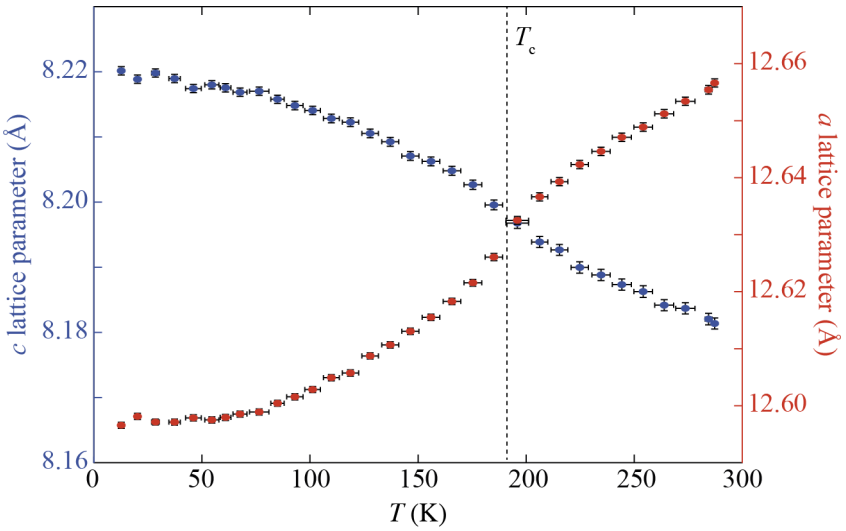

Figure E.11: Lattice parameter evolutions as a function of temperature for the a (red points) and c (blue points) lattice parameters. T_c indicates the phase transition temperature.

lattice parameters were changed for each temperature). The fourth model made use of the crystalline starting models for each temperature which were subsequently 'randomised' by excluding data and fitting only to the energy terms listed in Table E.4. This had the effect of running a Monte Carlo refinement. These configurations were run for $\sim$ 100 moves per atom, allowing the configurations to randomise while maintaining framework connectivity [Fig. E.10].

E.2.2 Temperature-induced mechanics

The variable-temperature lattice parameter evolutions, which were determined from the quick diffraction runs, show that the (a, b)-plane expands and the c-axis contracts upon increasing temperature [Fig. E.11]. In these evolutions, there are only subtle changes in gradient after T_c. The CTEs for the whole temperature range are $\alpha_a = 19.5(8)\,\mathrm{MK}^{-1}$, and $\alpha_c = -18.8(7)\,\mathrm{MK}^{-1}$. These anisotropic expansivities are indicative of a hinging mechanism and have the same anisotropy as the compressibilities observed in this compound.[185] As illustrated in Chapter 5, the geometry in this structure predicts the negative response to be along the c-axis.

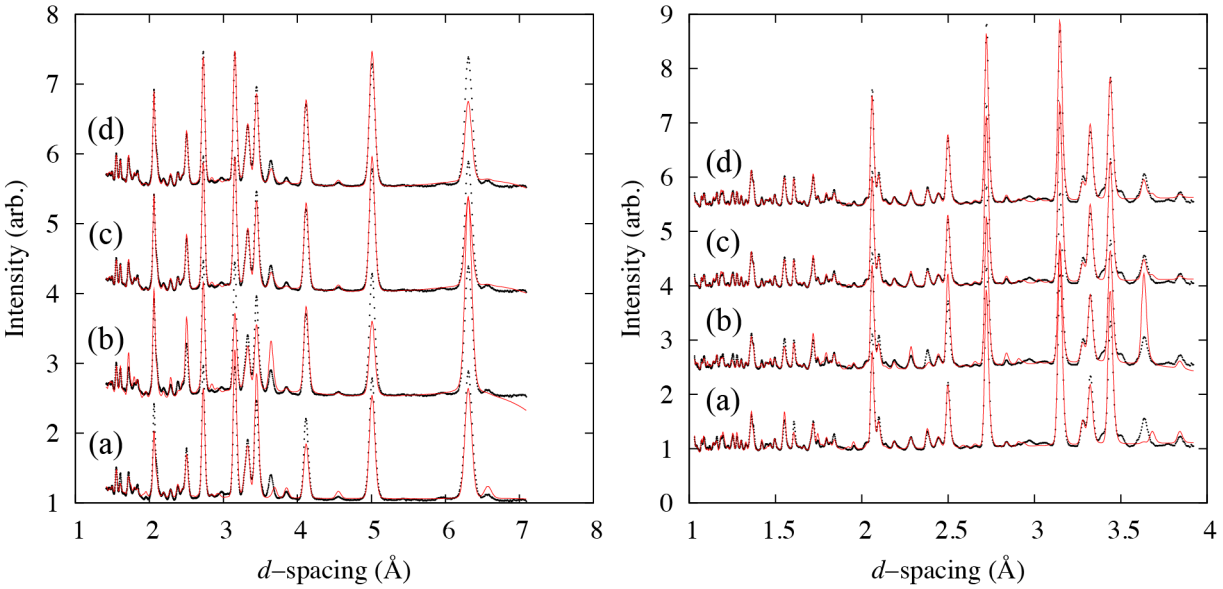

Figure E.12: Rietveld fits of the Bragg data at 50 K with different compositions of H and D on the ammonium cation in $[N(H/D)_4][Zn(DCOO)_3]$. The corresponding compositions include (a) ND_4, (b) NH_4, (c) N with no H or D, and (d) the mixed concentration $ND_{1.488}H_{2.512}$.

E.2.3 Average structure of $[N(H/D)_4][Zn(DCOO)_3]$

It was apparent from the Rietveld fits that the contribution of the ammonium deuterium to the scattering was minimal; its overall site occupancy was refined to 0.372, suggesting that a considerable quantity of hydrogen had substituted the deuterium position [Fig. E.12]. Due to the different neutron scattering lengths of D and H [Table 2.1], the average neutron scattering from this site is calculated as

$$(0.372 \times 6.671) - (0.628 \times 3.739) = 0.13252\,\text{fm}. \tag{E.6}$$

While it could be argued that subsequent analysis should have been carried out by excluding explicitly either H or D atoms on the ammonium cations, the total scattering data correction within GUDRUN required the H occupancy in order to correct the data properly. Within the sensitivity of the data, there was no sign that the formate ligands were anything but fully deuterated. Thus, the composition $[ND_{1.488}H_{2.512}][Zn(DCOO)_3]$ is used for all the subsequent analysis.

E.2.4 Local structure of $[N(H/D)_4][Zn(DCOO)_3]$

The mix of H and D was modelled in RMC by including H atoms on the ammonium with a scattering length of 0.13252 fm. The final RMC configurations that had started from their corresponding temperature Rietveld models gave similar fits to those obtained from Rietveld refinement [Fig. E.13(a)]. Likewise, the calculated $D(r)$ and $F(Q)$ from the final RMC configurations were consistent with the equivalent experimental functions [Fig. E.13(b)].

The RMC configuration for each temperature was 'collapsed' onto a single unit cell of $P6_3$ symmetry [Fig. E.14]. The atomic distributions from these 'collapsed' configurations show large anisotropy for the formate ligands, while those of N and Zn remain isotropic. The shapes of the formate distributions suggest a rocking movement about the Zn$\cdots$Zn axis. This is most accentuated for the D atomic distributions, which form an arc shape about the C distributions to which they are attached. This highlights a high degree of rotational freedom about the coordination bond. Another feature of the 'collapsed' configurations is the change in z-coordinate for the N atomic distributions as a function of temperature. In the LT-phase, the z-coordinate levels for the four N distributions shown along the b-axis are at different z heights, while they align to the same z level in the HT-phase. However, an overall offset can be seen in comparison to the zinc atomic distributions, which gives rise to non-zero polarisations even for the aligned N atomic distributions. This is probably due to the difficulty of shifting the whole framework origin during RMC fitting, while that of the ammonium cations is more readily achieved.

The local structure in the RMC configurations can be further analysed by the partial radial distribution functions $d_{ij}(r)$, which are generated by the RMC configurations. The $d_{ij}(r)$ function for the N$\cdots$O distances is shown in Figure E.15. From the crystal structures, the LT-phase shows two immediate N$\cdots$O distances, as the ammonium cation is off-centred within the pore, while in the HT-phase the ammonium cation is directly centred, giving rise to one unique N$\cdots$O distance.[314] However, as these are average structure models, it is only by examining the local structure of the ammonium cations that the displacements associated with the transition can be elucidated. For example, the same average structure would arise for the HT-phase from (*i*) uncorrelated ammonium cation off-centering, and (*ii*) the centred ammonium cation coordinates

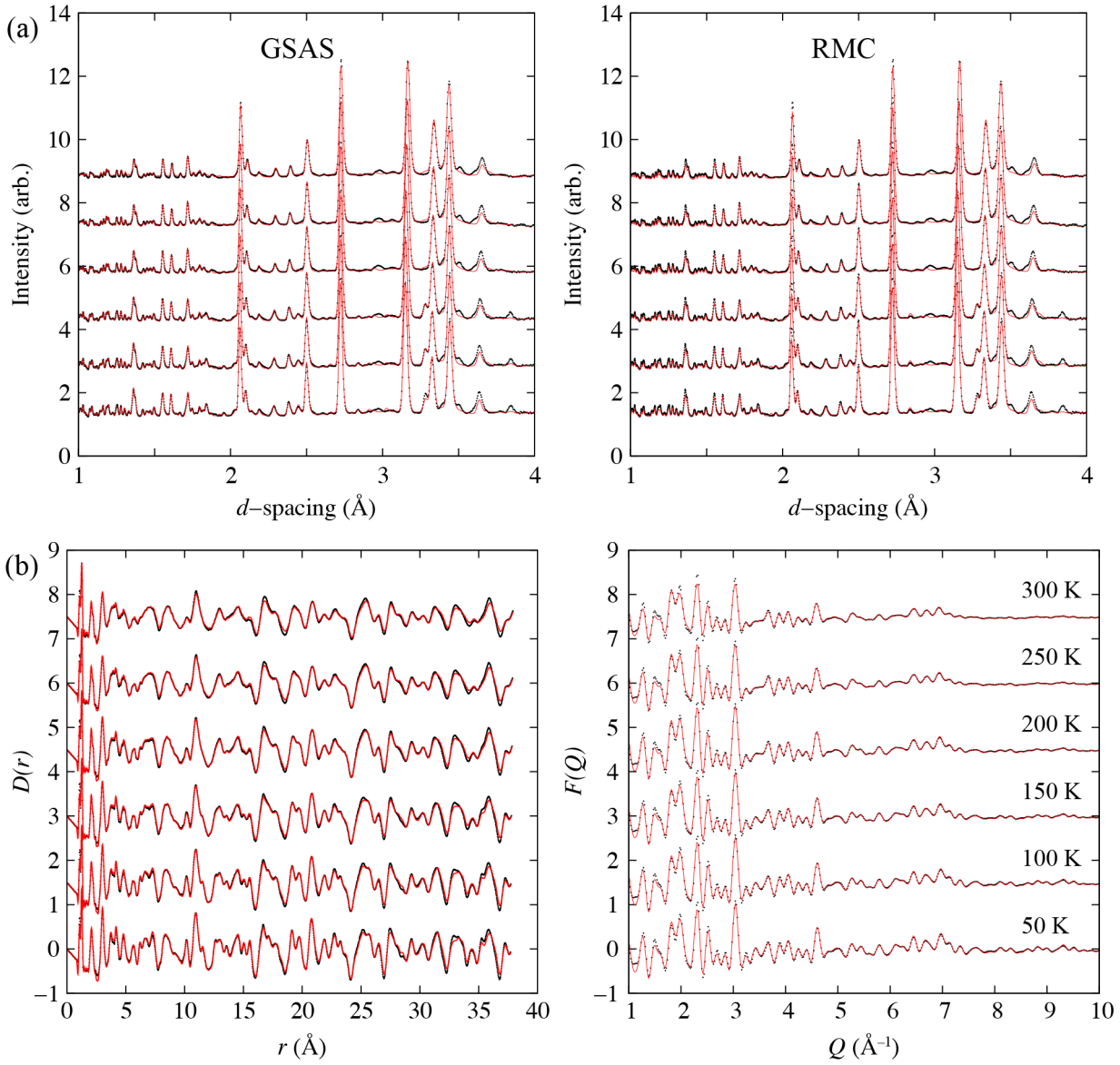

Figure E.13: (a) GSAS and RMC fits (solid red line) to the experimental Bragg diffraction pattern (points) and (b) RMC fits (red line) of experimental $D(r)$ and $F(Q)$ data (points) for $[N(D/H)_4][Zn(DCOO)_3]$. Plots for successive temperature points have been raised by intervals of 1.5 units for ease of representation (shown in order with 50 K at the bottom, as indicated in the $F(Q)$ graphic).

seen in the crystallographic HT-phase. The first peak of the $d_{ij}(r)$ in Figure E.15 corresponds to the shortest N···O distance and thus gives an indication of the H–O hydrogen bonding distance. However, this peak is too broad to show any peak splitting between the different temperatures [Fig. E.15]. The second N···O distance does exhibit two peaks for the LT-phase (50–150 K), while one broad peak is observed for the HT-phase (200–300 K). This indicates that the HT-phase

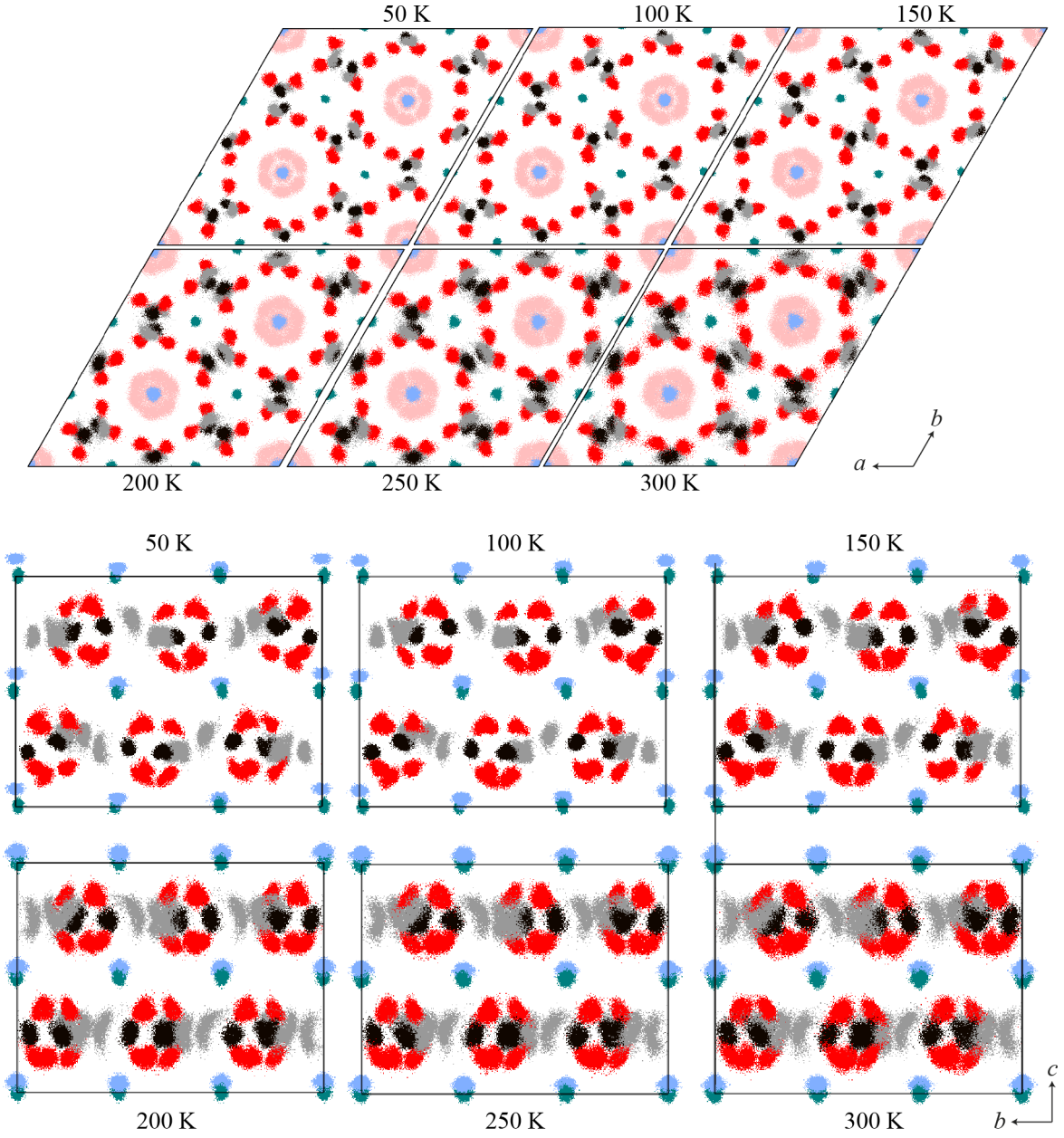

Figure E.14: Atomic distributions obtained by collapsing the RMC configuration onto a single unit cell and applying $P6_3$ symmetry. These projections are viewed down the c-axis (*top*), and a-axis (*bottom*). The hydrogens have been removed for the (100) projection for clarity (Zn: green, N: light blue, O: red, C: black, D: grey, H: pink).

contains ammonium cations which are centred within the zinc formate pore even on a local level, as well as on average. The local structure is therefore consistent with an average structure model and highlights some displacive character to the transition.

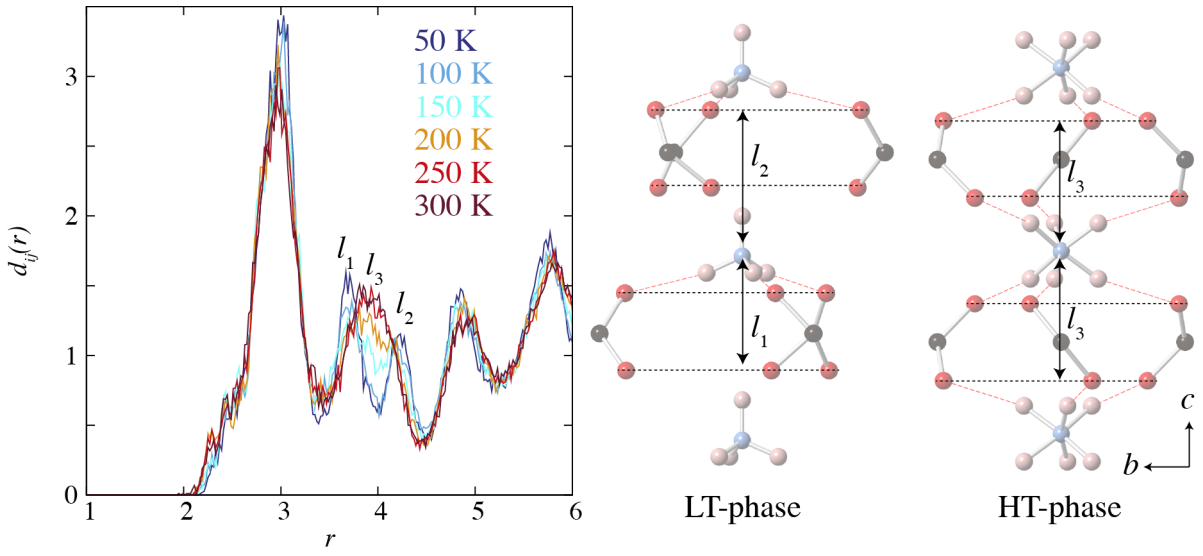

Figure E.15: N···O partial distribution functions as a function of temperature. The l_1, l_2, and l_3 indicate the N···O distances shown in the structural representations of the LT and HT crystal structures from Ref. 314.

E.2.5 Tracking the order–disorder transition with RMC

The order–disorder transition was investigated further by calculating two parameters from the RMC configurations. For these calculations, the RMC supercells were 'collapsed' onto a single unit cell. From this average atomic configuration, the z-coordinate positions of the three nitrogens (N1, N2, N3 mentioned in section E.2), and the standard deviation between them (σ_{z_N}) were calculated. Additionally, the polarisation along the c-axis (P_z) of the 'collapsed' unit cell was calculated by determining the average position of the framework atoms and comparing this to the average position of the nitrogen atoms. These were calculated for the different starting models mentioned in Section E.2.1.5.

Before considering the σ_{z_N} and P_z values from the data-fitted RMC configurations, it is worth assessing those of the initial and 'randomised' configurations. Three different starting configurations were generated from crystalline models. The first (labelled "GSAS") refers to each RMC refinement which had started from its corresponding temperature crystalline model refined in GSAS. The second model involved using the 50 K GSAS refined atomic coordinates for all temperatures

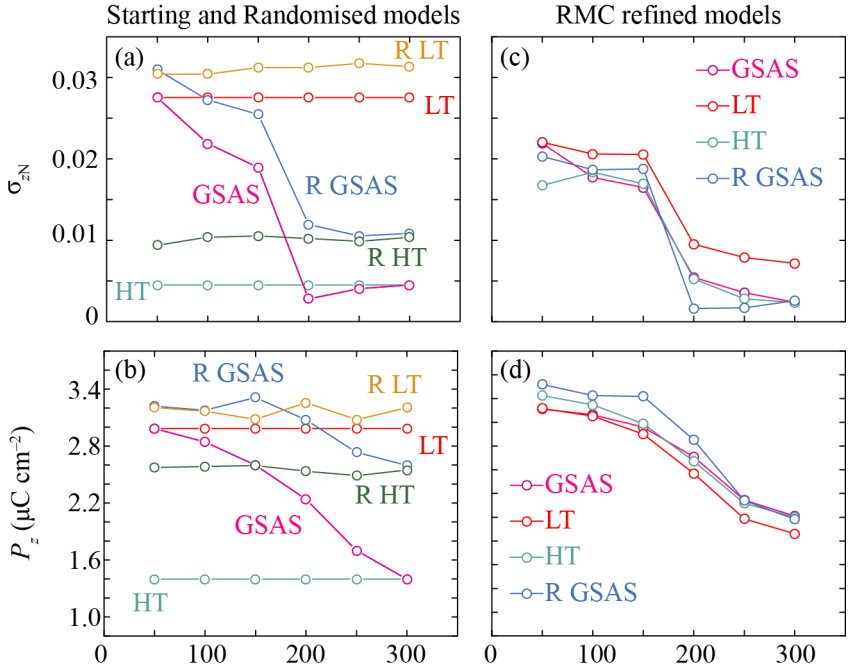

Figure E.16: The evolutions of the standard deviation of the N z-coordinates (σ_{z_N}) and the overall polarisation (P_z) over the 50–300 K temperature range for the GSAS, HT, LT starting models. Randomised models are indicated by 'R' prior to its starting model configuration name. Graphs (a) and (b) represent σ_{z_N} and P_z values from starting and randomised models, while (c) and (d) show these values after RMC refinement to the $G(r)$, $F(Q)$ and $I(t)$ data as described in the main text.

(labelled "LT"), and the third model used the 300 K GSAS refined atomic coordinates for all temperatures (labelled "HT"). Structure randomisation was performed on all three of these starting models by fitting only to the potentials shown in Table E.4, and the σ_{z_N} and P_z values were calculated for the six configurations associated with the different temperatures [Fig. E.16(a,b)]. What is immediately apparent is that the 'randomisation' process does not translate to a randomisation of σ_{z_N} and P_z values; instead similar trends to the starting models are observed as a function of temperature.

From the RMC-refined configurations, the evolutions of σ_{z_N} and P_z as a function of temperature are shown in Figure E.16(c,d). Both σ_{z_N} and P_z parameters decrease towards zero upon increasing temperature, as is expected from this type of transition. The GSAS and 'randomised' GSAS refined models both show very similar trends to their starting configuration, however, there is a clear data-driven change in temperature evolution of the HT and LT configurations. The variation in σ_{z_N} as a function of temperature is sensitive to the phase transition, where an abrupt change between

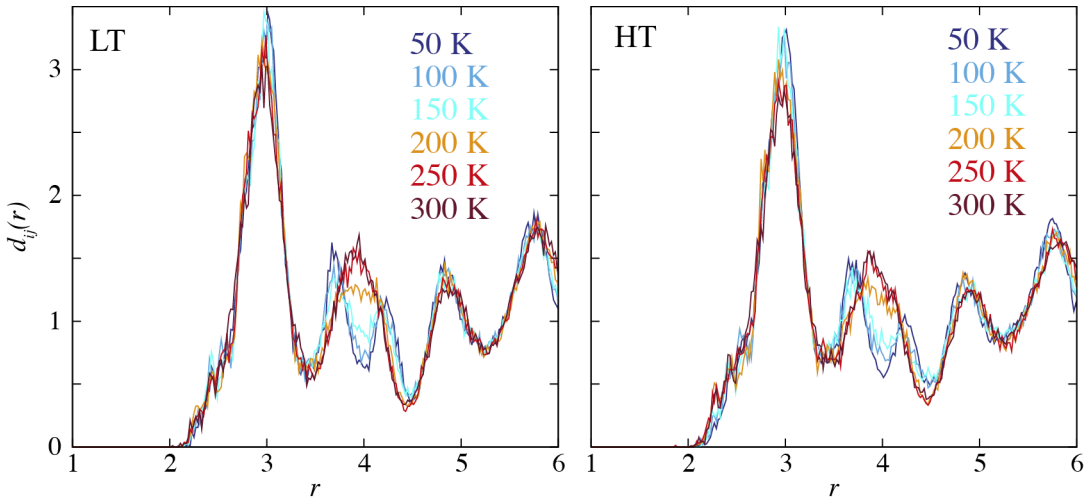

Figure E.17: N···O partial distribution functions as a function of temperature for the LT and HT models.

150 and 200 K configurations is observed. Conversely, the polarisation values show a continuous decrease upon increasing temperature, which may arise from the difficulty in modifying the whole framework origin in the RMC configurations.

Having established that the LT and HT starting models do not bias the temperature-dependent parameters relevant in the ferroelectric phase transition, the $d_{ij}(r)$ functions corresponding to N···O distances were re-calculated for these models [Fig. E.17]. The peak convergence for the HT-phase, and peak splitting in the LT-phase is clearly observed in both models despite the fact that these configurations had started with the same N···O distances for all temperatures.

E.2.6 Discussion and future work

The large dynamical motion of the formate ligand observed in the average collapsed RMC configurations may have important implications in the order–disorder transition. This is because the hydrogen bonding from the ammonium cation involves the oxygen atom of the formate linker, and greater motion of the latter would suggest weaker hydrogen bonding. While investigations have focused on variation of the A-site cation to improve ferroelectric polarisations,[355] the work shown here suggests that the dynamical properties of the ligand may also be an important contributing factor.

The local structure of $[N(H/D)_4][Zn(HCOO)_3]$ was consistent with the average crystallographic structural models. In particular, off-centred ammonium cations relative to the framework pore are found below T_c, while above this temperature, the ammonium cations assume a centred position within the framework cavity, thus exhibiting zero net polarisation. This local and average structural insight suggests that the ferroelectric transition has some displacive character. The positions of the hydrogens on the ammonium cations could not be reliably defined due to the H/D concentration, therefore the exact tumbling nature of the ammonium at HT could not be identified.

Future work on $[N(H/D)_4][Zn(HCOO)_3]$ would involve evaluating its local structure in more detail. The use of the GASP code would allow the octahedral displacements and distortions to be categorised. The tetrahedral Zn environment in $Zn(ISN)_2$ could then be contrasted to an octahedral one in $[N(H/D)_4][Zn(HCOO)_3]$. The RMC fitting of such a large supercell in $[N(H/D)_4][Zn(HCOO)_3]$ has highlighted the need for rigid body constraints, as found within Rietveld analysis, to be implemented in the RMC fitting procedure. For the N atoms in $[N(H/D)_4][Zn(HCOO)_3]$, their displacements within RMC are only accepted by evaluating the impact produced on the four hydrogens attached to each N, defined by the molecular potential terms. In this way, the N displacements are hindered, and this is highlighted in the 'randomised' models, which do not appear to adequately displace the ammonium cations.

E.2.7 Summary

Neutron total scattering at six different temperatures was used to investigate the order–disorder transition in ammonium zinc formate. The atomic distributions from RMC refinements allowed the local and average displacements that occurred before and after the transition temperature to be characterised. These displacements were consistent with a degree of displacive character to the phase transition, and also highlighted that the formate ligands had large anisotropic dynamics.

E.3 Conclusions

The local structure investigations of $Zn(ISN)_2$ and $[N(H/D)_4][Zn(HCOO)_3]$ have given insightful information regarding the static disorder of the ISN ligands, and the displacive character to the ferroelectric phase transition, respectively. However, both studies have been complicated by the ambiguity of the structure density, hence for future studies, the ability to deuterate fully should be the primary consideration when choosing the appropriate coordination polymer to be investigated. In addition, a completely empty pore structure will be challenging to maintain in porous MOFs; $Zn(ISN)_2$ even showed considerable uptake of CO_2 from the atmosphere.

Even with these considerations having been taken into account, there remain difficulties associated with the RMC refinement process itself. The RMCPROFILE program provides an ideal way to fit all the data from the total scattering experiment, but as the RMC configurations increase in size owing to the large unit cells of coordination polymers, the single atomic move algorithm is slow to realise the interesting dynamics of coordination polymers. RUMs, transverse vibration or rotational dynamics may involve whole molecules instead of atoms. Hence, implementation of 'rigid-body' type definition for ligands would speed up the RMC fitting of these large configurations, consequently allowing the relevant dynamics to be extracted more readily.

Appendix F

CD contents

Due to the large data sets used in this investigation, it was not possible to show all data in this thesis. Instead, all the raw data, TOPAS input files, CIF files, and the lattice parameters (in excel spreadsheets) can be found in the supplementary CD. These data are provided for each chapter, and are categorised by compound.